
Science
4 May 2012 | $10
AAAS

CONTENTS

Volume 336 Issue 6081

CONTENTS continued >>

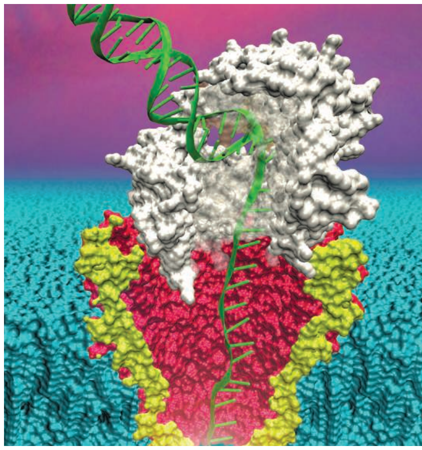

page 534

page 543

COVER

A jumble of icebergs forms in front of the heavily crevassed calving front of Jakobshavn Isbræ, one of the fastest outlet glaciers draining the Greenland Ice Sheet. The ~5-kilometer-wide ice front rises ~80 meters out of the water and extends more than 600 meters underwater. Recent research shows that the speeds of Greenland glaciers are increasing. See page 576.

Photo: Ian Joughin

DEPARTMENTS

RESEARCH ARTICLE

REPORTS

CONTENTS continued >>

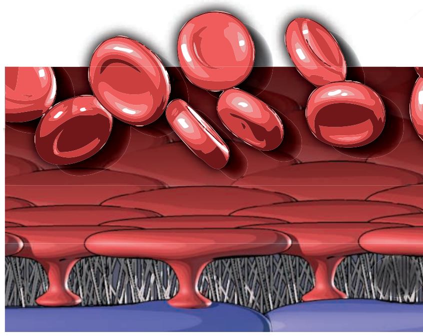

pages 546 & 597

page 570

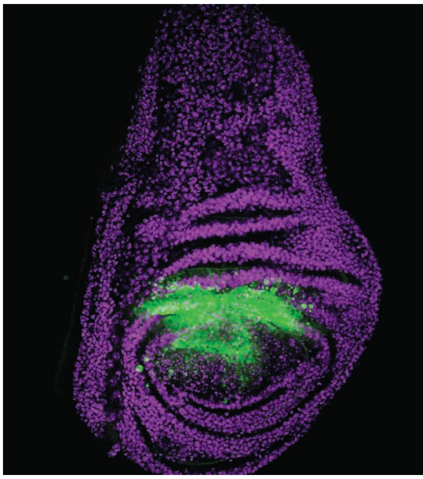

pages 579 & 582

CREDITS: (MIDDLE) NASA/JPL/CORNELL/ASU; (BOTTOM) ANDRES GARELLI, ALISSON GONTIJO, MARIA DOMINGUEZ

*SCIENCE*ONLINE

*SCIENCE*XPRESS

www.sciencexpress.org

TECHNICAL**COMMENTS**

*SCIENCE*NOW

www.sciencenow.org
Highlights From Our Daily News Coverage

*SCIENCE*SIGNALING

www.sciencesignaling.org
The Signal Transduction Knowledge Environment
1 May issue: http://scim.ag/ss050112

*SCIENCE*TRANSLATIONAL MEDICINE

www.sciencetranslationalmedicine.org
Integrating Medicine and Science
2 May issue: http://scim.ag/stm050212

*SCIENCE*CAREERS

www.sciencecareers.org/career_magazine
Free Career Resources for Scientists

*SCIENCE*PODCAST

www.sciencemag.org/multimedia/podcast
Free Weekly Show

On the 4 May *Science* Podcast: remotely controlled gene expression, evidence for water on ancient Mars, nanopore sequencing advances, and more.

*SCIENCE*INSIDER

news.sciencemag.org/scienceinsider
Science Policy News and Analysis

SCIENCE (ISSN 0036-8075) is published weekly on Friday, except the last week in December, by the American Association for the Advancement of Science, 1200 New York Avenue, NW, Washington, DC 20005. Periodicals Mail postage (publication No. 484460) paid at Washington, DC, and additional mailing offices. Domestic individual membership and subscription (51 issues): $149 ($74 allocated to subscription). Domestic institutional subscription (51 issues): $990; Foreign postage extra: Mexico, Caribbean (surface mail) $55; other countries (air assist delivery) $85. First class, airmail, student, and emeritus rates on request. Canadian rates with GST available upon request, GST #1254 88122. Publications Mail Agreement Number 1069624. **Printed in the U.S.A**.

Change of address: Allow 4 weeks, giving old and new addresses and 8-digit account number. **Postmaster:** Send change of address to AAAS, P.O. Box 96178, Washington, DC 20090–6178. **Single-copy sales:** $10.00 current issue, $15.00 back issue prepaid includes surface postage; bulk rates on request. The identification code for *Science* is 0036-8075. *Science* is indexed in the *Reader's Guide to Periodical Literature* and in several specialized indexes.

AAAS
ADVANCING SCIENCE, SERVING SOCIETY

EDITED BY STELLA HURTLEY

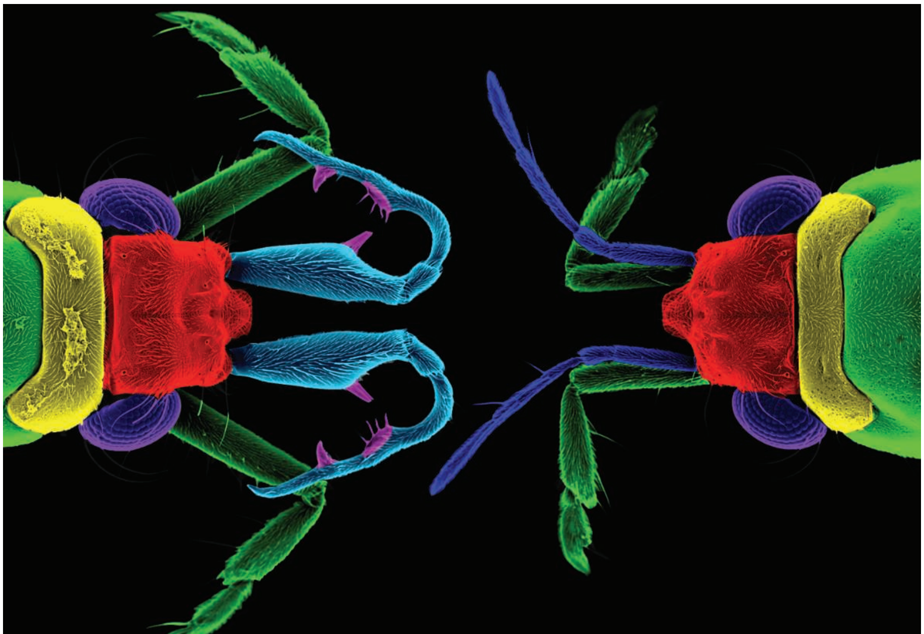

Hooking Up in Water Striders

The male water strider *Rheumatobates rileyi* has an extensively modified antenna that is used for forced copulations with females. **Khila *et al.*** (p. 585) describe several microscopic antenna attributes that make the antenna fit perfectly with the female head when the male grasps the female. The features depend upon the expression of the gene *distal-less* (*dll*) during antenna development. Reducing the expression of *dll* compromised male grasping traits, while female antennae were unaffected.

Giant Spin Hall

One of the primary challenges in the field of spin-electronics, which exploits the electron's spin rather than its charge, is to create strong currents of electrons with polarized spins. One way to do this is to use a ferromagnet as a polarizer, a principle used in magnetic tunnel junctions; however, these devices suffer from reliability problems. An alternative is the spin Hall effect, where running a charge current through a material generates a spin current in the transverse direction, but the efficiency of this process tends to be small. **Liu *et al.*** (p. 555) now show that the spin Hall effect in Tantalum in its high-resistance β phase generates spin currents strong enough to induce switching of the magnetization of an adjacent ferromagnet; at the same time, Ta does not cause energy dissipation in the ferromagnet. These properties allowed efficient and reliable operation of a prototype three-terminal device.

Uneven Gap

Electron pairs that are responsible for the phenomenon of superconductivity can only be broken by investing a finite amount of energy, called the energy gap. The size of the gap may depend on the position on the Fermi surface; in cuprates, the gap completely disappears at certain points. What happens in the pnictide superconductors is still a subject of debate, not least because there appear to be differences between the different pnictide families. **Allan *et al.*** (p. 563) used scanning tunneling spectroscopy to study the compound LiFeAs. The gap was mapped on three of the five bands on which the Fermi surface resides and was found to be anisotropic in momentum space.

Not So Fast

Recent observations of some of Greenland's outlet glaciers have shown large and rapid increases in the speeds at which their ice has streamed to the sea. Simple projections of ice loss and sea level rise, based only on these increases, result in alarmingly high values and correspondingly great public concern. In order to provide a more comprehensive and detailed picture of this type of ice sheet mass loss, **Moon *et al.*** (p. 576; see the cover) compiled a decade-long record of ice stream velocity measurements for nearly all of Greenland's major outlet glaciers. The pattern of flow variability around the ice sheet was both spatially and temporally complex, with clear differences between marine- and land-terminating types, as well as between regions. Furthermore, the integrated velocity of all of the outlet glaciers measured was considerably less than the upper bounds that have been proposed on the basis of a few rapidly accelerating locations, implying that sea level rise over the next century may be less than the 2 meters that have been suggested.

Magnetic Reconnection

Magnetic reconnection (MR) has been observed in the magnetospheres of planets with an intrinsic magnetic field, such as Earth, Mercury, Jupiter, and Saturn. MR is a universal plasma process that occurs in regions of strong magnetic shear and converts magnetic energy into kinetic energy. On Earth, MR is responsible for magnetic storms and auroral events. Using data from the European Space Agency Venus Express spacecraft, **Zhang *et al.*** (p. 567, published online 5 April; see the Perspective by **Slavin**) present surprising evidence for MR in the magnetosphere of Venus, which is a nonmagnetized body.

Going to Ground

Frustrated systems, in which the geometry of the crystal lattice stands in the way of achieving an energetic minimum on all lattice sites simultaneously, have the potential to remain disordered down to the lowest temperatures. Numerous experimental efforts to find a material with a truly fluctuating ground state have failed because ordering often sets in at a finite temperature owing to symmetry breaking. **Nakatsuji *et al.*** (p. 559; see the Perspective by **Balents**) identify the compound $Ba_3CuSb_2O_9$ as a promising candidate for this state; the Cu-Sb dipoles reside on a hexagonal structure, forming fluctuating spin singlets. Multiple lines of evidence suggest that the material does not order down to the millikelvin temperature range, remaining magnetically isotropic.

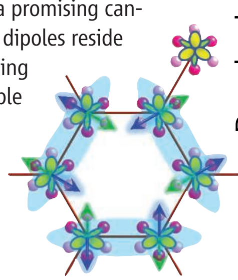

Martian Veins

After more than 7 years of traveling across the Meridiani Planum region of Mars, the Mars Exploration rover Opportunity reached the Endeavour Crater, a 22-km-impact crater made of materials older than those previously investigated by the rover. **Squyres *et al.*** (p. 570) present a comprehensive analysis of the rim of this crater. Localized zinc enrichments that provide evidence for hydrothermal alteration and gypsum-rich veins that were precipitated from liquid water at a relatively low temperature provide a compelling case for aqueous alteration processes in this area at ancient times.

Continued on page 518

CREDITS (TOP TO BOTTOM): ABDERRAHMAN KHILA; NAKATSUJI ET AL.

Published by AAAS

Continued from page 517

Small But Perfectly Formed

The imaginal discs of *Drosophila* represent defined larval tissues that give rise to the subsequent adult appendages. These tissues regenerate in response to damage. When the imaginal discs are injured or show tumor growth, they signal to the rest of the larval animal to slow down growth and delay morphogenesis. **Garelli *et al.*** (p. 579) and **Colombani *et al.*** (p. 582) now show that an insulin-like peptide, termed Dilp8, is secreted into the hemolymph (insect "blood") and participates in the communication between growing organs and the endocrine system to adjust the growth program and maturation time. This collaboration ensures that adults attain the normal size and maintain appropriate proportions and symmetry.

Not Broken Until Repaired

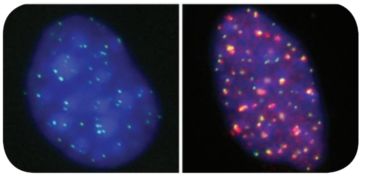

Humans, and indeed most eukaryotes, have linear chromosomes with two DNA ends, known as telomeres. Cells have evolved sophisticated systems to repair broken chromosomes, which specifically recognize DNA ends as damage. Telomeres are protected from these repair systems, which would otherwise wreak havoc in the cell, causing genome aberrations that, ironically, can lead to cancer. To understand all the possible threats to telomeres **Sfeir and de Lange** (p. 593) mutated components of the mouse shelterin protein complex, which forms a protective cap over the telomere ends, rendering telomeres completely devoid of the complex (and packaged only in nucleosomal chromatin). These "naked" telomeres were vulnerable to six DNA repair–related pathways: classical and alternative nonhomologous end joining; ATM and ATR signaling pathways; homology directed recombination; and unmitigated DNA resection.

Blood Pressure Gauge

Endothelial cells line blood vessels and, by interacting with smooth muscle, can help to control blood flow. **Sonkusare *et al.*** (p. 597; see the Perspective by **Lederer *et al.***) describe how signaling in endothelial cells controls contraction of surrounding smooth muscle cells, which provides an important mechanism for control of blood pressure. A calcium-sensitive fluorescent protein was expressed in endothelial cells of mouse arteries to image small changes in calcium concentration that appear to represent opening of single TRPV4 ion channels and consequent influx of calcium into the cell. Clustering of the channels allowed cooperative activation of a handful of channels, which appeared to produce a sufficient calcium signal to open another set of calcium-sensitive potassium channels. The resulting depolarization of the endothelial cells then passes an electrical connection to smooth muscle cells through gap junctions.

Gene Expression by Remote Control

Techniques that allow remote, noninvasive activation of specific genes in specific tissues could one day be applied to regulate expression of therapeutic proteins in a clinical setting. In a proof-of-concept study, **Stanley *et al.*** (p. 604) showed that heating of iron oxide nanoparticles by radiowaves can remotely activate insulin gene expression in cultured cells and in a mouse model. Heating of membrane-targeted nanoparticles induced opening of a temperature-sensitive membrane channel in the cells and triggered calcium entry. The intracellular calcium signal in turn stimulated expression of an engineered insulin gene, leading to the synthesis and release of insulin. In experiments with mice bearing tumors that expressed the engineered insulin gene, exposure to radiowaves promoted secretion of insulin from the tumors and lowered blood glucose levels in the animals.

No Regrets

As people grow older, the possibility to think about "missed chances" increases. When we are young, thinking about missed opportunities may help to optimize future behavior. However, the older we get the probability of "second chances" decreases and thus the benefit of ruminating upon them disappears. **Brassen *et al.*** (p. 612, published online 19 April) studied the behavioral and neural response to missed chances in young adults, the healthy elderly subjects and late-life depressed volunteers. Compared with young and depressed subjects, the healthy elderly subjects showed a reduced sensitivity to missed opportunities. The findings suggest a potential mechanism for preserved emotional health in older age.

CREDIT: SFEIR AND DE LANGE

Published by AAAS

Sheila Tobias writes about math and science education. E-mail: sheilax@sheilatobias.com.

Anne Baffert is a chemistry teacher at Salpointe Catholic High School, Tucson, AZ. E-mail: azchemmom@yahoo.com.

Empowering Science Teachers

AT ANY ONE TIME, THERE ARE THOUSANDS OF U.S. GRADUATE STUDENTS WITH STRONG SCIENCE expertise and an interest in education who would be more than qualified to stem the critical shortage of secondary chemistry, physics, earth sciences, and biology teachers, but who will most likely never set foot in a high-school (precollege) classroom. Instead, nearly all of them are choosing to pursue research rather than to teach the science that fascinates them to young people. To change this situation, and the widespread lack of understanding and appreciation for science in the United States, it is critical to pinpoint the major source of the problem.

A look at teaching in Finland is a useful place to start. Finland attracts and retains the best and the brightest to precollege teaching careers. There are 10 applicants for every teaching post in that country, corresponding to a 1-in-10 acceptance rate into teacher training programs.* In 1994, Finland established a Teacher Researcher Network to connect college education research faculty and precollege teachers, and to involve classroom teachers directly in education research. Finnish precollege teachers thereby become equipped to formulate changes in curricula.† This not only empowers classroom teachers but also appropriately treats them as education experts, further raising their social status.

Unfortunately, the United States is headed in the opposite direction. Too many precollege teachers work in a "command-and-control" environment, managed by those who lack any real understanding of how to improve the system. Yet the teachers who know how to make improvements are rarely empowered to do so. It is not surprising that an annual poll of U.S. teachers found that only 44% were "very satisfied" with their jobs in 2011, the lowest level recorded in the survey's 28-year history.‡ Science teachers rarely become superintendents in the nation's 14,000 school districts. In one state, only 6 of 189 district superintendents had ever taught science in the classroom.§ And yet science teachers have expertise that is important for wise system governance. We recommend that school districts select outstanding teachers to serve on a Science Teacher Council. This council should set criteria for hiring new precollege science teachers, assessing and promoting such teachers, achieving state science standards, and properly assessing student achievement.

Science teachers' professionalism also rests on their continual active involvement in science through structured collaborations with scientists. There are successful model programs in the United States (but far too few), such as the Partners in Science Program of the M.J. Murdoch Charitable Trust, California State University's Science Teacher and Researcher Program, and Columbia University's Summer Research Program for Science Teachers, where teachers partner with researchers in academic or industrial settings. Teachers often coauthor papers with their research colleagues and present findings at scientific meetings. And as local science faculty and researchers in industry become aware of the circumstances in which precollege science teachers work, many become active supporters of the teachers in their community. This support is crucial when rewards for teaching and broader school funding issues are at stake.

Online
sciencemag.org
Podcast interview (http://scim.ag/ed_6081) with author Sheila Tobias.

It will take time to reverse the diminishing professional status of precollege science educators in the United States, but surveys of the current generation of young people new to the workforce reveal that they are looking for challenges, problems to solve, and most importantly, a profession in which they can make an impact early on in their careers. Education would certainly fit the bill if the United States, like Finland, treated teachers as real professionals.

– Sheila Tobias and Anne Baffert

10.1126/science.1223116

*J. Burris, *Science* **335**, 146 (2012). †https://www.jyu.fi/edu/laitokset/okl/tutkivaopettaja/teacherresearcher. ‡www.metlife.com/about/corporate-profile/citizenship/metlife-foundation/metlife-survey-of-the-american-teacher.html. §S. Tobias, A. Baffert, *Science Teaching as a Profession: Why It Isn't. How It Could Be*. (National Science Teachers Association Press, Arlington, VA, 2010).

CREDITS: (TOP LEFT) CODY CONRAD; (BOTTOM LEFT) STUDIO Z IN TUCSON ARIZONA; (RIGHT) ISTOCKPHOTO.COM

EDITED BY KRISTEN MUELLER AND JAKE YESTON

ASTROPHYSICS

Planetary Confinement

Located 25 light-years away, the star Fomalhaut is surrounded by a spectacular eccentric disk of dust and debris somewhat similar to the Kuiper Belt in our solar system. Boley *et al.* traced the parent body population for this debris disk using observations of millimeter-sized grains obtained with the Atacama Large Millimeter Array, an observatory under construction on the Chajnantor plateau, 5000 m altitude in northern Chile. The 350-GHz images, which trace grains that do not respond to stellar radiation and hence manifest orbits that do not move away from their birth region, show that the disk is both narrower and thinner than previously thought and has very sharp inner and outer edges. N-body simulations suggest that the disk is being confined by two planets with masses around that of Earth, one orbiting between the star and the disk and the other outside the disk. This is analogous to the confinement of Saturn's F ring by the moons Pandora and Prometheus and that of Uranus's ε ring by Cordelia and Ophelia. — MJC

Astrophys. J. **750**, L21 (2012).

MOLECULAR BIOLOGY

Prions: A New Part to Play

MicroRNAs (miRNAs) are small noncoding RNAs that, when part of a miRNA-induced silencing complex (miRISC), repress the expression of fully or partially complementary mRNAs. Argonaute (Ago) proteins bind miRNAs and form the heart of the silencing machinery. Intriguingly, plasma membrane–associated forms of the human prion protein (PrP^C), which is associated with neurodegenerative diseases in humans, also interact with components of the miRNA pathway.

Gibbings *et al.* show that a transmembrane form of PrP^C exposes an AGO anchor sequence in the cytoplasm and that this repeat binds AGO1 and AGO2. These PrPC-AGO complexes are found on vesicles in cells that resemble multivesicular bodies (MVBs). During miRNA maturation, AGO protein bound to miRNA must be transferred from the RISC-loading complex (RLC) to the miRISC silencing complex. PrP^C binds components of both the RLC and the miRISC but seems to do so in distinct cellular locations. PrP^C promotes the association of AGO with the miRISC and/or the stability of this complex. Indeed, PrP^C is required for effective miRNA silencing of a number of target mRNAs. PrP^C may do this through subcellular trafficking, as it seems to increase the interaction between MVBs and AGO-rich structures, such as P or GW bodies, thence promoting shuttling of AGO between the RISC-loading complex and the miRNA-induced silencing complex. — GR

Nat. Struct. Mol. Biol. **19**, 10.1038/nsmb.2273 (2012).

CHEMISTRY

Making Methanol

If chemistry worked like Tinkertoys, it would be rather straightforward to make methanol from methane: You'd simply pull off a hydrogen atom and stick on an OH group. Alas, it's not that simple, and most scalable implementations of this reaction tend toward overoxidation; the primary industrial route circuitously oxidizes the carbon to CO before reducing it back down to the alcohol. Hammond *et al.* explored one means of taming the direct oxidation, so as to stop at the desired product. Specifically, they sought to optimize zeolite-catalyzed oxidation of methane by hydrogen peroxide. They first discovered that trace iron is essential to the catalytic activity and went on to map out a preliminary diiron-centered mechanism using a combination of spectroscopic probes and density functional theory simulations. Next, the authors observed that OH radicals underlie overoxidation processes and that the introduction of copper ions stems this activity. A combination of iron and copper additives to the zeolites offered >90% methanol selectivity at ~10% methane conversion. Although hydrogen peroxide is currently an expensive oxidant to apply to commodity-scale methanol synthesis, the selectivity principles uncovered in the study may enhance selective hydrocarbon oxidation processes more broadly. — JSY

Angew. Chem. Int. Ed. **51**, 10.1002/anie.201108706 (2012).

GENETICS

Isoform Identification

The differential reconnection of transcribed exons, termed alternative splicing, has the potential to result in one gene encoding multiple protein isoforms. The degree to which alternatively spliced transcripts are translated into functional proteins, however, is not well understood. Ezkurdia *et al.* used data across multiple mass spectrometry experiments to investigate the degree to which genes with alternative transcripts gave rise to protein isoforms. Comparison of the predicted proteins from the gene and genetic variant database of ENCODE (GENCODE) to the Swiss-Prot database allowed for the identification of 150 human genes that encoded at least one protein isoform and 13 with three or more, with the caveat that identification was biased toward those most likely to be detected. Heterogeneous nuclear ribonucleoproteins, which are involved in the regulation of alternative splicing, showed enrichment in alternative isoforms. Furthermore, the majority of differences detected among all predicted isoforms differed

CREDITS (TOP TO BOTTOM): ALMA (ESO/NAOJ/NRAO); GIBBINGS ET AL., NAT. STRUCT. MOL. BIOL. 19, 10.1038/NSMB.2273 (2012)

Published by AAAS

in sequence by the insertion/deletion of a single amino acid. Investigations into the *Drosophila* and mouse proteomes revealed similar patterns. Together, these results suggest that alternative splicing is under selective constraint. — LMZ

Mol. Biol. Evol. **29**, 10.1093/molbev/mss100 (2012).

BIOMEDICINE

Aiming Even Lower

The use of statins to lower plasma levels of LDL (low-density lipoprotein) cholesterol can reduce the risk of cardiovascular disease by an estimated 30 to 40%. Yet some experts have argued that lowering LDL cholesterol to levels below current recommendations—by coadministering drugs that act by a complementary mechanism, for example—may confer even more health benefits than statins alone. PCSK9 (proprotein convertase subtilisin/kexin type 9) is an appealing new drug target because it keeps plasma cholesterol levels high by promoting degradation of the receptor on liver cells that removes cholesterol from the blood. Interestingly, a small percentage of humans carry mutations in PCSK9 that reduce its activity and these individuals have a lower risk of heart disease, suggesting that therapeutic inhibition of PCSK9 will be safe. Stein *et al.* conducted small phase-1 trials of a human PCSK9 monoclonal antibody (REGN727) given to healthy volunteers and to individuals with familial and nonfamilial hypercholesterolemia. Injection of REGN727 induced no serious adverse effects in these short-duration trials, and in all groups the antibody significantly reduced LDL cholesterol levels as compared with placebo. — PAK

N. Engl. J. Med. **366**, 1108 (2012).

ENTOMOLOGY

A Toast to Fruitfly Health

A propensity for rotting fruit puts the fruit fly *Drosophila melanogaster* in contact with fermented material that can contain substantial amounts of alcohol. Milan *et al.* tested whether alcohol consumption by fly larvae might actually serve to protect them from nasty wasps that attack and lay their eggs in the fruit fly larvae. Indeed, the wasps appeared to be more sensitive to the toxic effects of alcohol than were the flies. The wasps laid fewer eggs on flies that were consuming ethanol and when they did, those eggs had disrupted development and were less likely to prevent proper development of the fly larvae. Furthermore, the flies seem to know what's good for them. When given a choice of food with or without alcohol, flies that were infected were more likely than control flies to seek out and consume the ethanol-spiked food. Whether humans might derive benefits from such a defense against parasites remains to be determined. — LBR

Curr. Biol. **22**, 488 (2012).

ECOLOGY

Fluctuating Forests

In the current era of rapidly changing climate, the past can provide useful lessons about the responses of ecological communities to climate fluctuations. Increased or repeated drought is a plausible scenario in some currently humid environments under climate change, although where and when this might occur is still hard to predict. The kinds of ecological change that might be expected, however, are illustrated in a study of historical ecological change in the humid western Great Lakes area of North America in response to the Medieval Climate Anomaly (MCA). The MCA began approximately 1050 years ago, lasted for 450 years, and was characterized by a warmer climate in north temperate regions and a series of droughts in the Great Lakes region. Booth *et al.* used pollen analyses and subfossil testate amoebae (which are sensitive indicators of water table depth in peatlands) to trace the population changes in drought-sensitive beech trees during this period. They show that beech declined in abundance sharply wherever drought and increased moisture fluctuations occurred, with associated effects on fire incidence and other components of the ecological community. These findings illustrate how currently moist regions could experience rapid ecological change as a result of increased climatic fluctuations in a warming world. — AMS

Ecology **93**, 219 (2012).

CREDIT: ISTOCKPHOTO.COM

AROUND THE WORLD

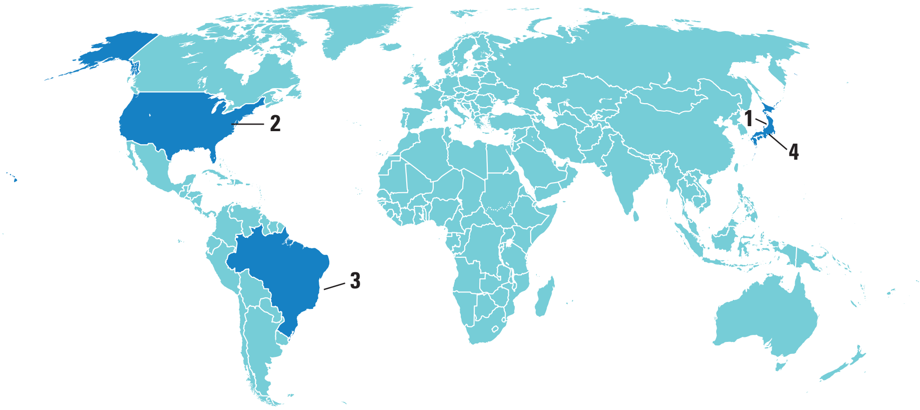

Sado Island, Japan 1

Back From the Brink

Japan went gaga last week when three crested ibis chicks pecked through their shells in a nest on Sado Island and became the first of their species born in the wild in the country in 36 years.

Scientists were equally thrilled. "We've learned a lot about captive breeding, preparing birds for release, and how to monitor them," says Satoshi Yamagishi, an ornithologist at Niigata University in Japan who heads a Ministry of the Environment task force on reestablishing the birds in the wild. He expects their experience to benefit breeding-and-release programs for other species.

Nipponia nippon once flew over much of Japan and northeastern Asia, but overhunting (for their feathers) and habitat loss devastated their numbers. In 1981, the environment ministry captured Japan's last five wild birds for breeding, but the last of those birds died in 2003. Efforts continued with birds donated by China, where a small wild population survives. Since 2008, Japan has released 78 birds; 45 are known to remain in the wild. Before claiming success, "we would like to see a second generation born in the wild and a stable population," Yamagishi says.

Washington, D.C. 2

Research Agencies Hear About The Possibility of More

Research increases weren't supposed to be an option for next year because the U.S. government was tightening its belt. But the Obama Administration is facing the unexpected—and not entirely unpleasant—job of deciding how to respond to preliminary steps by Congress to give some research programs more money in 2013 than the White House had requested.

A House of Representatives spending panel last week voted to add $76 million to the president's request for fusion research at the Department of Energy, reversing cuts for domestic programs and coming closer to the promised U.S. contribution to the ITER fusion reactor being built in France. Within NASA, the panel had previously added $150 million to the Administration's request for continued work on a Mars sample return mission, and $115 million for two programs supporting planetary missions.

While Congress is months away from a final decision on spending for next year, these initial moves raise a new issue for the White House: Is more money for research always a good thing? "Yes, as a general matter, increases [in research budgets] are good," presidential science adviser John Holdren said after a speech last week at the AAAS annual policy forum. "But, of course, under overall caps, whether particular increases are good depends on what they come out of. That's why we need to study the House proposals before offering an opinion." **http://scim.ag/budget_2013**

Abrolhos Shelf, Brazil 3

Massive Coral Beds Charted off Brazil

The Abrolhos Shelf of Brazil boasts the world's largest expanse of rhodoliths, a spherical type of coralline algae, according to a survey published last month in *PLoS ONE*. The beds cover a total area the size of El Salvador and produce an estimated 25 million metric tons of calcium carbonate a year, but face several threats. The slow-growing rhodoliths are made of magnesium-rich calcite, which is particularly vulnerable to ocean acidification. In addition, river sediments from deforestation may be harming the beds. Southern portions are also dredged as a source of lime for use as an additive to agricultural soils.

NOTED

>Alvin Ailey, Duke Ellington, and yes, Dr. Seuss—oh, the places you've gone! The International Astronomical Union (IAU) has approved a proposal by the science team of NASA's MESSENGER mission to assign new names to 23 impact craters on Mercury—including **Ailey, Ellington, and Seuss**.

Those will join 53 previously named craters since the MESSENGER spacecraft first flew by Mercury in January 2008—all honoring deceased artists, musicians, and authors.

CREDITS (TOP TO BOTTOM): © RODRIGO L. DE MOURA; MINISTRY OF THE ENVIRONMENT, JAPAN

Researchers have known about the rhodolith beds since the 1970s, but they had never been mapped in detail. So marine biologist Rodrigo Moura of Rio de Janeiro Federal University, along with colleagues from Brazil and Conservation International, spent 2 years surveying the beds with remotely operated vehicles, sonar, and SCUBA divers. The tennis ball–size rhodoliths cover 20,902 square kilometers. "It was very surprising to find beds these big," Moura says, adding that the rhodolith beds need to be protected in part because they may be important migration routes for species that live on coral reefs.

Oshika Peninsula, Japan **4**

A New Deep-Sea Drilling Record

The deep-sea drilling vessel *Chikyu*, operated by the Japan Agency for Marine-Earth Science and Technology, has set the record for the deepest undersea research borehole, extending to a total depth of 7740 meters below sea level (856 meters of which are

below the sea floor) in waters off the coast of Oshika Peninsula, the agency announced 27 April. The previous record was set in 1978, when the U.S. vessel *Glomar Challenger* drilled to a total of 7049.5 meters below sea level in the Mariana Trench—although only about 15.5 meters of that was below the sea floor.

Chikyu has been probing into the fault zone around the Japan Trench, where the 11 March 2011 Tohoku earthquake and tsunami were generated.

CREDITS (TOP TO BOTTOM): MEGHNA SACHDEV/*SCIENCE*; KYODO/LANDOV; FNAL.GOV

Psyched About STEM

Sumo-wrestling LEGO robots (pictured), jumbo squid dissections, and virtual helicopter rides were just a few of the attractions at the second USA Science & Engineering Festival held in Washington, D.C., last weekend. The festival included more than 3000 exhibits, as well as appearances by science celebrities such as Bill Nye the Science Guy, neuroscientist and TV actor Mayim Bialik (of *Blossom* and *The Big Bang Theory*), and the *MythBusters* team.

Designed to get kids interested in science, technology, math, and engineering (STEM), the festival's Finale Expo was packed with thousands of young attendees eager to build robots, test out fighter jet simulators, and play 3D videogames. It seems to be working, if the opinion of attendee 8-year-old Jacob Morey is any indication. "I like talking to the experts because I get responses and I can ask questions," Morey says. "I think science is the greatest invention since the Internet!"

NEWSMAKERS

Steven Koonin is preparing for a homecoming of sorts: The Brooklyn-born physicist has been named director of New York University's new Center for Urban Science and Progress (CUSP), which will study how to make cities work better. Koonin, once provost of the California Institute of Technology in Pasadena, stepped down last fall as under secretary for science at the U.S. Department of Energy.

Koonin

Last year, New York City Mayor Michael Bloomberg invited proposals to raise the city's academic applied science and engineering IQ. The winner, and recipient of $100 million in city funding, was a team led by Cornell University and the Technion–Israel Institute of Technology. But Koonin, 60, thinks that CUSP, supported by a consortium of universities and high-tech companies, can also make a big splash.

Q: How will CUSP differ from other research programs on sustainable cities?

We have the city and its agencies as a deeply engaged partner. That means work- >>

THEY SAID IT

"You have the right to prepare for interesting work and economic independence."

—Shorma Bianca Bailey, president of the Howard University Chapter of Engineers Without Borders, at a 24 April White House panel offering advice to young women entering science, technology, engineering, or mathematics fields.

Part Real, Part Fantasy: Disney's *Chimpanzee*

The Disney film *Chimpanzee* tells the story of Oscar, an orphan chimp in Ivory Coast's Taï Forest that was adopted by one of his troop's males. The movie tells a scientifically accurate story—in fact, "the main plot was decided by the chimps," says primatologist Christophe Boesch of the Max Planck Institute for Evolutionary Anthropology in Leipzig, Germany. Boesch and his colleagues described the real-life adoption of another young orphan chimp named Victor by an older male in his troop in a 2010 *PLoS ONE* paper. (The movie blends Victor's story with Oscar's.)

However, the story is also fictionalized in that it was pieced together from 3 years' worth of footage filmed not only in Taï but also among chimpanzee troops in Ngogo, Uganda—and, to Boesch's disappointment, the movie might not directly benefit its stars. Disney is donating some proceeds to the Jane Goodall Institute's sanctuary for orphaned chimps in the Republic of Congo. But Boesch says he'd hoped proceeds would also go to the Wild Chimpanzee Foundation, which works to protect the chimpanzees in Taï, and the Ngogo Chimpanzee Project, which supports conservation in Uganda. Both populations are severely threatened, he says. "They need support to have them survive."

>>NEWSMAKERS

ing with the people who actually run the subways and write the building codes. We have been promised the data and the opportunity to use the city as a living laboratory.

Q: What will industry contribute?
I know academics, and I love the freewheeling, curiosity-driven atmosphere of a university. But CUSP is meant to have an impact. That comes through demonstration projects and deployment, and industry knows how to do that.

Q: Any downsides to returning to New York?
I'm long enough out of California that I don't miss the sunshine. No, I can only think of upsides.

Epidemiologist Among Medal Of Freedom Winners

William Foege, a leader of the global campaign that wiped out smallpox, has been named a recipient of the Presidential Medal of Freedom, the nation's highest civilian honor.


Foege

Foege, 76, is a physician and epidemiologist who helped spearhead the massive immunization effort that eradicated smallpox in the 1970s. He directed the Centers for Disease Control and Prevention from 1977 to 1983, worked to boost immunization rates in the developing world, and served as executive director of The Carter Center in Atlanta. More recently, as a senior fellow at the Bill & Melinda Gates Foundation, he has helped shape the organization's global health efforts.

Foege is among 13 people recognized by President Barack Obama for their contributions to the United States or to the world who will receive the medal at the White House later this spring.

FINDINGS

Wind Farms Warm the Night

Large wind farms can boost nighttime temperatures, according to a study that analyzed satellite images of a 10,000-square-kilometer area of west-central Texas. More than 95% of the turbines in the area were erected between 2003 and 2011. And, during those 9 years, the areas where the wind farms were located warmed up on summer nights by, on average, 0.65°C more than nearby areas without wind turbines.

At night, the air at ground level is cooler than the air a few dozen meters up; turbulence generated by individual wind turbines brings warm air downward to heat the surface, the team reported online 29 April in *Nature Climate Change*. The warming rates measured in this study—the first to show temperature increases based on satellite data rather than computer simulations, the researchers note—are high simply because the region has experienced a rapid growth in wind farm development. The warming effect for any given wind farm will likely level off if no more turbines are added, the researchers report.

CREDITS (TOP TO BOTTOM): © DISNEY; WIKIMEDIA COMMONS; PHOTO BY EMORY PHOTO/VIDEO

BY THE NUMBERS

12% Percentage of clinical drug trials that are pediatric trials, although children bear nearly 60% of the disease burden for high-priority conditions such as malaria and HIV/AIDS, according to a study presented 28 April at the Pediatric Academic Societies' annual meeting in Boston.

7327 Number of family names among a population of 1.28 billion Chinese recorded in a study appearing in an upcoming issue of the *American Journal of Physical Anthropology*. By contrast, a study of 18 million people in the United States found nearly 900,000 last names.

Random Sample

Understanding the Lords of Time

The putative end of the Maya Long Count calendar on 21 December 2012 has unleashed a cottage industry of doomsaying. Books, articles, TV shows, and movies portray myriad cataclysmic events that the Maya are said to have foreseen. This can be a frustrating exercise for scientists; Maya scholars tend to think the end of the calendar is merely the end of a cycle—hardly the end of the world or of time itself. But Simon Martin, a noted Maya epigrapher and associate curator at the University of Pennsylvania's Museum of Archaeology and Anthropology, sees an upside to the doom and gloom. This, he says, is a "once-in-a-lifetime opportunity, when the world is focused on the ancient Maya," to inform people about the true role time played in the Maya's lives.

Martin is the co-curator of *Maya 2012: Lords of Time*, an exhibit opening 5 May at the museum. Despite the forecasts of doom, experts note there is only one reference to the portentous date in all of the Maya glyphs; that reference was found at Tortuguero, a small site in southern Mexico. And although the 2012 date itself is discernible, the inscription that follows is difficult to decipher because of its poor condition.

"Even in damaged form, (what comes after the date) doesn't appear to refer to 2012," said Martin. The syntax and structure of this glyph suggest the damaged script would refer to a much earlier event. There's also a reference to a much later date, 4772 C.E., in an inscription at Palenque, which indicates the Maya thought life would continue beyond 2012.

Plants More Sensitive to Global Warming Than Tests Suggest

Ecologists trying to anticipate the effects of climate change often set up "warming" experiments in which they artificially heat up an environment and monitor plants' reactions. But those results are falling short of reality, says Elizabeth Wolkovich, an ecologist at the University of British Columbia, Vancouver.

The timing of plants leafing out or blooming—part of a field called phenology—is a sensitive indicator of how ecosystems respond to climate change. Aside from using warming experiments, ecologists track phenology through long-term monitoring of plant populations. Wolkovich and her colleagues compared phenology data on 1643 different species in 36 warming studies and in 14 long-term data sets. The team determined how much sooner each species flowered or leafed out per degree of temperature rise. Plants in the longterm studies leafed out four times sooner and flowered eight times sooner than the warming experiments predicted, Wolkovich and her colleagues reported this week in *Nature*.

That discrepancy could present problems to scientists who use warming experiment data in modeling studies. "If the warming experiments are not providing an accurate prediction, then you can't predict how ecosystem services will respond," says Johanna Schmitt, a plant ecologist at Brown University, who was not involved with the work. **http://scim.ag/PlantsWarm**

CREDITS (TOP TO BOTTOM): ALEXANDRA FLEISCHMAN FOR PENN MUSEUM; DAREN EIRI

PARTICLE PHYSICS

Budget Cap Could Gut Next Big Fermilab Project

BATAVIA, ILLINOIS—How do you chop down the budget of a major experiment by two-thirds and still leave something that's worth doing? That's the riddle physicists here at Fermi National Accelerator Laboratory (Fermilab) are struggling to solve as they chart the lab's long-term future.

Last month, officials with the Department of Energy (DOE) told Fermilab that its proposed $1.9 billion flagship experiment for the next decade costs too much to construct all at once. They asked scientists for a plan to build it piecemeal (*Science*, 30 March, p. 1553). But, as became clear at a workshop last week at the lab,* the affordable options for the first stage of the Long-Baseline Neutrino Experiment (LBNE) would severely limit its scientific potential and could leave it only marginally more capable than an existing Fermilab experiment.

"We want to pick no more than a couple of options [for the experiment's first stage] in which the physics is good enough to justify the cost," says Young-Kee Kim, deputy director at Fermilab and chair of the LBNE reconfiguration steering committee. But some physicists worry that the affordable options won't be exciting enough scientifically to get funded. "When my colleagues go to some congressional committee and say that they want to spend $600 million to measure one parameter, they're going to get killed," says John Learned, a LBNE team member from the University of Hawaii, Manoa.

If built as proposed, LBNE would be a world-beater, say physicists at Fermilab, the sole remaining U.S. particle physics lab. LBNE would deploy a state-of-the-art detector filled with 34,000 tonnes of frigid liquid argon deep in the abandoned Homestake Mine in Lead, South Dakota. That detector would study nearly massless particles called neutrinos fired through Earth from Fermilab, 1300 kilometers away. Such particles come in three types—electron neutrinos, muon neutrinos, and tau neutrinos—that morph or "oscillate" into one another as they zip along. LBNE would search for a phenomenon called CP violation, an asymmetry in the way neutrinos and antineutrinos oscillate that could help explain how the universe generated so much more matter than antimatter.

The original plan for the LBNE detector would have been a multipurpose laboratory in itself. Located 2250 meters below the surface and shielded from interference from cosmic rays, it would perform a type of astronomy by detecting bursts of neutrinos from supernova explosions. It would also search for signs that, on a time scale far longer than the age of the universe, protons fall apart.

Carving Up LBNE

WHAT'S AFFORDABLE	
• 10-kilotonne detector on surface at Homestake Mine in South Dakota and new beamline	**$750 million**
• 17-kilotonne detector on surface at Soudan mine or Ash River in Minnesota	**$500 million–$600 million**

ORIGINAL PLAN	WHAT'S TOO EXPENSIVE OR NOT WORTH DOING
• 34-kilotonne detector underground at Homestake, new beamline and small detector at Fermilab **$1.9 billion**	• 5-kilotonne underground detector at Homestake and new beamline **$1.0 billion–$1.2 billion** • 17-kilotonne detector underground at Soudan mine **$900 million–$1.1 billion** • 17-kilotonne or 34 kilotonne detector alone at Homestake **$700 million–$1.2 billion** • New beamline and small detector at Fermilab **$600 million–$700 million**

A delicate balance. Fermilab's Young-Kee Kim leads a panel that's revising plans for the Long-Baseline Neutrino Experiment.

But facing stiff competition from DOE's other priorities, DOE's high-energy physics program cannot afford such a grand experiment. The program's annual budget, now $792 million, is unlikely to grow anytime soon. That means DOE can spend roughly $150 million a year on LBNE, DOE project manager Eli Rosenberg said at the workshop. However, LBNE's projected 10-year construction budget would have peaked at $280 million per year. In addition, Rosenberg said, DOE has capped the cost of the first 5 to 6 years of the project at $600 million to $700 million, including inflation.

But whittling down LBNE to that level won't be easy. The project consists of several pieces, each costing hundreds of millions of dollars. The huge detector alone is projected to cost $399 million. Excavation of a cavern to house the detector and other construction at Homestake is priced at $449 million. A new beamline at Fermilab to generate the neutrinos would run $400 million, and a smaller "near" detector at Fermilab that would compare the neutrinos leaving the lab to those reaching Homestake is pegged at $100 million. Those prices do *not* account for any inflationary growth.

To make the first phase affordable, physicists would have to give up key features of LBNE. The first casualty would be plans to build the detector underground, as excavation for even a 5000-tonne detector, one of the reduced sizes now under consideration, would cost $266 million. But some physicists say a surface detector makes little sense because cosmic rays would swamp any signals from supernovae or proton decay. "Why would you cut out half your program by putting your detector on the surface?" asked Alexander Friedland, a theorist at Los Alamos National Laboratory in New Mexico.

Physicists also say a much smaller detector would be less likely to nail down the complete picture of neutrino oscillations. In particular, physicists know that two types of neutrinos have nearly the same mass, but they don't know if there are two lighter types and one heavier type, or the other way around. A 34,000-tonne LNBE detector would easily resolve that "mass hierarchy." Most importantly, if neutrinos and antineutrinos oscillate differently, then LBNE could make a definitive measurement of that effect, provided it's not very small.

If scaled to 5000 tonnes, however, the detector would be able to resolve the mass hierarchy only somewhat better than Fer-

*LBNE Reconfiguration Workshop, 25–26 April.

TABLE SOURCE: JAMES STRAIT/FERMILAB; PHOTO: CINDY ARNOLD

milab's NOυA experiment. That project, to begin next year, will study neutrinos fired 810 kilometers to a lower-tech surface detector in Ash River, Minnesota. (Fermilab also runs an experiment called MINOS that uses the same beamline to fire neutrinos 735 kilometers to a detector in the Soudan mine in Minnesota.) At 10,000 tonnes, LBNE could resolve the mass hierarchy and detect evidence of CP violation—although it couldn't make a definite discovery. "I would feel that anything less than 10,000 tonnes wouldn't be compelling," says Fermilab's Regina Rameika. But small doesn't mean cheap. The 5000-tonne detector would cost $132 million; the 10,000-tonne model would run roughly $170 million.

Physicists may even have to give up on Homestake entirely. Some researchers want to reuse Fermilab's existing beamline, which is more powerful than neutrino beams in Europe or Japan, and build the LBNE detector at Soudan or Ash River. But others argue that the distance to either site in Minnesota is too short to ever fulfill LBNE's complete scientific program.

The two most likely options appear to be a 17,000-tonne detector on the surface at Soudan or—if DOE is willing to spend just a bit more—a 10,000-tonne detector on the surface at Homestake, said Charles Baltay, a steering committee member from Yale University. But his summary of the day-and-a-half-long workshop left some physicists feeling rushed. "I spent 3 months choosing my last car; we're going to make a decision to go to Soudan in 3 weeks?" asked Robert Svoboda of the University of California, Davis, who is co-spokesperson for the LBNE collaboration.

But nothing will be gained by waiting, says Fermilab Director Pier Oddone. "If you want to take a year to make a decision when everything is known, you're only adding a year to an already long process," he says. And the clock is ticking. LBNE's reconfiguration steering committee has promised to deliver a report to DOE on 1 July, in time for agency officials to digest it before submitting their 2014 budget request to the White House.

–ADRIAN CHO

INFLUENZA

One H5N1 Paper Finally Goes to Press; Second Greenlighted

They have been called the most famous papers that were never published. But now, one of two controversial studies that shows how to make H5N1 avian influenza more transmissible in mammals is up on *Nature*'s Web site for all the world to scrutinize—including, some worry, would-be bioterrorists who might use the information to set off a pandemic. The other paper received a crucial go-ahead from the Dutch government last week and will likely be published by *Science* soon.

In December, the U.S. National Science Advisory Board for Biosecurity (NSABB) recommended that the two studies—both of which use ferrets, a popular model for human influenza—not be published in full. But after an expert panel convened by the World Health Organization (WHO) disagreed with the decision, NSABB reviewed revised versions of the manuscripts and changed its position (*Science*, 6 April, p. 19). That cleared the way for *Nature* on 2 May to publish the first of the two experiments, led by Yoshihiro Kawaoka of the University of Wisconsin, Madison, and the University of Tokyo.

Kawaoka's unusually long, 11-page article describes how his group stitched a mutated version of the hemagglutinin protein of the bird flu virus—the H5—onto the H1N1 virus that caused a relatively mild pandemic in 2009. The team explains that introducing into H5 a mere four mutations, which are delicately balanced with each other, allowed this hybrid virus to bind more strongly to mammalian cells and copy itself at high enough levels to readily transmit via respiratory droplets. Although the researchers don't know whether these mutations would "support sustained human-to-human transmission," many virologists worry mightily about this scenario. To date, H5N1 has not spread easily between humans, but in 355 of 602 confirmed cases, the patient has died.

First to finish. Yoshihiro Kawaoka (*above*) had his paper published this week.

CREDIT: M. ENSERINK/SCIENCE

The second paper has been held up in an extra bureaucratic tangle. After NSABB's initial recommendation, the Dutch government insisted that Ron Fouchier of Erasmus MC in Rotterdam apply for an export license before submitting his revised manuscript (*Science*, 20 April, p. 285). He called the decision "pure censorship," but on 24 April he filed the application, still disputing his obligation to do so and stressing that he did not want to set a precedent. Fouchier sent the paper to *Science* soon after the Dutch government issued the permit on 27 April.

Early this week, the paper was still under review and being edited. Both Fouchier and Kawaoka had hoped the two papers, whose fates had been closely linked for 6 months, would appear simultaneously, which *Science* Executive Editor Monica Bradford says would have been "ideal" as well. "I regret that both papers will not appear online together, but our priority must be to serve our authors and readers," *Nature* Editor-in-Chief Philip Campbell said in a statement. "You can't blame them," Fouchier says.

Despite the massive debate about these two papers, the Kawaoka study adds only a piece to a puzzle that his and other groups have been putting together for years. Influenza researchers have long attempted to understand the mutations and mechanisms that make a strain spread readily in humans. Kawaoka's study is an "important additional step along the way," says Malik Peiris, a flu researcher at the University of Hong Kong, who co-wrote an article in *Nature* about the Kawaoka paper.

Influenza infection begins when hemag-

glutinin binds to receptors on the host cell. The protein is shaped like a mushroom, with a long stalk and a globular head that contains the binding site. Three of the mutations Kawaoka's group describes are in or near the binding site. They make the virus prefer receptors on human cells to avian ones.

Several groups revealed similar binding site mutations earlier. Indeed, on 5 November 2011, while NSABB was debating the wisdom of publishing the Kawaoka and Fouchier papers in full, a report appeared online in *Virology* that showed respiratory transmission in one of two ferrets with a lab-made H5 virus that had two of the binding-site mutations also reported by Kawaoka's group. But these researchers stressed that respiratory transmission required additional mutations.

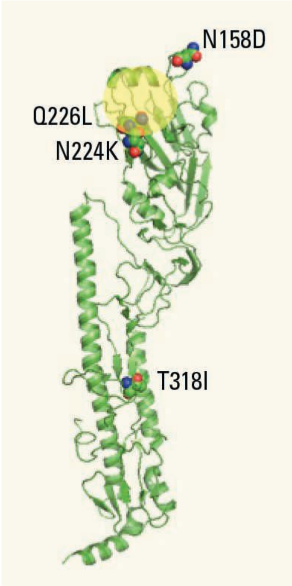

Hot spots. Mutations near hemagglutinin's binding site (yellow) and stalk increased transmissibility.

Nancy Cox, a flu researcher at the U.S. Centers for Disease Control and Prevention in Atlanta who co-authored that study—which an internal biosecurity committee said could be published—applauds Kawaoka and his colleagues for their "absolutely fantastic work" and says their mutant "definitely moved the transmission bar to the right towards being fully transmissible." But she notes that even the new mutant does not spread as readily as common, seasonal flu strains.

Cox and others say the most novel finding in the Kawaoka study involves a mutation in the stalk. This fourth mutation surfaced after a series of experiments that coaxed out mutations to make the virus spread more easily in ferrets. The effort included screening 2 million randomly created mutants and infecting ferrets to let strains further adapt to them. The best transmitter spread from infected animals to four of six healthy ferrets in neighboring cages. It did not kill any of the animals.

The role of the stalk mutation became clear in a set of additional experiments. Hemagluttinin's second job—after latching onto the host receptor—is to fuse viral and host cells' membranes as the virus enters the cell. The mutations at the binding site make it difficult for the protein to do that in the slightly acidic environment of human mucosa, the researchers say, but the mutation on the stalk compensates by enabling the protein to operate in a more acidic environment. "It's the major discovery in the study," says James Paulson, a co-author of the *Virology* paper with Cox who studies influenza binding at the Scripps Research Institute in San Diego, California.

Keiji Fukuda, a flu expert at WHO, says the paper will help guide surveillance for viruses that may cause great harm in humans. That's not just because they highlight specific mutations, Cox adds. "What we're really looking for is generalizable patterns of changes that occur when viruses become more transmissible in a mammalian model. … You can't be focused on a set of four specific mutations."

Now, influenza scientists are eagerly awaiting publication of Fouchier's study, still under wraps, which Kawaoka recently said has "striking similarities" with his own. It's unclear how these publications will affect a self-imposed moratorium on studies that involve modifying the transmissibility or lethality of H5N1. Announced by researchers from the world's most active H5N1 labs in January, the moratorium was extended indefinitely at a February meeting organized by WHO.

A related, vigorous debate continues about whether H5N1 modification studies should be confined to the most secure laboratories—known in the United States as biosafety level 4 facilities—or "enhanced" BSL-3 laboratories, where both Kawaoka and Fouchier performed their experiments. WHO will not take sides, nor will it advise on the moratorium, Fukuda says. Others say the moratorium should remain in force until the safety issues are resolved. "We should not rush forward when the stakes are so high," Thomas Inglesby, director of the Center for Biosecurity at the University of Pittsburgh Medical Center in Pennsylvania, told a U.S. Senate committee at a hearing on 26 April.

Anthony Fauci, head of the U.S. National Institute of Allergy and Infectious Diseases, which funded the two studies, agrees. Before U.S. officials support lifting the ban, he said at last week's hearing, they will have to "feel comfortable" that H5N1 labs understand how to evaluate the dual-use potential of their work and take steps to mitigate safety and security risks.

–MARTIN ENSERINK AND JON COHEN

With reporting by David Malakoff.

ARCHAEOLOGY

New Light on Revolutions That Weren't

MEMPHIS, TENNESSEE—Back in 2000, a now-famous scientific paper called "The Revolution That Wasn't" argued that the then-conventional wisdom that modern human behavior had erupted in a "creative explosion" about 50,000 years ago in Europe was wrong. Rather, anthropologists Sally McBrearty and Alison Brooks contended that modern behavior, including creativity, has deep and ancient roots, going back some 300,000 years ago in Africa (*Science*, 15 February 2002, p. 1219).

At a meeting* here last month, researchers heard new evidence that human evolution took a gradual, rather than revolutionary, course during two other key junctures in prehistory. A study of ancient stone tools from South Africa concludes that hunters manufactured spears with stone points—a sign of complex behavior—200,000 years earlier than had previously been thought. And new excavations at a 20,000-year-old settlement in Jordan, laden with artifacts typical of much later sites, suggest that the dramatic rise of farming villages in the Near East also had early and deep roots.

The pair of talks provides still more reasons "why we should be skeptical of revolutions in archaeology," says archaeologist Nicholas Conard of the University of Tübingen in Germany. Indeed, many archaeologists now think that apparent "revolutions" are due to gaps in the record or to behavioral shifts triggered by changing conditions, rather than sudden advances in cognition. What appear to be precociously sophisticated behaviors are really reflections of what prehistoric humans were capable of all along, says archaeologist John Shea of Stony Brook University in New York state.

Humans were getting smart about how to hunt wild animals much earlier than previously known, according to a talk by archaeologist Jayne Wilkins of the University of Toronto in Canada. Wilkins, Benjamin Schoville of Arizona State University (ASU), Tempe, and Kyle Brown of the University of Cape Town in South Africa analyzed stone

*Paleoanthropology Society 2012 Annual Meeting. Memphis, Tennessee, 17–18 April.

Published by AAAS

points from the site of Kathu Pan 1 (KP1); the tools came from a level dated by two relatively new dating techniques to about 500,000 years ago.

Archaeologists have considered two primary uses for stone points: as knives to cut animal flesh and plants, a function that dates to the earliest days of hominin evolution; or as weapons to hunt animals, probably hafted to long wooden handles and used as spears, a behavior thought to date to the beginning of the Middle Stone Age (MSA), about 300,000 years ago. During the MSA, hominin stone tools shifted from large, symmetrical hand axes to smaller and more sophisticated blades, which may reflect the beginnings of modern behavior.

Wilkins's team studied the shapes and use wear of 210 stone artifacts from KP1 as compared to ancient tools from other sites. The KP1 points met several criteria for use as spears but were not consistent with cutting. For example, both smaller and larger points were symmetrical rather than asymmetrical, as would be expected if they had been used as spear points rather than cutting tools. The KP1 points also showed a clear pattern of fractures at their tips, typical of the impact damage seen when spears are thrown or thrust at animals. To verify this, the team manufactured 32 of its own experimental spears and thrust them into the carcass of a springbok; the experimental points showed fracture and use wear patterns very similar to those found at KP1.

Wilkins concluded that the spear points from KP1 are the "oldest known evidence" of this type of weapon. Their early appearance suggests that the first glimmers of modern human behavior "could be pushed back to 500,000 years ago," she said.

The KP1 study provides "convincing evidence that the pointed flakes were hafted to spears," says archaeologist Curtis Marean of ASU Tempe. "If the ages are correct, this would set this technology back 200,000 years earlier than previously known in Africa."

He and Brooks of George Washington University in Washington, D.C., caution that the dating needs to be confirmed. Nevertheless, Brooks, who co-organized the meeting, calls the work "fantastic" and agrees with Wilkins that technologies often associated with modern humans, such as spear points, were invented by hominins who lived long before the first *Homo sapiens* appeared about 200,000 years ago.

If the evolution of modern behavior is no longer seen as sudden, a similar fate may be in store for one of archaeology's greatest upheavals: the so-called Neolithic Revolution in the Near East, which began about 11,000 years ago, when hunter-gatherers began to farm and settle down in sedentary villages. Many researchers have seen the roots of the Neolithic Revolution in a hunter-gatherer culture that immediately preceded it called the Natufian, which lasted from about 15,000 to 11,500 years ago. The practices of Natufians apparently foreshadowed many of the features of the Neolithic: sedentary communities of huts, elaborate ritual burials, cultivation of wild plants, and intricate personal ornaments (*Science*, 22 January 2010, p. 404).

But a presentation here by archaeologist Lisa Maher of the University of California, Berkeley, suggests that the novel behaviors of the Natufian culture, and by extension those of the Neolithic Age, were also the result of a long and gradual process. Maher and Tobias Richter of the University of Copenhagen lead a dig at a site called Kharaneh IV in Jordan, where they see glimpses of Neolithic origins. Radiocarbon dating puts occupation of Kharaneh IV between 19,900 and 18,600 years ago, near the beginning of what is called the Epipaleolithic Period. The site is "incredibly dense in archaeological material," including thousands of stone tools, animal bones, and perforated shell beads, along with a few ritual human burials, Maher said at the meeting.

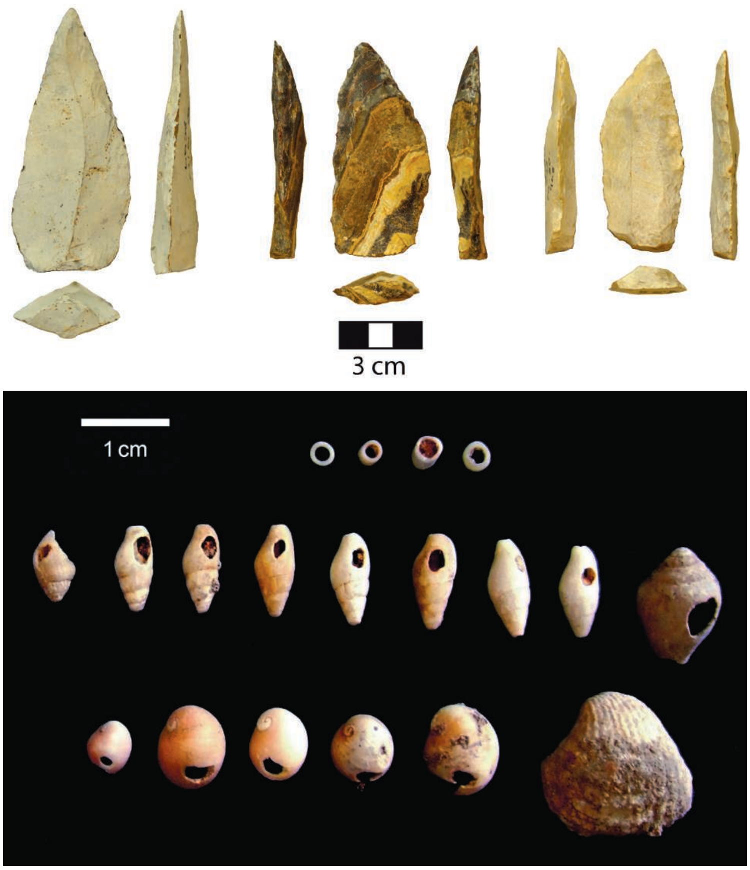

Evolutionary, not revolutionary? 500,000-year-old spear points from South Africa (*top*) and 20,000-year-old shell ornaments from Jordan suggest that sophisticated human behaviors developed gradually over time, rather than in sudden bursts.

In many ways, Kharaneh IV looks like a typical Natufian site, complete with residential huts and evidence of nearly year-round occupation, Maher said. It also provides evidence of long-range social networks more typical of the Neolithic itself. Many of the shells used to make personal ornaments came from the Red Sea and the Mediterranean, several hundred kilometers away, and some came from the Indian Ocean, more than 2000 kilometers away. The "changes we see in the Neolithic extend back over 10,000 years of prehistory. If we want to look for their origins, we need to look at least to the beginning of the Epipaleolithic," Maher said. "It's a second revolution that wasn't."

Marean agrees that Kharaneh IV suggests a "long run-up" to the Neolithic accompanied by far-flung social networks. Says Shea, "The 'holy shit' moment in Lisa's talk was when she announced they had shells from the Indian Ocean. That tells us these Epipaleolithic people were networking over immense spans of geography."

But Conard cautions that despite the growing evidence that the development of farming and settled life was a gradual process, archaeologists should not understate the enormous changes that the Neolithic ultimately brought about, such as the rise of cities. "Life as we know it today would not be possible without these major changes," Conard says. "Revolutions are in the eye of the beholder."

–MICHAEL BALTER

CREDITS (TOP TO BOTTOM): J. WILKINS & M. CHAZAN, *JOURNAL OF ARCHAEOLOGICAL SCIENCE* (ADVANCED ONLINE EDITION) 4 FEBRUARY; LISA A. MAHER

Published by AAAS

Work hard, play hard. AIMS Senegal students Diogène Pongui and Odumodu Nneka Chigozie, and lecturer Abdellah Sebbar (*left to right*).

DEVELOPMENT

First Spinoff of African Math Institute Takes Root in Senegal

M'BOUR, SENEGAL—Golden sand, the Atlantic Ocean, beach volleyball—these are just occasional distractions for the 31 students from all over Africa who are doing 10 months of intensive training at the newest branch of the African Institute for Mathematical Sciences (AIMS). A few steps from the beach on a small nature reserve in this town 2.5 hours south of the Senegalese capital, Dakar, the institute is their home, cafeteria, and lecture hall. Top lecturers are flown in from around the world to teach; in this first year, two Fields Medal winners were among them. Life at AIMS Senegal is mostly "very hard work," says Diogène Pongui, a student from the Republic of the Congo.

AIMS Senegal is the little sister of AIMS South Africa—a similar institute founded in 2003 just outside Cape Town—and part of a story that has captivated mathematicians and triggered an outpouring of support in money, time, and brainpower. The institutes are the brainchild of Neil Turok, a South African–born mathematician who heads the Perimeter Institute for Theoretical Physics in Waterloo, Canada.

Turok, whose parents were jailed as anti-apartheid activists, believes excellence in math is one of the keys to development in Africa. He has a dream to create a network of 15 AIMS institutes around the struggling continent. He ambitiously dubbed it the Next Einstein Initiative—the idea being that the 21st century's most revolutionary mathematicians might well be Africans (*Science*, 2 May 2008, p. 604).

At first the dream proved harder to realize than Turok hoped. Despite lots of sympathy, "we were often at the brink of bankruptcy during the first few years," he says. Big donors tend to shun higher education projects, which aren't among the U.N.'s Millennium Development Goals (wrongly, Turok says). The plan to open a second AIMS institute in Nigeria, Africa's most populous country, was stranded over differences with the local partner, the African University of Science and Technology in Abuja. Small-scale by nature, AIMS didn't feel at home in the grandiose plans for the university, a World Bank project. AIMS also insists on not charging tuition and recruiting women as 30% of its student body.

The past 2 years have brought a "transformation," Turok says. Several big donors came through—most notably the Canadian government, which pledged \$20 million in 2010 to expand the network. The money supports not just the Senegal franchise but also one in Ghana, to be opened in September, and a fourth slated to launch in Ethiopia next year. Each will be co-administered by local universities.

In Senegal, the plan found a willing ear in then-president Abdoulaye Wade, whose government donated €1 million for a new building that will replace the current, modest dwellings loaned from a French institute. Wade was defeated in elections in February, but his successor, Macky Sall, is a geological engineer and a science supporter as well, says Mamadou Sangharé, a mathematician at University Cheikh Anta Diop in Dakar and the president of AIMS Senegal.

Despite some differences from AIMS South Africa—both English and French are spoken here, and the atmosphere is a bit more relaxed, Turok says—the idea behind AIMS Senegal is the same. Students come for months of day-and-night immersion in high-level mathematics. For many students, the focus on problem-solving rather than rote learning is like "shock therapy," Turok says. "The first 2 months, they are typically very unhappy. Then, a light bulb goes on, and they realize they can learn by playing and discovering."

To avoid distractions, AIMS deliberately picked this regional city as a home; Dakar, the capital, has more intellectual life but also a famed music and nightlife scene. The students have mostly stayed focused, Sangharé says, and have grand ambitions. Several have lined up Ph.D. training at universities in Europe and North America.

Perhaps the main attraction here is the lecturers: internationally renowned mathematicians, who each come to spend 3 full weeks. They're extremely accessible; discussions often continue during the communal meals and into the night. "It's amazing and very inspiring," says Nigerian student Odumodu Nneka Chigozie. It's a big investment for the faculty, says Abdellah Sebbar of the University of Ottawa, who did his stint earlier this year—especially because he has three children and a wife with a job of her own. But Sebbar, who hails from Morocco, says that as an African, "I want to be in this process for the long run."

Turok, too, has plenty of plans for the long run. After next month's graduations here and in South Africa, AIMS will have generated 450 alumni. With more money, there could be a fifth AIMS, and a sixth, and so on, leading to a pan-African network of thousands of well-trained alumni—including, perhaps, that new Einstein. "I really think that will transform development," Turok says. And then, as the mathematician takes over from the dreamer: "It would cost \$100 million over the next 10 years—that's about 0.003% of Africa's total aid budget." **–MARTIN ENSERINK**

CREDITS: (PHOTOS) M. ENSERINK/*SCIENCE*

Published by AAAS

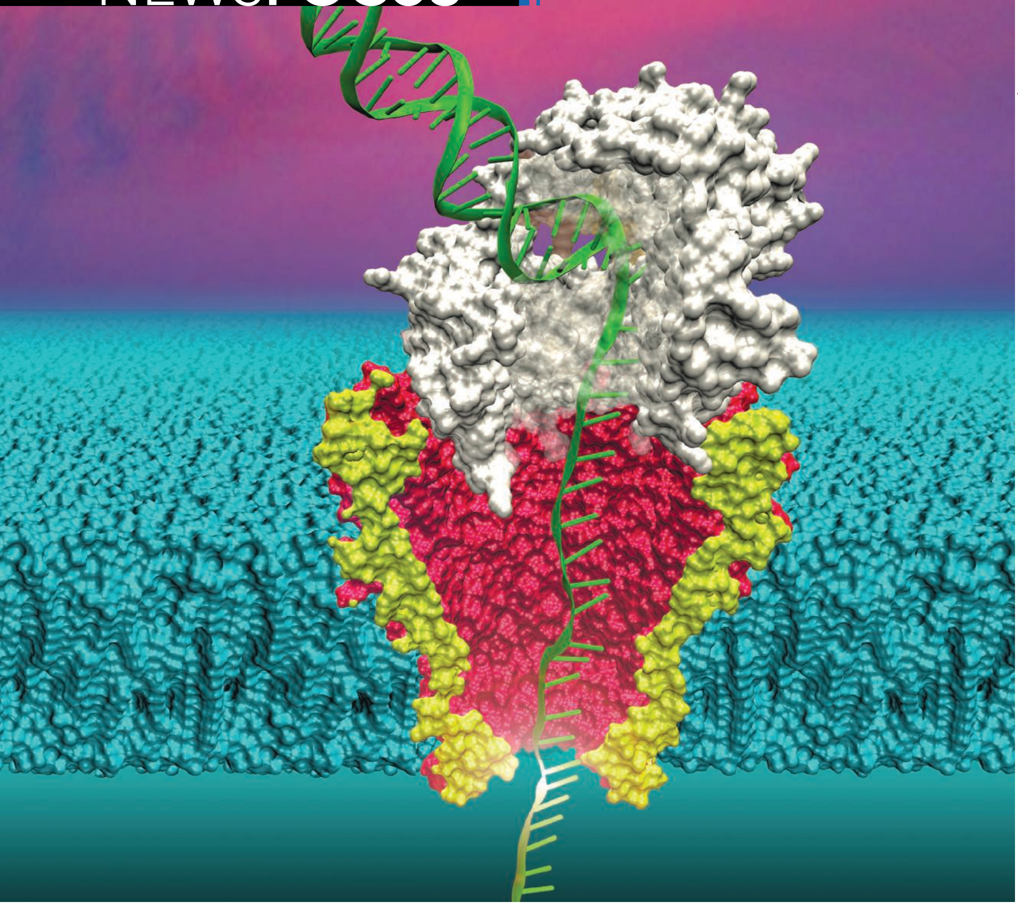

Threading the pore. With nanopore sequencing, single molecules of DNA will be deciphered as they pass through a tiny channel.

Search for Pore-fection

At long last, nanopore sequencing seems poised to leave the lab, promising a new and better way to decode DNA

In a packed Florida conference center 3 months ago, Clive Brown introduced an audience of scientists, engineers, and biotech analysts to a device resembling an oversized thumb drive. He promised it would decipher almost a billion DNA bases in 6 hours and sell for $900. As backing for that claim, Brown described how Oxford Nanopore Technologies, where he is chief technology officer, had used a prototype to decode the genome of a virus in a single pass of a complete strand of its DNA. "There was an audible gasp from the audience," recalls Oxford Nanopore's CEO, Gordon Sanghera.

If Oxford Nanopore's claims and promises are borne out—and some scientists remain skeptical—the company is set to achieve the first commercialization of a long-awaited and oft-doubted technology called nanopore sequencing. The technology, based on protein pores so tiny that 25,000 of them can fit on the cross section of a human hair, could be the next big thing in genome sequencing and analysis.

Although they've gotten much cheaper and smaller in recent years, machines that read DNA and RNA still usually cost hundreds of thousands of dollars, take up entire lab benches, and require much upfront and postsequencing processing to generate a genome. Nanopore sequencing could change all that. This new technology "really requires you to think about things in a completely different way," says Elaine Mardis, co-director of the Washington University Genome Institute in St. Louis.

As the tweeters and bloggers in Brown's audience went wild, sending missives out onto the Internet, David Deamer, a biophysicist at the University of California, Santa Cruz (UCSC), and Harvard University cell biologist Daniel Branton sat in the front row, beaming. In 1996, 7 years after Deamer initially had the idea, they had publicly proposed that threading DNA through a tiny pore and monitoring changes in the current going through the pore could yield a more direct, faster way to sequence genomes. Yet until the Florida meeting, no one had claimed success in reading DNA as it moved through a pore, leaving many to wonder whether the technology would ever pan out. "Over the years, the number of people who truly believed in nanopore sequencing you could probably count on your two hands," says Mark Akeson, a molecular biologist at UCSC. "Now both companies and academics are seeing [evidence] that this stuff actually works. This technology is going to really take off."

Sequencing gold rush

Over the 2 decades that nanopore sequencing has lingered backstage, many other advances have greatly reduced the cost and increased the speed of reading the strings of adenines, guanines, thymines, and cytosines that compose strands of DNA. Whereas that first human genome sequence cost an estimated $1 billion to complete, the all-inclusive price at a high-throughput sequencing center today is about $18,000, and a few companies are promising costs approaching $1000 per genome. The pace has also quickened. It took 3 years at the turn of the century to produce a draft of a human genome; the same can now be done in a week. Since the human genome sequence was completed in 2003, researchers have decoded hundreds of genomes of plants, animals, cancer cells, and even ancient humans, proving that sequencing is a valuable tool for biomedicine and all sorts of other disciplines, from ecology to anthropology. Researchers are calling for 10,000 vertebrates to be sequenced, for example, and physicians may soon routinely order up a patient's genome sequence for diagnostic or preventive purposes.

Nanopore sequencing has not been part of this revolution. Instead, it was an appealing idea for which every aspect needed to be developed. When they first considered the concept, Deamer and Branton didn't have an appropriate pore or a way to control DNA's flow through such a pore, and they didn't know for sure that they could distinguish the different bases on a strand of nucleic acid. Ever so slowly, they and a handful of others have made advances on all those fronts, with several key publications in the past 2 years signaling progress, not just with protein pores but also with solid

Online
sciencemag.org
Podcast interview with author Elizabeth Pennisi (http://scim.ag/pod_6081).

CREDIT: DR. IAN M. DERRINGTON

Published by AAAS

state ones (see sidebar, p. 536).

Oxford Nanopore has promised to sell its new protein-pore sequencers by the end of the year, and if those machines pan out, it could set off another genomics revolution, many scientists predict. "Current sequencing has an awful lot of complications that just go away with nanopore sequencing," says Stuart Lindsay, a physicist at Arizona State University, Tempe.

Nanopore sequencing should require little upfront preparation beyond isolating an organism's DNA, and even that might be done away with in some applications. In contrast, current approaches require that the DNA be copied many times over and, typically, labeled with a fluorescent tag that can be read by an optical sensor. Such preparation takes time and money and erases any of the chemical modifications that result in the epigenetic control of gene expression—something researchers increasingly want to know about that nanopore devices may be able to read.

Furthermore, current sequencers work by decoding many short stretches of DNA—typically 200 bases or so—and that information has to be painstakingly pieced together. Nanopore technology can read much longer stretches of DNA: At the February meeting, Brown reported decoding a 48,000-base genome of a bacteriophage, a virus that infects bacteria, by first linking the ends of the two strands of its DNA, then threading the entire genome, first one strand and then the other, through a pore in one pass. "That really stunned the audience," Deamer says.

While no scientist outside of Oxford Nanopore has reported seeing the prototype sequencers Brown bragged about in Florida, the company says it will eventually have an 8000-pore version—many pores will be needed to sequence genomes much larger than a phage's DNA. With 20 of these machines, it should be possible to reveal a human genome sequence in 15 minutes. "You don't have to wait 2 weeks to do the assembly; you are watching it on the fly," Akeson says. "If [nanopore sequencing] works, there's not going to be anybody in genomics who is not using the device in some fashion."

That's a big "if," Mardis notes. "It's such a beautiful possibility, but there are many technical hurdles to getting it to actually produce sequence data."

Not just an idea

Deamer began trying to jump those hurdles almost 25 years ago, long before Oxford Nanopore formed. In 1989, Deamer was working on the origins of life and was struggling to figure out how to get the molecule adenosine triphosphate (ATP) across a lipid membrane to supply energy to enzymes trapped inside his synthetic "cell." He quickly realized that his theoretical solution—to insert a channel of some sort into the membrane—had other possibilities. If ATP could squeeze through, so might DNA. And as DNA crossed the channel, he reasoned, it would alter the ion flow through the channel. Finally, if the changes in this hypothetical channel's ionic current differed with each of DNA's bases, then that could open up a whole new way of sequencing. At the time, the idea seemed fanciful even to Deamer. For starters, he recalls, "there was no pore available." Nevertheless, he sketched out his idea in a lab notebook.

Showstopper. If it works, this device could enable DNA sequencing to be done from a laptop.

Deamer also shared the scheme with Branton, and they approached Harvard about patenting it. They weren't the only ones thinking along those lines: They discovered that a colleague, geneticist George Church, had independently come up with a similar plan to sequence DNA using a pore from a bacteriophage. The three of them decided to join forces and eventually filed for a patent together. The chief missing ingredient was still a big enough pore. Church moved on to other sequencing projects, but Deamer kept an eye out for a way to make his idea reality.

Deamer learned about α-hemolysin, a protein that *Staphylococcus aureus* uses to bust open red blood cells. John Kasianowicz, a researcher at the National Institute of Standards and Technology (NIST) in Gaithersburg, Maryland, was testing pores formed by this protein as biosensors for toxic heavy metals in solution. Working with Hagan Bayley, now at the University of Oxford in the United Kingdom, he had embedded an α-hemolysin pore in a membrane and applied a voltage to produce an electrical current of potassium and chloride ions through the pore. Sensitive electronics measured the ion flow. Kasianowicz hoped the heavy metals would bind to the pore and alter the ionic current in distinctive ways.

"It occurred to me that this pore might in fact be large enough" to allow strands of RNA or DNA to move through, Deamer says. In 1993, he went to NIST with some RNA to test the concept. Because DNA and RNA are negatively charged, they would be pulled through the pore. As Deamer suspected, as the strand of RNA passed the narrow point of the pore, it interfered with the ion flow, changing the current. "We immediately got huge numbers of signals from the recorder," indicating that the RNA was blocking the pore's ionic current as

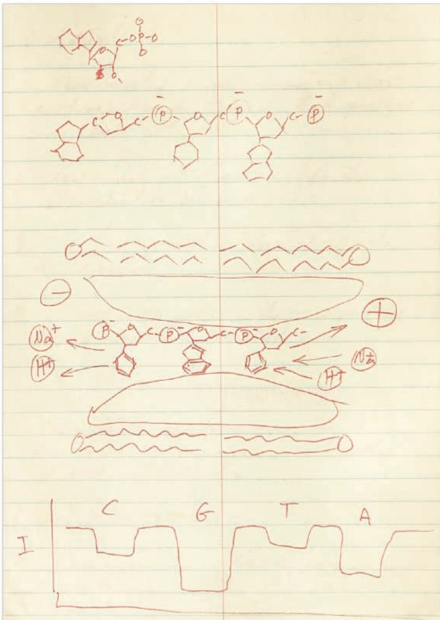

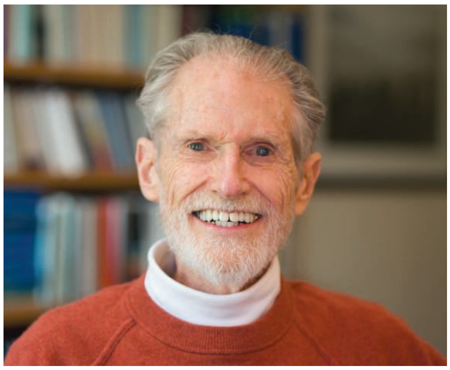

Nanopore dreamers. After David Deamer (*top right*) sketched out nanopore sequencing in 1989, he teamed up with Daniel Branton (*bottom right*).

CREDITS: (TOP) NIGEL CHAPMAN PHOTOGRAPHY; (BOTTOM CLOCKWISE FROM LEFT) DAVID DEAMER (2); PAUL HOROWITZ

Published by AAAS

it threaded its way through, Deamer says.

In 1996, he, Kasianowicz, and Branton published a paper in the *Proceedings of the National Academy of Sciences*, in which they reported that they could unravel a coiled nucleic acid so that its bases move through the pore single file. They could tell the length of a strand of DNA going through the pore by the amount of time the ionic current signal was altered. In the article, they suggested that this approach could also be used to sequence DNA. "That was the pioneering paper," says Henry White, a chemist at the University of Utah in Salt Lake City.

Even with a potential pore in hand, Deamer and his colleagues realized that DNA's bases were whipping through the channel too fast to be identified. One solution was to harness another protein to latch onto the DNA and control its movement through the pore. Reza Ghadiri of the Scripps Research Institute in San Diego, California, was also interested in nanopore sequencing and had taken the first steps toward controlling DNA movement using a polymerase, an enzyme that copies DNA by ratcheting a DNA strand along base by base, like a sprocket moving the links of a bicycle chain, as it adds the complementary base. Independently, Akeson, working with Deamer, started buying and testing various polymerases from different species and other proteins. The first ones he and his colleagues tested quickly fell off the DNA, only briefly moving the strand through the pore. After many years of trying, in 2010, they discovered that a polymerase from a phage called φ29 would move long stretches of DNA, one base at a time, at a reasonable pace through α-hemolysin.

Yet although the φ29 polymerase slowed the DNA down as desired, the stem of the mushroom-shaped pore was so long that more than a dozen bases were passing through at any one time, creating a fuzzy ionic current signal at best. The signals weren't distinctive enough to tell one base from another. They needed a different pore.

A better pore

Fortunately, Jens Gundlach, a gravitational physicist at the University of Washington, Seattle, had heard about nanopore sequencing and was intrigued enough to move into biophysics. In 2003, Gundlach started looking into alternatives to α-hemolysin. A literature search yielded no promising candidates, but then he saw in *Science* a pore in a different bacterium with a potentially better geometry—it was shaped like a funnel—for

Going Solid-State

The first nanopore sequencers will depend on protein pores, but many in the field envision replacing these biological channels with solid-state ones. They also foresee controlling DNA's movement through a sequencer's channels electrically rather than depending on another protein to ratchet the bases along the pore. Ditching the proteins could pave the way to even cheaper devices that take advantage of semiconductor manufacturing technology to mass-produce and shrink these sequencers.

Since 2005, Tomoji Kawai, a physical chemist at Osaka University in Japan, and his colleagues have experimented with a pore in a silicon wafer. In Kawai's device, a quantum-dynamics effect known as electron tunneling, in which electrons jump from one place to another through what should be a barrier, has replaced the ionic current of the protein pore nanosequencers (see main text, p. 534) as a means of reading the bases. Two nanoelectrodes flank the pore and are close enough to produce quantum tunneling across the pore. As they pass between the electrodes, DNA's four bases alter the tunneling current in specific ways that are detected by the electrodes.

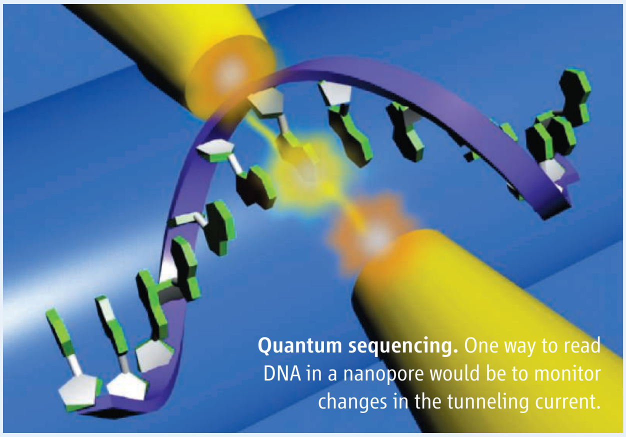

Quantum sequencing. One way to read DNA in a nanopore would be to monitor changes in the tunneling current.

Instead of controlling the movement of the RNA or DNA strands with motor proteins, Kawai uses an electrical field that starts and stops the passage of the negatively charged nucleic acids through the wafer. Thus far, he has used the technology to read up to 20 bases of RNA. Toshiba is looking into using the technology to detect viruses, and Toray Industries Inc. plans to develop a test for an RNA cancer marker.

Working together, IBM and Roche are also exploring an electronics-based approach. At the core of their nanopore-sequencing technology is a "DNA transistor," a chip that consists of a stack of alternating metal and insulating layers, with the pore drilled through the layers. Sequential electric fields will pull the DNA through base by base. In 2010, researchers at IBM T. J. Watson Research Center in Yorktown Heights, New York, published a simulation showing the potential of this approach, and they have since been working on making a device. "We are pushing the limits" of chip technology, says Gustavo Stolovitzky of IBM.

Like Kawai, Stolovitzky and his colleagues aim to detect tunneling differences. But his team decided that simply placing the electrode pair in the pore would work poorly, so they approached Stuart Lindsay, a physicist at Arizona State University, Tempe, who has developed a way to fit each electrode with a small organic molecule that is prone to making hydrogen bonds. These molecules recognize and latch onto each DNA base, briefly holding on to it until a signal is registered. In 2011, Lindsay licensed the technology to Roche.

Neither IBM nor Roche will say exactly where their collaboration is in the development of this nanopore-sequencing technology. The "main challenges" are engineering, Lindsay says—"These are tiny devices that need to be made precisely."

Another potential solid-state pore material is graphene, which consists of a layer of carbon molecules arranged in adjoining hexagons. In theory, a graphene pore could be one atomic layer thick, just deep enough for a single base to pass by at one time, which might make detection more precise. In 2010, Daniel Branton and Jene Golovchenko of Harvard University and colleagues, along with two other independent groups, reported that they could detect DNA moving through graphene pores. They have since been working on building pores more reliably.

The idea would be to apply semiconductor manufacturing technology to build large arrays of solid-state pores that allow for very fast sequencing. If these can be developed, they "offer the possibility to obtain genome sequences in less time than it takes to unravel a stethoscope" and could be a "compelling" technology for personalized genome sequencing, Hagan Bayley, a pioneer in nanopore sequencing at the University of Oxford in the United Kingdom, wrote in 2010. **–E.P.**

CREDIT: MASATERU TANIGUCHI/THE INSTITUTE OF SCIENTIFIC AND INDUSTRIAL RESEARCH, OSAKA UNIVERSITY

Published by AAAS

getting a strong ionic current signal. Called MspA (for *Mycobacterium smegmatis* porin A), this channel has a single narrow section long enough for just four bases. The natural MspA had limitations, however: The constricted section carries a negative charge, making it hard for the similarly charged DNA to get through.

Gundlach and his colleagues tweaked MspA's gene, changing the protein so that the constricted part of the pore was neutral, and produced the modified pore by expressing the altered gene in bacteria. They had also added some positive charges at the pore entrance to enhance the inflow of DNA. When DNA was suspended in the modified pore, the signal for each base was almost 10 times stronger than the signal for immobilized bases in α-hemolysin, Gundlach's team reported in 2010. A sequencer using this unnatural MspA in theory "could resolve in much finer detail the DNA strands," Akeson says.

But each base still zipped by in a microsecond, 1000 times faster than could be read. And the only way Gundlach could slow them down required modifying the DNA itself, an impractical solution. So last year, he and Akeson joined forces. "The φ29 polymerase provides a mechanism to move the DNA through the pore at a reasonable speed," about one base every 30 milliseconds, Gundlach says. With the combination of Gundlach's pore and Akeson's polymerase, nanopore sequencing finally made its public debut, at least in the academic sense. Gundlach and his colleagues reported at the Florida meeting and online 25 March in *Nature Biotechnology* that they had could distinguish the bases in six DNA strands ranging from 42 to 53 bases long. "This is the first paper where somebody has actually [read] DNA," says chemist Geoffrey Barrall, president of Electronic BioSciences in San Diego, California, which is also developing nanopore sequencing technology. (Oxford Nanopore has yet to publish a scientific paper on the phage genome sequencing Brown described in Florida.) Gundlach says he has since tested longer stretches of DNA.

A company is born

While Deamer and the other U.S. researchers were struggling to make nanopore sequencing a reality, Bayley was modifying the α-hemolysin pore with a different primary goal in mind: sensing devices. He had started looking at α-hemolysin in the 1980s to learn how water-soluble proteins made it through membranes, but he got interested in engineering pore proteins for biotechnology. Bayley envisioned pores that would help kill tumor cells or detect metals, sugars, and other proteins, and he had been modifying this pore for these different applications, making much progress. In 2005, he started a company to commercialize these biosensors.

About the same time, the push for the $1000 genome (*Science*, 17 March 2006, p. 1544) had resulted in a new U.S. National Human Genome Research Institute (NHGRI) program for technology development. Bayley decided to apply and see what his modified α-hemolysins could do with respect to sensing DNA. Since he knew that he could make pores that could distinguish mirror versions of the same molecule, he was confident he could distinguish DNA's bases. With Ghadiri, he got an NHGRI grant and eventually published that the pore could tell DNA's building blocks apart when they were in solution. He decided to pursue the idea of feeding individual bases through the pore and started looking into using an enzyme that would break off each base as the DNA entered the pore. In 2008, his company, now renamed Oxford Nanopore Technologies, stepped up its efforts in nanopore sequencing, first pursuing the idea of reading cut-up bases and later following the path others had taken, decoding long, intact DNA strands.

Oxford Nanopore went after a better pore in earnest, developing a high-throughput approach toward testing and modifying potential protein candidates. The company licensed technology developed and patented by Bayley, Deamer, Branton, Akeson, and others. Because the natural lipid bilayers of the cell membrane originally used to hold the pores are not very stable, the company developed a polymer alternative that could withstand exposure to blood or pollutants. And Oxford Nanopore has its own proprietary motor protein to control the DNA's flow through the pore. The company won't disclose any details yet but says it will have data and machines for academics to evaluate in the coming months.

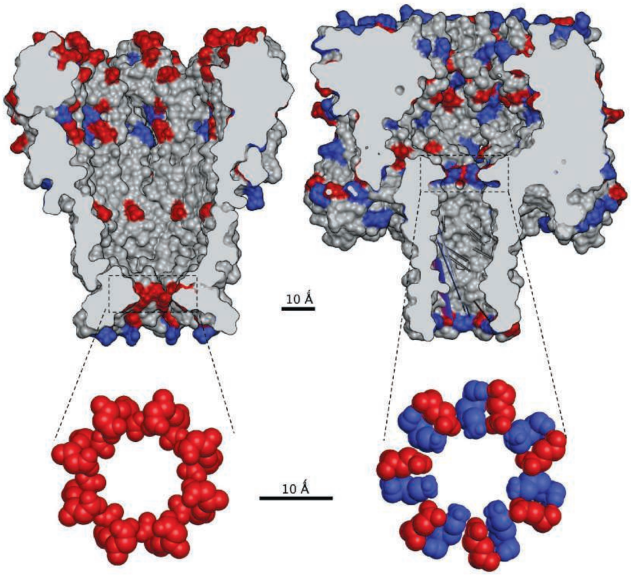

Perfecting pores. Cross sections of the MspA (*left*) and α-hemolysin (*right*) pores show their different geometries.

One challenge, the company acknowledged in Florida, is getting the error rate down from its current 4%. Academics concur that errors are a problem. As a polymerase ratchets along, it sometimes backtracks so that a base is read twice; other times, the base gets through the pore without being read. One can compensate for these random errors by sequencing each DNA strand multiple times. With the pore setup developed by Akeson and Gundlach, they can read the DNA as it is first pulled down through the pore and then again as it is pulled up and turned into double-stranded DNA by the polymerase. In theory, one could repeat those two steps with the same strand as many times as needed. With its sequenced viral genome, Oxford Nanopore showed it could tackle the problem by connecting the DNA's two complementary strands so that each is sequenced, the second providing an accuracy check on the first.

Neither approach solves another problem, accurately reading long stretches in which the same base is repeated, a not-infrequent occurrence in genomes. But nanopore proponents point out that this repetitive DNA is difficult for all sequencing techniques.

How solvable this and other problems are and whether they can be overcome in the coming months is not yet clear. Oxford Nanopore has a good reputation, but some rival sequencing companies and genome experts won't believe the sequencers work as advertised until they can test one. They caution that nanopore technology has been "coming" for so long that it's hard to believe the hurdles are finally overcome. However, "if they could pull it off," Mardis says, "it would be a complete game changer." And Deamer and Branton's smiles may get even wider.

–ELIZABETH PENNISI

CREDIT: IAN M. DERRINGTON

Published by AAAS

For Early Hominins in Africa, Many Ways To Take a Walk

If the bureaucrats of Monty Python's Ministry of Silly Walks were to establish a hall of fame, they might consider inducting *Australopithecus sediba*, who walked with its weight balanced oddly on the inside edge of its soles about 2 million years ago in South Africa. Or they might ponder the contrasting way two types of australopithecines strolled across the same region of Ethiopia's Rift Valley about 3.4 million years ago. While one strode much like humans do today, the other tucked in its opposable big toe and swayed from side to side. "The take-home message here this morning is … there were different ways of being a good biped throughout early human evolution," paleoanthropologist Jeremy DeSilva of Boston University reported.

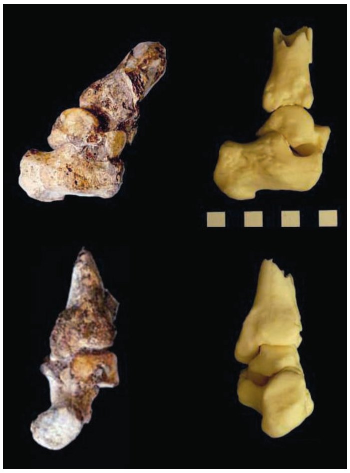

Different steps. The Burtele foot from Ethiopia (*left*) and the *Au. sediba* foot from South Africa show different ways of walking upright.

Of course, the walks weren't silly to these early hominins, the group that includes humans and our ancestors but not other apes. At the time, these gaits were adaptive, and so they shed light on how upright walking evolved in different habitats. Several new studies of incredibly rare fossils of feet and partial skeletons reported at the meeting reveal the complexity of early bipedalism. "By seeing subtle differences in different species, we're moving beyond the (simple) debate of whether a hominin had a humanlike bipedalism or not," says paleoanthropologist Brian Richmond of George Washington University in Washington, D.C.

Until recently, many thought that upright walking—a defining trait of being a hominin—evolved step by step in one lineage relatively quickly, perhaps just before the emergence of *Au. afarensis*—the species of the famous fossil Lucy—about 3.6 million years ago. But the discovery of older upright walkers, including the 4.4-million-year-old *Ardipithecus ramidus* and the 6-million-year-old *Orrorin tugenensis*, have pushed back the origins of bipedalism to 6 million years ago (*Science*, 2 October 2009, p. 36).

This spring, researchers unveiled the more primitive foot of a still-unnamed species of *Australopithecus* from Burtele, near Hadar, Lucy's home in Ethiopia. That showed that at least two kinds of hominins walked upright in different ways at the same time 4 million to 3 million years ago (see http://scim.ag/EarlyAncestor).

In a talk, paleoanthropologist Yohannes Haile-Selassie of the Cleveland Museum of Natural History in Ohio showed how the new foot shared features such as an opposable big toe with older *Ar. ramidus*, which suggests that both hominins still spent considerable time in trees. The foot also shared a key trait (the shape of a toe bone) with *Au. africanus*, which lived about 2 million years ago in South Africa. Neither of those features is found in *Au. afarensis*, suggesting that Lucy's species cannot be the direct ancestor of *Au. africanus*. That means that a second hominin lineage, with a different way of walking, must have led to *Au. africanus*, Haile-Selassie notes. (Lucy's species is still the leading candidate for ancestor to early *Homo*.)

Meanwhile, DeSilva reported at the meeting that his analysis of the feet of two newly discovered partial skeletons of *Au. sediba*, considered a relative of *Au. africanus*, shows that this species walked with "excessive" pronation. It landed on its primitive, narrow heel and shifted its weight to the inside of its sole. "The big question now is why did it walk this way?" DeSilva says. All this variation in bipedalism shows that "through much of human evolution, there were several experiments in bipedalism going on," he adds.

One long-standing hypothesis holds that bipedalism arose because it's energetically more efficient to walk upright on two legs rather than on four. But paleoanthropologist Herman Pontzer of Hunter College in New York City and David Raichlen of the University of Arizona in Tucson reported in a poster that that idea doesn't hold up. They modeled the energy cost of walking and found that long-legged hominins are energetically efficient because they walk with straight legs, with their knees directly over their lower legs. In contrast, the crouched, bent-knee posture of the earliest hominins, such as *Ardipithecus,* required more muscle activation and energy. Simply walking on two legs instead of four doesn't save energy, so the earliest hominins must have begun walking upright for other reasons. Taken together, the flurry of new reports suggest to Pontzer that "our models of the origins of bipedalism are overly simple."

How the Modern Body Shaped Up

Modern humans have gone through a lot of changes in the past 30,000 years. We switched from hunting and gathering to farming and herding; from life as nomads to settling in urban centers; from eating meat, nuts, and tubers to consuming grains, sugars, and dairy products. Now, a remarkably comprehensive analysis of more than 2000 European skeletons presented at the meeting reveals how these cultural changes have altered our physiques. "When you become a modern human, what happens to your body?" asked paleoanthropologist Christopher Ruff of Johns Hopkins University in Baltimore, Maryland, co-chair of the session on skeletal adaptation in recent Europeans.

While other studies have documented a decrease in height after the transition to agriculture, this is the first systematic study

CREDITS (LEFT TO RIGHT): COURTESY OF YOHANNES HAILE-SELASSIE/CLEVELAND MUSEUM OF NATURAL HISTORY; JEREMY DESILVA

Older Dads Have Healthier Kids Than You Think

Older fathers often get blamed for passing on genetic mutations to their children, causing some types of autism, schizophrenia, and other disorders. But new data presented at the meeting suggest that children of older fathers and grandfathers may inherit at least one advantage from aging patriarchs: longer telomeres, structures at the tips of chromosomes that may protect against aging and disease. And the effect is amplified over the generations: "We've shown that the paternal grandfather's age is associated with longer telomeres in his grandchildren," graduate student Dan Eisenberg of Northwestern University in Evanston, Illinois, reported in a talk.

Telomeres are repetitive sequences of DNA that prevent the ends of chromosomes from unraveling, much like the plastic tips on the ends of shoelaces. As cells divide and replicate, telomeres get shorter and eventually can no longer prevent the fraying of DNA and the decay of aging. Recent studies have found a link between living to 100 and having a hyperactive version of telomerase, an enzyme that keeps telomeres long.

Telomeres in sperm cells, however, are exceptional: Several studies have shown that they grow longer, not shorter, over the years, probably because telomerase activity is high in testes. As a result, sperm cells from older men have longer telomeres than those of younger men. That would suggest that the older a father is at conception, the longer the telomeres his sons and daughters inherit.

Working with Northwestern biological anthropologist Christopher Kuzawa and anthropological geneticist Geoff Hayes, Eisenberg examined data from a long-term study of 3327 women who were pregnant in 1983 in the Cebu Longitudinal Health and Nutrition Survey in the Philippines. They had gathered the ages of fathers and in 2005 measured telomere length in the blood of 1845 moms and 1681 children.

Children of older fathers did indeed have longer telomeres than those of younger dads: For each additional decade of age in fathers at conception, sons and daughters had 4% longer telomeres, a finding that corroborates earlier work. The Northwestern group also found that for every additional decade of age in grandfathers, the grandchildren's telomeres added another 4%. But grandfathers did not pass on their longer telomeres to their daughters' children, only their sons', suggesting that this is a paternal effect.

Grandfather effect. Older fathers in the Philippines passed on long telomeres to their sons and grandsons.

The increase in telomere length per year of fathers' age is just about the same amount as telomere length lost per year in normal aging, Eisenberg says. So the longer telomeres in sperm roughly offset normal aging, giving children of older dads an advantage. "It's as if you delay reproduction, you earn this kind of higher fitness for your offspring," says biological anthropologist Koji Lum of Binghamton University in New York.

Any benefit in telomere length may still be swamped out by the risk of passing on more mutations, Eisenberg warns: "We don't know yet the net health effect." So at the moment, he's not advising anyone to delay fatherhood. –**A.G.**

of how the skeleton changed from the time modern humans spread through Europe 30,000 years ago until they were circling the globe in jets by the 1960s. In 10 posters, Ruff and his colleagues focused on how each part of the body, from the spine to leg and arm bones, evolved over time through both genetic and cultural change.

One of the most significant findings is a dramatic drop in strength in leg bones. Leg bending strength, or resistance to fracture, declined by 25% to 33% from 27,000 years ago to 1900 C.E., as shown by the cross-sectional dimensions of the upper and lower leg bones of 1834 men and 786 women, according to a poster by Brigitte Holt of the University of Massachusetts, Amherst, and her colleagues. This is "huge," Ruff says. "We interpret this to reflect the move from a hunting-gathering lifestyle to a more sedentary agricultural lifestyle across Europe." Our ancestors needed stronger legs to walk farther, especially if carrying goods.

Over the same 30,000-year period, upper body strength declined after the introduction of agriculture. In males, it then increased in the Medieval period, possibly due to intensive upper-body labor such as blacksmithing. One trend through time is that the right arm lost much of its asymmetric larger size compared to the left arm, perhaps due to fewer strongly lateralized activities such as spear throwing. Women show particularly symmetrical arms from the beginning of agriculture 7000 years ago to Europe's Bronze Age, 3000 years ago. The researchers suspect that this stems from using both arms to make flour with grinding stones.

Strong-arm tactics. Men had stronger right arms, perhaps from throwing spears and other activities, before the invention of agriculture.

As for overall height, about 30,000 years ago, European men stood 1.72 meters tall, almost as tall as Europeans today. Their height and weight dropped steadily until 4000 years ago, probably because of poorer nutrition and health, particularly with the advent of agriculture 10,000 years ago. With a few exceptions—for example, milk-drinking Scandinavians—Europeans got even shorter during the Medieval period and stayed short until 1900.

The study has produced "an awesomely comprehensive picture of skeletal adaptation," says bioarchaeologist Clark Spencer Larsen of Ohio State University in Columbus, who was not part of the team. Jay Stock of the University of Cambridge in the United Kingdom agrees that the study is a "major milestone. … It is a major achievement to quantify human variation through time and space with this resolution." **–ANN GIBBONS**

CREDITS (TOP TO BOTTOM): E. A. QUINN; PETER V. BIANCHI/NATIONAL GEOGRAPHIC COLLECTION

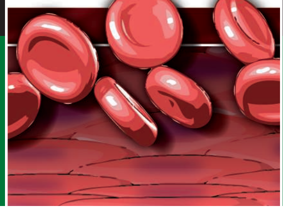

LETTERS

edited by Jennifer Sills

Food Price Complexities Require Nuance

I WAS DISAPPOINTED BY J. SWINNEN AND P. SQUICCIARINI'S POLICY FORUM, "MIXED MESSAGES ON prices and food security" (27 January, p. 405). Ironically, in making their case that the nuanced challenges of food prices are "too often absent in public debate," the authors paint a misleading picture of Oxfam's positions, lacking exactly the type of nuance they claim to promote.

To represent Oxfam's views, the authors cite an obscure press release, the primary purpose of which was to announce celebrity photos. In choosing this source, they excluded dozens of communications and policy papers on trade and agriculture policy that provide more extensive analysis, some of which directly undermine the authors' core case. For example, an Oxfam report on the 2008 food price crisis goes to great lengths to describe a "false dilemma," arguing that food prices, whether high or low, are like a double-edged sword bound to hurt either consumers or producers (*1*).

Swinnen and Squicciarini also imply that maintaining consistent policy positions is bullheaded. They fail to consider that Oxfam has a coherent understanding of the impact of food prices on poor people. We have highlighted both the dangers of drastic price spikes (*2*) and the hazards of unfair trade policies for poor farmers (*3*). If the messages seem "mixed" at first glance, it is because the problems are complex and not well suited to headline-length explanation.

Providing massive subsidies for agriculture in rich countries is unfair and an extremely inefficient way to reduce food prices for poor people (*1*); likewise, spiraling food prices can harm vulnerable people, so measures to moderate the price volatility and mediate the impacts on poor families are needed. If one's concern is for the well-being and livelihoods of poor people, as ours is, then these are consistent positions.

Ultimately, the authors' argument rests on the idea that press releases are not nuanced enough and advocacy messages oversimplify problems. This may be a compelling revelation for some academics. But in the real world, where Oxfam works to respond to emergencies, fight special interests, and empower the most vulnerable, we recognize that some measure of simplicity and accessibility in our messaging is required to achieve change.

GAWAIN KRIPKE

Oxfam America, Washington, DC 20005, USA. E-mail: gkripke@oxfamamerica.org

References

1. Oxfam International, "Double-edged prices" (Oxfam Briefing Paper 121, 2008); www.oxfamamerica.org/files/double-edged-prices.pdf.
2. Oxfam International, "Global food prices in 2011: Questions & answers" (www.oxfam.org/en/campaigns/agriculture/food-price-crisis-questions-answers).
3. J. M. Alston, D. A. Sumner, H. Brunke "Impacts of reductions in US cotton subsidies on West African cotton producers" (Oxfam America, Boston, MA, 2007); www.oxfamamerica.org/files/paying-the-price.pdf.

Response

KRIPKE TAKES ISSUE WITH THE REFERENCES we cited in our Policy Forum. We based our arguments on a thorough analysis of many reports and communications of all the institutions we discussed, including Oxfam's (*1*). For example, a substantive 2008 Oxfam report (*2*) (written after prices increased) concludes that "only in a few countries are small producers benefiting from higher prices," and emphasizes that farmers are often net consumers who face many constraints, implying that they would benefit from lower prices. Yet a 2005 Oxfam report (*3*) (written before prices started to rise) does not mention that small farmers and rural households are net consumers of food. These inconsistencies demonstrate our points. Kripke argues that the issue of food security is too complex to fit into a headline, but we found simplistic explanations in lengthy reports as well.

We agree with Kripke that massive subsidies for agriculture in rich countries are an inefficient way to reduce food prices for poor people. However, tariffs on food imports are inefficient as well (*4*, *5*), as a policy instrument to address farmers' weaknesses and certainly as a mechanism to reduce food prices for poor people. Yet Oxfam has defended these policies, both before (*6*) and after (*2*) the food price crisis.

Finally, our concerns did not emerge from "academic" considerations. We are intensely involved in policy discussions on food policy and poverty (*7*–*9*), and we have seen firsthand that the absence of nuance in communications and reports has real-world implications on public debate and decision-making. For instance, there is currently extensive lobbying about the future of European agricultural policy—at stake are about US$500 billion of farm subsidies over the next 7 years. Pressure groups are referring

Ice sheets and sea-level change

550

Biodiversity and ecosystem function

552

to simplistic statements about the effects of high food prices on poverty and food security to argue that these subsidies are helping to address global food security (*10*, *11*). Those who do not realize that simplistic messages may lead to undesirable policy outcomes are the ones who seem to live in an ivory tower.

JOHAN SWINNEN[1,2] AND PASQUAMARIA SQUICCIARINI[1,3]*

[1]LICOS Centre for Institutions and Economic Performance and Department of Economics, University of Leuven, Leuven, 3000, Belgium. [2]Center for Food Security and the Environment, Stanford University, Palo Alto, CA 94305, USA. [3]Anderson School of Management, University of California Los Angeles, Los Angeles, CA 90095, USA.

*To whom correspondence should be addressed. E-mail: pasquamaria.squicciarini@anderson.ucla.edu

References

1. J. F. M. Swinnen, *Dev. Pol. Rev*. **29**, 667 (2011).
2. Oxfam International, "Double-edged prices" (Oxfam Briefing Paper 121, 2008); www.oxfamamerica.org/files/double-edged-prices.pdf.
3. Oxfam International, "A round for free" (Oxfam Briefing Paper 76, 2005); www.maketradefair.com/en/assets/english/aroundforfree.pdf.
4. J. Brooks, Ed., *Agricultural Policies for Poverty Reduction* (OECD Publications, Paris, 2012).
5. World Bank, *Agriculture for Development; World Development Report 2008* (World Bank Publications, Washington, DC, 2008).
6. Oxfam International, "The rural poverty trap" (Oxfam Briefing Paper 59, 2004); www.tanzaniagateway.org/docs/Why_agricultural_trade_rules_need_to_change_and_what_UNCTAD.pdf.
7. Bureau of European Policy Advisers, EU Budget Review—Workshops (http://ec.europa.eu/dgs/policy_advisers/activities/conferences_workshops/budget3_en.htm).
8. CEPS, 1st Brussels High Level Lecture on Food Security and Development (www.ceps.eu/content/1st-brussels-high-level-lecture-food-security-and-development).
9. FAO Investment Centre, Investment Days—Staff Invest Time in Sharing Their Work (www.fao.org/investment/newsandmeetings/meetings-archive/detail/en/?dyna_fef%5Buid%5D=48875).
10. Copa-Cogeca, "The future of the common agricultural policy post-2013" (Copa-Cogeca, Brussels, 2010); www.copa-cogeca.be/img/user/file/7142_PAC_E.pdf.
11. European Landowners' Organization (ELO), BirdLife International, "Proposals for the future CAP: A joint position from the European Landowners' Organization and BirdLife International" (ELO and BirdLife International, Brussels, 2010); www.birdlife.org/eu/pdfs/Proposal_for_the_future_cap_FINAL_*21*_01_2010.pdf.

Letters to the Editor

Letters (~300 words) discuss material published in *Science* in the past 3 months or matters of general interest. Letters are not acknowledged upon receipt. Whether published in full or in part, Letters are subject to editing for clarity and space. Letters submitted, published, or posted elsewhere, in print or online, will be disqualified. To submit a Letter, go to www.submit2science.org.

A Step Backward for Italy's Meritocracy

ITALIAN SCIENTISTS HAVE LONG LAMENTED THE lack of resources, political attention, and meritocracy in assigning taxpayers' money. In 2007, things began to change. The 2007 and 2008 national budget laws allocated €81 million (US$107 million) to projects submitted by researchers under 40 years old. They were judged by an international committee of scientists under age 40 that was appointed according to impact factor and citation index scores. Even though this fund accounted for only 10% of the entire public research money, it was a crucial turning point toward meritocracy. Finally, the international rules of peer review were entering the Italian system, acknowledging meritocracy and setting researchers free from the virtual servitude under which they had been kept by old academicians.

Recently, inexplicably, Italy has fallen back to the old way of allocating taxpayers' research money and has done so in spite of government promises of open competition and meritocracy. The so-called "Simplification Decree" includes anti-crisis measures suggested by several departments, including the one led by the Minister of Education, University, and Research: Francesco Profumo. He has canceled the articles of the laws that brought peer review to Italy, explaining that the method introduced in 2007 was too cumbersome to apply. Minister Profumo now promises a new, simpler law, but for the time being, young researchers applying for grants in Italy will have to rely on the old questionable, nontransparent evaluation method that rewards clients of godfathers, rather than merit.

It is not only money for valuable researchers that will be lacking from now on, but hope for their future and for that of the country. The only way out is to adopt strict peer-review rules for the allocation of all research funds, at all times.

IGNAZIO ROBERTO MARINO

Department of Surgery, Jefferson Medical College, Philadelphia, PA 19107, USA, and Senate of the Republic of Italy, Piazza Madama snc, 00186 Rome, Italy. E-mail: ignazio.marino@jefferson.edu

CORRECTIONS AND CLARIFICATIONS

Letters: "Finding a good research question, in theory" by N. Bodemer and A. Ruggeri (23 March, p. 1439). The volume in Reference 1 should be 52, not 57. The correct reference is: A. W. Kimball, *J. Am. Stat. Assoc.* **52**, 133 (1957).

News & Analysis: "New institute aims to help academics make medicines" by R. F. Service (16 March, p. 1288). Merck should have been referred to as Merck & Co. based in Whitehouse Station, New Jersey.

Reports: "Sexual deprivation increases ethanol intake in *Drosophila*" by G. Shohat-Ophir *et al*. (16 March, p. 1351). In the abstract of the print version, the sentence "Activation or inhibition of the NPF system in turn enhanced or reduced ethanol preference" should read: "Activation or inhibition of the NPF system in turn reduced or enhanced ethanol preference." The error has been corrected in the HTML and PDF versions online.

Editorial: "Worldwide lessons from 11 March" by K. Omi (9 March, p. 1147). The Editorial referred to "statement issued in October 2010 by the Science and Technology in Society forum." The statement was issued in 2011. The date has been corrected in the HTML and PDF versions online.

TECHNICAL COMMENT ABSTRACTS

Comment on "Global Resilience of Tropical Forest and Savanna to Critical Transitions"

Zak Ratajczak and Jesse B. Nippert

Hirota *et al*. (Reports, 14 October 2011, p. 232) used spatial data to show that grasslands, savannas, and forests represent opposing stable states. Reanalyzing their data and drawing from temporal studies, we argue that spatial analyses underestimate the bistability of grasslands and savannas due to limitations of substituting space for time. We propose that temporal and spatial data are needed to predict critical transitions between grasslands and savannas.

Full text at www.sciencemag.org/cgi/content/full/336/6081/541-c

Response to Comment on "Global Resilience of Tropical Forest and Savanna to Critical Transitions"

Egbert H. Van Nes, Milena Holmgren, Marina Hirota, Marten Scheffer

Ratajczak and Nippert note that transient states between treeless and savanna states are more common than between savanna and forest, and suggest that this can be explained by a slower rate of change in the intermediate conditions at drier sites. We show that probability distributions of tree cover rather reflect the interplay between intrinsic rates of change and perturbation regimes.

Full text at www.sciencemag.org/cgi/content/full/336/6081/541-d

Comment on "Global Resilience of Tropical Forest and Savanna to Critical Transitions"

Zak Ratajczak* **and Jesse B. Nippert**

Hirota *et al*. (Reports, 14 October 2011, p. 232) used spatial data to show that grasslands, savannas, and forests represent opposing stable states. Reanalyzing their data and drawing from temporal studies, we argue that spatial analyses underestimate the bistability of grasslands and savannas due to limitations of substituting space for time. We propose that temporal and spatial data are needed to predict critical transitions between grasslands and savannas.

Determining the bistability of tree cover is critical to forecasting how terrestrial ecosystems will respond to global change. Using spatial satellite data, Hirota *et al*. (*1*) found that tree cover in the tropics and subtropics is distinctly trimodal: Areas with a tree cover of 0 to 5% (grassland), 10 to 50% (savanna), or 60 to 80% (forest) predominate, whereas ecosystems with a tree cover of ~5 to 10% (grassland/savanna intermediate) and ~50 to 60% (savanna/forest intermediate) are comparatively rare. The authors propose that the frequency of these tree-cover ranges is proportional to stability and, thus, low-frequency ranges of tree cover constitute unstable intermediates situated between high-frequency stable states. These spatial analyses can reach unparalleled levels of replication but are limited by an inability to distinguish between environmental variability and error due to substituting space for time. In this comment, we test assumptions of spatial analyses by reanalyzing data from Hirota *et al*. (*1*) to determine the frequency of unstable states. Our results suggest that spatial techniques accurately capture savanna-forest bistability but underestimate the bistability of grasslands and savannas.

Spatial analyses of bistability ultimately seek to quantify temporal processes. Even if all patches of vegetation are strictly bistable, patches with an "unstable" level of tree cover occur as patches transition from one stable state to another. In a given area, the frequency of "unstable intermediates" will be greater when (i) state changes occur slowly; (ii) state changes occur frequently; and (iii) patches do not conform to stable-state dynamics and exist as otherwise unstable levels of tree cover. The first two factors are confounding and will make unstable intermediates appear stable across space, even if they are unstable across time. Differentiating these transitional patches from nonbistable patches is impossible with temporally limited satellite data.

Division of Biology, Kansas State University, 116 Ackert Hall, Manhattan, KS 66506, USA.

*To whom correspondence should be addressed. E-mail: zarata@ksu.edu

To test the potential influence of confounding factors, we reanalyzed frequency diagrams of tree cover from Hirota *et al*. (*1*), reporting the frequency of unstable intermediates as discrete states, instead of including them as part of the savanna state. We used the same tree-cover classes as (*1*) because a limited number of sites were used to calibrate low tree cover of satellite data (*2*), making narrower tree-cover classes inappropriate. However, we note that using narrower tree-cover classes results in similar, if not more dramatic, results than those reported below [figure S1 in (*1*)].

Along a precipitation gradient, the frequency of both unstable intermediate types reaches their peak magnitude when the proportion of two opposing stable states is equal (Fig. 1). Peaks probably occur at these junctures because the attraction to any one stable state is not particularly strong, making the system more response to internal and external variation, and the unstable intermediates slightly more stable than usual.

More surprisingly, we found that the grassland-savanna intermediate is actually common at some levels of precipitation (Fig. 1). The grassland-savanna intermediate reaches a ~13.5% frequency for both 600 and 900 mm precipitation per year, which is 30% of either stable state and equivalent to 2000 km^2 (*1*). This frequency is impressive considering that the grassland/savanna intermediate only encompasses a 5% tree cover range, compared with an average range of 25% for stable states and a 10% range for the savanna/forest intermediate. In contrast, the savanna/forest intermediate peaks for just one value of mean annual precipitation (MAP) and reaches a 7% frequency (i.e., 15% as common as the opposing savanna/forest states).

The low frequency of the savanna-forest intermediate suggests that savannas and forests are highly bistable and that state shifts could occur rapidly in low-resilience areas identified by Hirota *et al*. (*1*). The high frequency of the grassland/savanna intermediate could indicate that grasslands and savannas are less bistable but several lines of evidence suggest that this over-representation is due to slow transition rates in semiarid ecosystems (600 mm

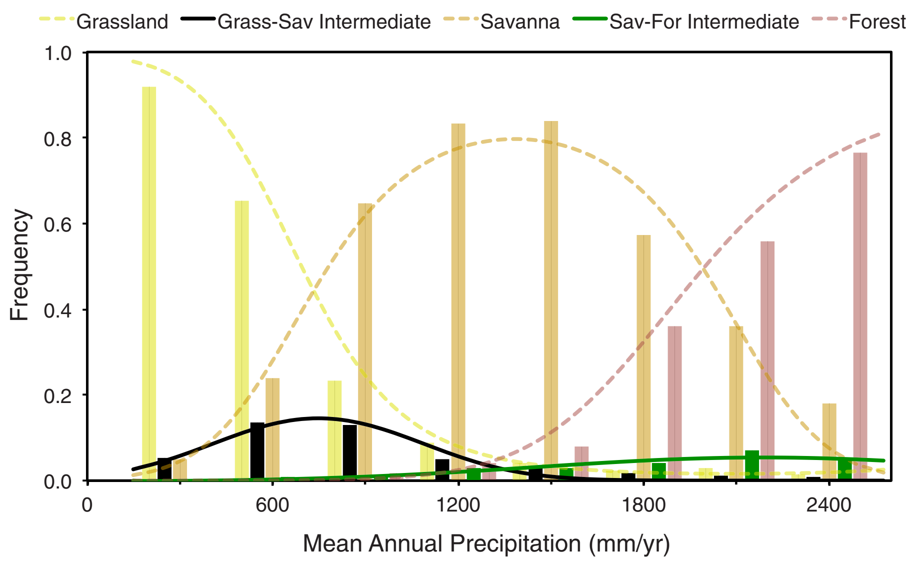

Fig. 1. The frequency of unstable states: grassland/savanna intermediate (black) and savanna/forest intermediate (green), compared with the frequency of stable states: treeless (yellow), savanna (orange), and forest (red). Following Hirota *et al*. (*1*), the grassland/savanna intermediate is all areas with a tree cover of 5 to 10%, the savanna/forest intermediate is 50 to 60%, the grassland state is 0 to 5%, the savanna state is 10 to 50%, and the forest state is 60 to 80%. Even though the unstable range for savanna/forest is smaller for some continents (e.g., 55 to 60%), we used this wider range of 50 to 60% because the results presented by (*1*) consider all continents together. Thus, the frequency of the savanna/forest intermediate should be considered to be an overestimate. Curves are fit to frequency diagrams using the same logistic regression model as Hirota and colleagues (*1*). Data encompass the tropics and subtropics of Africa, Australia, and South America, excluding mountainous and developed areas.

Table 1. A summary of existing fine-scale studies on grassland/savanna transitions over time.

Country	MAP (mm)	Transition type	Min. transition time (years)	Max. transition time (years)	Min. time-step (years)*	Transition mechanism	Woody plant type	Ref.†
North America	300	Grassland→ Savanna	5	37	5	Soil feedbacks	Shrubs	(*12*)
North America	600	Savanna→ Grassland	2	>2	2	Acute drought	Trees	(*14*)
North America	635	Savanna→ Grassland	5	>5	5	Fire/soil feedbacks	Trees	(*11*)
Swaziland	675	Grassland→ Savanna	8	50	8	Grazing/fire manipulation	Shrubs	(*10*)
Botswana	680	Grassland→ Savanna	3	–	3	–	Trees	(*15*)
North America	850	Grassland→ Savanna	2	–	1	Fire feedbacks	Tall shrubs	(*9*)

*Minimum time-step refers to the minimum number of years between temporal samplings. This variable is included so that minimum transition rates can be compared to the minimum transition rates detectable by each study. †We identified studies using the Thomson Reuters Web of Knowledge (wokinfo.com) and searching for "'tree cover' time." We included only studies with reasonably small time-steps between sampling and excluded areas where the grassland state was dominated by C_4 grasses (the dominant type of grasses in most tropical and subtropical grasslands).

precipitation per year) and frequent state transitions in mesic ecosystems (900 mm precipitation per year).

In semiarid regions, population growth rates, especially for trees and shrubs, should be limited by water availability (*1*, *3*–*5*). Likewise, the primary feedback mechanism responsible for semiarid state shifts (changes in soil properties) can take decades to act but creates highly stable states in the process (*6*). Together, these factors should make semiarid state shifts less frequent, but slow when they occur.

In mesic areas, grassland/savanna transitions should occur quickly because population growth is less water-limited (*1*, *3*–*5*) and, along with savanna/forest transitions, these transitions are almost exclusively facilitated by fire (*3*, *5*, *7*). Fire feedbacks have an almost immediate effect and are more easily reversed (*3*, *8*, *9*), which should theoretically lead to quicker, but more frequent, state shifts. Indeed, dramatic tree-cover changes have occurred in Africa and North America after just 10 to 20 years of fire manipulation (*3*, *9*, *10*). This resilience is qualitatively lower than that of semiarid ecosystems, which can withstand several decades of exogenous forcing before undergoing a state change [e.g., (*11*, *12*)].

The limited number of temporal tree-cover records supports our hypothesis that grassland/savanna transitions occur slowly in drier ecosystems (Table 1). For example, it takes ~35 years for desert grassland to increase from 5 to 10% shrub cover (*12*), whereas the fire-driven transition of wetter tallgrass prairie to savanna can occur in 2 years (*9*). Temporal studies also support the ideas that grasslands and savannas are opposing stable states and that 5 to 10% tree cover is also an unstable ecosystem state across space (*1*) and time (Table 1). In both tallgrass prairie of North America and savanna of southern Africa, the cover of tall shrubs increases slowly when the system is within 0 to 5% cover, but increases rapidly and consistently when the system is between 5 and 10% cover (*9*, *10*).

Spatial data and novel techniques [e.g., (*1*, *7*, *13*)] can greatly expand the understanding of tree-cover stable states and identify areas that are highly susceptible to critical transitions. We argue that these techniques are appropriate for savanna-forest transitions but that temporal studies are needed to properly quantify grassland-savanna bistability and predict how these ecosystems will respond to global change (Fig. 1, Table 1). It will be 10 to 20 years before Moderate-Resolution Imaging Spectroradiometer (MODIS) data can provide such temporal records; therefore, identifying existing records is crucial to understanding and predicting often-catastrophic tree-cover state shifts in grasslands and savannas.

References and Notes

1. M. Hirota, M. Holmgren, E. H. Van Nes, M. Scheffer, *Science* **334**, 232 (2011).
2. M. C. Hansen *et al.*, *Earth Interact.* **7**, 1 (2003).
3. W. J. Bond, G. F. Midgley, F. I. Woodward, *S. Afr. J. Bot.* **69**, 79 (2003).
4. N. N. Barger *et al.*, *J. Geophys. Res. Biogeosci.* **116**, G00K07 (2011).
5. Z. Ratajczak, J. B. Nippert, S. L. Collins, *Ecology* **93**, 697 (2012).
6. P. D'Odorico, G. S. Okin, B. T. Bestelmeyer, *Ecohydrology*, published online 20 October 2011; 10.1002/eco259
7. A. C. Staver, S. Archibald, S. A. Levin, *Science* **334**, 230 (2011).
8. S. Archibald, D. P. Roy, B. W. Van Wilgen, R. J. Scholes, *Glob. Change Biol.* **15**, 613 (2009).
9. Z. Ratajczak, J. B. Nippert, J. C. Hartman, T. W. Ocheltree, *Ecosphere* **2**, art121 (2011).
10. K. G. Roques, T. G. O'Connor, A. R. Watkinson, *J. Appl. Ecol.* **38**, 268 (2001).
11. R. J. Ansley *et al.*, *Rangeland Ecol. Manag.* **63**, 286 (2010).
12. D. M. Browning, A. S. Laliberte, A. Rango, *Int. J. Geogr. Inf.* **25**, 913 (2011).
13. M. Hirota, C. Nobre, M. D. Oyama, M. M. C. Bustamante, *New Phytol.* **187**, 707 (2010).
14. M. J. Clifford, N. S. Cobb, M. Buenemann, *Ecosystems (N.Y.)* **14**, 949 (2011).
15. J. M. Kalwij *et al.*, *Ecol. Appl.* **20**, 222 (2010).

Acknowledgments: We thank S. M. Matherly, J. M. Blair, T. W. Ocheltree, A. C. Staver, and S. Archibald for valuable input on an earlier version of this comment. This work was supported by the Konza Prairie LTER Program (DEB-0823341). Z.R. was supported by a Graduate Assistance in Areas of National Need fellowship from the U.S. Department of Education.

19 January 2012; accepted 22 March 2012
10.1126/science.1219346

Response to Comment on "Global Resilience of Tropical Forest and Savanna to Critical Transitions"

Egbert H. Van Nes,[1]* Milena Holmgren,[2] Marina Hirota,[1] Marten Scheffer[1]

Ratajczak and Nippert note that transient states between treeless and savanna states are more common than between savanna and forest, and suggest that this can be explained by a slower rate of change in the intermediate conditions at drier sites. We show that probability distributions of tree cover rather reflect the interplay between intrinsic rates of change and perturbation regimes.

Although the concept of a stable state is a useful abstraction, fluctuations in the environment and perturbations prevent ecosystems from being in a stationary stable state. Our approach to reconstruct the alternative states and their basins of attraction (*1*) is based on the idea that the probability distribution of states reflects the balance of such stochasticity with the tendency to return to underlying attractors.

To illustrate this, we simulate dynamics of a simple model with alternative stable states, subject to stochastic forcing (Fig. 1). The system tends to be farther away from the equilibrium if its dynamics are slower (Fig. 1B) but also if the level of stochastic forcing is higher (Fig. 1D). Although it seems plausible that the transition from a treeless state to savanna is slow, one cannot directly deduce that from the stability landscapes. Also, the results from six (mostly nontropical) studies on treeless-savanna transitions summarized in table 1 of Ratajczak and Nippert (*2*) are too variable to infer the suggested relationship between rainfall and rates of change. This is not surprising in view of the likely role of factors such as initial tree cover, grazing, soils, and other factors that will differ between the cases.

We do not agree that our substitution of space for time would be problematic for reconstructing stability landscapes. As sampled points from satellite images can be considered snapshots from different time series, the theory, albeit originally developed for time series (*3*), still holds. Although we fully agree that there is an urgent need for long-term research, time series are certainly no panacea when it comes to inferring the existence of multiple attractors (*4*). Controlled field experiments are better in this sense but are not easy to realize at relevant scales of time and space. Unraveling the stability properties and their governing mechanisms in such large complex systems will inevitably require a multifaceted approach (*5*), and the potential analysis is a modest but useful addition to the toolbox we have.

Importantly, the frequency of intermediate states does not imply that bistability would be underestimated, as suggested by Ratajczak and Nippert. As the results in Fig. 1 illustrate, rather than a problem, slowness of transients and stochasticity are actually a prerequisite for detecting basins of attraction. Obviously, there is a limit to that, in the sense that attraction basins are no longer found if stochasticity overwhelms the rates of return to underlying attractors. However, in such situations, the relevance of alternative attractors is questionable. The elegance of the potential analysis is that the results directly reflect the interplay between stochasticity and determinism that shapes the dynamics of ecosystems in nature. The fact that we find three distinct modes in the frequency distributions of tropical tree cover indicates that alternative attractors are

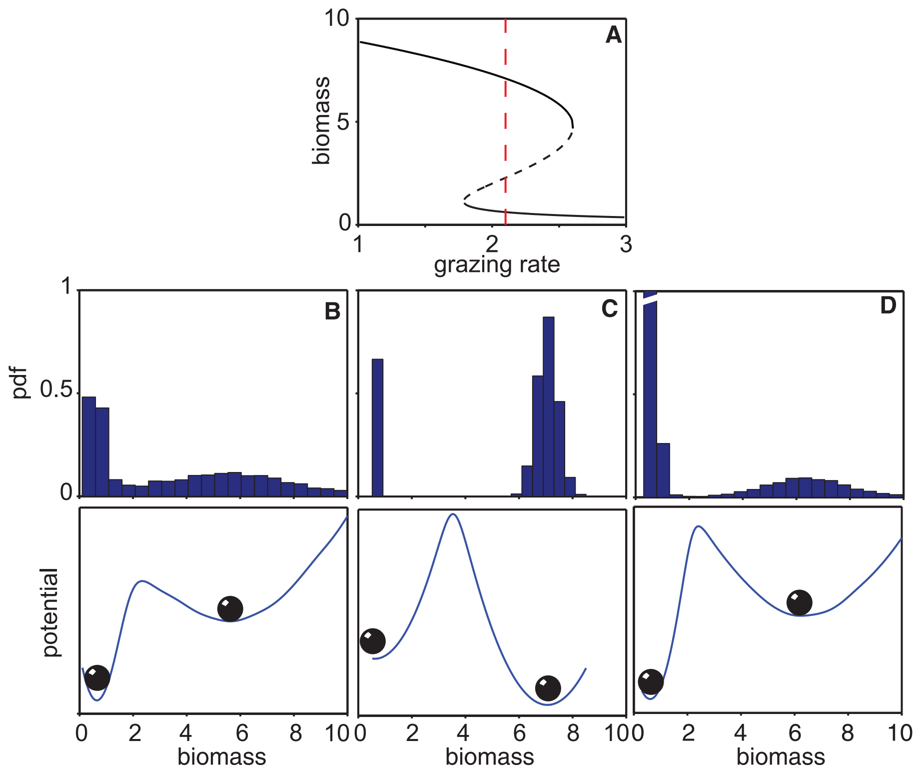

Fig. 1. The effect of the speed of change and the noise level to the occurrence of transient states in a simple bistable model. We use a stochastic version of a classical model of an exploited population (*6*) (N): $dN = \gamma\left(rN\left(1-\frac{N}{K}\right) - c\frac{N^2}{H^2+N^2}\right)dt + \epsilon N\, dW$, where r is the growth rate, K the carrying capacity, c the maximum grazing rate, H the half-saturation of the Holling type II functional response, W a normally distributed Wiener process, and the scaling factor γ is used to tune the slowness of the system. To obtain snapshots of this model in time, we drew 1000 random initial conditions (between 0 and 10) and ran the model for 1100 steps. The first 100 steps were discarded, and after that, for each 100 steps one value was saved. We analyzed these values using potential analysis (*1*, *3*). The nonstochastic version of the model can have two alternative stable states over a range of conditions (**A**). The red dashed line indicates the used grazing rate. The probability density function (pdf) and the estimated potentials (*3*) are calculated for (**B**) a slow system ($\gamma = 0.03$); (**C**) the default conditions ($\gamma = 1$; $c = 2.1$; $H = 1$; $K = 10$; $r = 1$; and $\epsilon = 0.05$) [the bandwidth of the kernel distribution was twice the default value (*3*) to get a continuous potential]; and (**D**) a highly stochastic system $\epsilon = 0.2$.

[1]Department of Aquatic Ecology and Water Quality Management, Wageningen University, Post Office Box 47, NL-6700 AA, Wageningen, Netherlands. [2]Resource Ecology Group, Wageningen University, Post Office Box 47, NL-6700 AA, Wageningen, Netherlands.

*To whom correspondence should be addressed. E-mail: egbert.vannes@wur.nl

sufficiently pronounced to dominate dynamics despite stochasticity and slow transients.

References

1. M. Hirota, M. Holmgren, E. H. Van Nes, M. Scheffer, *Science* **334**, 232 (2011).
2. Z. Ratajczak, J. B. Nippert, *Science* **336**, 541 (2012); www.sciencemag.org/cgi/content/full/336/6081/541-c.
3. V. N. Livina, F. Kwasniok, T. M. Lenton, *Climate of the Past* **6**, 77 (2010).
4. M. Scheffer, S. R. Carpenter, *Trends Ecol. Evol.* **18**, 648 (2003).
5. M. Scheffer, *Critical Transitions in Nature and Society* (Princeton Univ. Press, Princeton and Oxford, 2009).
6. R. M. May, *Nature* **269**, 471 (1977).

13 February 2012; accepted 22 March 2012
10.1126/science.1219711

LITERARY CRITICISM

The Place of Words

Christopher Cokinos

A conference room in a Reno casino was the unlikely birthplace in 1992 of the Association for the Study of Literature and Environment (ASLE). It formed because many literary critics and nature writers felt that English departments needed to add place and environment to the lenses of race, class, gender, and arcane philosophical forms of literary criticism such as deconstruction when evaluating texts of all kinds—from traditional nature writing to, say, car commercials filmed in apparent wilderness settings. Importantly, ASLE was an offshoot of a place-based literary studies organization, the Western Literature Association. From the start of this organized "ecocritical" movement, then, linking textual study to environmental awareness was filtered through an emphasis on the local, on place itself.

While some critics, such as Ursula Heise, have pushed back—arguing for a more globally inflected approach to studying the relations among environments, texts, animals, plants, and people—the bulk of ecocriticism partakes of an investment in the local because the bulk of nature writing does so. And to speak of the local is to ask just what we mean by that. The question is not academic. As *The Bioregional Imagination* makes very clear, it is ecological and historical. To understand literary expressions of the environment is almost always to grapple with place, with scales of place, and, therefore, to encounter (or be immersed in) "bioregionalism."

The anthology's editors—well-known writers and ecocritics Tom Lynch, Cheryll Glotfelty, and Karla Armbruster—note: "As part of the development of the environmental movement during the 1970s, a school of thought emerged calling itself bioregionalism. Located primarily in western North America, especially California and British Columbia, this movement included thinkers such as Peter Berg, Raymond Dasmann, Gary Snyder, and Stephanie Mills." As the editors explain in a useful introduction, bioregionalism sought "to address matters of pressing environmental concern through a politics derived from a local sense of place, an approach ... [that] would effectively complement efforts focused at the national and international levels." A kind of rooted counterculture of art and activism, bioregionalism contrasted with the corporate-style environmentalism that began to take hold with such groups as the National Audubon Society during the era of big federal legislation. Bioregionalists typically point to similar geographic features and watersheds when they try to define the local; they also insist on place-based expressions of citizenship, which include poems, essays, stories, and art of all kinds.

The Bioregional Imagination
Literature, Ecology, and Place
by Tom Lynch, Cheryll Glotfelty, and Karla Armbruster, Eds.
University of Georgia Press, Athens, GA, 2012. 454 pp. $69.95. ISBN 9780820341712. Paper, $24.95. ISBN 9780820335926.

This hefty critical collection contains a diverse mix of close readings of place-based texts, philosophical discussions of bioregionalism, and practical advice on engaging the public and students in bioregional studies that combine science and creative expression. It is this latter category of work that will be most useful to readers of *Science*. The anthology has an international flavor, with contributions on places in the United States, Canada, South Africa, Nigeria, Australia, and Italy. Nature writing and ecocriticism have been criticized as being elitist, white, and First World. Those seeking a range of work that defies this stereotype will find the volume welcome.

Following the editors' overview, a relaxed narrative conversation with two bioregionalist pioneers, David Robertson and Robert L. Thayer Jr., serves to introduce some of the philosophy and history associated with bioregionalism. The first section ("Reinhabiting") continues with essays about public bioregional projects in Spartanburg, South Carolina, and Chicago, Illinois, which inspired everything from local atlases to anthologies of place-based writing. Much of the material in here and in the second section ("Rereading") may be best suited for casual page-flipping. Bioregionalist works, by definition, have a local flavor. So unless you know (or want to know) about Italy's Po Valley, Australian Beverley Farmer's novel *The Seal Woman*, or Russell Banks's depiction of economic and ecological connections in the northeast United States, many of these close textual readings will not be of particular interest. It's worth noting, though, that many contributors do an excellent job of showing their natural history chops in contextualizing the poems, essays, and fiction under consideration. As well, readers can find moments of example praxis in articles even about material that may not be personally or environmentally compelling. For example, one essay reveals the fascinating ways strollers encounter an installation of Sherman Alexie's poem "That Place Where the Ghosts of Salmon Jump" in Spokane.

Two chapters that likely will interest a broader range of scientists, especially ecologists and anthropologists, consider science-fiction authors Ursula Le Guin and Frank Herbert, and both papers are mostly free of the often-dense jargon that (still and alas) obfuscates much prose in literary studies these days. (The same cannot be said of all the contributions; e.g., Anne Milne's discussion of ferality and bioregionalism will be hard going unless you are used to critical theory and the deployment of a great deal to say something simple.) This inclusion of science-fiction studies in a text essentially focused on place-based realist work is a breath of fresh air and a continuing acknowledgment that there are important intellectual connections between these two genres—each, after all, being concerned with change.

It's really the last two sections that may shine brightest for conservation-minded scientists. "Reimagining" includes two pieces that give bioregionalist perspectives of large territories—Australia (with a focus on nomadic connections to the local) and the circumpolar north—as well as an analysis of the work of South African marine biologist–poet Douglas Livingstone and his surprisingly lyrical explorations triggered by water-quality monitoring. Most useful of all are the descriptions (in "Renewal") of three classes: Canadian Laurie Ricou's habitat studies course (his contribution is a compelling hybrid of an essay and a syllabus, a really engaging read, and a course I plan on using), Kentuckian Wes Berry's energy-focused eco-literacy general-education class, and New Englander Laird Christensen's discussion of an online master of science in environmental studies at Green Mountain College. These are well suited for adaptation in either humanities or science courses—or, better yet, for team teaching. Rounding out the anthology are an engaging and perceptive discussion of student attitudes by Unity College's Kathryn Miles and

The reviewer is at the Department of English, University of Arizona, Post Ofiice Box 210067, Tucson, AZ 85721, USA. E-mail: cokinos@email.arizona.edu

Mitchell Thomashow and Kyle Bladow's helpful bioregionalist book list.

Overall, *The Bioregional Imagination* makes a valuable contribution to the Venn diagram field of ecocriticism, where literature, science, and, yes, activism, can and should coexist. If the contents are of varying interest to specific readers, that's to be expected. Your locale may not speak to me. But it's reassuring to know that from places I may not be especially interested in there comes creativity rooted in the ground and crafted with a natural historian's approach to understanding the world almost literally at hand.

10.1126/science.1221362

HISTORY

The Environment Makes History

J. R. McNeill

While seated at a diplomatic dinner in Paris in the 1780s, Benjamin Franklin sought to refute the Comte de Buffon's famous contentions that in America a decadent nature produced degenerate human beings. Franklin asked the company, half Americans and half Frenchmen, to rise and judge for themselves. They did. As one of the Americans saw it, "there was not one American present who could not have tost out of the Windows one or perhaps two of the rest of the Company, if this effort depended merely on muscular force." Franklin's strapping Americans did not have to defenestrate their French friends to convince themselves there was something special about America.

The Republic of Nature
An Environmental History of the United States
by Mark Fiege
University of Washington Press, Seattle, 2012. 600 pp. $34.95. ISBN 9780295991672. Weyerhaeuser Environmental Books.

Mark Fiege thinks that Americans' different experience of nature (which included better childhood nutrition, leading to greater stature) helped them to see themselves as American and to think that it was right and proper that they should have a government of their own. Part of the explanation for the American Revolution, he claims, lies in the American environment.

The reviewer is in the Walsh School of Foreign Service and the Department of History, Georgetown University, Washington, DC 20057–1035, USA. E-mail: mcneillj@georgetown.edu

Topeka, 1953. Linda and Terry Lynn Brown walking to their school bus stop.

CREDIT: CARL IWASAKI/TIME LIFE PICTURES/GETTY IMAGES

Indeed, Fiege (a historian at Colorado State University) thinks that everything in American history has environmental components to it. In *The Republic of Nature*, he argues the case by selecting nine familiar episodes in U.S. history; recounting them at chapter length; and emphasizing how the environment constrained freedom of action, how the events changed the environment, or how participants' thoughts about nature affected their actions. So, for example, he presents the 1954 Supreme Court case *Brown* v. *Board of Education* in an unorthodox way, in which social change and ideologies take a back seat to the racial geography of Topeka, Kansas, as it evolved from the 1860s onward and to the physical layout of the city. If young Linda Brown had not had to walk through an environment unfit for children, a switching yard of the Rock Island railroad, to get to her school bus stop in the early 1950s, that landmark case might well never have been heard.

In addition to the American Revolution and the school desegregation case, Fiege offers environmental histories of the Massachusetts witch craze of the 1690s, the slave-plantation South, the life of Abraham Lincoln, Gettysburg and the Civil War, the building of the transcontinental railroad, the race to make the first atomic bomb, and the 1973–74 oil crisis. At the end of the book, he wonders what environmental histories of the pivotal election of 1800, the legendary sit-down strikes in the auto industry in the late 1930s, and the conservative movement since the 1980s might look like.

Practicing scientists will find little grist for their professional mills in Fiege's pages. They may need little convincing that nature is always present in history in one way or another. Fiege wrote the book for his fellow historians, steeped in their standard accounts of American history, and for their students, struggling to understand these accounts. Both audiences are unaccustomed to seeing a role for the environment in the important parts of American history. Nature typically makes only cameo appearances in connection with Theodore Roosevelt and the first conservation movement of a century ago, the 1930s Dust Bowl, or the rise of popular environmentalism in the 1960s and 1970s. But for readers swayed by Fiege's persuasive pages, American history will never look quite the same again.

Environmental historians will find Fiege stands their field on its head. He intentionally skips over Henry David Thoreau and Aldo Leopold, the national parks movement, the Dust Bowl, and the agro-ecosystems of California. He has only a little to say about the West, the arena where U.S. environmental history was born, and the standard fare of that history is conspicuous by its absence. This is unconventional environmental history just as it is unorthodox American history.

Practicing scientists might enjoy the book even if it provides them no grist. They may need no convincing that nature matters, but they too will find American history in a new light. Lee's gamble in the 1863 Gettysburg campaign was a response to the desperate food situation in Virginia that summer. Several scientists at Los Alamos had a keen love of the outdoors and did their best thinking in New Mexico's pine groves.

The Republic of Nature reads well, having none of the jargon that mars much academic history. Wherever possible, Fiege tells his stories through the lives of individuals, whether schoolgirl Linda Brown or theoretical physicist Robert Oppenheimer. It is not a book to whip through in search of useful data—there are no charts or tables—but one to savor on Sunday afternoons.

10.1126/science.1221363

RESEARCH ETHICS

Rethinking Research Ethics: The Case of Postmarketing Trials

Human subjects research ethics needs to directly address threats to the evidence base of the medical information economy.

Alex John London,[1] Jonathan Kimmelman,[2]* Benjamin Carlisle[2]

From the Nuremberg Code onward, the core mission of human subjects research ethics has been to protect study participants from infringements motivated by a zeal for medical progress. However, with individuals, clinicians, and policy-makers increasingly dependent on scientific information for decision-making and with vast social resources invested in developing and utilizing the fruits of research, actors have powerful incentives to coopt research for narrow ends. Contemplated revisions to human subjects research ethics policies in the United States (*1*) and existing policy in Canada (*2*) and the United Kingdom (*3*) fail to capture harms that, although they may not threaten participants, nonetheless undermine the social value of research. This is illustrated by postmarketing (phase IV) research. As a corrective, research ethics should focus on safeguarding the integrity of research as a critical component of an evidence-driven, health information economy.

Postmarketing Research as a Case Study

Phase IV studies investigate drugs, devices, or biologics that have already received regulatory licensure. Generally, they are funded by drug companies and provide a means of testing findings from fastidiously designed trials in less stylized settings. They also provide greater statistical power for safety assessment. Initiatives like the U.S. Patient-Centered Outcomes Research Institute (PCORI) in the 2010 Affordable Care Act signal a renewed commitment to harnessing phase IV studies to address evidentiary gaps in comparative effectiveness, drug safety, and real-world utility (*4*). Yet studies often fall short of these ambitions. In contrast with premarketing trials, drug regulators have very limited influence over the production of phase IV evidence (*5*). This removes a critical check on design and reporting quality.

To their harshest critics, postmarketing trials are a backwater in which pharmaceutical companies use the simulacrum of scientific investigation to hawk their products. Studies sometimes enlist hundreds of physicians to recruit only a few patients each, thereby exposing more prescribers to the product; other studies are alleged to pay investigators extravagant fees (*6*). Sponsors sometimes obscure the nature of their interest in phase IV studies from volunteers and investigators. Using research in this way allows drug and device companies to circumvent rules against directly remunerating physicians for prescriptions (*7*). Recruiting physician-investigators with the promise of peer-reviewed publication confers an aura of scientific authenticity to the enterprise.

In 1996, several postmarketing studies of the antiseizure medication gabapentin were exposed as "seeding" use of the drug for unapproved indications (*8*). The prominently published ADVANTAGE trial of the anti-inflammatory drug rofecoxib also was revealed to be a seeding study (*6*). Postmarketing studies instigated over safety concerns surrounding two recently withdrawn drugs were found unsuited to the goal of pharmacovigilance (*9*, *10*). More systematic analysis shows that many other phase IV studies suffer various deficiencies, including statistical underpowering, absence of comparator arms, and publication bias (*11*).

The Current Research Ethics Framework

Because few, if any, of these branding practices violate laws and because institutional review boards (IRBs) may be the only venue where phase IV protocols receive formalized prospective review, critics have turned to research ethics to mount objections. These take two forms. First, policies stipulate that risks to volunteers must be reasonable in light of benefits to volunteers, if any, and society. Some critics charge that marketing objectives cannot justify risks to study participants (*6*, *12*). Second, some argue that phase IV studies' hidden marketing agenda compromises informed consent (*13*). If volunteers are unaware that a trial is a branding exercise, they may not be adequately informed about the ends to which they are contributing.

These criticisms accord well with the reigning model of research ethics, which locates the moral tension in clinical research at the interface between subjects—who may be unable to adequately safeguard their own welfare—and investigators. However, by shoehorning the problems of phase IV studies into the familiar categories of risk and informed consent, they miss much of what makes these practices objectionable.

Current ethical guidelines ...[are] inadequate ... for challenging studies that pose little risk but that generate biased evidence.

Concerning the first objection, many postmarketing studies have little impact on participant welfare and involve no more than a chart review or inclusion in a registry. Studies that go beyond this often enroll patients only after they have opted for an intervention in a clinical setting or entail little departure from standard of care. Current ethical guidelines evaluate social value only insofar as it justifies risk to volunteers: the less the risk, the less the need to substantiate social value. Thus, they provide inadequate bases for challenging studies that pose little risk but that generate biased evidence. These difficulties would be exacerbated by proportionate review, a central plank in many policies governing human subjects research, including proposals to amend those in the United States (*1*–*3*). This approach, which calibrates depth of protocol scrutiny to the level of volunteer risk, is motivated by the sensible observation that low-risk studies can divert review resources from riskier ones. Yet many problematic phase IV practices pose little threat to volunteers and thus escape review.

As for the second objection, disclosure of marketing aims would defuse concerns about deception, but do little to improve the value of such studies or diminish the social harms caused by production of biased evidence and the cooptation of research systems.

[1]Department of Philosophy, Carnegie Mellon University, Pittsburgh, PA 15213, USA. [2]Biomedical Ethics Unit, McGill University, Montreal, Quebec H3A 1X1, Canada.

*Author for correspondence. E-mail: jonathan.kimmelman@mcgill.ca

Published by AAAS

The Integrity of the Research System

A more robust ethical framework should focus on preserving the integrity of research as the foundation of an evidence-driven, health information economy. By a health information economy, we mean a system in which various parties collaborate in producing health-related information that is then consumed by others. Sometimes information is used to produce interventions, improve health services, or set policy. Other times it is an input into further inquiry. The ability of the parties who use this information to advance care, improve knowledge, and increase efficiency depends critically on its validity, relevance, credibility, and accessibility to stakeholders. Although studies are often financed and performed by private actors, they have public repercussions. How research is conducted not only affects the quality of the information that others consume, but also patient expectations, provider practices, the expenditure of scarce resources, and the efficiency of health-care systems.

Deficiencies in phase IV studies like those above are not always detectable for editors, policy-makers, or other evidence users. Adverse events might be withheld, primary end points altered, and provider practices or patient expectations influenced by engaging with a trial rather than its results. These threaten the integrity of research as the foundation of an evidence-driven health information economy in three ways.

First, policy-makers, clinicians, and third-party payers who base treatment decisions, guidelines, or reimbursement on biased studies harm patients and misallocate resources. As the social resources dedicated to the health sector balloon, so, too, do the stakes of ensuring that resources are used efficiently.

Second, the "bench-to-bedside" process of translating basic research into clinical treatments is a series of investigations in which many different actors both produce and consume scientific information. Just as unreliable preclinical research can derail promising therapeutic avenues (*14*), the cumulative human and capital investment in inquiry and development can be squandered where biased phase IV evidence promotes inappropriate application of interventions.

Third, confidence in scientific medicine and the social influence associated with it is eroded when the outward signs of scientific merit are used solely as a vehicle for marketing. To ensure that confidence in medical information is warranted for those who rely on it, the system of knowledge production and utilization must be designed to either leverage or limit the influence of parochial motives on evidence production.

Those who fund, conduct, take part in, and ultimately benefit from the results of scientific inquiry participate in research to advance a diverse mix of personal or social goals. Whether this is antithetical to the efficient production of reliable medical evidence depends on whether ethical and policy frameworks bring individual interests into alignment with the social goals of research. When demand is driven by high-quality evidence of superiority on clinically relevant comparisons, expanding an intervention's market share advances both parochial and social ends. Influencing clinician practice and increasing stakeholder familiarity with such treatments advances social ends when it reduces unwarranted variation and expense, and improves patient outcomes. Profit seeking advances social interests when incentives channel human ingenuity toward bridging knowledge gaps about best practices.

Preserving the integrity of the research system also requires protecting the rights and welfare of participants, because knowledge cannot be produced within a liberal democracy without the participation of volunteers who are confident that their basic interests will be safeguarded. But subject protections should be seen as one important facet of a broader effort to ensure that, as contributors to the health information economy advance their individual agendas, they are also helping to produce important social benefits.

Ethics Should Inform Oversight

A framework that highlights the ethical significance of threats to the health information economy should facilitate a search for mechanisms that empower actors and institutions to promote more informative and valuable forms of inquiry.

One strategy would be to rectify discontinuities between pre- and postmarketing oversight by granting regulators greater authority over postmarketing research (*15*). Creating a centralized entity for certifying phase IV trial protocols or expanding the purview of existing institutions, such as the U.S. Food and Drug Administration or the PCORI, could provide incentives for conducting higher-quality studies (*16*). At least, registration and reporting requirements should be expanded to include phase IV observational studies (*17*).

Absent these ambitious institution-making proposals, the burdens of promoting high standards of design and clinical relevance would fall to three actors that presently have some—albeit limited—role in shaping incentives in this arena. First, if IRBs are to play a role in strengthening such studies, their mandate will have to be expanded to permit greater scrutiny of study quality, reporting plans, and clinical relevance. This might also require strengthening their membership to ensure the relevant scientific and statistical expertise. Nevertheless, such changes would have limited impact on deficient trial reporting.

Second, medical journals could adopt phase IV–specific review and reporting criteria. These might include expanded requirements for review; submission (e.g., provision of an approved protocol); and disclosure of data. Even if studies are not published, the clear articulation of quality benchmarks and registration obligations can impact the upstream conduct of sponsors and investigators.

Finally, there should be a broad-based discussion of the responsibilities of medical societies for articulating and implementing standards for member participation in postmarketing studies (*18*).

Unlike private transactions in many other spheres, research transactions serve crucial social ends. Because those ends can be frustrated without putting study participants at risk, research ethics and policies need to adopt a broader focus—one that directly addresses threats to the evidence base of the medical information economy.

References and Notes

1. U.S. Department of Health and Human Services, *Fed. Regist.* **76**, 44512 (2011).
2. Canadian Institutes of Health Research, Natural Sciences and Engineering Research Council of Canada, Social Sciences and Humanities Research Council of Canada, *Tri-Council Policy Statement: Ethical Conduct for Research Involving Humans* (CIHR, NSERC, SSHRC, Ottawa, 2010).
3. U.K. Department of Health, *Research Governance Framework for Health and Social Care* (HMSO, London, ed. 2, 2005).
4. Patient Protection and Affordable Care Act. Public Law 111-148 (2010).
5. D. Carpenter, *Reputation and Power* (Princeton Univ. Press, Princeton, NJ, 2010).
6. H. C. Sox, D. Rennie, *Ann. Intern. Med.* **149**, 279 (2008).
7. B. M. Psaty, D. Rennie, *JAMA* **295**, 2787 (2006).
8. M. A. Steinman, L. A. Bero, M. M. Chren, C. S. Landefeld, *Ann. Intern. Med.* **145**, 284 (2006).
9. B. M. Psaty, C. D. Furberg, W. A. Ray, N. S. Weiss, *JAMA* **292**, 2622 (2004).
10. S. E. Nissen, *Eur. Heart J.* **31**, 773 (2010).
11. J. Hasford, T. Lamprecht, *Eur. J. Clin. Pharmacol.* **53**, 369 (1998).
12. C. Elliott, *Mother Jones* **2010** (September–October), 55 (2010).
13. J. N. Rao, L. J. Cassia, *BMJ* **325**, 36 (2002).
14. A. J. London, J. Kimmelman, M. E. Emborg, *Science* **328**, 829 (2010).
15. D. Carpenter, *Health Aff.* **W5**, 469 (2005).
16. B. P. Falit, *Seton Hall Law Rev.* **37**, 969 (2007).
17. D. A. Zarin, T. Tse, *Science* **319**, 1340 (2008).
18. M. Teehan, *Can. J. Psychiatry* **39**, 629 (1994).

Acknowledgments: Funded by the Canadian Institutes of Health Research (EOG 102824).

10.1126/science.1216086

CELL BIOLOGY

Superresolution Subspace Signaling

Highly localized activity of ion channels in vascular endothelial cells controls the contraction of surrounding muscle cells and blood flow.

W. Jonathan Lederer, Brian M. Hagen, Guiling Zhao

Exquisitely local signaling provides robust, precise, and rapid communication in single cells. Nanometer-wide regions constitute the signaling conduit that separates interacting ion channels, organelles, and sensor and effector proteins. Such signaling domains are primary features of many systems, including those responsible for excitation-contraction coupling in the heart (*1*, *2*), smooth muscle tone in the vasculature (*3*, *4*), and Ca^{2+} signaling in neurons (*5*). These intimate pathways, also known as "fuzzy spaces" (*1*), "subspaces" (*6*), or "nanoscopic spaces," permit efficient signaling with rapid and reliable information transfer, yet are too small to be seen with a standard optical microscope. Such superresolution domains may become experimentally visible with the implementation of optical superresolution microscopy (*7*–*9*). On page 597 in this issue, Sonkusare *et al.* (*10*) identify a specific and broadly important local signaling organization in small mesenteric arteries (~100 μm in diameter) that uses nanometer-wide communication regions to regulate local vascular blood flow.

Endothelial cells form intimate spot-welded contacts with vascular smooth muscle cells at "holes" in the internal elastic lamina that are micrometers in diameter (see the figure). These regions of close contact can include gap junctions that create an electrical conduit from the endothelial cells to the effector smooth muscle cells. Sonkusare *et al.* suggest that this specific organization is used by endothelial cells in two signaling pathways. In one pathway, inositol trisphosphate receptor (IP_3R)–dependent Ca^{2+} release from endoplasmic reticulum (ER) in endothelial cells can produce regions with very high local concentrations of intracellular free calcium ($[Ca^{2+}]_i$) called "pulsars" (*4*). In the other pathway, clustered transient receptor potential vanilloid 4 (TRPV4) channels in the plasmalemma can produce regions with locally very high $[Ca^{2+}]_i$ called "sparklets" (*10*–*12*). In both cases, local increase of $[Ca^{2+}]_i$ activates nearby Ca^{2+}-activated K^+ channels [intermediate-conductance (IK; $K_{Ca}3.1$) and small-conductance (SK; $K_{Ca}2.3$)] to hyperpolarize endothelial cells. These two signaling pathways converge on the same functional target—the K^+ channels. The efficacy of this activation depends in part on the proximity of the K^+ channels to the Ca^{2+} source, hence the importance of subspaces or fuzzy spaces (*1*, *3*). As endothelial cells hyperpolarize relative to smooth muscle cells, current flows from smooth muscle cells to hyperpolarize and thus relax the smooth muscle cells (*3*). The effect is to increase blood flow. Sonkusare *et al.* point out that there may also be a role for the increase in nearby extracellular $[K^+]$ in the restricted extracellular spaces between the cells. If so, they can increase inward-rectifier K^+ channel (K_{ir}) efflux of K^+ to augment smooth muscle cell hyperpolarization and relaxation (*4*, *13*). Perhaps this is also how the restricted but larger internal elastic lamina (up to several micrometers) between endothelial cells and smooth muscle cells, of presumed varying thickness (*14*), contributes to this process.

Important to the study by Sonkusare *et al.* and other investigations was the development of a critical tool: the expression of the genetically encoded Ca^{2+} indicator protein

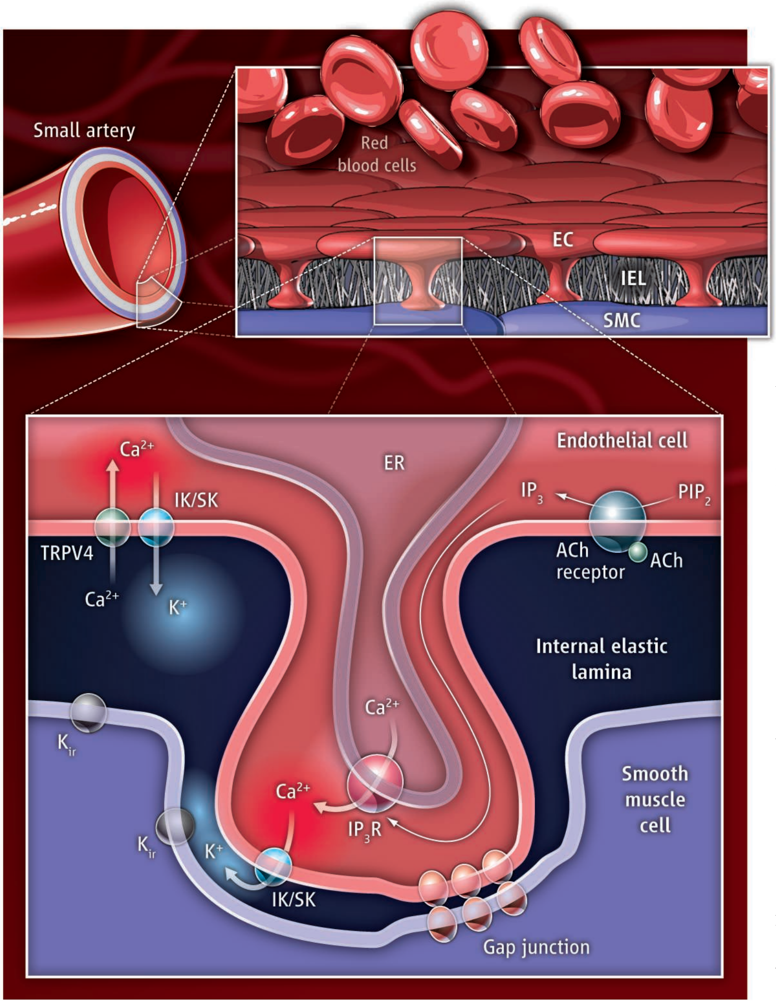

Arterial relaxation. The superresolution signaling system in vascular endothelial cells may be organized with respect to smooth muscle cells. Sonkusare *et al*. examined 100-μm-diameter arterioles in mice. Cooperative gating of clustered TRPV4 channels of a vascular endothelial cell (EC) allows Ca^{2+} influx. This localized increase in $[Ca^{2+}]_i$ activates local K^+ channels, hyperpolarizes endothelial cells, and increases nearby $[K^+]$ in the internal elastic lamina (IEL). Activated IP_3Rs in the endothelial cell ER produce locally high $[Ca^{2+}]_i$ signals. Locally elevated $[K^+]$ increases inward-rectifier K^+ channel (K_{ir}) current in the smooth muscle cell (SMC) to hyperpolarize the cells, which underlies vascular relaxation and increased blood flow. ACh, acetylcholine; PIP_2, phosphatidylinositol 4,5-bisphosphate.

CREDIT: C. BICKEL/SCIENCE

Center of BioMedical Engineering and Technology and Department of Physiology, University of Maryland School of Medicine, 725 West Lombard Street, Baltimore, MD 21201, USA. E-mail: jlederer@umaryland.edu

GCaMP2 specifically in endothelial cells in mice (*4*, *10*), which provides a Ca^{2+} sensor tool with high signal to noise specific only to endothelial cells. This tool allows the systematic identification of signals that depend on fuzzy-space Ca^{2+} that would otherwise be masked by neighboring cell signals if standard Ca^{2+} probes were used.

The principle demonstrated by Sonkusare *et al*. is critically important for the rapid regulation of tone in small mesenteric arteries. This finding is likely to be broadly relevant to all tissues where local factors control blood flow. For example, smooth muscle cells encircle the endothelial cells in an end arteriole from rat heart. This 15- to 20-μm-diameter arteriole has little or no apparent internal elastic lamina, consistent with its smaller size (*14*). The functional consequences of the finding of Sonkusare *et al*. in regulating cardiac blood flow are clear and consistent with the speculative hypothesis of electrotonic blood flow regulation in heart. Here, the electrical consequences of cardiac myocyte metabolism are linked to smooth muscle cell tone in precapillary sphincters via endothelial cells (*15*). The energetic demand of gut smooth muscle would appear to be equally important for mesenteric vascular flow and the regulation of flow in other important vascular beds. Understanding the intricate signaling of various vascular beds will allow for identification of potential therapeutic targets—especially important in diseases that result in vascular remodeling such as diabetes and hypertension.

References and Notes

1. W. J. Lederer, E. Niggli, R. W. Hadley, *Science* **248**, 283 (1990).
2. B. L. Prosser, C. W. Ward, W. J. Lederer, *Science* **333**, 1440 (2011).
3. M. T. Nelson *et al*., *Science* **270**, 633 (1995).
4. J. Ledoux *et al*., *Proc. Natl. Acad. Sci. U.S.A.* **105**, 9627 (2008).
5. K. Ouyang *et al*., *Proc. Natl. Acad. Sci. U.S.A.* **102**, 12259 (2005).
6. G. S. Williams *et al*., *Biophys. J.* **101**, 1287 (2011).
7. T. A. Klar, S. Jakobs, M. Dyba, A. Egner, S. W. Hell, *Proc. Natl. Acad. Sci. U.S.A.* **97**, 8206 (2000).
8. E. Betzig *et al*., *Science* **313**, 1642 (2006).
9. S. A. Jones, S. H. Shim, J. He, X. Zhuang, *Nat. Methods* **8**, 499 (2011).
10. S. K. Sonkusare *et al*., *Science* **336**, 597 (2012).
11. S. Q. Wang, L. S. Song, E. G. Lakatta, H. Cheng, *Nature* **410**, 592 (2001).
12. M. F. Navedo, G. C. Amberg, M. Nieves, J. D. Molkentin, L. F. Santana, *J. Gen. Physiol.* **127**, 611 (2006).
13. J. A. Filosa *et al*., *Nat. Neurosci.* **9**, 1397 (2006).
14. V. D. Aiello *et al*., *Mod. Pathol.* **16**, 411 (2003).
15. W. J. Lederer *et al*., in *Molecular Understanding of Excitation-Contraction Coupling and Vascular Flow Control in Heart Muscle*, G. G. Haddad, G. Lister, Eds. (Dekker, New York, 1996), vol. 95, pp. 497–513.

Acknowledgments: This work was supported by National Heart, Lung, and Blood Institute grants R01 HL106059, P01 HL67849, and R01 HL36974 (W.J.L.); the Leducq North American–European Atrial Fibrillation Research Alliance (W.J.L.); European Union Seventh Framework Program (FP7), Georg August University, "Identification and therapeutic targeting of common arrhythmia trigger mechanisms" (W.J.L.); and the American Heart Association National Scientist Development grant 10SDG4030042 (G.Z.).

10.1126/science.1222540

PHYSICS

The Impact of Ionic Frustration on Electronic Order

The frustrated ordering of dipoles created by copper and antimony ions in an oxide material may help to create an exotic quantum electronic state.

Leon Balents

For some metal oxides, the simplest applications of band theory predict that they should be good electrical conductors, but in fact they are Mott insulators—that is, the electrons that should be mobile are localized to metal atoms. These electrons retain internal degrees of freedom; they may occupy more than one type of orbital of the metal (they have an orbital degree of freedom) and also may adopt different spin states. These degrees of freedom, along with accompanying structural changes, can create materials with exotic electronic ordering that have potential applications such as magnetoelectric devices and quantum computing. If the spins and orbital degrees of freedom can both adopt more than one quantum state, they may entangle—that is, a measurement of spin determines the orbital state, and vice versa (*1*). On page 559 of this issue, Nakatsuji *et al*. (*2*) introduce a new ingredient, an ionic degree of freedom that creates a lattice of dipoles that is "frustrated"—incapable of completely ordering locally. Ordering is seen on nanometer dimensions, and it strongly affects the spin and orbital character of the electronic state.

The authors' study of $Ba_3CuSb_2O_9$ revealed that its key structural elements are Cu-Sb "dumbbells" aligned along the crystallographic *c* axis and distributed on triangular lattice planes normal to the *c* direction (see the figure). Each dumbbell has a large electric dipole moment, caused by the difference of charge of the Cu^{2+} and Sb^{5+} ions, and this moment can point up or down (i.e., parallel or antiparallel to the *c* axis). Neighboring dipoles would prefer to align antiparallel to lower

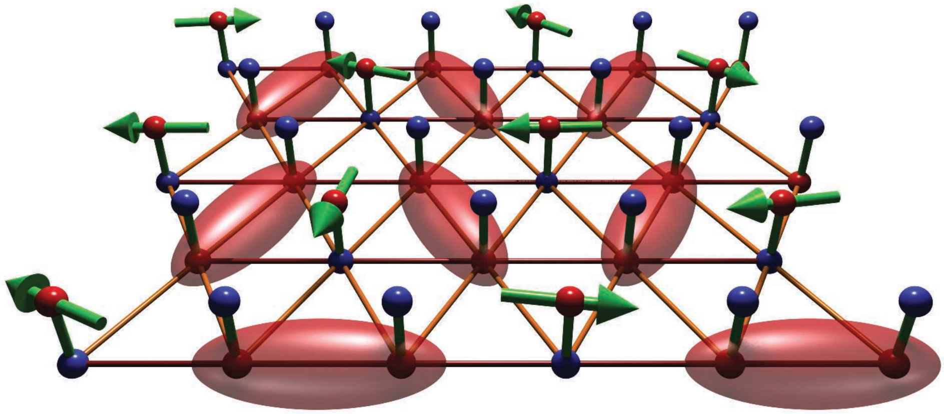

Frustrated ordering. Artist's conception of a nanoscale region of honeycomb lattice of ionic and spin structure in $Ba_3CuSb_2O_9$ studied by Nakatsuji *et al*. Copper-antimony (Cu-Sb) dumbbells are oriented vertically, with Cu atoms in red and Sb in blue. The Cu sites that are out of the honeycomb plane are separated from other Cu sites, and so may host quasi-free spins (green arrows). The Cu sites in the plane form a quantum spin liquid state composed of spin singlets, drawn as translucent ellipsoids enclosing two Cu sites. Oxygen sites are not shown, so neither Jahn-Teller distortions of the oxygen octahedral (which may be structurally inhomogeneous or time-dependent or both) nor the consequent orbital ordering are depicted.

Kavli Institute of Theoretical Physics, University of California, Santa Barbara, CA 93106, USA. E-mail: balents@kitp.ucsb.edu

their electrostatic energy, but the triangular arrangement makes this impossible for all neighbors, hence the alignment is frustrated.

The frustrated ordering of these ionic dipoles, which was only revealed by neutron scattering for single-crystal samples, creates a nanoscale pattern of short-range order consistent with a honeycomb structure. Such a honeycomb structure is indeed expected from theoretical models of frustrated dumbbells, dating back to the classic work of Wannier on the so-called antiferromagnetic Ising model on the honeycomb lattice (*3*). Because of the short-range nature of the dumbbell order, the corresponding Bragg peaks are diffuse and would probably be entirely unobservable in powder measurements. Indeed, the structure reported by Nakatsuji *et al*. disagrees with the results of previous diffraction studies on powder samples (*4*).

This structure affects the types of spin and orbital states that can be manifested. Each Cu^{2+} ion has a single unpaired hole (positive charge carrier) that can adopt two spin states and two orbital states, as well as superpositions of these states. Situations of this type are not uncommon [and were seen in (*2*)] and have the potential to lead to intriguing exotic states. However, this ordering is almost always thwarted in real materials by Jahn-Teller (J-T) effects (*5*), in which degenerate states with unpaired electrons or holes undergo a structural distortion. This distortion lifts the degeneracy and lowers the electronic energy by placing the carriers in a lower energy level. The atoms around the unpaired electron or hole (usually oxygens) move so that their electronic potential selects a preferred orbital (and often spin) state. This distortion creates a rather classical ordered magnet below the J-T transition.

Usually a J-T effect manifests itself as a structural phase transition, visible in averaged probes such as x-ray or neutron scattering. Indeed, the experiments in (*4*) see just such a transition in samples for which the concentration of Cu to Sb is different from the ideal 1:2 ratio. For temperatures below about 200 K, these samples became orthorhombic rather than hexagonal. However, for the samples with the ideal stoichiometry, the structural transition was apparently suppressed or absent, and macroscopic hexagonal symmetry was retained.

Remarkably, the CuO_6 octahedra were distorted even in the hexagonal samples, as shown by very fast (10^{-16} s) local x-ray absorption measurements, and this distortion was indistinguishable from that of their counterparts in the orthorhombic samples. The J-T effect still operated, although in more subtle ways, in the more ideal material. The difference between local and averaged measurements might be caused by fluctuations: The distortions might vary with time, so measurements that average over longer times would reveal octahedra that appear largely undistorted. A more likely explanation is that the J-T distortions are static but spatially inhomogeneous, tracking in some way the nanoscale dumbbell pattern, so that the spatially averaged structure remains hexagonal.

While these local J-T distortions are occurring (and orbitals are ordering, at least on short time scales), the spins in $Ba_3CuSb_2O_9$ appear to remain strongly fluctuating. The spins remain paramagnetic, with no static moments down to at least 100 mK, which is much less than the structural transition temperature in the nonstoichiometric samples (~200 K) and the estimated exchange coupling between spins (~50 K). At these low temperatures, quantum fluctuations of spins must be involved. This result raises the possibility of a quantum spin liquid ground state (*6*), a massive coherent quantum superposition of spin states capable of supporting strange excitations that behave like particles with fractional quantum numbers and statistics.

The lack of spin ordering or freezing is surprising because the short-range ionic ordering naïvely reduces the frustration of the underlying triangular structure. A simple nearest-neighbor antiferromagnet on a honeycomb lattice would be expected to undergo a robust magnetic transition. Evidently, the impact of the nanoscale dumbbell pattern and local J-T distortion on the spin physics is nontrivial and unexpected. Could it be that ionic disorder actually facilitates quantum spin liquid formation? An alternative picture might be that the local ionic and lattice structures favor a frozen but random pattern of pairs of anti-aligned spins, known as a random singlet phase (*7*). Either way, this work points to new directions for theoretical and experimental searches for exotic magnetism. Certainly, the interplay of ionic and electronic degrees of freedom seen here suggests reexamination of the physics of quantum spin liquid states in other materials for which only powder samples have been studied, such as related $Ba_3NiSb_2O_9$ compounds (*8*).

References

1. L. F. Feiner *et al*., *Phys. Rev. Lett.* **78**, 2799 (1997).
2. S. Nakatsuji *et al*., *Science* **336**, 559 (2012).
3. G. H. Wannier, *Phys. Rev.* **79**, 357 (1950).
4. H. D. Zhou *et al*., *Phys. Rev. Lett.* **106**, 147204 (2011).
5. J. B. Goodenough, *Annu. Rev. Mater. Sci.* **28**, 1 (1998).
6. L. Balents, *Nature* **464**, 199 (2010).
7. R. N. Bhatt, P. A. Lee, *Phys. Rev. Lett.* **48**, 344 (1982).
8. J. G. Cheng *et al*., *Phys. Rev. Lett.* **107**, 197204 (2011).

10.1126/science.1221364

PLANETARY SCIENCE

A Dynamic Twist in the Tail

James A. Slavin

Observations by Venus Express suggest that the magnetic tails of Venus and, by implication, comets may be more dynamic than originally thought.

All planetary bodies with intrinsic magnetic fields or atmospheres possess very long magnetic tails (*1*, *2*). If they possess the same intrinsic magnetic field dipole orientation as Earth, then the northern half of the tail is composed of open magnetic fields oriented back toward the planet, and the southern half has the opposite orientation (see the figure, panel A). Sandwiched between these two lobes of the tail is a sheet of hot plasma derived from the solar wind and the atmospheres of the planet and its moons. The cross-tail electric current sheet that separates the sunward magnetic field in the northern lobe from the antisunward flux in the southern lobe lies at the center of the plasma sheet. The intrinsic magnetotails of Mercury and Earth store magnetic energy in their tail lobes and then rapidly convert it into plasma heating and high-speed jetting (*3*, *4*) through the process of magnetic reconnection (*5*). Venus and comets lack intrinsic magnetic fields, but magnetotails still form as a result of the heliospheric magnetic field lines carried by the solar wind draping about these bodies (see the figure, panel B). The Venera 9 and 10 and Pioneer Venus Orbiter missions to Venus found that the structure of its draped field magnetotail has many similarities to those of magnetized planets, but found no evidence for magnetic reconnection (*6*, *7*). Now, on page 567 of this issue, Zhang

Department of Atmospheric, Oceanic and Space Sciences, University of Michigan, Ann Arbor, MI 48176, USA. E-mail: jaslavin@umich.edu

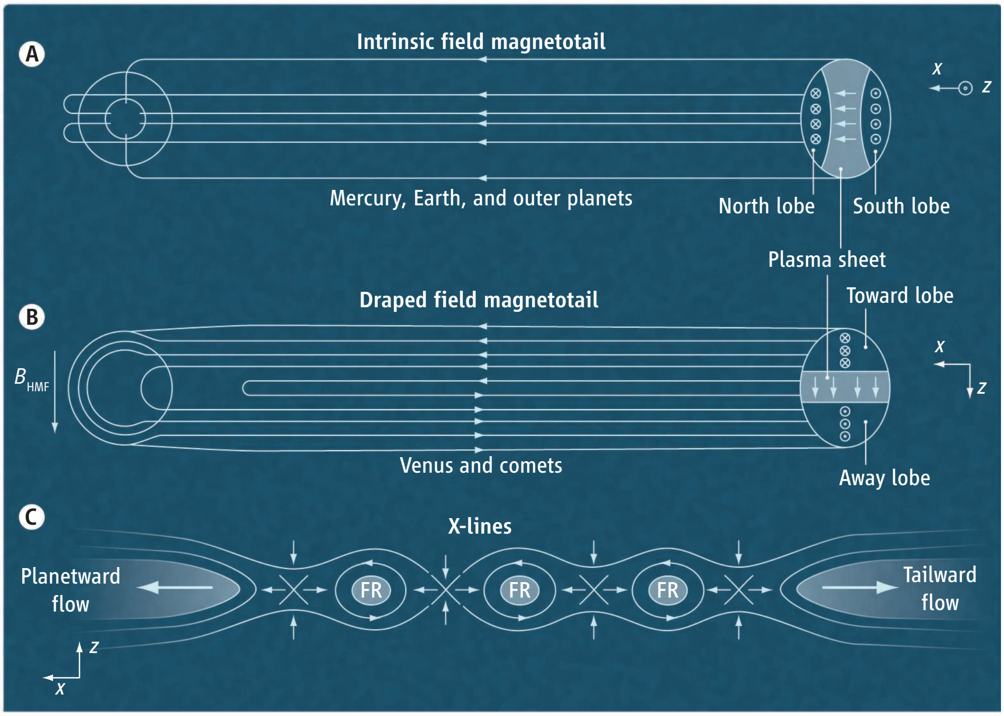

Making a reconnection. (**A**) For planets with intrinsic magnetic fields, the orientation and structure of their magnetotails is largely controlled by the bodies' properties; the *x* axis is directed toward the Sun and the *z* axis is normal to the plasma sheet. (**B**) For Venus, comets, and any other bodies lacking appreciable intrinsic magnetic fields but possessing atmospheres, magnetotails form as a result of the draping of the heliospheric magnetic field (B_{HMF}) about the body as the incident solar wind is slowed by its interaction with the outermost ionized atoms and molecules arising from the neutral atmosphere. (**C**) The oppositely directed magnetic fields found in all magnetotails make them susceptible to the formation of reconnection X-lines and flux ropes (FR) commonly referred to as plasmoids; arrows indicate the motion of the plasma and magnetic field lines as the central current sheet embedded in the plasma sheet is reconfigured by reconnection.

et al. (*8*) report observations of clear magnetic reconnection signatures in the Venus Express data, representing an unexpected discovery with important ramifications for our understanding of Venus.

Magnetic reconnection is a fundamental process in cosmic plasmas that reconfigures sheared magnetic fields separated by thin current sheets with a transfer of energy to the charged particles. The ions and electrons in collisionless plasmas are free to move along magnetic field lines, but their motion in the perpendicular direction is severely restricted. This property of such plasmas is called the frozen-in-field condition. Reconnection takes place when external forces, such as energy storage in tail magnetic fields, cause electric current sheets to become thin relative to the scale of the gyromotion of these charged particles around the magnetic field lines (*9*, *10*). When this point is reached, the plasma ions and electrons are no longer frozen onto the field lines. Magnetic nulls ("X-lines") form in the current sheet and magnetic field lines from opposite sides come together and exchange partners. This process causes the current sheet to fragment into magnetic flux ropes called plasmoids (see the figure, panel C). These flux ropes may be carried sunward or antisunward depending upon the intensity of the flows of plasma away from the different X-lines. This flux rope motion produces a distinctive bipolar variation in the magnetic field component normal to the cross-tail current sheet. Flux ropes are perhaps the most frequently observed reconnection phenomenon observed in planetary magnetotails, in part because of the magnetic field strength along the central axes of flux ropes, which often exceeds the intensity of the magnetic field in the surrounding magnetotail (*11*). It was these flux rope–type plasmoid magnetic field and plasma flow signatures that Zhang *et al*. found in the Venus Express magnetotail measurements.

As described by Zhang *et al*., reconnection in the draped field magnetotail of Venus will change the topology of the magnetic fields near the planet and channel solar wind energy to the nightside ionosphere in a manner not previously envisioned. For example, this tail reconnection is expected to generate loops of the magnetic flux that encircle Venus near its "magnetic equator" (i.e., the plane containing the heliospheric magnetic field and the center of the planet). But how do these loops of magnetic flux affect the dayside interaction between the solar wind and the Venus ionosphere, and how do they dissipate? Will reconnection and plasmoid formation in Venus' magnetotail increase the global rate of atmosphere loss, and if so, by how much? What factors control the thickness of the cross-tail current layer in the Venus plasma sheet and cause it to thin to the point where magnetic reconnection occurs?

Cometary magnetotails also form as a result of the draping of heliospheric field lines about the dayside ionosphere (*12*). The occurrence of reconnection in these cometary magnetotails is believed to cause the dramatic disconnection events during which the plasma sheet is observed to separate from the coma in images taken by ground-based observatories (*13*–*15*). What do these new observations of magnetic reconnection in the draped magnetotail of Venus tell us about reconnection in cometary magnetic tails? These and many other questions relating to the effect of magnetic reconnection on magnetotails will have to await the analysis of measurements yet to be returned by the European Space Agency's Rosetta mission to Comet 67P/Churyumov-Gerasimenko arriving in 2014. At the same time, NASA will launch the Magnetospheric MultiScale mission, which should reveal how magnetic reconnection operates on multiple scale lengths and its crucial role in the initiation of space weather phenomena in Earth's near-space environment.

References

1. A. Nishida *et al*., *J. Geophys. Res.* **100**, 23663 (1995).
2. F. L. Scarf *et al*., *Nature* **292**, 585 (1981).
3. J. A. Slavin *et al*., *Science* **329**, 665 (2010).
4. V. Angelopoulos *et al*., *Science* **321**, 931 (2008).
5. J. L. Burch, J. F. Drake, *Am. Sci.* **97**, 392 (2009).
6. M. A. Saunders, C. T. Russell, *J. Geophys. Res.* **91**, 5589 (1986).
7. J. A. Slavin *et al*., *J. Geophys. Res.* **94**, 2383 (1989).
8. T. L. Zhang *et al*., *Science* **336**, 567 (2012).
9. M. Hesse *et al*., *Space Sci. Rev.* **160**, 3 (2011).
10. P. A. Cassak, M. Shay, *Space Sci. Rev.*; 10.1007/s11214-011-9755-2 (2011).
11. J. A. Slavin *et al*., *J. Geophys. Res.* **108**, 1015 (2003).
12. E. J. Smith *et al*., *Science* **232**, 382 (1986).
13. M. B. Neidner Jr., J. C. Brandt, *Astrophys. J.* **223**, 655 (1978).
14. C. T. Russell *et al*., *J. Geophys. Res.* **91**, 1417 (1986).
15. Y.-D. Jia *et al*., *J. Geophys. Res.* **112**, A05223 (2007).

10.1126/science.1221805

CLIMATE CHANGE

Regional Sea-Level Projection

More accurate projections of regional sea levels are needed to inform adaptation and mitigation planning.

Josh K. Willis[1] and John A. Church[2]

Projections of global sea-level rise by 2100 C.E. range from 20 cm (*1*) to as much as 2 m (*2*, *3*), and sea level will not stop rising then. For civilization, the stakes are high. Without adaptation, a rise by 0.5 m would displace 3.8 million people in the most fertile part of the Nile River Delta (*4*). A rise by 2 m could displace 187 million people globally (*5*). Credible projections of sea-level rise in the 21st century are essential for devising adaptation or mitigation measures. Yet, present estimates of future sea-level rise are too imprecise to inform such decisions.

Earth system models used in the last Intergovermental Panel on Climate Change report (*1*) project a total global sea-level rise of 20 to 60 cm by 2100 C.E. from thermal expansion of the ocean, glacier melt, and the balance between melting, snowfall, and the regular outflow of glaciers from the ice sheets. However, potential contributions from accelerated ice-sheet outflow or the rapid collapse of glaciers that are in direct contact with the oceans are not currently included in these models.

[1]Jet Propulsion Laboratory, California Institute of Technology, Pasadena, CA 91109, USA. [2]Centre for Australian Weather and Climate Research, Hobart, Tasmania, Australia. E-mail: joshua.k.willis@jpl.nasa.gov; john.church@csiro.au

Furthermore, complex regional patterns lead to a larger rise in some regions and to considerable but poorly quantified interannual and decadal variability of sea level.

Global climate models approximately reproduce the thermal expansion of ocean waters over recent decades (*6*). However, the observational record is short, the deep ocean is poorly observed, and discrepancies between observations and simulations remain. Large discrepancies between regional projections from different models suggest that the ocean's dynamic response to climate forcing is poorly understood (*1*). Local geological influences in important urban settings like New Orleans (*7*) could result in tens of centimeters of additional rise by 2100 C.E.

Critical comparisons between models and observations are needed to better constrain regional projections. However, adequate ocean salinity and temperature data have only become available in the past decade, since the completion of the Argo array of profiling floats (*8*). Before the 2000s, large regions were undersampled, particularly in the Southern Ocean, making ocean warming estimates uncertain. Glaciers are projected to make an increasing contribution to sea-level rise. A new glacier inventory (location, elevation, areas, and volumes) has just been completed (*9*), but fewer than 100 glaciers have observations that allow mass balance to be estimated over decades. Addressing these shortfalls will be critical to improving 21st-century projections.

The global sea-level rise observed in recent decades can be approximately attributed to thermal expansion and glacier ice loss (*10*), but contributions from the ice sheets in Greenland and Antarctica over this period are poorly constrained. Mass loss from these ice sheets also remains the largest uncertainty in projections of sea-level rise for the 21st century and beyond. The problem is not purely a glaciological one, with ice, ocean, air, and land each playing a role (see the figure) (*11*). Accurate representation of ice-sheet response and ice-ocean interactions in models remains an enormous scientific challenge.

Upper bounds on sea-level rise have been estimated from kinematic constraints on glacier outflow (*3*) and paleoclimate analogs (*12*), but these provide no information about the likelihood of such scenarios. Projections with semi-empirical models, which depend on historical statistical relationships between sea level (mostly since about 1850) and surface temperature (*13*) or radiative forcing (*14*), have been developed. These models project much higher sea level (more than twice) than do current Earth system models (fig. S1). Is this discrepancy a result of incomplete understanding of the physical processes, or are the semi-empirical models unable to accurately project future sea-level rise?

Earth system models have significant uncertainties in abyssal ocean heat uptake, snowfall on Antarctica, ocean circulation beneath the ice shelves and the resulting basal melting, and glacier and ice-sheet response. In the case of the semi-empirical models, it is unclear whether the statistical relationships are robust in a changing climate. These models are sensitive to the formulation and training data used, they may be improperly scaling contributions from terrestrial water storage and non–climate change–related glacier and ice-sheet loss, and they do not account for reduced ocean heat uptake and reduced glacier contributions (from reduced area) during the 21st century (*15*). Also, semi-empirical projections pro-

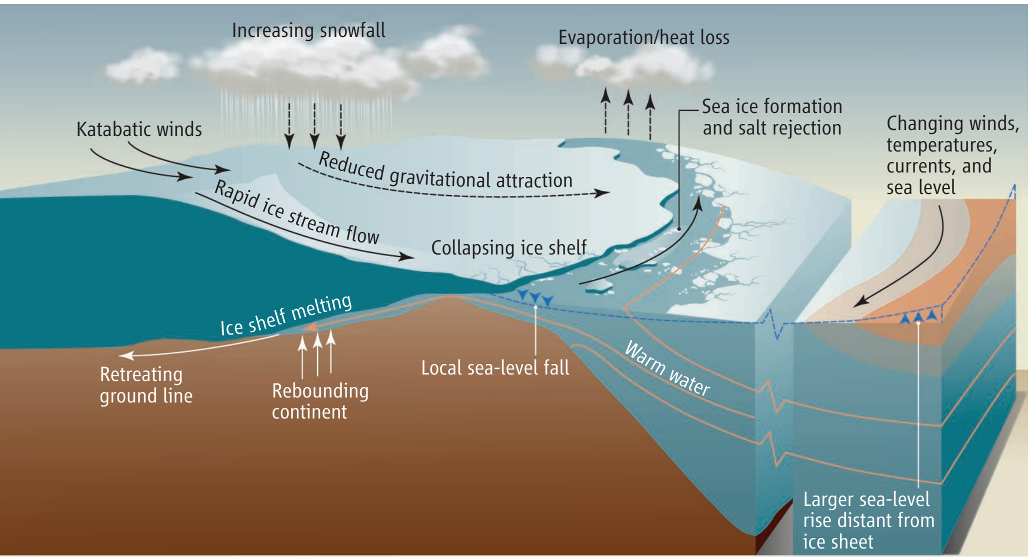

All change. Interactions between ice sheets, ocean, and atmosphere affect the balance of mass of the Greenland and Antarctic ice sheets. The dynamic response of the ocean, which affects regional sea level, may bring warmer waters in contact with marine glaciers, leading to the decay of ice shelves. Rapid changes at the boundary of the ice sheets can be communicated far into the interior of the ice sheets by ice streams, leading to unloading of the continent and changes in the global gravitational field and thus sea level. Changes in atmospheric temperatures and circulation may bring more precipitation to the Antarctic, offsetting ice loss at the boundaries.

Published by AAAS

vide no information on regional variations.

To advance sea-level projections, particularly at the regional level, it is crucial to understand the dynamical interactions between the ice sheets and the oceans, quantify changes in precipitation over Antarctica, advance understanding of the ocean's dynamic response to climate change, and continually monitor the ongoing changes. Given the difficulties and time required to develop fully coupled Earth system models that include full-stress ice-sheet models (*11*) that can reliably project sea-level rise, it is important to question and understand the accuracy and fidelity of the semi-empirical models. Resolving the discrepancies between these two approaches may lead to new projections that exploit advantages of both and may provide more reliable scenarios in a timely fashion.

References and Notes

1. G. A. Meehl *et al.*, in *Climate Change 2007: The Physical Science Basis*, S. Solomon *et al.*, Eds. (Cambridge Univ. Press, Cambridge, UK, 2007), pp. 749–845.
2. M. Vermeer, S. Rahmstorf, *Proc. Natl. Acad. Sci. U.S.A.* **106**, 21527 (2009).
3. W. T. Pfeffer *et al.*, *Science* **321**, 1340 (2008).
4. D. M. FitzGerald, M. S. Fenster, B. A. Argow, I. V. Buynevich, *Annu. Rev. Earth Planet. Sci.* **36**, 601 (2008).
5. R. Nicholls *et al.*, *Philos. Trans. R. Soc. A* **369**, 161 (2011).
6. C. M. Domingues *et al.*, *Nature* **453**, 1090 (2008).
7. E. R. Ivins *et al.*, *Geophys. Res. Lett.* **34**, L16303 (2007).
8. www.argo.net
9. A. Ardent *et al.*, *Randolph Glacier Inventory [v1.0]: A Dataset of Global Glacier Outlines* (Global Land Ice Measurements from Space, Boulder, CO, 2012).
10. J. A. Church *et al.*, *Geophys. Res. Lett.* **38**, L18601 (2011).
11. R. B. Alley, I. Joughin, *Science* **336**, 551 (2012).
12. E. Rohling *et al.*, *Nat. Geosci.* **1**, 38 (2008).
13. S. Rahmstorf, M. Perrette, M. Vermeer, *Clim. Dyn.*; 10.1007/s00382-011-1226-7 (2011).
14. S. Jevrejeva *et al.*, *Global Planet. Change* **80-81**, 14 (2011).
15. J. A. Church, J. M. Gregory, N. J. White, S. M. Platten, J. X. Mitrovica, *Oceanography* **24**, 130 (2011).

Acknowledgements: We thank C. Boening and D. Halkides for guidance and comments on early drafts of this manuscript and for organizing the workshop "Understanding Sea Level Rise: The Roles of Coupled Systems," held at Jet Propulsion Lab, Pasadena, CA, on 29 to 31 August 2011, that sparked this discussion.

Supplementary Materials
www.sciencemag.org/cgi/content/full/336/6081/550/DC1
Fig. S1
References

10.1126/science.1220366

CLIMATE CHANGE

Modeling Ice-Sheet Flow

Full-stress flow models for ice sheets promise improved projections of sea-level change.

Richard B. Alley[1] and Ian Joughin[2]

The great Greenland and Antarctic ice sheets are the "wild cards" in projections of sea-level change (*1*). Early models of the coupled ocean-atmosphere system treated the ice sheets as static white mountains. Observations since then have shown that ice sheets can change quickly (*2*): In some places, the tides strongly modulate coastal ice flow; in others, warming-induced ice-shelf loss has caused the flow speed of the subsequently unbuttressed inland ice to increase almost 10-fold within a few weeks (*3*, *4*). A new generation of full-stress ice-sheet models incorporates the physics needed to reproduce such processes (see the figure) (*5*–*7*). Including full stresses does improve ice-flow simulations (*8*). Well-validated, robust projections of ice-sheet behavior under climate change nevertheless remain a challenge, as they will require an ensemble of model ice sheets coupled to the rest of the climate system.

Complex crevasses on Pine Island Glacier, West Antarctica. A new generation of ice-flow models allows simulation of the stress states that give rise to crevasse patterns and their effect on the ice (*15*).

CREDIT: I. JOUGHIN

Part of the computational difficulty in ice-sheet modeling arises from the orders-of-magnitude variations of the frictional drag at the ice bed and margins that balances the gravitational driving stress. Although the governing equations have long been known, they are numerically challenging to solve. Earlier models relied on simplified representations of how ice flow redistributes these stresses from low-drag to high-drag regions. In contrast, the new models include all stresses without simplifying assumptions, and offer improved coupling to the ocean and atmosphere, in an era when computing speeds are beginning to make such approaches feasible.

Despite advances in the speed, stability, comprehensiveness, and coupling of models, difficulties remain. Even full-stress models are limited by poor knowledge of the bedrock surface on which the ice rests, where features a few kilometers or less in extent may be important to ice flow. The location of these features in Earth's more remote areas and beneath kilometers-thick, continental-scale sheets of ice makes them difficult to measure at the necessary scale. Programs such as NASA's Operation IceBridge are beginning to collect data at the scale necessary to address this problem.

Also, understanding of where freezing fixes the ice to its bed and to what extent melting facilitates fast basal motion remains limited. The bed's thermal state is in part determined by the geothermal flux, which has yet to be measured anywhere beneath an ice sheet with sufficient accuracy and extent to usefully constrain the frozen-thawed boundary. In addition, ice deformation increases exponentially with temperature and is influenced by flow-induced preferred orientations of the anisotropic ice crystals; yet, few direct ice-core and borehole measurements of anisotropy and temperatures exist for the deep ice layers that control deformation. Geophysical techniques can be used to interpolate these data between core sites and to map the frozen-thawed boundary and the distribution of lubricating till, but insufficient data exist to allow detailed estimates for entire ice sheets.

Until sufficient data are produced (if ever), ice-sheet models must rely on assimilation of surface velocities and other available data to estimate the unknown quantities. A difficulty is that differently parameterized models applied to regions where the ice flow is currently not changing may provide statistically similar fits to modern data but very different responses to future forcing. Such ambiguities about future response can, however, often be

[1]Department of Geosciences, and Earth and Environmental Systems Institute, Pennsylvania State University, University Park, PA 16802, USA. [2]Polar Science Center, Applied Physics Laboratory, University of Washington, Seattle, WA 98105, USA. E-mail: rba6@psu.edu; ian@apl.washington.edu

resolved in places where large recent changes have occurred (*9*), providing a basis for process understanding that can be extrapolated to regions that are still stable.

Guidance for integrating the new glaciological models with existing research can be gained from the experience of the Intergovernmental Panel on Climate Change and related efforts to assess likely ocean-atmosphere change. The results presented to policy-makers with greatest confidence are those that are derived from fundamental physics, are seen in a hierarchy of models for physically similar reasons, and have been successfully "retrodicted" in paleoclimatic and instrumental records; failure of any of these reduces confidence.

A coordinated modeling effort is essential to gain the understanding and achieve the successful retrodiction that increase confidence in projections. However, a measure of heterogeneity in such activity is just as important. The mean behavior of ~20 general circulation models matches observed climate data much better than any single model (*10*), providing reason to doubt the apparent efficiency of moving forward with one model.

The improvement provided by full-stress models comes at a large computational cost, leaving much room for nimble but simplified models. For example, the need to test against paleoclimatic archives, together with the >100,000-year time scales of central ice-sheet regions, cannot be met with the full-resolution versions of the most complex models. Also, performance of simpler models is easier to test in situations with analytic solutions. During assimilation and forward modeling, uncertainties in a host of parameters can affect outcomes; "massive ensemble" analyses (*11*), which show whether particular solutions are excluded, allowed, or likely, are almost entirely the realm of simplified models. Comprehensive model runs can be viewed as numerical experiments; efforts to understand the outcomes of such experiments at a more fundamental level can provide important insights to the climate system (*12*, *13*). Thus, the advent of the comprehensive modeling tools is likely to increase the need for simpler models.

Complex modeling is far from the only challenge on the road to useful ice-sheet projections. Model results and data both show that ice sheets can exhibit threshold behavior (*14*), which may depend on small features that are not well sampled by available data sets. Maintenance of observational capacity, from ice cores to satellites, will be crucial to ensure that current and future ice-flow and ice-thickness changes are measured. The lack of a firm understanding of ice-sheet–ocean interaction, constrained by reliable ocean data, remains a critical obstacle to understanding future changes.

Still, there is cause for optimism. With the ability to determine thickness, speed, elevation change, and other characteristics of the ice sheets from space and aircraft, to survey them from the surface, to plumb their depths with cores, and to model them with a hierarchy of approaches, including full-stress models coupled to global climate models, today looks like the start of a new phase of glaciological research. Until rigorous model-based sea-level projections can be brought to fruition, however, guidance is likely to continue to rely on semi-empirical approaches (*1*), analogy to paleoclimatic situations, physically limiting estimates, expert elicitations, and results of simpler models.

References and Notes

1. J. K. Willis, J. A. Church, *Science* **336**, 550 (2012).
2. T. Moon, I. Joughin, B. Smith, I. Howat, *Science*, **336**, 576 (2012).
3. E. Rignot *et al.*, *Geophys. Res. Lett.* **31**, L18401 (2004).
4. T. A. Scambos, J. A. Bohlander, C. A. Shuman, P. Skvarca, *Geophys. Res. Lett.* **31**, L18402 (2004).
5. E. Larour, H. Seroussi, M. Morlighem, E. Rignot, *J. Geophys. Res.* **117**, F01022 (2012).
6. W. Leng *et al.*, *J. Geophys. Res.* **117**, F01001 (2012).
7. Additional information on the Ice Sheet System Model (ISSM) (*5*) is available at http://issm.jpl.nasa.gov/. Also see (*16*). The Community Ice Sheet Model GLIMMER-CISM (Community Ice Sheet Modeling Initiative) (*6*) is described at http://oceans11.lanl.gov/trac/CISM. For GLIMMER, see (*17*). The Assessment Group of the Community Ice Sheet Model has evolved into the SeaRISE effort; see http://websrv.cs.umt.edu/isis/index.php/SeaRISE_Assessment. The Parallel Ice Sheet Model (PISM-PIK) is described at www.pism-docs.org/wiki/doku.php?id=home. Also see (*18*).
8. F. Pattyn *et al.*, *Cryosphere* **2**, 95 (2008).
9. I. Joughin *et al.*, *Geophys. Res. Lett.* **37**, L20502 (2010).
10. R. Knutti *et al.*, *J. Clim.* **23**, 2739 (2010).
11. M. Huber, R. Knutti, *Nat. Geosci.* **5**, 31 (2012).
12. I. M. Held, *Bull. Am. Meteorol. Soc.* **86**, 1609 (2005).
13. R. T. Pierrehumbert, G. Brogniez, R. Roca, in *The Global Circulation of the Atmosphere*, T. Schneider, A. Sobel, Eds. (Princeton Univ. Press, Princeton, NJ, 2007), p. 150.
14. R. B. Alley *et al.*, *Science* **315**, 1838 (2007).
15. T. Albrecht, A. Levermann, *J. Glaciol.* **58**, 165 (2012).
16. M. Morlighem *et al.*, *Geophys. Res. Lett.* **37**, L14502 (2010).
17. I. C. Rutt *et al.*, *J. Geophys. Res.* **114**, F02004 (2009).
18. R. Winkelmann *et al.*, *Cryosphere* **5**, 715 (2011).

Acknowledgments: Partial funding was provided to R.B.A. through grants NSF 0424589, 0909335, ANT-0944286, and NASA NNX-10-AI04G, and to I.J. through grants NASA NNX-11AC23G and NSF ANT-0852697.

10.1126/science.1220530

ECOLOGY

Impacts of Biodiversity Loss

How much diversity is needed to maintain the productivity of ecosystems?

Bradley Cardinale

Historically, ecologists and evolutionary biologists have treated the variety of life on Earth as if it were a simple by-product of the physical and chemical variation that generates biological diversity and allows it to persist. However, this perspective changed in the 1990s, when scientists began to manipulate biodiversity in controlled environments and found that it can act as an independent variable that directly controls ecosystem-level functions, such as nutrient cycling and biomass production (*1*–*4*). The idea that biodiversity might control—rather than just respond to—Earth's biophysical processes was foreign to many researchers (*5*). But by 2010, more than 600 manipulative experiments had been performed, spanning much of the tree of life and most major biomes on the planet (*6*). We now know that biodiversity regulates many ecosystem-level processes, including some that are essential for providing goods and services to humanity (*6*–*9*). On page 589 of this issue, Reich *et al.* (*10*) provide important novel insights into how much diversity is needed to maintain the productivity of ecosystems.

School of Natural Resources and Environment, University of Michigan, 440 Church Street, Ann Arbor, MI 48109, USA. E-mail: bradcard@umich.edu

The authors reanalyze data from two classic biodiversity studies that have been running for more than a decade at the Cedar Creek Ecosystem Science Reserve in Minnesota. By fitting data collected over a 15-year period to several mathematical functions (linear, log, power, and hyperbolic), the authors quantify the form of the relationship that describes how plant species richness influences the production of plant biomass. They show that the effects of biodiversity on productivity change from saturating functions that are prominent

Published by AAAS

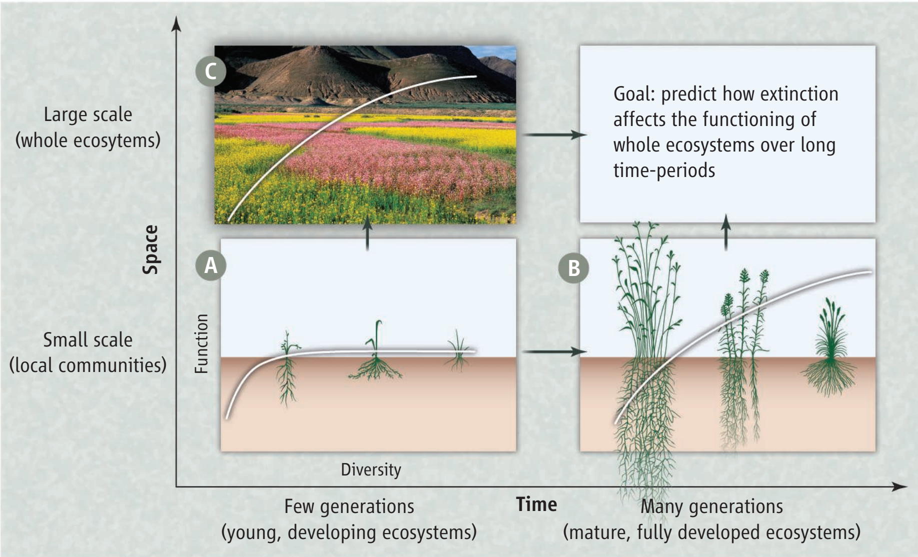

Scaling diversity-function relationships. Since 1990, more than 600 experiments have manipulated the diversity of plants, animals, fungi, protozoa, and bacteria in a variety of Earth's biomes. These studies have shown that ecosystem functions like nutrient cycling and biomass production are positively related to biodiversity, but that relationships saturate at relatively low levels of diversity (**A**). Reich *et al*. have reanalyzed results from two long-term studies of grassland plants and found that although saturating functions are prominent early in the studies, diversity-function relationships ultimately become monotonically increasing given enough time (**B**). Short-term experiments may thus underestimate the number of species needed to maintain ecosystem-level processes. If the results prove to be general, Reich *et al*. will have quantified how the ecological impacts of extinction scale through time (A to B). If others can similarly quantify how diversity-function relationships change with the spatial extent of studies (A to **C**), we would have scaling relationships to estimate the fraction of species needed to maintain ecological processes in more realistic ecosystems (**D**).

early in the experiments (see the figure, panel A), to monotonically increasing functions later in the experiments (panel B).

Reich *et al*. argue that the reason for this change is that it takes time for species to express the biological traits that allow them to fill their various ecological niches. They present a set of calculations that estimate how much of the diversity effect in any given year is driven by processes involving two or more species (called complementarity). They show that complementarity grows stronger through time, and this trend is associated with a greater divergence in the biological traits of species in the experimental plots. These trends are not conclusive evidence that niche differences are the underlying cause of the reported patterns, but they hint at the possibility that biological "niche space" becomes more completely filled as communities interact and assemble through time.

Several studies have shown that diversity effects grow stronger with time (*11*, *12*), but Reich *et al*. go further by quantifying how the shape of the diversity-function relationship—which tells us what fraction of species is required to maintain ecosystem functions—changes through time. If biodiversity has a saturating effect on ecosystem processes, as most prior studies suggest, this implies that some fraction of species are functionally "redundant," and can be lost with little or no impact on ecosystem processes. Ehrlich and Ehrlich (*13*) compared biological redundancy to the redundancy of rivets on an airplane wing. Loss of one or few rivets will not affect the performance of the plane, because wings are engineered with an excess of rivets. But lose one too many rivets, and the loss could have catastrophic consequences for passengers on the plane.

If, however, the relationship between biodiversity and ecosystem functioning is monotonically increasing, as Reich *et al*.'s reanalyses suggest, then each extinction would produce an incremental decrease in the functioning of ecosystems. This scenario would be far more pressing for conservation. A notable fraction of Earth's biodiversity has already been lost, and given current rates of extinction, much more is likely to be lost in the coming century (*14*). If the results of Reich *et al*. hold generally true, then biodiversity loss has probably already begun to degrade essential processes that sustain the productivity of ecosystems.

Reich *et al*.'s findings emphasize the importance of long-term studies, such as those sponsored by the U.S. National Science Foundation's Long Term Ecological Research Program that partially funded the Cedar Creek experiments. Most natural communities do not develop on the 1- to 3-year time frame of a typical grant, which is the scale of the average experiment. It is, therefore, possible that many biodiversity experiments to date have revealed just the tip of the iceberg—the short-term, transient effects of biodiversity on ecosystem processes. The real impacts of diversity loss could be much greater.

It remains to be shown whether the results of Reich *et al*.'s study are general, or whether something unique about the species pool, environmental conditions, or experimental methodologies make the experiments at Cedar Creek the exception rather than the rule. Resolving this will require comparison to other long-term studies, and reanalysis of data from biodiversity experiments involving even longer population dynamics than those at Cedar Creek (such as studies performed with model systems of bacteria or algae).

But if the conclusions of Reich *et al*. hold generally true, and monotonically increasing diversity-function relationships are indeed the norm, then this study moves us an important step closer to predicting the ecological consequences of diversity loss in real ecosystems, where life forms have evolved and interacted for many generations (see the figure, panel B). The study should also stimulate others to ask similar questions about how the form of diversity-function relationships changes with the spatial scale of experiments (see the figure, panel C). Once we know how diversity-function relationships scale in both time and space, we will have the statistical models needed to forecast the ecological consequences of extinction from whole ecosystems. For a field of research that did not even exist until the 1990s, development of such models would represent monumental progress in a remarkably short time.

References

1. S. Naeem *et al*., *Nature* **368**, 734 (1994).
2. A. Hector *et al*., *Science* **286**, 1123 (1999).
3. D. Tilman, D. Wedin, J. Knops, *Nature* **379**, 718 (1996).
4. P. B. Reich *et al*., *Nature* **410**, 809 (2001).
5. S. Naeem, *Ecology* **83**, 1537 (2002).
6. B. J. Cardinale *et al*., *Am. J. Bot.* **98**, 572 (2011).
7. P. Balvanera *et al*., *Ecol. Lett.* **9**, 1146 (2006).
8. B. J. Cardinale *et al*., *Nature* **443**, 989 (2006).
9. J. J. Stachowicz, J. F. Bruno, J. E. Duffy, *Annu. Rev. Ecol. Evol. Syst.* **38**, 739 (2007).
10. P. B. Reich *et al*., *Science* **336**, 589 (2012).
11. B. J. Cardinale *et al*., *Proc. Natl. Acad. Sci. U.S.A.* **104**, 18123 (2007).
12. J. J. Stachowicz *et al*., *Ecology* **89**, 3008 (2008).
13. P. R. Ehrlich, A. H. Ehrlich, *Extinction: The Causes and Consequences of the Disappearance of Species* (Random House, New York, ed. 1, 1981).
14. A. D. Barnosky *et al*., *Nature* **471**, 51 (2011).

10.1126/science.1222102

PHOTO CREDIT: WANG JUANJUN/TAO IMAGES LIMITED/ALAMY

Melanesian Blond Hair Is Caused by an Amino Acid Change in TYRP1

Eimear E. Kenny,[1]* Nicholas J. Timpson,[2]* Martin Sikora,[1] Muh-Ching Yee,[1] Andrés Moreno-Estrada,[1] Celeste Eng,[3] Scott Huntsman,[3] Esteban González Burchard,[3] Mark Stoneking,[4] Carlos D. Bustamante,[1,5]† Sean Myles[1,5,6]†

Human pigmentation varies considerably within and among populations and is a function of both variation in exposure to ultraviolet radiation (UVR) and the type and quantity of melanin produced in melanocytes (*1*). We examined the genetic basis of blond hair in Solomon Islanders, a population that differs from the general trend of darker skin and hair pigmentation near the equator where there is higher UVR (*1*). Although individuals from the Solomon Islands and Equatorial Oceania have the darkest skin pigmentation outside of Africa, they also have the highest prevalence of blond hair (5 to 10%) outside of Europe (Fig. 1A) (*2*).

We performed a case-control genome-wide association (GWA) study on 43 blond- and 42 dark-haired Solomon Islanders and observed a single strong association signal on chromosome 9p23; the most significant single-nucleotide polymorphism (SNP) (rs13289810; $P = 1.11 \times 10^{-19}$) had a frequency of 0.93 and 0.31 in blond- and dark-haired individuals, respectively (Fig. 1B). The mapping interval contained one known gene, tyrosinase-related protein 1 (*TYRP1*; Fig. 1C), which encodes a melanosomal enzyme involved in mammalian pigmentation and is highly conserved in vertebrates (*3*). Mutations in *TYRP1* lighten skin and/or hair pigmentation in several species (*3*), and *TYRP1* null alleles cause rufous albinism in humans (*4*, *5*).

Resequencing of *TYRP1* exons detected a single previously unknown polymorphism, a C-to-T transition at chr9:12,694,273 (GrCH37/hg19), that corresponds to a predicted arginine-to-cysteine mutation (R93C) in exon 2 of *TYRP1* at amino acid position 93 (TT in blond- and CT or CC in dark-haired individuals). This variant was genotyped in the GWA panel, and association analyses were repeated, including R93C. R93C was more strongly associated with blond hair ($P = 9.60 \times 10^{-23}$) than the top GWA SNP (Fig. 1C), and the GWA signal was lost on conditioning for R93C (fig. S5). This suggests a primary role for the missense mutation, although the involvement of noncoding and/or regulatory variants in strong linkage disequilibrium (LD) with R93C cannot be ruled out.

We genotyped R93C in 918 Solomon Islanders for whom we had measured hair pigmentation with spectrometry. A recessive model provided the best fit for the data, and R93C genotypes accounted for 46.4% of the variance in hair color (linear regression; $P = 2.19 \times 10^{-90}$; Fig. 1D and table S2). The frequency of the 93C allele in the Solomon Islands is 0.26, and genotyping of R93C in an additional 941 individuals from 52 worldwide populations revealed that the 93C allele is rare or absent outside of Oceania (table S3). Furthermore, we found no evidence for recent gene flow from Europe (i.e., admixture) (figs. S5 and S6) nor a strong signature of recent positive selection for the 93C allele (figs. S9 to S11).

The 93C blond hair mutation in human *TYRP1* resides in an epidermal growth factor (EGF)–like repeat near the N terminus and is similar to the molecular alteration observed in the *TYRP1* allele in the brown^{light} mouse (fig. S12). The brown^{light} phenotype is caused by an Arg→Cys substitution located 55 amino acids upstream of R93C (R38C) and likely interferes with disulfide bridges formed by the 15-Cys EGF repeat. The brown^{light} mouse exhibits reduced *TYRP1* stability and catalytic function, resulting in decreased melanin content in hair (*6*), and it is likely that the human 93C mutation operates via a similar mechanism.

The present study realizes the benefits of extending genetic mapping to humans worldwide, and we predict that many novel genetic variants with large phenotypic effects remain to be discovered in populations currently underrepresented in genomic research (*7*). Our results strongly support the notion that the study of diverse populations is crucial to elucidating the genetic basis of phenotypic variation.

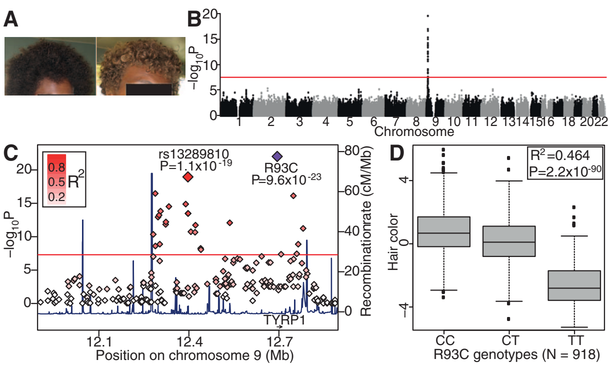

Fig. 1. (**A**) Two individuals from the Solomon Islands with dark (left) and blond hair (right). (**B**) GWA scores comparing blond- and dark-haired individuals show a strong signal at 9p23; the genome-wide significance threshold is indicated by the red line. (**C**) Association scores at 9p23 with the top GWA SNP (red diamond), TYRP1 R93C (purple diamond), and the *TYRP1* gene (arrow) indicated. The degree of red color in each diamond indicates the strength of LD with R93C. (**D**) Age and sex-corrected hair color by R93C genotype and the result of a linear model assuming a recessive mode of inheritance (boxed in). Boxes denote upper and lower quartiles, and error bars indicate ±2.7 SD.

References and Notes

1. N. G. Jablonski, G. Chaplin, *Proc. Natl. Acad. Sci. U.S.A.* **107** (suppl. 2), 8962 (2010).
2. H. L. Norton *et al.*, *Am. J. Phys. Anthropol.* **130**, 254 (2006).
3. V. del Marmol, F. Beermann, *FEBS Lett.* **381**, 165 (1996).
4. R. E. Boissy *et al.*, *Am. J. Hum. Genet.* **58**, 1145 (1996).
5. P. Manga *et al.*, *Am. J. Hum. Genet.* **61**, 1095 (1997).
6. R. Johnson, I. J. Jackson, *Nat. Genet.* **1**, 226 (1992).
7. C. D. Bustamante, E. G. Burchard, F. M. De la Vega, *Nature* **475**, 163 (2011).

Acknowledgments: We are grateful to the people of the Solomon Islands for their participation in this study. We thank the Kosrae consortium for access to genetic data, G. Coop and G. Barsh for helpful comments, and C. Wegener for technical assistance. Funded by a Wenner-Gren Foundation for Anthropological Research grant to S.M., MRC Centre for Causal Analyses in Translational Epidemiology grant RD1634 to N.J.T., National Heart, Lung, and Blood Institute and National Human Genome Research Institute funding to C.D.B., and the Max Planck Society. Allele frequency data for this study are available from dbGAP (study accession phs000493.v1.p1). De-identified genotype data are available through a data access agreement for transfer of genetic data by contacting C.D.B.

Supplementary Materials
www.sciencemag.org/cgi/content/full/336/6081/554/DC1
Materials and Methods
Figs. S1 to S12
Tables S1 to S3
References (*8*–*29*)

13 December 2011; accepted 14 February 2012
10.1126/science.1217849

[1]Department of Genetics, Stanford University, Stanford, CA 94305, USA. [2]Medical Research Council (MRC) Centre for Causal Analyses in Translational Epidemiology, School of Social and Community Medicine, University of Bristol, Oakfield Grove, Bristol BS8 2BN, UK. [3]Department of Bioengineering and Therapeutic Sciences and Medicine, University of California San Francisco, San Francisco, CA 94143, USA. [4]Department of Evolutionary Genetics, Max Planck Institute for Evolutionary Anthropology, Deutscher Platz 6, D04103 Leipzig, Germany. [5]Department of Biological Statistics and Computational Biology, Cornell University, Ithaca, NY 14853, USA. [6]Department of Plant and Animal Sciences, Nova Scotia Agricultural College, Truro, Nova Scotia B2N 5E3, Canada.

*These authors contributed equally to this work.
†To whom correspondence should be addressed. E-mail: smyles@nsac.ca (S.M.); cdbustam@stanford.edu (C.D.B.)

Spin-Torque Switching with the Giant Spin Hall Effect of Tantalum

Luqiao Liu,[1]* Chi-Feng Pai,[1]* Y. Li,[1] H. W. Tseng,[1] D. C. Ralph,[1,2] R. A. Buhrman[1]†

Spin currents can apply useful torques in spintronic devices. The spin Hall effect has been proposed as a source of spin current, but its modest strength has limited its usefulness. We report a giant spin Hall effect (SHE) in β-tantalum that generates spin currents intense enough to induce efficient spin-torque switching of ferromagnets at room temperature. We quantify this SHE by three independent methods and demonstrate spin-torque switching of both out-of-plane and in-plane magnetized layers. We furthermore implement a three-terminal device that uses current passing through a tantalum-ferromagnet bilayer to switch a nanomagnet, with a magnetic tunnel junction for read-out. This simple, reliable, and efficient design may eliminate the main obstacles to the development of magnetic memory and nonvolatile spin logic technologies.

Spin-polarized currents can be used to apply torques to magnetic moments by direct transfer of spin angular momentum, enabling manipulation of nanoscale magnetic devices with currents that are orders of magnitude lower than those required for magnetic-field–based control (*1*–*5*). The usual way to generate spin currents strong enough for spin-torque manipulation of magnets has been to send an electron current through a ferromagnetic (FM) polarizing layer, part of a two-terminal magnetic tunnel junction (MTJ) with a layered FM/tunnel barrier/FM structure. Although MTJs can have excellent spin-torque efficiency, they can be challenging to operate reliably; it is difficult to manufacture large-scale memories in which enough spin current can pass through the tunnel barriers to drive reliable magnetic switching without occasionally damaging a barrier. Achieving reliable reading of the MTJ resistance without ever causing switching is also a challenge. It has been known for some time that a spin current can, alternatively, be generated in nonmagnetic materials by the spin Hall effect (SHE) (*6*–*12*), in which spin-orbit coupling causes electrons with different spins to deflect in different directions, yielding a pure spin current transverse to an applied charge current. However, very few attempts have been carried out to use this spin current for manipulating magnetic moments (*13*, *14*).

We report the discovery of a giant SHE in the high-resistivity form of tantalum (β-Ta) (*15*) and demonstrate that this allows an electrical current in a thin Ta layer to efficiently induce spin-torque switching of an adjacent thin-film ferromagnet, for both perpendicular-to-plane and in-plane magnetized samples at room temperature. High-resistivity β-Ta is produced when Ta is sputter-deposited or evaporated onto amorphous surfaces such as oxidized Si (*16*) or CoFeB. Ab initio calculations (*17*) have predicted that highly resistive Ta may have a large spin Hall angle, comparable to or greater than that of Pt and with the opposite sign in comparison to Pt or Au. [Here, the spin Hall angle is defined as $\theta_{SH} = J_S/J_e$, where J_e is the charge current density and $[\hbar/(2e)]J_S$ is the spin current density arising from the SHE ($\hbar$, Planck's constant h divided by 2π; e, charge on an electron).] In contrast, a nonlocal spin valve measurement (*18*) reported a very low value for the Ta spin Hall angle, 0.0037 (albeit with the predicted sign). However, this measurement technique can greatly underestimate the spin Hall angle (*19*, *20*), particularly in highly resistive spin Hall materials such as Ta. We have quantified the magnitude of the SHE in Ta using three different methods, and we find the spin Hall angle to be $\theta_{SH}^{Ta} = 0.12$ to 0.15; in comparison with the spin Hall angle of Pt, $|\theta_{SH}^{Pt}| \approx 0.07$ (*19*–*24*), θ_{SH}^{Ta} is of opposite sign and larger, whereas it is comparable to one reported value for Pt-doped Au, $|\theta_{SH}^{Au(Pt)}| = 0.12 \pm 0.04$ (*25*). Unlike Pt, Ta does not substantially increase the magnetic damping (energy dissipation) in an adjacent thin-film magnet; consequently, we show that the giant spin Hall effect spin torque (SHE-ST) from Ta is effective in driving magnetic reversal of in-plane–polarized magnetic layers via an antidamping spin-torque mechanism (*5*). We use this effect to implement a three-terminal device geometry in which the SHE-ST from Ta produces current-induced switching of the in-plane polarized CoFeB layer, with read-out using a MTJ with a large magnetoresistance. This geometry is straightforward to fabricate and can have comparable efficiency to conventional two-terminal MTJs while providing greatly improved reliability and output signal levels.

Measurement of the SHE in Ta. To determine the spin Hall angle in β-Ta, we used the ST-induced ferromagnetic resonance (ST-FMR) technique, previously introduced in studies of Pt (*19*). Our samples consisted of $Co_{40}Fe_{40}B_{20}(4)/Ta(8)$ (the numbers in parentheses represent layers; thickness in nanometers) bilayers sputter-deposited onto oxidized Si substrates and patterned into 10-μm-wide strips. We took measurements of the bilayer resistance as a function of varying Ta thickness to determine that the Ta resistivity was $\rho_{Ta} \approx 190$ microhm·cm, confirming the β-Ta phase. The CoFeB resistivity was $\rho_{CoFeB} \approx 170$ microhm·cm, and for a 4-nm-thick film, the magnetic moment was oriented in-plane. We applied an oscillating radio frequency current I_{RF} along the strips in the current in-plane configuration, with an external magnetic field B_{ext} in the film plane at a 45° angle with respect to the current direction (Fig. 1A). Because of the SHE, the oscillating current in the Ta generated an oscillating spin current that flowed perpendicular to the sample plane and exerted an oscillating spin torque on the magnetic moment of the CoFeB layer. When the frequency of the bias current and the magnitude of the bias magnetic field satisfied the ferromagnetic resonance condition, magnetic precession occurred. Mixing of I_{RF} and the oscillating anisotropic magnetoresistance of the CoFeB then resulted in a measurable dc voltage. A typical resonance signal is shown in Fig. 1B, where the resonance peak is fitted by the sum of a symmetric Lorentzian and an antisymmetric Lorentzian. The symmetric component of the peak arises from the SHE-ST, whereas the antisymmetric peak is a consequence of the torque generated by the Oersted field from the current in the Ta; the difference in line shape is due to the orthogonal directions of the two torques (Fig. 1A) [for a detailed discussion of the line shapes, see (*19*, *20*)]. We measured the resonant signal for different applied frequencies and found that the positions of the resonant peaks agree well with the Kittel formula $f = (\gamma/2\pi)[B(B + \mu_0 M_{eff})]^{1/2}$ (Fig. 1B, inset), where $\gamma = 1.76 \times 10^{11}$ Hz T^{-1} is the gyromagnetic ratio and $\mu_0 M_{eff}$ is the effective demagnetization field determined to be 1.3 T from the fit.

To compare the SHE in Ta with that of Pt, we made and measured a different sample with the stack structure: substrate/CoFeB(3)/Pt(6) (thicknesses in nanometers), with the result shown in Fig. 1C. Comparing the resonant signals of CoFeB/Ta and CoFeB/Pt in Fig. 1, B and C, we see that the antisymmetric peaks of the two samples have the same sign, as expected from their common origin (*26*). The symmetric peaks in the two cases are opposite in sign, which directly shows that the SHE in Ta is opposite to that in Pt, in agreement with the prediction (*17*) and the previous measurement (*18*).

We measured the magnitude of the SHE using a self-calibrated technique that uses the ratio of the symmetric peak amplitude S to the antisymmetric peak A to determine the strength of the spin Hall torque relative to the Oersted-field torque (*19*).

[1]Cornell University, Ithaca, NY 14853, USA. [2]Kavli Institute at Cornell, Ithaca, NY 14853, USA.

*These authors contributed equally to this work.
†To whom correspondence should be addressed. E-mail: rab8@cornell.edu

Independent of the frequency employed, we found the consistent result that $J_S/J_e = 0.15 \pm 0.03$ in our 8-nm Ta films. This value of J_S/J_e represents the spin Hall angle θ_{SH} if the spin diffusion length λ_{sf} in Ta is much less than the Ta thickness (*19*, *20*). If λ_{sf} is comparable to or larger than the film thickness, then the bulk value of θ_{SH} is even larger than 0.15 ± 0.03.

If the spin torque from the SHE is to be used for switching nanomagnets by the conventional antidamping ST switching mechanism (*5*), it is important that the nonmagnetic layer does not substantially increase the effective magnetic damping of the adjacent FM by the spin-pumping effect (*27*, *28*). The ST-FMR measurements discussed above allow a determination of the Gilbert damping coefficient α from the linewidth ΔB (half width at half maximum) of the FMR peak, using the relation $\alpha = (\gamma/2\pi f)\Delta B$. The results shown in Fig. 1D indicate that $\alpha = 0.008$ for the CoFeB(4)/Ta(8) bilayer film, close to the intrinsic value expected for a 4-nm-thick CoFeB layer (*29*) and much smaller than the corresponding $\alpha \approx 0.025$ for the CoFeB(3)/Pt(6) sample. This is consistent with (*27*), in which damping caused by spin pumping was determined to be much stronger in FM/Pt bilayers than in FM/Ta, although the phase of Ta studied in (*27*) was not reported. Our observation of a strong spin Hall effect in β-Ta is not in conflict with the weakness of the spin-pumping effect in Ta films, because the strength of the spin pumping depends not only on the strength of spin-orbit coupling, but also on the ratio of the elastic scattering time to the spin-flip scattering time and the value of the spin-mixing conductance (*28*), either or both of which might be smaller in β-Ta than Pt.

Switching a perpendicularly magnetized ferromagnetic layer with the spin Hall effect. Previous experiments (*14*) using a perpendicularly magnetized FM deposited on Pt, and with a small magnetic field applied in the direction of the electrical current, have demonstrated that the SHE-ST will (once it is strong enough relative to the magnetic anisotropy field) abruptly rotate the out-of-plane moment from the nearly vertical positive (upward) orientation to the nearly vertical negative (downward) orientation, or vice versa, depending on the direction of the current flow and the SHE sign. [Such switching was first reported in (*30*), but Miron *et al.* argued that the spin Hall effect was not strong enough to explain their measurements, asserting instead that a Rashba mechanism was dominant.] We have verified that the stronger SHE in Ta can achieve the same switching effect but with the opposite sign compared to Pt. For this measurement, we deposited a thin-film stack with the structure substrate/Ta(4)/$Co_{40}Fe_{40}B_{20}$(1)/MgO(1.6)/Ta(1) (thicknesses in nanometers) and patterned it into Hall bars 2.5 to 20 μm wide and 3 to 200 μm long (Fig. 2A, inset). MgO was used as a capping layer because previous studies (*31*) have shown that for a sufficiently thin CoFeB layer, the Ta/CoFeB/MgO structure has a strong perpendicular magnetic anisotropy; this was confirmed by our measurements (Fig. 2A). (The top Ta layer served merely to protect the MgO from exposure to atmosphere.) For the ST switching measurement, a dc current was applied along the strip, and the anomalous Hall resistance R_H was recorded to monitor the change in the vertical component of the CoFeB magnetization because $R_H \propto M_z = M_S\sin\theta$, where θ represents the angle between the magnetic moment and film plane; M_z is the vertical component of the magnetization, and M_S is the saturation magnetization. A static magnetic field B_{ext} was applied almost parallel (or antiparallel) to the in-plane current direction, keeping the angle β between B_{ext} and the film plane fixed, initially at $\beta = 0°$. Figure 2B shows an example of the abrupt current-induced switching caused by the SHE-ST, as measured for a 2.5-μm-wide sample with $\beta = 0°$ and $B_{ext} = \pm 10$ mT. The switching curves shown in Fig. 2B are obtained under the same bias conditions as in figure 1 of (*14*), which reported a similar effect for the Pt/Co/AlO_x system. Comparison between the two reveals that the switching direction caused by the in-plane current in Fig. 2B is opposite to that in the Pt/Co/AlO_x system. We made additional control samples from a Pt/CoFeB/MgO multilayer and found that the switching direction is the same as with Pt/Co/AlO_x (fig. S5) (*32*), demonstrating that the sign reversal comes from the difference between the sign of the SHE in Pt and Ta, and not from any differences between the FM/oxide interfaces or between Co and CoFeB.

To quantitatively determine the magnitude of the spin Hall angle from the response of perpendicularly magnetized Ta/CoFeB/MgO samples, we swept the magnetic field, keeping its direction at a small field angle $\beta \approx 2°$. With a nonzero β, the vertical component of the external magnetic field $B_z = B_{ext}\sin\beta$ causes the magnetization of the Hall bar structure to remain uniformly magnetized as long as the current is well below the switching point, so that the magnetization rotates coherently with field and current (Fig. 2C). For convenience in the data analysis, we will treat B_{ext} as function of R_H instead of the reverse. As demonstrated in (*14*), the difference between

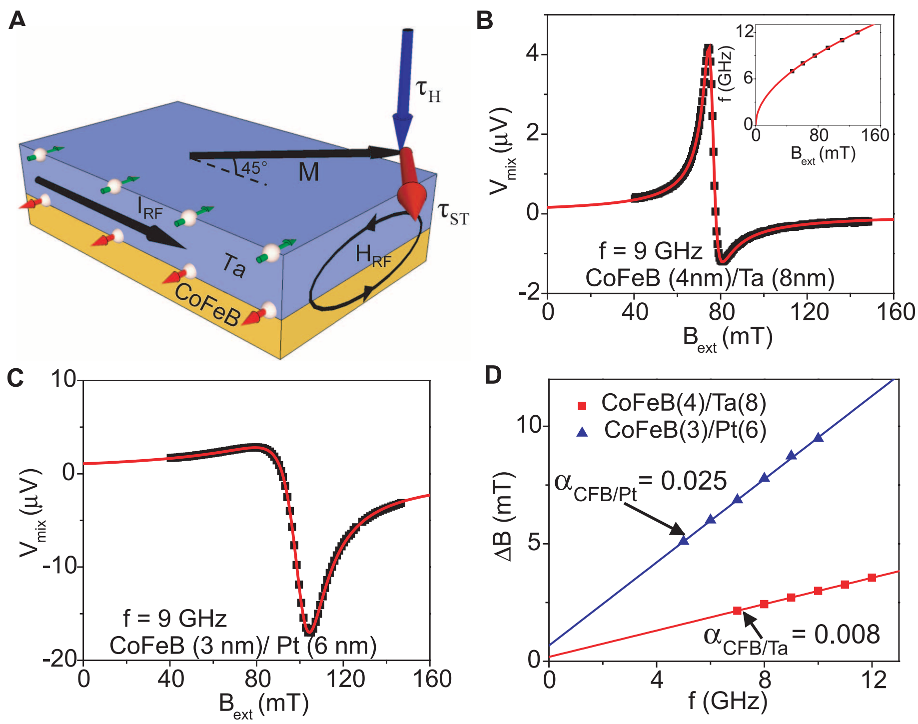

Fig. 1. ST-FMR induced by the spin Hall effect at room temperature. (**A**) Sample geometry for the ST-FMR measurement. I_{RF} and H_{RF} represent the applied radio frequency current and the corresponding Oersted field. $\vec{\tau}_H = -\vec{M} \times \vec{H}_{RF}$ is the torque on the magnetization due to the Oersted field, and $\vec{\tau}_{ST}$ is the spin-transfer torque from the spin Hall effect. Resonant line shapes of the ST-FMR signals under a driving frequency $f = 9$ GHz for (**B**) CoFeB(4 nm)/Ta(8 nm) and (**C**) CoFeB(3 nm)/Pt (6 nm). The squares represent experimental data, whereas the red curves are fits to a sum of symmetric and antisymmetric Lorentzians. From the ratio of the symmetric and antisymmeteric peak components in (C), we determine the J_S/J_e ratio for Pt to be ~0.07, consistent with earlier work (*19*). V_{mix} is the measured dc voltage due to the mixing of oscillating resistance and radio frequency current. The inset to (B) shows the dependence of the frequency f on the resonance magnetic field, in agreement with the Kittel formula (solid curve). (**D**) The resonance linewidth as determined from ST-FMR signals such as those shown in (B) and (C) at different resonance frequencies. The Gilbert damping coefficients α for Ta and Pt are calculated from the linear fits to these linewidth data. CFB, CoFeB.

the $B_{ext}(R_H)$ curves for $I = +0.7$ mA and -0.7 mA can be shown, within a macrospin model, to be proportional to the applied spin torque: $\Delta B[R_H(\theta)] = B_+(\theta) - B_-(\theta) = 2\tau_{ST}^0/\sin(\theta - \beta)$. Here, $B_{+/-}(\theta)$ is defined as the value of B_{ext} required to produce a given value of the magnetization angle θ when I is positive/negative. Figure 2D shows $\Delta B(R_H)$ determined by subtracting the two data sets in Fig. 2C. We plot R_H normalized with respect to its maximum value, so that it is equal to sinθ. Using a one-parameter fit, the magnitude of the spin torque can be determined to be $\tau_{ST}^0 \approx 2.1$mT for $|I| = 0.7$ mA. The τ_{ST}^0/I ratios obtained for different values of applied current are summarized in the inset of Fig. 2D; on average, we find $\tau_{ST}^0/I \approx 2.8 \pm 0.6$ mT/mA. By using the formula $J_S = 2eM_S t\tau_{ST}^0/\hbar$ with saturation magnetization $M_S = (1.1 \pm 0.2) \times 10^6$ A/m and CoFeB film thickness $t = 1.0 \pm 0.1$ nm, we obtain $J_S/J_e = 0.12 \pm 0.03$ for the 4-nm Ta layer, consistent with the value $J_S/J_e = 0.15 \pm 0.03$ from the ST-FMR study for an 8-nm Ta layer. Here, we assume a uniform current density throughout both the Ta and CoFeB layers, because their resistivities are similar: $\rho_{Ta} \approx 190$ microhm·cmm and $\rho_{CoFeB} \approx 170$ microhm·cm (32).

Spin-torque switching of an in-plane polarized magnet using a three-terminal spin Hall device. The giant SHE in Ta, together with its small effect on the damping of adjacent magnetic layers, makes Ta an excellent material for effecting ST switching of an in-plane magnetized nanomagnet. In conventional antidamping ST switching where the spins are injected either nearly parallel or antiparallel to the initial orientation of the local magnetic moment, the critical current density for switching in the absence of thermal fluctuations is given by (3, 33)

$$J_{C0} \approx \frac{2e}{\hbar}\mu_0 M_S t\alpha(H_C + M_{eff}/2)/(J_S/J_e) \quad (1)$$

where H_C represents the coercive field of the FM nanomagnet.

To demonstrate in-plane magnetic switching induced by the SHE, we fabricated a three-terminal device, consisting of the multilayer substrate/Ta(6.2)/$Co_{40}Fe_{40}B_{20}$(1.6)/MgO(1.6)/CoFeB(3.8)/Ta(5)/Ru(5) (thicknesses in nanometers) patterned (32) into the geometry shown in Fig. 3A. The Ta bottom layer was patterned into a 1-μm-wide, 5-μm-long strip (with resistance 3 kilohm), and the rest of the layers were etched to form a MTJ nanopillar on top of the Ta with lateral dimensions ~100 by 350 nm and with the long axis of the nanopillar perpendicular to the long axis of the Ta microstrip.

The magnetoresistance response of one of these MTJs is shown in Fig. 3B, which indicates a coercive field $B_C \approx 4$ mT, a zero-bias MTJ resistance $R_{MTJ} \approx 65$ kilohm, and a tunneling magnetoresistance (TMR) ≈ 50%. During subsequent magnetic switching measurements, we applied a –3.5-mT in-plane magnetic field along the long axis of the MTJ to cancel the dipole field from the top layer of the MTJ acting on the bottom layer and, thus, biased the junction at the midpoint of its minor magnetoresistance loop. We then applied a dc current I_{Ta} to the Ta microstrip while monitoring the differential resistance dV/dI of the MTJ (Fig. 3A). Figure 3C shows that abrupt hysteretic switching of the MTJ resistance occurred when I_{Ta} was swept through 1 mA, which resulted in antiparallel to parallel (AP-P) switching, and then this switching was reversed (P-AP switching) when the current was swept back past –1 mA.

We have considered other potential mechanisms for this switching besides the SHE-ST. The Oersted field generated by the current can be ruled out because it has the polarity to oppose the switching that we observe, and it is small [0.7 mT at 1 mA (32)] relative to the coercive field. We can also rule out the effect of any in-plane Rashba field (30, 34) that might be generated by I_{Ta}, because we measured the switching phase diagram of our three-terminal devices as the function of current and applied in-plane magnetic field (fig. S4) (32). The result is as expected for thermally assisted antidamping ST switching (35) and is inconsistent with switching resulting from any type of current-generated effective field. In addition, the direction that has been reported (36) for the in-plane Rashba field in a Ta/CoFeB/MgO multilayer, if it exists, is the same as the Oersted field and would therefore also act to oppose the switching that we observe. We conclude that the switching we measure is indeed the result of the ST exerted on the bottom MTJ electrode by the transverse spin current from the giant SHE in Ta.

By varying the current ramp rate (Fig. 3D) and using the standard model for thermally activated ST switching (35), we determined both the zero–thermal-fluctuation ST critical currents and the energy barriers for the thermally activated AP-P and P-AP transitions. We found the two critical currents ($|I_{c0}| = 2.0 \pm 0.1$ mA) and energy barriers [$U = 45.7 \pm 0.5k_BT$ (k_B, the Boltzmann constant; T, temperature)] to be essentially the same. The latter is not surprising, but the former, although consistent with a SHE origin, is distinctly different from the case for ST switching by the spin-polarized current generated by spin filtering within a spin valve or MTJ, where, in general,

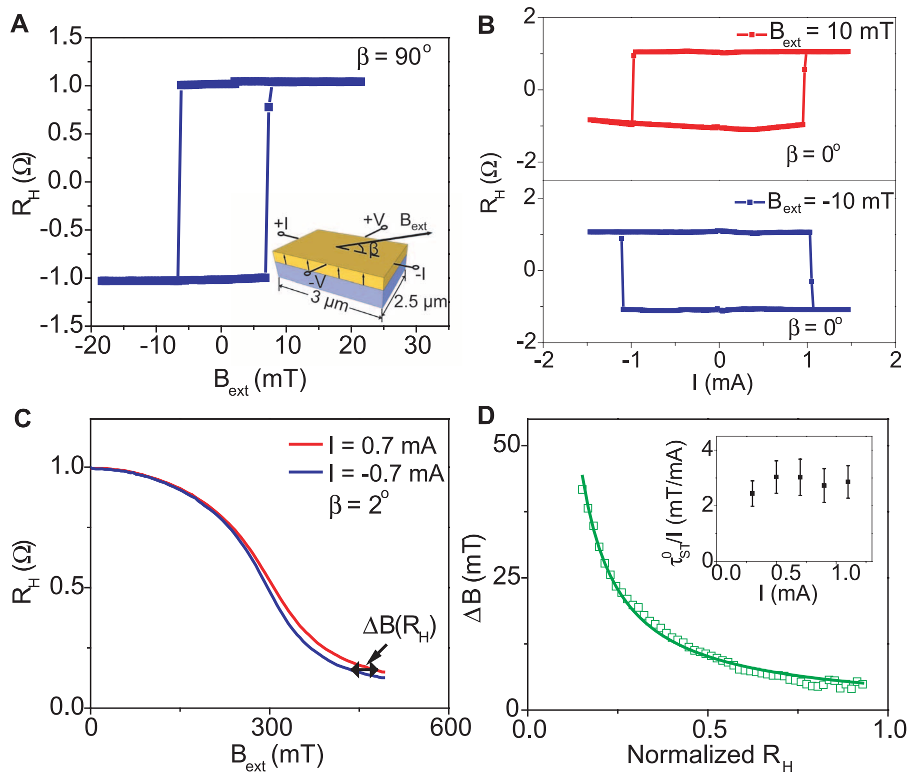

Fig. 2. Spin Hall effect–induced magnetic switching in a perpendicularly magnetized Ta/CoFeB/MgO/Ta film at room temperature. (**A**) The anomalous Hall resistance R_H as a function of magnetic field when B_{ext} is applied along the easy axis (perpendicular to the film plane). (Inset) Device geometry used for the measurement. B_{ext} is applied in the plane defined by the direction of current flow and the normal vector to the sample plane. β is the angle between the direction of B_{ext} and the applied current. (**B**) Current-induced switching when B_{ext} is parallel (top) or antiparallel (bottom) to the current direction defined as in the inset to (A). In both panels, β = 0°. (**C**) R_H versus B_{ext} determined experimentally when the field is applied at the angle β = 2°. Constant currents of ±0.7 mA were applied to the sample while sweeping the field. (**D**) $\Delta B(R_H)$ as determined from the difference of the two data sets in (C). The green curve is a fit to the macrospin model. (Inset) Values of τ_{ST}^0/I determined at different bias currents.

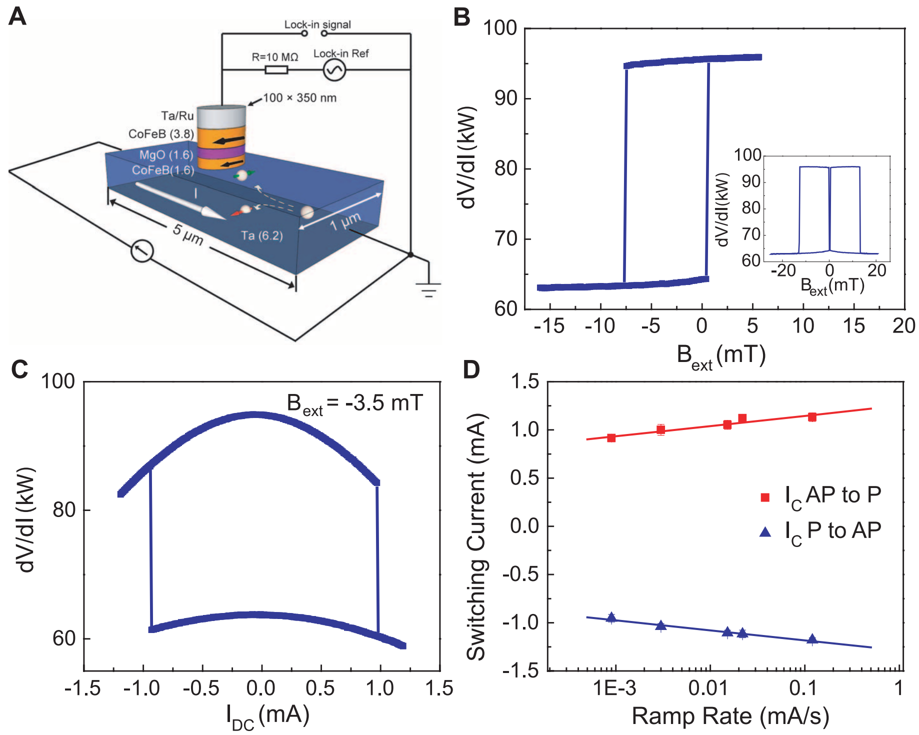

Fig. 3. Spin Hall effect–induced switching for an in-plane magnetized nanomagnet at room temperature. (**A**) Schematic of the three-terminal SHE devices and the circuit for measurements. The direction of the spin Hall spin transfer torque is not the same as in Fig. 1A because the CoFeB layer now lies above the Ta rather than below. (**B**) TMR minor loop of the MTJ as a function of the external applied field B_{ext} applied in-plane along the long axis of the sample. (Inset) TMR major loop of the device. (**C**) TMR of the device as a function of applied dc current I_{DC}. An in-plane external field of –3.5 mT is applied to set the device at the center of the minor loop. (**D**) Switching currents as a function of the ramp rate for sweeping current. Red squares indicate switching from AP to P; blue triangles indicate switching from P to AP. Solid lines represent linear fits of switching current versus log(ramp rate). Error bars are smaller than the symbol size.

$|I_{c0,P\text{-}AP}| \neq |I_{c0,AP\text{-}P}|$ due to spin accumulation in the spin valve and the MTJ magnetoresistance behavior, respectively. The equivalence of the two critical currents for a SHE-ST switching device could be a major technical advantage. From our measured values of $|I_{c0}|$ and using Eq. 1 with $\mu_0 M_{eff}$ = 0.76 T (*32*), we determine J_S/J_e for this device to be 0.12 ± 0.04 (*32*), in accord with our two other spin Hall angle measurements. We note that our three determinations of J_S/J_e are consistent for FM layer thicknesses ranging from 1 to 4 nm and are not sensitive to whether the FM layer is magnetized in plane or out of plane.

Technology applications. Improvements to this initial three-terminal SHE device can be very reasonably expected to result in substantial reductions in the switching currents for thermally stable nanomagnets. By reducing the width of the Ta microstrip to be equal to the dimension of the long axis of the nanopillar, we can easily decrease I_{c0} by a factor of 3 without affecting thermal stability. A further reduction in I_{c0} could be achieved by reducing the demagnetization field of the FM free layer from 700 mT to ≤100 mT (*37*, *38*). With such improvements, I_{c0} could be reduced to <100 μA, at which point the three-terminal SHE devices would be competitive with the efficiency of conventional ST switching in optimized MTJs (*31*, *33*, *39*) while providing the added advantage of a separation between the low-impedance switching (write) process and high-impedance sensing (read) process. This separation solves the reliability challenges that presently limit applications based on conventional two-terminal MTJs while also giving improved output signals. Other three-terminal spin-torque devices based on conventional spin-filtering have been demonstrated previously (*40*–*43*), but the SHE-ST design can provide better spin-torque efficiency and is much easier to fabricate. Moreover, the discovery of materials with even larger values of the spin Hall angle than in β-Ta could also add to the competitiveness of the SHE-ST.

References and Notes

1. J. C. Slonczewski, *J. Magn. Magn. Mater.* **159**, L1 (1996).
2. L. Berger, *Phys. Rev. B* **54**, 9353 (1996).
3. J. A. Katine, F. J. Albert, R. A. Buhrman, E. B. Myers, D. C. Ralph, *Phys. Rev. Lett.* **84**, 3149 (2000).
4. S. I. Kiselev *et al.*, *Nature* **425**, 380 (2003).
5. D. C. Ralph, M. D. Stiles, *J. Magn. Magn. Mater.* **320**, 1190 (2008).
6. M. I. Dyakonov, V. I. Perel, *Phys. Lett. A* **35**, 459 (1971).
7. J. E. Hirsch, *Phys. Rev. Lett.* **83**, 1834 (1999).
8. S. F. Zhang, *Phys. Rev. Lett.* **85**, 393 (2000).
9. J. Sinova *et al.*, *Phys. Rev. Lett.* **92**, 126603 (2004).
10. S. Murakami, N. Nagaosa, S.-C. Zhang, *Science* **301**, 1348 (2003).
11. Y. K. Kato, R. C. Myers, A. C. Gossard, D. D. Awschalom, *Science* **306**, 1910 (2004).
12. S. O. Valenzuela, M. Tinkham, *Nature* **442**, 176 (2006).
13. Y. Kajiwara *et al.*, *Nature* **464**, 262 (2010).
14. L. Q. Liu, O. J. Lee, T. D. Gudmundsen, D. C. Ralph, R. A. Buhrman, http://arXiv.org/abs/1110.6846.
15. M. H. Read, C. Altman, *Appl. Phys. Lett.* **7**, 51 (1965).
16. R. Hoogeveen, M. Moske, H. Geisler, K. Samwer, *Thin Solid Films* **275**, 203 (1996).
17. T. Tanaka *et al.*, *Phys. Rev. B* **77**, 165117 (2008).
18. M. Morota *et al.*, *Phys. Rev. B* **83**, 174405 (2011).
19. L. Q. Liu, T. Moriyama, D. C. Ralph, R. A. Buhrman, *Phys. Rev. Lett.* **106**, 036601 (2011).
20. L. Q. Liu, R. A. Buhrman, D. C. Ralph, http://arXiv.org/abs/1111.3702.
21. T. Kimura, Y. Otani, T. Sato, S. Takahashi, S. Maekawa, *Phys. Rev. Lett.* **98**, 156601 (2007).
22. K. Ando *et al.*, *Phys. Rev. Lett.* **101**, 036601 (2008).
23. O. Mosendz *et al.*, *Phys. Rev. Lett.* **104**, 046601 (2010).
24. O. Mosendz *et al.*, *Phys. Rev. B* **82**, 214403 (2010).
25. B. Gu *et al.*, *Phys. Rev. Lett.* **105**, 216401 (2010).
26. The antisymmetric peaks shown here for these two samples are opposite to what was illustrated in (*20*) for a substrate/Pt/Permalloy sample, because the relative order of the FM/nonmagnetic layers was reversed in that case.
27. S. Mizukami, Y. Ando, T. Miyazaki, *J. Magn. Magn. Mater.* **226–230**, 1640 (2001).
28. Y. Tserkovnyak, A. Brataas, G. E. W. Bauer, *Phys. Rev. Lett.* **88**, 117601 (2002).
29. H. Lee *et al.*, *J. Phys. D* **41**, 215001 (2008).
30. I. M. Miron *et al.*, *Nature* **476**, 189 (2011).
31. S. Ikeda *et al.*, *Nat. Mater.* **9**, 721 (2010).
32. Supplementary materials are available on *Science* Online.
33. J. Z. Sun, *Phys. Rev. B* **62**, 570 (2000).
34. I. M. Miron *et al.*, *Nat. Mater.* **9**, 230 (2010).
35. E. B. Myers *et al.*, *Phys. Rev. Lett.* **89**, 196801 (2002).
36. T. Suzuki *et al.*, *Appl. Phys. Lett.* **98**, 142505 (2011).
37. L. Q. Liu, T. Moriyama, D. C. Ralph, R. A. Buhrman, *Appl. Phys. Lett.* **94**, 122508 (2009).
38. T. Moriyama *et al.*, *Appl. Phys. Lett.* **97**, 072513 (2010).
39. T. Kishi *et al.*, in *Proceedings of the IEEE International Electron Devices Meeting 2008*, San Francisco, 15 to 17 December 2008 (IEEE, New York, 2008); 10.1109/IEDM.2008.4796680.
40. T. Kimura, Y. Otani, J. Hamrle, *Phys. Rev. Lett.* **96**, 037201 (2006).
41. T. Yang, T. Kimura, Y. Otani, *Nat. Phys.* **4**, 851 (2008).
42. J. Z. Sun *et al.*, *Appl. Phys. Lett.* **95**, 109901 (2009).
43. P. M. Braganca *et al.*, *IEEE Trans. NanoTechnol.* **8**, 190 (2009).

Acknowledgments: We acknowledge support from the Army Research Office, Defense Advanced Research Projects Agency, Office of Naval Research, and NSF/Materials Research Science and Engineering Center (DMR-1120296) through the Cornell Center for Materials Research (CCMR), as well as the NSF/Nanoscale Science and Engineering Center Program through the Cornell Center for Nanoscale Systems. We also acknowledge NSF support through use of the Cornell Nanofabrication Facility/National Nanofabrication Infrastructure Network and the CCMR facilities. Patent disclosures have been filed on behalf of the authors regarding the use of the spin Hall effect in Ta for magnetic memory and logic applications.

Supplementary Materials

www.sciencemag.org/cgi/content/full/336/6081/555/DC1
Materials and Methods
Supplementary Text
Figs. S1 to S5
Reference (*44*)

20 December 2011; accepted 29 March 2012
10.1126/science.1218197

Spin-Orbital Short-Range Order on a Honeycomb-Based Lattice

S. Nakatsuji,[1]* K. Kuga,[1] K. Kimura,[1] R. Satake,[2] N. Katayama,[2] E. Nishibori,[2] H. Sawa,[2] R. Ishii,[3] M. Hagiwara,[3] F. Bridges,[4] T. U. Ito,[5] W. Higemoto,[5] Y. Karaki,[6] M. Halim,[7] A. A. Nugroho,[7] J. A. Rodriguez-Rivera,[8,9] M. A. Green,[8,9] C. Broholm[8,10]

Frustrated magnetic materials, in which local conditions for energy minimization are incompatible because of the lattice structure, can remain disordered to the lowest temperatures. Such is the case for $Ba_3CuSb_2O_9$, which is magnetically anisotropic at the atomic scale but curiously isotropic on mesoscopic length and time scales. We find that the frustration of Wannier's Ising model on the triangular lattice is imprinted in a nanostructured honeycomb lattice of Cu^{2+} ions that resists a coherent static Jahn-Teller distortion. The resulting two-dimensional random-bond spin-1/2 system on the honeycomb lattice has a broad spectrum of spin-dimer–like excitations and low-energy spin degrees of freedom that retain overall hexagonal symmetry.

The realization of quantum-correlated matter beyond one dimension has been vigorously pursued in geometrically frustrated spin systems for decades (*1*, *2*). However, very few of a rich variety of theoretically predicted phases (*3*–*6*) have so far been experimentally observed (*7*–*10*). A persistent challenge is symmetry breaking of orbital and chemical origin leading to semiclassical spin freezing. We present the case of $Ba_3CuSb_2O_9$ where, by contrast, chemical and orbital nanostructure conspire to produce a unique quantum-correlated state of matter.

Our comprehensive experimental analysis reveals that the geometrical frustration of Wannier's Ising antiferromagnet (*11*) on a triangular lattice can be exploited to build a nanostructured bipartite honeycomb lattice from electric dipolar spin-1/2 molecules. Despite a strong local Jahn-Teller (JT) distortion about the Cu^{2+} ion, the resulting spin-orbital, random-bond lattice not only retains hexagonal symmetry averaged over time and space, but it supports a gapless excitation spectrum without spin freezing down to ultralow temperatures.

Figure 1A shows the structure of $Ba_3CuSb_2O_9$ at room temperature (T) as determined by synchrotron x-ray and neutron diffraction from single crystals and powder samples; the refinement yields a centrosymmetric ($P6_3/mmc$) structure in which the two central sites of the face-sharing octahedra are symmetrically equivalent and equally occupied

[1]Institute for Solid State Physics, University of Tokyo, Kashiwa, Chiba 277-8581, Japan. [2]Department of Applied Physics, Graduate School of Engineering, Nagoya University, Nagoya 464-8603, Japan. [3]KYOKUGEN, Osaka University, Toyonaka, Osaka 560-8531, Japan. [4]Physics Department, University of California, Santa Cruz, CA 95064, USA. [5]Advanced Science Research Center, Japan Atomic Energy Agency, Tokai, Ibaraki 319-1195, Japan. [6]Faculty of Education, University of the Ryukyus, Nishihara, Okinawa 903-0213, Japan. [7]Faculty of Mathematics and Natural Sciences, Institut Teknologi Bandung, Jl. Ganesha 10, Bandung 40132, Indonesia. [8]NIST Center for Neutron Research, National Institute of Standards and Technology, Gaithersburg, MD 20899, USA. [9]Department of Materials Science and Engineering, University of Maryland, College Park, MD 20742, USA. [10]Institute for Quantum Matter (IQM) and Department of Physics and Astronomy, Johns Hopkins University, Baltimore, MD 21218, USA.

*To whom correspondence should be addressed. E-mail: satoru@issp.u-tokyo.ac.jp

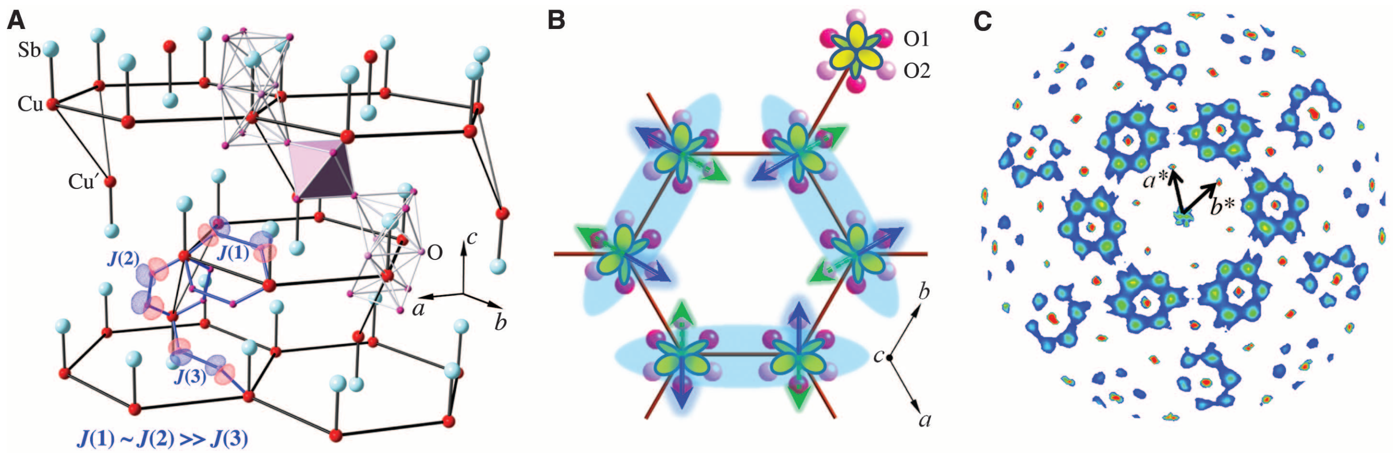

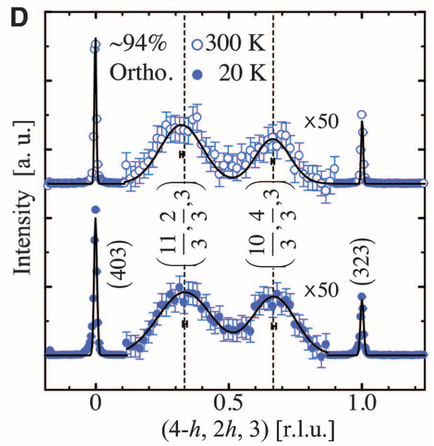

Fig. 1. (**A**) Centrosymmetric $P6_3/mmc$ high-T structure of $Ba_3CuSb_2O_9$ indicating nanoscale Cu-Sb dumbbell ordering. Ba ions are omitted for clarity. See fig. S1 for the complete structure. Oxygen 2p orbitals (shaded blue and red) associated with superexchange interactions $J(1)$ to $J(3)$ are indicated. $J(1)$ and $J(2)$ have a nearly equivalent superexchange path consisting of O 2p–2p transfer of $\sim(-pp\sigma + pp\pi)/\sqrt{2}$; $J(3)$ is much weaker because it is associated with O 2p–2p transfer of $\sim -pp\pi/\sqrt{2}$. (**B**) A characteristic vertex with spin-orbital degrees of freedom for the Cu-honeycomb lattice of $Ba_3CuSb_2O_9$. A trigonal coverage of a Cu-hexagon by spin singlets (pair of blue or green arrows) based on a $d_{x^2-y^2}$ ferro-orbital (green) state at two Cu sites (blue shaded) is shown. There are two different sites for oxygen in the CuO_6 octahedra, O1 (purple) and O2 (light purple), with different heights, z (fig. S1). Coupling through the Cu-O1-O1-Cu superexchange path allows resonance between singlets and is absent in the uniform $d_{x^2-y^2}$ order of the orthorhombic phase. (**C**) Superstructure peaks found in an (h k 10) slice extracted from a 3D volume of synchrotron x-ray diffraction data at 20 K for an orthorhombic single-crystalline sample (*12*). (**D**) Intensity profiles at 20 and 300 K along the (4–h, 2h, 3) direction for an orthorhombic single-crystalline sample indicating temperature-independent broad superlattice peaks between integer Miller index resolution-limited Bragg peaks (*12*). Error bars indicate SE; r.l.u., reciprocal lattice unit.

by Cu and Sb ions (Fig. 1 and figs. S1 to S3) (*12*). This differs from the previously reported noncentrosymmetric ($P6_3mc$) structure (*13*, *14*). The key units of this 6H perovskite structure are $CuSbO_9$ (Cu-Sb "dumbbells") with a threefold axis oriented along **c** and connected through corner-sharing SbO_6 octahedra and Ba counterions. Our extended x-ray absorption fine structure (EXAFS) measurements show that >95% of the face-sharing octahedral sites are Cu-Sb dumbbells and place an upper limit of 5% on face-sharing Cu-Cu pairs.

Because of the charge difference between Cu^{2+} and Sb^{5+}, Cu-Sb dumbbells carry an electric dipole moment. The previously reported structure found uniform pyroelectric ordering of Cu-Sb dumbbells along **c** (*13*, *14*); however, our measurement of the *T*-dependent pyroelectric current in $Ba_3CuSb_2O_9$ places a strict limit of 0.9 $\mu C/m^2$ K on pyroelectricity below 300 K (fig. S4) (*12*). In addition, scanning microscope second-harmonic generation (SHG) measurements (*15*) confirmed the absence of average polarization over a sampling volume of ~1 μm by 1 μm by 50 μm. These results indicate staggered Cu-Sb dumbbells and cancellation of the electric polarization.

In addition, our single-crystal x-ray diffraction patterns (Fig. 1, C and D) show strong, temperature-independent, diffuse scattering that is offset by (1/3, 1/3, 0) from reciprocal lattice points. This indicates three-sublattice, ferrielectric short-range order of Cu-Sb dumbbell orientations (up/down) in the *ab* plane (Fig. 1A). The broad superlattice peaks indicate isotropic ~10 Å domains consistent with the absence of SHG (*12*). We propose that this unusual chemical short-range order is formed as a result of frustrated electric dipole-dipole interactions between Cu-Sb dumbbells that emulate Ising spins on a triangular lattice (*11*). This short-range order in turn freezes in place as the material is cooled in the solid-state synthesis process.

The dominant superexchange interactions in the resulting structure are associated with Cu-O-O-Cu pathways. Among three variants, we anticipate the in-plane *J*(1) and out-of-plane *J*(2) interactions (Fig. 1A) to be the largest, thanks to the σ bonding component of O 2p-2p hybridization. For neighboring Cu-Sb dumbbells of opposite orientations, the putative superexchange interaction *J*(3) between nearest neighbor Cu^{2+} again has a Cu-O-O-Cu path. However, in this case, the absence of O-O σ bonding (Fig. 1A) indicates *J*(3) is at least one order of magnitude smaller than *J*(1) and *J*(2). The result of this is a quasi–two-dimensional spin orbital system in which interacting Cu^{2+} atoms form a honeycomb lattice with identical nearest-neighbor interactions, *J*(1). The characteristic spin orbital configuration is illustrated in Fig. 1B. An out-of-plane Cu′ site forms a magnetically frustrated isosceles spin triangle with two members of each hexagonal ring through an exchange interaction *J*(2) (Fig. 1A and fig. S2).

The threefold rotation axis for Cu^{2+} at room *T* suggests degenerate e_g orbitals and thus, instability toward a static JT distortion. Indeed, samples where the Sb/Cu stoichiometry differs from 2/1 by

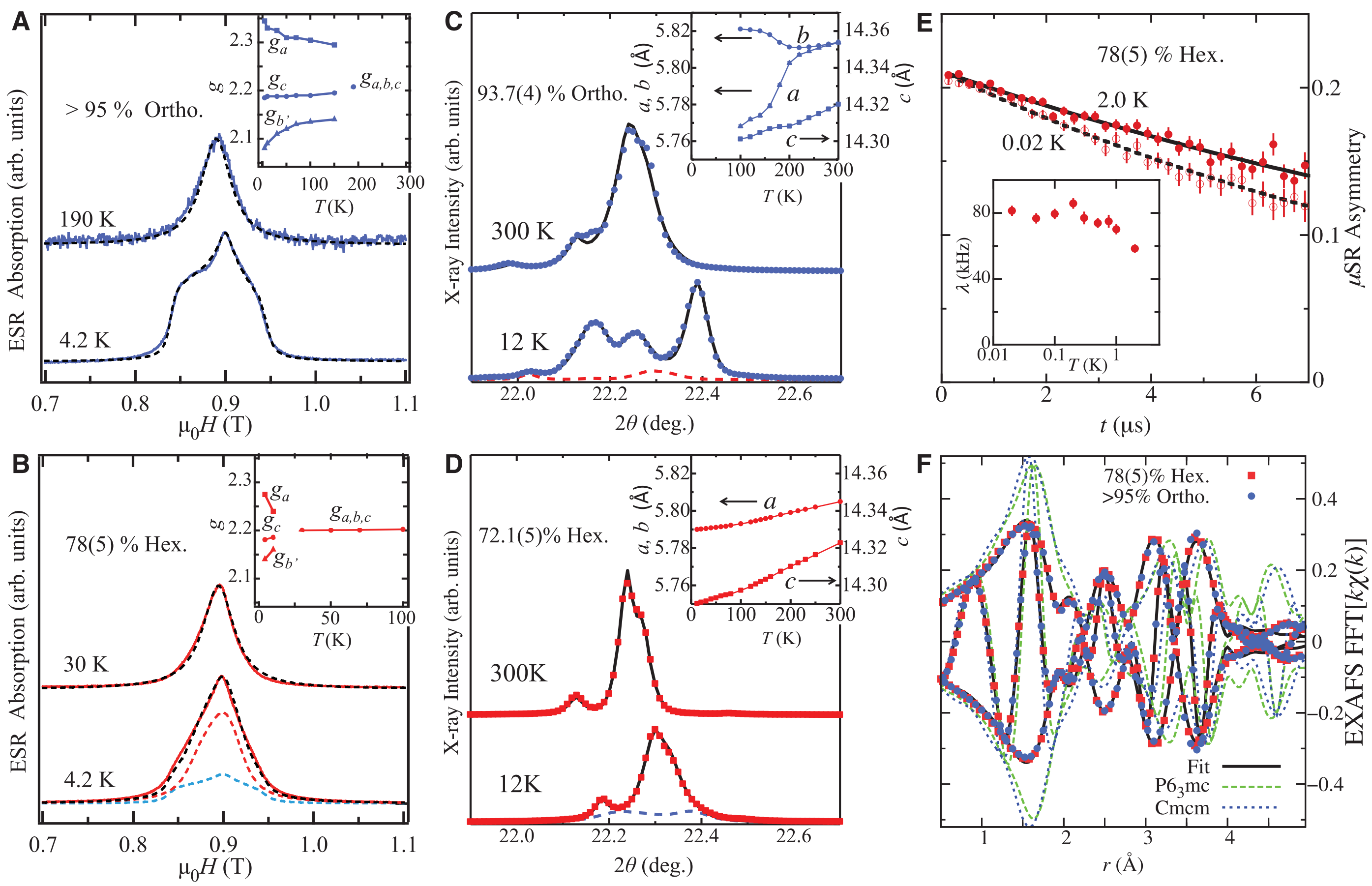

Fig. 2. K-band ESR spectra obtained at 27.5 GHz for (**A**) orthorhombic and (**B**) hexagonal powder samples. Dashed lines indicate the results of ESR powder pattern simulation (*12*). Red and blue dashed lines in (B) are simulation results for the hexagonal and the orthorhombic phases, respectively; dashed black line in (B) is formed by their superposition. X-ray spectra for (**C**) orthorhombic and (**D**) hexagonal samples. Solid curves, simulated pattern by Rietveld analysis. The blue dashed line indicates the minority phase spectrum at *T* = 12 K. (Insets) *T*-dependent *g*-factors and lattice parameters. For the orthorhombic phase, we plot the quasi-trigonal lattice parameter given by $b = \sqrt{(a/2)^2 + (b'/2)^2}$. (**E**) Zero-field μSR data for a hexagonal sample. (**F**) EXAFS fast Fourier transformed data at 10 K for an orthorhombic (blue circles) and a hexagonal sample (red squares). The solid black line is a fit up to 4 Å (*12*). The dashed green line is a simulation based on a $P6_3mc$ structure (*13*), whereas the blue dotted line is a simulation based on *Cmcm* from high-resolution x-ray diffraction (*12*). In each panel, the volume fraction of the majority phase determined by x-ray diffraction at 12 K is indicated.

~10% display a hexagonal-to-orthorhombic JT type transition for $T \sim 200$ K, which is broadened by short-range dumbbell order. Figure 2C shows the corresponding splitting of the ($\bar{3}$ 0 0) Bragg peak at low T (strain $\varepsilon_{JT} \equiv \delta a/a = 1.0\%$, where a is the in-plane lattice constant). Such nonstoichiometric samples where a volume fraction (>90%) becomes orthorhombic at low T's, shall henceforth be labeled orthorhombic. Structural refinement based on low-T single-crystal synchrotron diffraction data for the orthorhombic samples yields four short [$d_s = 2.038(3)$ Å, where the number in parentheses indicates SE of 0.0003 Å] and two long [$d_l = 2.246(5)$ Å] Cu-O bond lengths, consistent with a uniform $d_{x^2-y^2}$ orbital state and static JT distortion of the CuO_6 octahedra (*12*).

Correspondingly, K-band electron spin resonance (ESR) spectra of powdered orthorhombic $Ba_3CuSb_2O_9$ at 4.2 K indicate local g-factor anisotropy with $g_a = 2.35$, $g_{b'} = 2.08$, and $g_c = 2.19$ (Fig. 2A). Here a, b', and c are the orthogonal axes of the orthorhombic structure. The T dependence of g and the lattice parameters (insets to Fig. 2, A and C) confirms the development of static JT distortions for $T_{JT} \sim 190$ K. A specific heat peak was also detected around T_{JT} in crystalline samples with an orthorhombic volume fraction beyond 90% (fig. S5) (*12*).

In contrast, for samples with the stoichiometric Cu/Sb ratio, our synchrotron x-ray diffraction data find the majority phase to be hexagonal to the lowest $T = 12$ K (Fig. 2D), and K-band ESR data show no broadening down to $T = 30$ K (Fig. 2B). For $T < 30$ K, subtle deviations from a symmetric Lorentzian are consistent with remnants of the JT-distorted orthorhombic phase and reduced g-factor anisotropy ($g_a = 2.28$, $g_{b'} = 2.14$, $g_c = 2.18$) as might arise from a dynamic JT effect (*16*) or symmetry-breaking short-range $\sqrt{3} \times \sqrt{3}$ order.

Hexagonal and orthorhombic samples are, however, indistinguishable on the ~10^{-16}-s time scale probed by EXAFS. Both feature a large JT-like distortion of the CuO_6 octahedra (Fig. 2F) (*12*). Possible explanations for the isotropic ESR signal in hexagonal samples include the following: (i) Spatial averaging. The coherent ESR resonance may sample superexchange-linked spin clusters (such as the hexagonal ring in Fig. 1B) with approximate trigonal symmetry. (ii) Temporal averaging. Orbital fluctuations may restore trigonal symmetry on the ESR time scale. (iii) Spatiotemporal averaging, a combination of (i) and (ii). We examine the magnetism of $Ba_3CuSb_2O_9$ to distinguish these scenarios.

Figure 3A shows the T dependence of the inverse dc susceptibility of both orthorhombic single crystals and hexagonal polycrystalline samples. Similar data were recently reported as possible evidence for spin liquid formation on a triangular lattice in $Ba_3CuSb_2O_9$ (*14*). The approximate data collapse indicates magnetic isotropy. Curie-Weiss fitting in the hexagonal phase for 300 K < T < 600 K consistently yields $P_{eff} = 1.87\mu_B$ (where P_{eff} is effective moment and μ_B is the Bohr magneton) and $g \approx 2.15$ for poly- and single-crystalline samples. The antiferromagnetic Weiss T is $\Theta_W = -47$ K for polycrystals and $\Theta_W = -42$ K for both field directions in single crystals (where Θ_W is the Curie-Weiss temperature). By using $\Theta_W = [(-z)/3]JS(S+1)$, where $-z = 10/3$ is the average coordination number on the decorated honeycomb lattice and $S = 1/2$ is the spin quantum number, we extract an average of $J(1)$ and $J(2) \approx 54$ K, which is typical for Cu-O-O-Cu superexchange (*17*).

At lower T, the inverse susceptibility shows nearly isotropic Curie behavior; the ratio of the Curie constant to its value at high T is about 1/4 for polycrystalline samples and varies between 1/4 and 1/3 for single crystals (*12*). This Curie tail is reminiscent of "orphan" spins in geometrically frustrated magnets (*18*, *19*). The associated isotropic ESR response indicates that these are distributed over multiple sites or associated with orbital fluctuations corresponding to spatial or temporal averaging over the potentially fluctuating anisotropic local environment. Upon further cooling, a cusp in ac susceptibility indicates spin freezing at $T_f = 110$ mK (Fig. 3A, inset). The reduced magnitude of this peak in predominantly hexagonal samples indicates that it could arise from an orthorhombic minority phase, which Rietveld refinement of x-ray powder diffraction data finds present in proportions consistent with such an interpretation.

After subtraction of the predominant lattice contribution, the T dependence of the electronic specific heat C_M for samples with varying hexagonal/orthorhombic phase content is shown in Fig. 3B (*12*). For all samples, C_M remains large (~ 0.3 J/mol-Cu K) at 2 K, consistent with gapless low-energy spin fluctuations. A 5-T magnetic field induces a Schottky anomaly (Fig. 3B, inset), which indicates that a significant part of

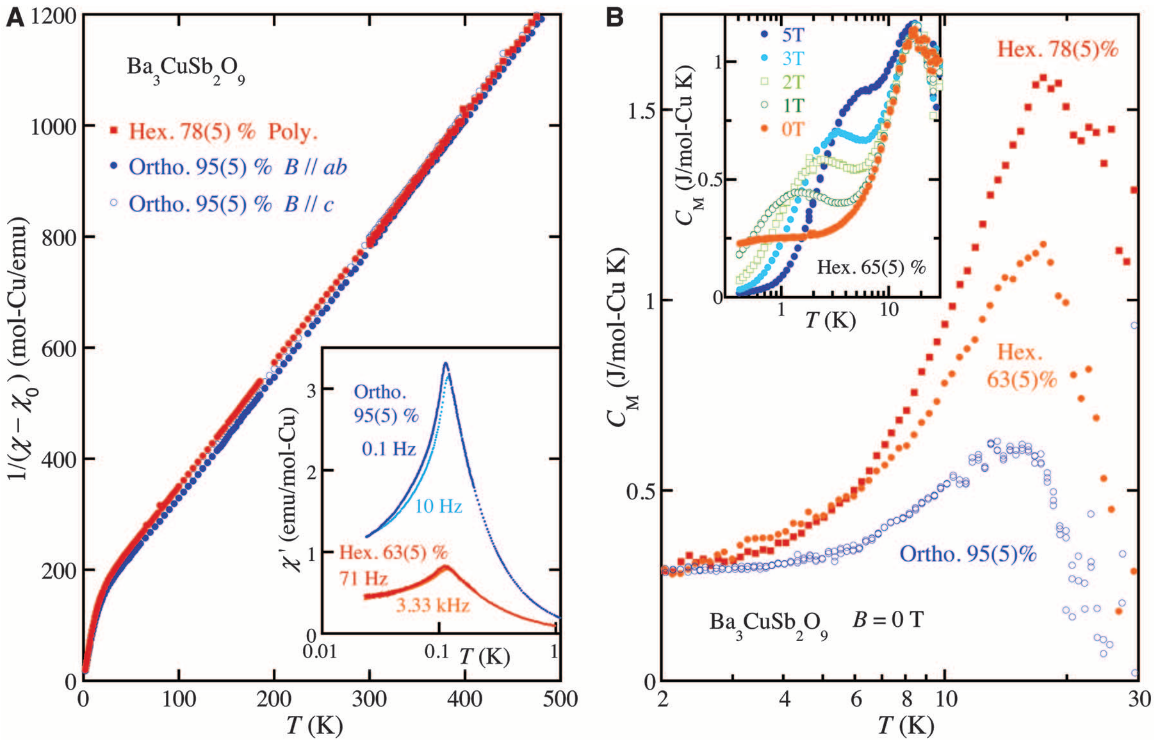

Fig. 3. (**A**) T dependence of the inverse dc susceptibility $1/(\chi - \chi_0)$ of $Ba_3CuSb_2O_9$ measured for a hexagonal polycrystalline sample and orthorhombic single crystals under fields along [100] and [001]. Here, $\chi = M/H$ (M is magnetization and H is magnetic field strength), and $\chi_0 \sim -1 \times 10^{-4}$ emu/mol-Cu is the diamagnetic contribution. (Inset) Real part of ac susceptibility data at two frequencies. (**B**) T dependence of the magnetic specific heat, $C_M(T)$. The data indicate more degrees of freedom for predominantly hexagonal over orthorhombic samples possibly associated with orbital fluctuations. (Inset) $C_M(T)$ under various fields for a hexagonal polycrystalline sample. B indicates magnetic field.

the low-T specific heat can be associated with orphan spins found in all samples. The zero-field peak at 20 K is, however, stronger for hexagonal samples, and this indicates enhanced fluctuations in an energy range that approximately matches the spin exchange constant and the pseudogap inferred from high-T susceptibility data (fig. S6) (*12*).

The spherically averaged dynamic spin correlation function $\tilde{S}(Q, \omega)$ obtained from inelastic powder neutron scattering (Fig. 4, A to C) provides direct evidence for a peak in the magnetic excitation spectrum near $J(1) \approx J(2) \approx 54$ K (Fig. 4E). Here Q and $\hbar\omega$ are wave vector and energy transfer, respectively. The Q dependence of the equal time-correlation function in Fig. 4D links this excitation with a singlet-to-triplet transition for a spin-1/2 pair with a characteristic spatial separation [$d = 5.6(1)$ Å] that is indistinguishable from the near neighbor Cu-Cu spacing (5.6 to 5.8 Å). Contrary to isolated spin pairs, the spectrum is broad and T-dependent. Even the spectral weight within our 10-meV window is T-dependent (Fig. 4E, inset) and, including estimated contributions from orphan spins in the elastic line, carries only half the spectral weight of spin-1/2 copper. The low T spectrum appears to be gapless to the 0.2-meV energy scale set by resolution; subtraction of elastic data measured at 25 K from the 1.5-K data does not show a frozen moment developing between these temperatures. Related thermomagnetic (*20*) and neutron (*21*) data were recently reported for the $S = 1/2$ double perovskite Ba_2YMoO_6.

For greater sensitivity to spin freezing, we turned to zero-field muon spin relaxation (μSR) shown (Fig. 2E). μSR spectra exhibit a single-exponential decay $\exp(-\lambda t)$ from the instrumental initial asymmetry with a nearly T-independent relaxation rate, λ, that shows no indications of freezing at $T_f = 110$ mK (inset to Fig. 2E). The size of λ is consistent with the motionally narrowed regime for Cu spin fluctuations (*12*) and a predominantly dynamic spin state in the hexagonal phase down to 20 mK. Note that conventional two-sublattice Néel order is disfavored by hexagonal close-packing interlayer frustration, which exists in $Ba_3CuSb_2O_9$ but not in magnetically ordered $Ba_3NiSb_2O_9$ (*22*).

We have shown that, despite an environment that is magnetically and structurally anisotropic on atomic time and length scales, the unit cell–averaged spin and orbital configuration for hexagonal $Ba_3CuSb_2O_9$ retains hexagonal symmetry and fails to develop a frozen moment down to low T. Thermodynamic and neutron data further show near-neighbor singlet formation is prevalent with a range of coupling strengths that peaks near $J(1) \approx J(2)$. To explain these unique features, we see two viable hypothesis distinguished by the JT time scale: (i) A static JT distortion combined with the overall hexagonal symmetry implies static orbital disorder seeded by the dumbbell disorder. In this scenario, the magnetic state might be a two-dimensional (2D) random singlet (*23*) with spin degrees of freedom that extend over spin clusters with an approximate threefold rotation axis, such as the hexagonal spin-orbital ring shown in Fig. 1B. (ii) A dynamic JT distortion, on the other hand, would involve fluctuations between three possible directions of the apical axis of distorted O^{2-} octahedra. Given the proximity of relevant spin [$J(1) \approx 50$ K] and orbital ($T_{JT} \approx 190$ K) energy scales, the latter state could involve spin-orbital entanglement (*24*–*26*), which was initially proposed for $LiNiO_2$ and $FeSc_2S_4$ (*27*, *28*). Here, magnetic correlations stabilize a symmetric and dynamic orbital state (*29*), and the ESR line remains sharp because of motional narrowing. In this scenario, the observed gapless spectra indicate long-range singlet formation with distributed orphan spins in which spin and orbital frustration associated with the isosceles Cu-Cu'-Cu triangle may play an important role.

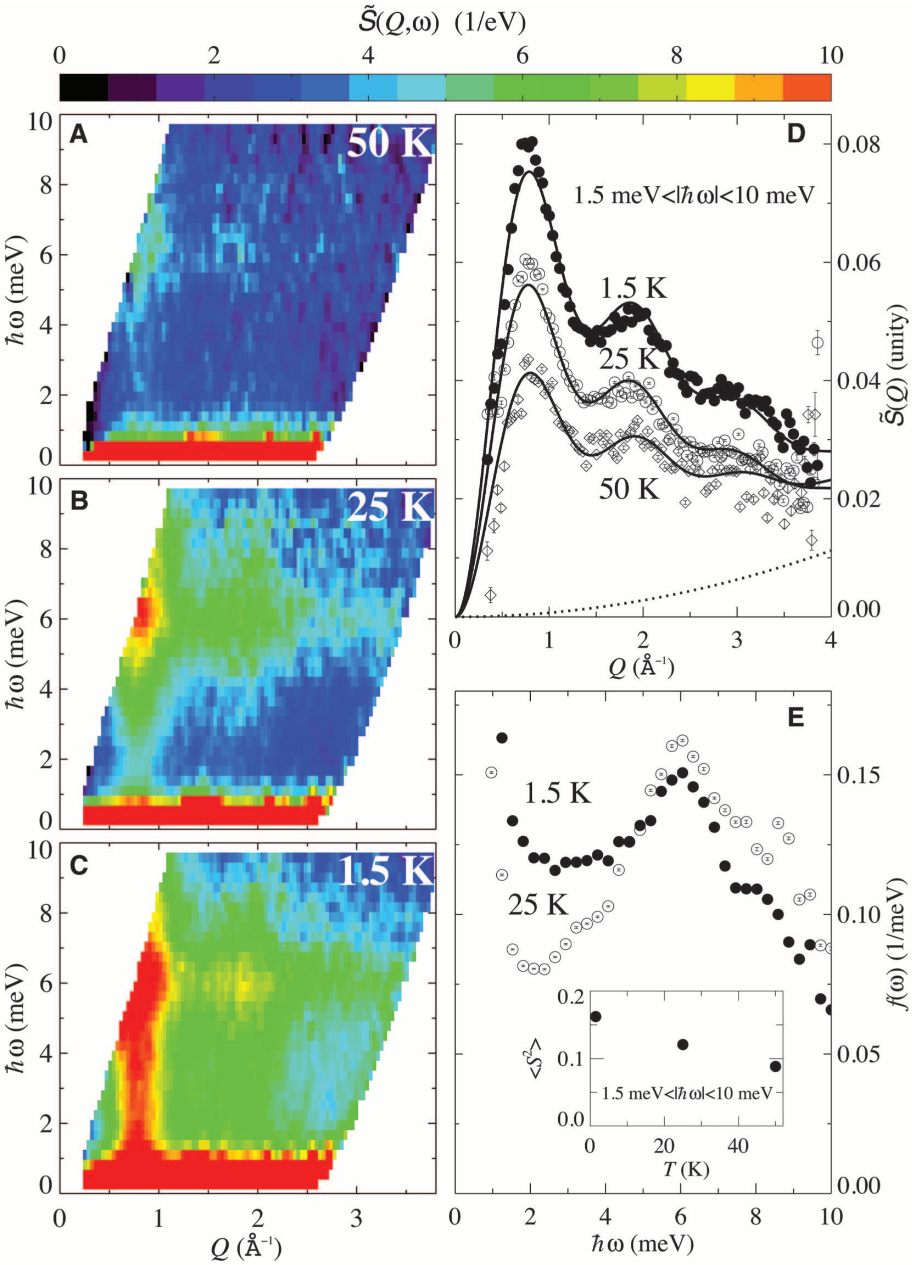

Fig. 4. (**A** to **C**) Inelastic magnetic neutron scattering from a hexagonal powder sample of $Ba_3CuSb_2O_9$ in absolute units for $T = 50$, 25, and 1.5 K (*12*). Thermal diffuse nuclear scattering inferred from 100 K data was subtracted. (**D**) Wave vector dependence inferred by averaging data from 1.5 to 10 meV under the assumption of a separable dynamic correlation function $\tilde{S}(Q,\omega) \equiv \tilde{S}(Q)f(\omega)$. Solid lines are fits to a single-dimer correlation function. The dotted line indicates an additive term in the fits to account for under subtraction of phonon scattering (*12*). The normalized spectral function, $f(\omega)$, averaged over the 1.1 Å^{-1} < Q < 1.6 Å^{-1} range is shown in (**E**). (Inset) The T dependence of the integrated magnetic scattering in absolute units for 1.5 meV < $|\hbar\omega|$ < 10 meV.

Our experiments thus far do not clearly distinguish between these two interesting scenarios; they have, however, unveiled a previously unknown route to complex structures such as the honeycomb and kagome lattices: self-assembly of magnetic molecules that carry electric dipole moments (*30*). The data also indicate that inclusion of a JT-inactive, oxygen-coordinated transition metal ion (here SbO_6) favors spin-orbital entanglement over a conventional cooperative static JT-phase transition. An unexpected outcome is the response to nanoscale disorder. Rather than forming a glassy state as in typical geometrically frustrated magnets, the spin-orbital quantum state in $Ba_3CuSb_2O_9$ is robust within linked nanoscale domains. A key question to be addressed through theory and experiments is whether a short-range dynamic spin-orbital state is a property of the bulk decorated honeycomb lattice or contingent on linked nanoscale structural domains.

References and Notes

1. P. A. Lee, *Science* **321**, 1306 (2008).
2. L. Balents, *Nature* **464**, 199 (2010).
3. S. Sachdev, *Phys. Rev. B* **45**, 12377 (1992).
4. X.-G. Wen, *Phys. Rev. B* **65**, 165113 (2002).
5. H. Morita, S. Watanabe, M. Imada, *J. Phys. Soc. Jpn.* **71**, 2109 (2002).
6. A. Kitaev, *Ann. Phys.* **321**, 2 (2006).
7. J. S. Helton *et al.*, *Phys. Rev. Lett.* **98**, 107204 (2007).
8. Y. Shimizu, K. Miyagawa, K. Kanoda, M. Maesato, G. Saito, *Phys. Rev. Lett.* **91**, 107001 (2003).
9. T. Itou, A. Oyamada, S. Maegawa, M. Tamura, R. Kato, *Phys. Rev. B* **77**, 104413 (2008).
10. M. Yamashita *et al.*, *Science* **328**, 1246 (2010).
11. G. H. Wannier, *Phys. Rev.* **79**, 357 (1950).
12. Supplementary material is available on *Science* Online.
13. V. P. Köhl, *Z. Anorg. Allg. Chem.* **442**, 280 (1978).
14. H. D. Zhou *et al.*, *Phys. Rev. Lett.* **106**, 147204 (2011).
15. J. Kaneshiro, S. Kawado, H. Yokota, Y. Uesu, T. Fukui, *J. Appl. Phys.* **104**, 054112 (2008).
16. F. S. Ham, *Phys. Rev.* **166**, 307 (1968).
17. M. Enderle *et al.*, *Europhys. Lett.* **70**, 237 (2005).
18. P. Schiffer, I. Daruka, *Phys. Rev. B* **56**, 13712 (1997).
19. A. J. Willans, J. T. Chalker, R. Moessner, *Phys. Rev. Lett.* **104**, 237203 (2010).
20. T. Aharen *et al.*, *Phys. Rev. B* **81**, 224409 (2010).
21. J. P. Carlo *et al.*, *Phys. Rev. B* **84**, 100404 (2011).
22. Y. Doi, Y. Hinatsu, K. Ohoyama, *J. Phys. Condens. Matter* **16**, 8923 (2004).
23. D. S. Fisher, *Phys. Rev. B* **50**, 3799 (1994).
24. L. F. Feiner, A. Oleś, J. Zaanen, *Phys. Rev. Lett.* **78**, 2799 (1997).
25. Y. Q. Li, M. Ma, D. N. Shi, F. C. Zhang, *Phys. Rev. Lett.* **81**, 3527 (1998).
26. F. Vernay, K. Penc, P. Fazekas, F. Mila, *Phys. Rev. B* **70**, 014428 (2004).
27. F. Reynaud *et al.*, *Phys. Rev. Lett.* **86**, 3638 (2001).
28. V. Fritsch *et al.*, *Phys. Rev. Lett.* **92**, 116401 (2004).
29. J. Nasu, A. Nagano, M. Naka, S. Ishihara, *Phys. Rev. B* **78**, 024416 (2008).
30. B. D. Metcalf, *Phys. Lett. A* **46**, 325 (1974).

Acknowledgments: We thank Y. Uesu, J. Kaneshiro, and H. Yokota for scanning SHG microscope measurements; Y. Kiuchi for ICP analysis; T. Nakano and Y. Nozue for X-band ESR measurements; and V. Thampy for assistance in neutron-scattering data analysis. We are also grateful for fruitful discussions with N. Drichko, Z. Hao, D. Hamane, S. Ishihara, M. Isobe, T. M. McQueen, T. Mizokawa, Y. Nakanishi, N. Nagaosa, S. Onoda, K. Takada, O. Tchernyshyov, Y. Wakabayashi, and J. Yamaura. This work is partially supported by Grants-in-Aid for Scientific Research from Japan Society for the Promotion of Science (JSPS) (nos. 20340089, 21684019, and 23244074) and from Ministry of Education, Culture, Sports, Science, and Technology (MEXT) on Priority Areas (nos. 19051010, 19051015, and 19052003), by Global Centers of Excellence (COE) programs “the Physical Sciences Frontier” and “Core Research and Engineering Science of Advanced Materials” MEXT, by a Toray Science and Technology grant, and by the U.S.-Japan Cooperative Program, ISSP. Work at IQM was supported by U.S. Department of Energy (DOE), Office of Basic Energy Sciences, Division of Materials Sciences and Engineering under award DE-FG02-08ER46544. This work used facilities supported in part by the NSF (no. DMR-0944772). Part of this work was conducted while C.B. was a JSPS fellow at ISSP. The x-ray diffraction experiments were carried out at SPring-8 (Super Photon ring-8 GeV). The EXAFS experiments were carried out at Stanford Synchrotron Radiation Lightsource, supported by DOE. Muon spin relaxation experiments were performed at TRIUMF (Canada’s national laboratory for particle and nuclear physics).

Supplementary Materials

www.sciencemag.org/cgi/content/full/336/6081/559/DC1
Materials and Methods
Supplementary Text
Figs. S1 to S7
Tables S1 and S2
References (*31–41*)

3 August 2011; accepted 9 March 2012
10.1126/science.1212154

Anisotropic Energy Gaps of Iron-Based Superconductivity from Intraband Quasiparticle Interference in LiFeAs

M. P. Allan,[1,2,3]* A. W. Rost,[2,3]* A. P. Mackenzie,[3] Yang Xie,[2] J. C. Davis,[1,2,3,4]† K. Kihou,[5,6] C. H. Lee,[5,6] A. Iyo,[5,6] H. Eisaki,[5,6] T.-M. Chuang[1,2,7]†

If strong electron-electron interactions between neighboring Fe atoms mediate the Cooper pairing in iron-pnictide superconductors, then specific and distinct anisotropic superconducting energy gaps $\Delta_i(\vec{k})$ should appear on the different electronic bands *i*. Here, we introduce intraband Bogoliubov quasiparticle scattering interference (QPI) techniques for determination of $\Delta_i(\vec{k})$ in such materials, focusing on lithium iron arsenide (LiFeAs). We identify the three hole-like bands assigned previously as γ, α_2, and α_1, and we determine the anisotropy, magnitude, and relative orientations of their $\Delta_i(\vec{k})$. These measurements will advance quantitative theoretical analysis of the mechanism of Cooper pairing in iron-based superconductivity.

In typical FeAs-based materials, every second As atom lies above or below the FeAs layer (Fig. 1A) so that the crystallographic unit cell, instead of being a square with an Fe atom at each corner (Fig. 1A, dashed box), is rotated by 45° and has an As at each corner (Fig. 1A, solid box). The corresponding momentum space ($\vec{k}$-space) Brillouin zone (BZ) then contains five electronic bands; the hole-like α_1, α_2, and γ bands surround the Γ point, and the electron-like β_1 and β_2 bands surround the $\tilde{M}$ point (Fig. 1B). The superconductivity derives (*1*) from a commensurate antiferromagnetic and orthorhombic “parent” state [see supplementary materials (*2*)]. The highest superconducting critical temperatures (T_c) occur when the magnetic and structural transitions are suppressed toward zero temperature. Theories describing the FeAs superconductivity can be quite complex (*1*, *3*–*9*), but they typically contain two essential ingredients: (i) the predominant superconducting order parameter (OP) symmetry is $s\pm$, that is, it has *s*-wave symmetry but changes sign between different bands; and (ii) the superconducting energy gap functions $\Delta_i(\vec{k})$ on different bands *i* are anisotropic in $\vec{k}$-space, with each exhibiting distinct 90° rotational (C_4) symmetry and a specific relationship of gap minima/maxima relative to the BZ axes. Figure 1C shows a schematic of such a situation for just two electronic bands, with contours of constant energy (CCE) for their Bogoliubov quasiparticles shown in Fig. 1D.

Although there is evidence for $s\pm$ OP symmetry (*10*, *11*), the structure of any anisotropic gaps $\Delta_i(\vec{k})$ on different bands and their relative $\vec{k}$-space orientation is an open question for virtually all iron-based superconductors (*1*). However, it is the structure of these $\Delta_i(\vec{k})$ that is crucial for understanding the pairing interactions. Thermodynamic and transport studies [which cannot reveal $\Delta_i(\vec{k})$] provide good evidence for electronic anisotropy (*1*, *12*–*14*). By contrast, almost all $\vec{k}$-space angle-resolved photoemission spectroscopy (ARPES) studies of these materials, including LiFeAs (*15*),

[1]Condensed Matter Physics and Materials Science (CMPMS) Department, Brookhaven National Laboratory, Upton, NY 11973, USA. [2]Laboratory of Solid State Physics, Department of Physics, Cornell University, Ithaca, NY 14853, USA. [3]Scottish Universities Physics Alliance (SUPA), School of Physics and Astronomy, University of St Andrews, St Andrews, Fife KY16 9SS, UK. [4]Kavli Institute at Cornell for Nanoscale Science, Cornell University, Ithaca, NY 14853, USA. [5]Institute of Advanced Industrial Science and Technology, Tsukuba, Ibaraki 305-8568, Japan. [6]Japan Science and Technology Agency (JST), Transformative Research-Project on Iron Pnictides (TRIP), Tokyo 102-0075, Japan. [7]Institute of Physics, Academia Sinica, Nankang, Taipei 11529, Taiwan.

*These authors contributed equally to this work.
†To whom correspondence should be addressed. E-mail: jcdavis@ccmr.cornell.edu (J.C.D.); chuangtm@phys.sinica.edu.tw (T.-M.C.)

have reported the $\Delta_i(\vec{k})$ to be isotropic in the k_x/k_y plane (*1*). Subsequent to our submission, however, nodeless anisotropic gaps with values spanning the range 2meV→4meV on the γ band and 5meV→6meV on the α_2 band (surrounding Γ) were reported in LiFeAs (*16*, *17*). For the electron-like pocket at $\tilde{M}$, an anisotropic 3meV→4.5meV gap is also described, but the reported $\vec{k}$-space positions of gap maxima/minima appear mutually inconsistent (*16*, *17*). High-resolution determination of $\Delta_i(\vec{k})$ should help to more accurately quantify these fundamental characteristics of the superconductivity.

Bogoliubov quasiparticle scattering interference (QPI) imaging is a suitable technique for high-resolution determination of $\Delta_i(\vec{k})$ (*18*–*24*). The scattering interference patterns can be visualized in real space ($\vec{r}$-space) using spectroscopic imaging scanning tunneling microscopy (SI-STM) in which the tip-sample differential tunneling conductance $dI/dV(\vec{r},E) \equiv g(\vec{r}, E)$ is measured as a function of location $\vec{r}$ and electron energy E. However, using QPI to determine the $\Delta_i(\vec{k})$ of iron-pnictide superconductors may be problematic because (i) the large field-of-view $g(\vec{r},E)$ imaging [and equivalent high $\vec{q}$-space resolution in $g(\vec{q},E)$] necessary to obtain $\Delta_i(\vec{k})$ is technically difficult; (ii) complex overlapping QPI patterns are expected from multiple bands; and (iii) most iron-pnictide compounds exhibit poor cleave-surface morphology. This latter point can be mitigated by using a material with a charge-neutral cleave plane (e.g., *11*). An iron-pnictide that satisfies this requirement is LiFeAs (*25*–*28*), which has a glide plane between two Li layers [(*2*), section I].

Bogoliubov QPI can be influenced by a variety of effects in the iron-pnictides (*21*–*24*). To explore the expected QPI signatures of the $\Delta_i(\vec{k})$, we consider the model two-gap structure in Fig. 1, C and D. Within one band, each energy $\Delta_1^{\min} \le E \le \Delta_1^{\max}$ at which $\Delta_1(\vec{k}) \doteq E$ picks out eight specific $\vec{k}$-space locations $\vec{k}_j(E)$. In a generalization of the "octet" model of QPI in copper-based superconductors (*18*–*20*), scattering between these $\vec{k}_j(E)$ should produce interference patterns with the seven characteristic QPI wave vectors $\vec{q}_1 \ldots\ \vec{q}_7$ shown in Fig. 1D. An equivalent set of QPI wave vectors, but now with different lengths and orientations, would be generated by a different $\Delta_2(\vec{k})$ on the second band (Fig. 1, C and D, yellow). Thus, conventional octet analysis could be challenging for a multiband anisotropic superconductor, as many intraband QPI wave vectors coincide near the center of $\vec{q}$-space.

To achieve a more robust QPI prediction, we next consider the joint-density-of-states (JDOS) approximation for the whole Bogoliubov quasiparticle spectrum (Fig. 1D). In this case, for $\Delta_1^{\min} \le E \le \Delta_1^{\max}$ within a given band (e.g., red band in Fig. 1, C and D), the tips of the "bananas" still strongly influence QPI because of the enhanced JDOS for scattering between these locations and effects inherent to the structure of the coherence factors. Figure 1E shows $g[\vec{q},E = (\Delta_{\max}+\Delta_{\min})/2]$ simulated by calculating the JDOS for a single hole-like band (red band of Fig. 1C) [(*2*), section II]. Although the JDOS approximation gives an intuitive picture of how $g(\vec{q},E)$ relates to regions of high density of states in $\vec{k}$-space, the T-matrix formalism is needed for a rigorous description (*18*–*24*). In Fig. 1F, we show a T-matrix simulation of $g[\vec{q},E = (\Delta_{\max}+\Delta_{\min})/2]$ for equivalent parameters as those in Fig. 1E [(*2*), section II]. By comparison of Fig. 1, E and F, we see that the two types of simulations are virtually indistinguishable and that the expected octet wave vectors

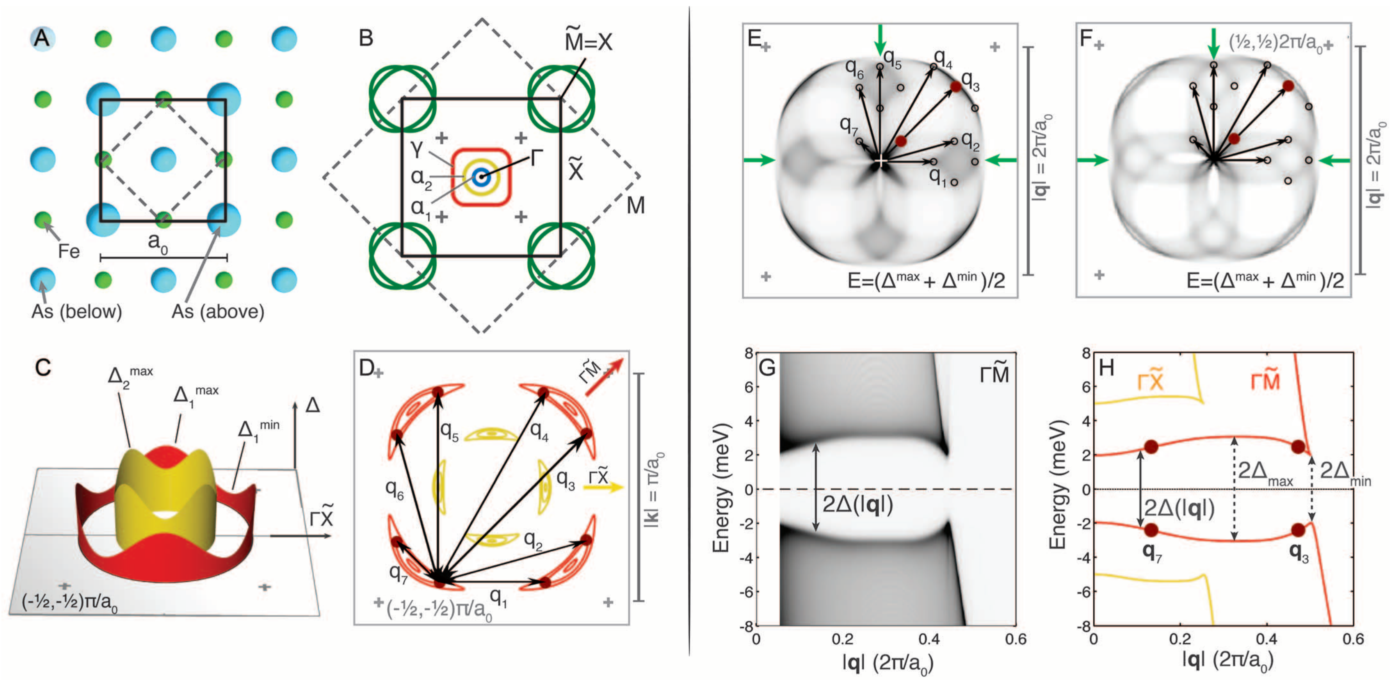

Fig. 1. (**A**) Top view of crystal structure in the FeAs plane. Dashed lines represent the one-Fe unit cell that would exist if all As were coplanar, and the actual unit cell of dimension $a_0 \approx 0.38$ nm is shown using solid lines. (**B**) Schematic Fermi surface of an iron-based superconductor like LiFeAs in the tetragonal nonmagnetic Brillouin zone (solid line). The "one-Fe zone" is shown as a dashed line. The blue, yellow, and red curves show the hole-like pockets surrounding the Γ point, and the green curves show electron pockets surrounding the $\tilde{M}$ point. The gray crosses mark the $(\pm1/2, \pm1/2)\pi/a_0$ points. (**C**) Model system exhibiting two distinct anisotropic energy gaps $\Delta_i(\vec{k})$ on two hole-like bands. (**D**) CCE of the Bogoliubov quasiparticle excitation spectrum for the two bands in (C), each in the same color as its $\Delta_i(\vec{k})$. Contours enclose diminishing areas surrounding the gap minimum in each case. Black arrows indicate the octet scattering vectors $\vec{q}_1 \ldots \vec{q}_7$ between the CCE banana tips (red dots). The red and yellow vectors indicate the high-symmetry directions along which $g(|\vec{q}|,E)$ should be measured to determine $\Delta_i(\vec{k})$ for the respective bands separately; see (H). (**E** and **F**) Theoretically simulated $g[\vec{q},E = (\Delta^{\max} + \Delta^{\min})/2]$ for a single hole-like band with band- and gap-anisotropy parameters shown in (D), using the JDOS (E) and T-matrix (F) approaches. In $\vec{q}$-space, the gray crosses occur at the $(\pm1/2, \pm1/2)2\pi/a_0$ points. The arrows show the scattering vectors $\vec{q}_1 \ldots \vec{q}_7$ from the octet model in (D). The red dots indicate the vectors that lie along $\Gamma\tilde{M}$, the direction studied in (G) and (H). (**G**) JDOS simulation of dependence of scattering intensity in $g(|\vec{q}|,E)$, with $\vec{q}$ parallel to $\Gamma\tilde{M}$ for a single hole-like band with gap anisotropy parameters shown in (C) and (D). Note the curved shapes of scattering intensity maxima, which we then extract in (H). (**H**) Red curves: Expected trajectory of maxima in scattering intensity $g(|\vec{q}|,E)$ with $\vec{q}$ parallel to $\Gamma\tilde{M}$ for h_3. Yellow curves: Expected maxima in scattering intensity $g(|\vec{q}|,E)$ with $\vec{q}$ parallel to $\Gamma\tilde{X}$ for h_2.

(overlaid by black arrows) are in excellent agreement (as is true for all $\Delta_1^{\min} \le E \le \Delta_1^{\max}$). The key QPI signatures of an anisotropic but nodeless $\Delta_i(\vec{k})$ are therefore expected to be arcs of strong scattering centered along the direction of the gap minima, with regions of minimal scattering intensity located toward the gap maxima (green arrows, Fig. 1, E and F).

The complexity of the simulated $g(\vec{q},E)$ (Fig. 1, E and F) also reveals the considerable practical challenges if measured $g(\vec{q},E)$ are to be inverted to yield the underlying $\Delta_i(\vec{k})$. Therefore, we developed a restricted analysis scheme that still allows the pertinent $\Delta_i(\vec{k})$ information to be easily extracted. Instead of the usual constant energy $g(\vec{q},E)$ images, this approach is based on measuring the maximum scattering intensity in a $|\vec{q}|$-E plane along a specific high-symmetry direction—for example, $\vec{q} \parallel \Gamma\tilde{M}$ for the red band in Fig. 1D. Figure 1G shows a simulation of such a $|\vec{q}|$-E intensity plot ($\vec{q} \parallel \Gamma\tilde{M}$) revealing two curved trajectories of maximal scattering intensity. They are extracted and plotted as red curves in Fig. 1H [(2), section III]. Such a plot of intensity maxima in a $g(|\vec{q}|,E)$ plane along a high symmetry direction actually contains all the information on $\Delta(\vec{k})$ for that C_4-symmetric band. Another band with a different $\vec{q}$-space radius and whose gap maxima are rotated by 45° to the first (e.g., yellow in Fig. 1D) can be analyzed similarly; a plot of maxima in $g(|\vec{q}|,E)$ for $\vec{q} \parallel \Gamma\tilde{X}$ (yellow arrow, Fig. 1D) would then yield distinct interference maxima from the $\Delta(\vec{k})$ of that band (yellow curves, Fig. 1H). The magnitude and relative orientation of $\Delta_i(\vec{k})$ on multiple C_4-symmetric bands of different $|\vec{q}|$ radius can be determined simultaneously by using this multiband QPI approach. Importantly, the $\Delta_i(\vec{k})$ are then determined experimentally, not from comparison to simulation but directly from a combination of (i) the measured normal-state band dispersions, (ii) the BZ symmetry, and (iii) the measured geometrical characteristics of the scattering intensity $g(|\vec{q}|,E)$ in a specific $|\vec{q}|$-E plane [(2), section III].

We implement this approach using LiFeAs crystals with $T_c \approx 15$ K. Their cleaved surfaces are atomically flat (Fig. 2A) and exhibit the a_0 = 0.38 nm periodicity of either the As or Li layer [(2), section I]. As the glide plane is between Li layers we are probably observing a Li-termination layer. We image $g(\vec{r},E)$ with atomic resolution and with a thermal energy resolution $\delta E \le 350$ μeV at T = 1.2 K. Figure 2A inset shows the spatially averaged differential conductance $g(E)$ far from in-gap impurity states [(2), section V]. The density of electronic states $N(E) \propto g(E)$ (Fig. 2A, inset) is in agreement with the $N(E)$ first reported for LiFeAs (29, 30). It indicates (i) a fully gapped superconductor because $g(E) \sim 0$ for $|E| < 1$ meV, (ii) a maximum energy gap of ~6 meV, and (iii) a complex internal structure to $N(E)$ consistent with strong $\vec{k}$-space gap anisotropy.

Next, we image $g(\vec{r},E)$ in ~90 nm square fields of view (FOV) at temperatures between 1.2 K and 16 K and in the energy range associated with Cooper pairing [(2), section VI]. The large FOV is required to achieve sufficient $\vec{q}$-space resolution. Figure 2, B and C, shows a typical $g(\vec{r},E)$ and its Fourier transform $g(\vec{q},E)$ with E = 7.7 meV, and the inset shows a typical $\vec{r}$-space example of the interference patterns. Figure 2, C and D, shows representative Fourier transforms $g(\vec{q},E)$ from energies above the maximum superconducting gap magnitude (E = +7.7 meV, –6.6 meV). The scattering interference signatures for three distinct bands can be detected as closed contours in $\vec{q}$-space; we refer to them as h_3, h_2, and h_1 throughout. The measured $|\vec{q}(E)|$ of these bands in Fig. 2E shows them all to be hole-like. A quantitative comparison of QPI to both ARPES (15–17) and quantum oscillation measurements (31) [(2), section VII] identifies h_1, h_2, and h_3 with the three hole-like bands assigned α_1, α_2, and γ. The QPI signatures of electron-like bands are weak and complex, perhaps because they share the same $\vec{q}$-space regions as the signature of h_2, or because of the stronger k_z dispersion of these bands, or because of weak overlap between high-$|\vec{k}|$ states and the localized tip electron wave function; we do not consider them further here.

Figure 3, A and B, shows the $g(\vec{q},E)$ measured within the energy gaps in Fig. 2E. Scattering interference is virtually nonexistent in the $\vec{q}$-space direction parallel to $\Gamma\tilde{X}$ for the h_3 band (Fig. 3A, green arrows) and is similarly faint in a direction parallel to $\Gamma\tilde{M}$ for the h_2 band (Fig. 3B, green arrows). The disappearance in the superconducting phase of QPI in these two directions is a result of an anisotropic gap opening at relevant $\vec{k}$-space locations on these bands (see insets in Fig. 3, A and B), as predicted from both the T-matrix and JDOS simulations in Fig. 1, E and F. Figure 3C shows $g(\theta,E)$, the strongly anisotropic scattering intensity versus angle in $\vec{q}$-space

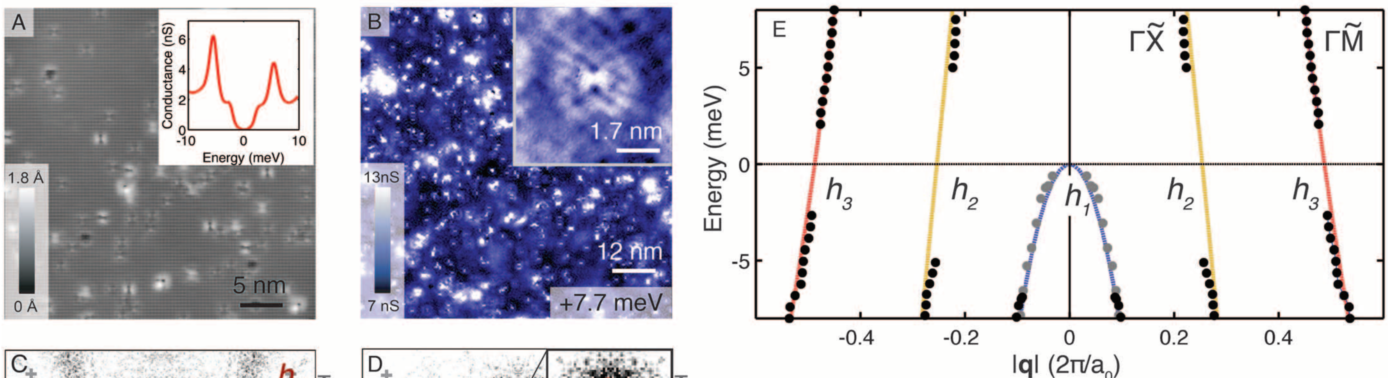

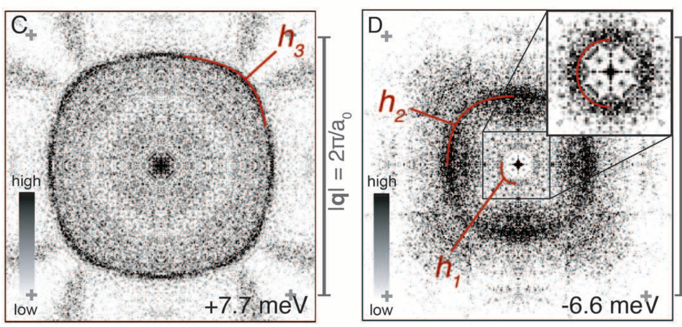

Fig. 2. (**A**) An ~35 nm square topographic image of LiFeAs surface, taken at voltage V_B = –20 mV junction resistance R_J = 2 GΩ, temperature T = 1.2 K. (Inset) Average spectrum over an area without impurities [see (2), section V]. The maximum gap superconducting coherence peaks and the zero conductance near E_F are clear. (**B**) Typical differential conductance image $g(\vec{r},E = 7.7\text{meV})$ at T = 1.2 K. (Inset) Typical QPI oscillations in $g(\vec{r},E)$ surrounding an impurity atom. (**C**) The $g(\vec{q},E = 7.7\text{meV})$ that is the power-spectral-density Fourier transform of $g(\vec{r},E = 7.7\text{meV})$, from (B). The high-intensity closed contour is a consequence of scattering interference within a large hole-like band h_3. (**D**) The $g(\vec{q},E = -6.6\text{meV})$ showing the high-intensity closed contours resulting from scattering interference from a smaller hole-like band h_2, and h_1 (inset). These data are measured at T = 1.2 K. (**E**) The measured energy dependence of the $\vec{q}(E) = 2\vec{k}(E)$ for all three bands in h_1 (blue line), h_2 (yellow), and h_3 (red) along the marked directions. Black dots are measured in the superconducting phase at T = 1.2 K; gray dots are measured in the normal state at T = 16 K.

$g(\vec{q},E)$ on the h_3 Fermi surface. The $g(\vec{q},E)$ data in Fig. 3, A and B, together with the $g(\theta,E)$ data in Fig. 3C, reveal unambiguous QPI signatures for anisotropic gaps of different orientations on different bands in LiFeAs.

To quantify the $\Delta_i(\vec{k})$, we examine the scattering intensity in $g(\vec{q},E)$ within a $|\vec{q}|$-E plane defined first by $\vec{q}$ parallel to $\Gamma\tilde{M}$ and then by $\vec{q}$ parallel to $\Gamma\tilde{X}$. The locus of maximum intensity in the $g(|\vec{q}|,E)$ plane with $|\vec{q}|$ parallel to the $\Gamma\tilde{M}$ direction is extracted [(2), section VIII] and plotted in Fig. 3D. The evolution of the normal-state h_3 band (red in Fig. 2E) is indicated here by red arrows. The superconducting energy gap minimum of h_3 is seen, along with the curved trajectories of scattering intensity maxima expected from an anisotropic $\Delta(\vec{k})$ (Fig. 1, G and H) [(2), section VIII]. Similarly, by measuring $g(|\vec{q}|,E)$ in the plane with $|\vec{q}|$ parallel to $\Gamma\tilde{X}$, the locus of maximum intensity of the h_2 band is extracted [(2), section VIII] and plotted in Fig. 3E. The energy gap minimum is again obvious along with the curved scattering intensity maxima expected from a different anisotropic $\Delta(\vec{k})$

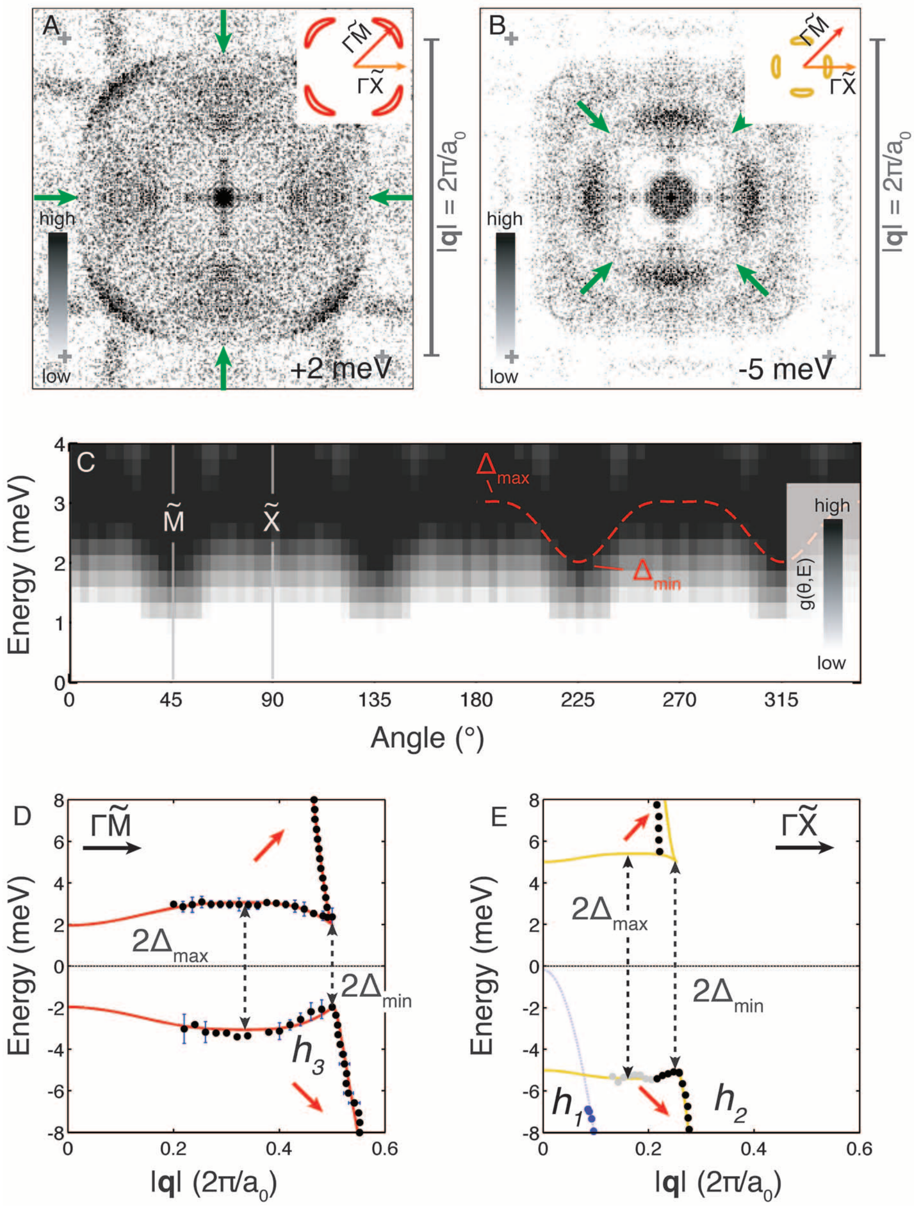

Fig. 3. (**A**) $g(\vec{q},E = 2\text{meV})$ measured at $T = 1.2$ K. The scattering on the h_3 band has become highly anisotropic within its energy gap range, with vanishing intensity in the $\Gamma\tilde{M}$ direction (green arrows). The inset shows schematically in $\vec{k}$-space how this is indicative of a lower energy gap along $\Gamma\tilde{M}$ and a higher energy gap along $\Gamma\tilde{X}$. (**B**) $g(\vec{q},E = -5\text{ meV})$ measured at $T = 1.2$ K. The scattering on the h_2 band has become highly anisotropic within its energy gap range (green arrows), indicative of a lower energy gap along $\Gamma\tilde{X}$ and a higher energy gap along $\Gamma\tilde{M}$. (**C**) A projection of the QPI intensity $g(\vec{q},E)$ (a three-dimensional data set) onto the measured normal-state band dispersion $\varepsilon(\vec{k}) = \varepsilon(\vec{q}/2)$. In the direction of minimal gap ($\Gamma\tilde{M}$), the intensity is gapped up to around 2meV $\approx \Delta_{h3}^{min}$, whereas in the direction of maximal gap ($\Gamma\tilde{X}$), it is gapped up to around 3meV $\approx \Delta_{h3}^{max}$. (**D**) Extracted maximum scattering intensity trajectory from $g(|\vec{q}|,E)$ for $\vec{q} \parallel \Gamma\tilde{X}$ [(2), section VIII] containing the information on $\Delta(\vec{k})$ for h_3. (**E**) Extracted maximum scattering intensity trajectory from $g(|\vec{q}|,E)$ for $\vec{q} \parallel \Gamma\tilde{X}$ [(2), section VIII] containing the information on $\Delta(\vec{k})$ for h_2. Blue: Gap opening on the h_1 band.

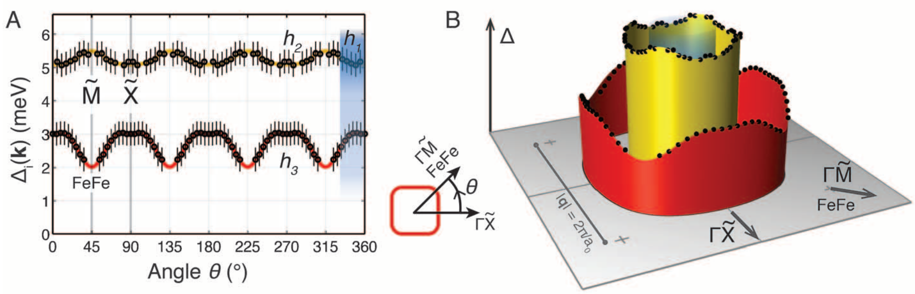

Fig. 4. (**A**) Anisotropic energy gap structure Δ_i measured using QPI at $T = 1.2$ K on the three hole-like bands h_3, h_2, and h_1 (Fig. 2E). These bands have been labeled γ, α_1, and α_2 before. Here, the 0.35-meV error bars stem from the thermal resolution of SI-STM at 1.2 K. (**B**) A three-dimensional rendering of the measured (solid dots) anisotropic energy gap structure Δ on the three hole-like bands at $T = 1.2$ K.

(see Fig. 1H); the data for the upper branch cannot be obtained because of interference from other signals (possibly the electron-like band). The QPI signature of the third band h_1 becomes unidentifiable within -6 ± 1.5 meV below E_F in the superconducting phase, consistent with the opening of a gap of this magnitude (Figs. 2E and 3E), but we cannot yet resolve any gap modulations.

The magnitude, anisotropy, and relative position of $\Delta_i(\vec{k})$ on bands h_3, h_2, and h_1 are then determined from Fig. 3, D and E, using the previously described procedure [(*2*), section III]. The resulting anisotropic superconducting gaps on bands h_3, h_2, and h_1 of LiFeAs are displayed in Fig. 4, A and B. Although our $g(|\vec{q}|,E)$ agree well with pioneering QPI studies of LiFeAs where common data exist, no studies of $\Delta_i(\vec{k})$ were reported therein (*30*). Moreover, although field-dependent Bogoliubov QPI can reveal OP symmetry (*11*), these techniques were not applied here to LiFeAs, and no OP symmetry conclusions were drawn herein. The anisotropic Δ_i reported recently in ARPES studies of LiFeAs (*16*, *17*) appear in agreement with our observations for the h_3 (Fig. 1, γ) and h_2 (Fig. 1, α_2) bands. Lastly, our measurements are quite consistent with deductions on LiFeAs band structure from quantum oscillation studies (*31*). Overall, the growing confidence and concord in the structure of $\Delta_i(\vec{k})$ for LiFeAs will advance the quantitative theoretical study of the mechanism of its Cooper pairing. Moreover, the multiband anisotropic-gap QPI techniques introduced here will allow equivalent $\Delta_i(\vec{k})$ observations in other iron-pnictide superconductors.

References and Notes

1. P. J. Hirschfeld, M. M. Korshunov, I. I. Mazin, *Rep. Prog. Phys.* **74**, 124508 (2011).
2. Materials and methods are available as supplementary materials on *Science* Online.
3. F. Wang, H. Zhai, Y. Ran, A. Vishwanath, D.-H. Lee, *Phys. Rev. Lett.* **102**, 047005 (2009).
4. T. A. Maier, S. Graser, D. J. Scalapino, P. J. Hirschfeld, *Phys. Rev. B* **79**, 224510 (2009).
5. R. Thomale, C. Platt, J. Hu, C. Honerkamp, B. A. Bernevig, *Phys. Rev. B* **80**, 180505R (2009).
6. S. Raghu, X.-L. Qi, C.-X. Liu, D. J. Scalapino, S.-C. Zhang, *Phys. Rev. B* **77**, 220503R (2008).
7. R. Sknepnek, G. Samolyuk, Y.-B. Lee, J. Schmalian, *Phys. Rev. B* **79**, 054511 (2009).
8. S. Maiti, A. V. Chubukov, *Phys. Rev. B* **82**, 214515 (2010).
9. H. Kontani, S. Onari, *Phys. Rev. Lett.* **104**, 157001 (2010).
10. A. D. Christianson *et al.*, *Nature* **456**, 930 (2008).
11. T. Hanaguri, S. Niitaka, K. Kuroki, H. Takagi, *Science* **328**, 474 (2010).
12. B. Zeng *et al.*, *Nat. Comms.* **1**, 112 (2010).
13. J.-Ph. Reid *et al.*, *Phys. Rev. B* **82**, 064501 (2010).
14. M. A. Tanatar *et al.*, *Phys. Rev. Lett.* **104**, 067002 (2010).
15. S. V. Borisenko *et al.*, *Phys. Rev. Lett.* **105**, 067002 (2010).
16. S. V. Borisenko *et al.*, *Symmetry* **4**, 251 (2012).
17. K. Umezawa *et al.*, *Phys. Rev. Lett.* **108**, 037002 (2012).
18. Q.-H. Wang, D.-H. Lee, *Phys. Rev. B* **67**, 020511R (2003).
19. L. Capriotti, D. J. Scalapino, R. D. Sedgewick, *Phys. Rev. B* **68**, 014508 (2003).
20. T. S. Nunner, W. Chen, B. M. Andersen, A. Melikyan, P. J. Hirschfeld, *Phys. Rev. B* **73**, 104511 (2006).
21. Y.-Y. Zhang *et al.*, *Phys. Rev. B* **80**, 094528 (2009).
22. A. Akbari, J. Knolle, I. Eremin, R. Moessner, *Phys. Rev. B* **82**, 224506 (2010).
23. S. Sykora, P. Coleman, *Phys. Rev. B* **84**, 054501 (2011).
24. I. I. Mazin, S. A. J. Kimber, D. N. Argyriou, *Phys. Rev. B* **83**, 052501 (2011).
25. X. C. Wang *et al.*, *Solid State Commun.* **148**, 538 (2008).
26. M. J. Pitcher *et al.*, *J. Am. Chem. Soc.* **132**, 10467 (2010).
27. C. W. Chu *et al.*, *Physica C* **469**, 326 (2009).
28. D. J. Singh, *Phys. Rev. B* **78**, 094511 (2008).
29. T. Hanaguri *et al.*, *Meeting Abstracts of the Phys. Soc. of Japan*, **65**, 617 (2010).
30. T. Hänke *et al.*, *Phys. Rev. Lett.* **108**, 127001 (2012).
31. C. Putzke *et al.*, *Phys. Rev. Lett.* **108**, 047002 (2012).

Acknowledgments: We are particularly grateful to D.-H. Lee for advice and discussions, and we acknowledge and thank F. Baumberger, A. Carrington, P. C. Canfield, A. V. Chubukov, A. I. Coldea, M. H. Fischer, T. Hanaguri, P. J. Hirschfeld, B. Keimer, E.-A. Kim, M. J. Lawler, C. Putzke, J. Schmalian, H. Takagi, Z. Tesanovic, R. Thomale, S. Uchida, and F. Wang for helpful discussions and communications. Studies were supported by the Center for Emergent Superconductivity, an Energy Frontier Research Center, funded by the U.S. Department of Energy under DE-2009-BNL-PM015; by the UK Engineering and Physical Sciences Research Council (EPSRC); and by a Grant-in-Aid for Scientific Research C (no. 22540380) from the Japan Society for the Promotion of Science. Y.X. acknowledges support by the Cornell Center for Materials Research (CCMR) under NSF/DMR-0520404. T.-M.C. acknowledges support by Academia Sinica Research Program on Nanoscience and Nanotechnology, and A.P.M. the receipt of a Royal Society-Wolfson Research Merit Award. The data described in the paper are archived by the Davis Research Group at Cornell University.

Supplementary Materials

www.sciencemag.org/cgi/content/full/336/6081/563/DC1
Materials and Methods
Supplementary Text
Figs. S1 to S10
References (*32*–*36*)

10 October 2011; accepted 3 April 2012
10.1126/science.1218726

Magnetic Reconnection in the Near Venusian Magnetotail

T. L. Zhang,[1,2]* Q. M. Lu,[1] W. Baumjohann,[2] C. T. Russell,[3] A. Fedorov,[4] S. Barabash,[5] A. J. Coates,[6] A. M. Du,[7] J. B. Cao,[8] R. Nakamura,[2] W. L. Teh,[2] R. S. Wang,[2] X. K. Dou,[1] S. Wang,[1] K. H. Glassmeier,[9] H. U. Auster,[9] M. Balikhin[10]

Observations with the Venus Express magnetometer and low-energy particle detector revealed magnetic field and plasma behavior in the near-Venus wake that is symptomatic of magnetic reconnection, a process that occurs in Earth's magnetotail but is not expected in the magnetotail of a nonmagnetized planet such as Venus. On 15 May 2006, the plasma flow in this region was toward the planet, and the magnetic field component transverse to the flow was reversed. Magnetic reconnection is a plasma process that changes the topology of the magnetic field and results in energy exchange between the magnetic field and the plasma. Thus, the energetics of the Venus magnetotail resembles that of the terrestrial tail, where energy is stored and later released from the magnetic field to the plasma.

Magnetic reconnection is an important process in many astrophysical plasma environments, which leads to efficient and fast conversion of magnetic energy into kinetic energy of plasma particles. As a result of the rapid reconfiguration of the magnetic topology, it also transfers mass between different astrophysical plasma regimes. In particular, reconnection is associated with the formation of solar coronal mass ejections (*1*) and plasmoid ejections from the magnetotails of Earth, Jupiter, Saturn, and Mercury (*2*–*5*), all of which lead to substantial plasma loss. Magnetic reconnection may also be responsible for comet tail disconnection, which releases much of a comet's plasma tail into space (*6*, *7*). Although understanding atmospheric loss is a key to establishing the evolutionary history of planets, the role of magnetic reconnection is still poorly understood because of the scarcity of in situ observations at planets other than Earth.

Three mechanisms of atmospheric loss have been identified at Venus: $V \times B$ pick-up processes (where V is velocity and B is the magnetic field), $J \times B$ acceleration in the plasma sheet (where J is current density), and the polar wind–type process in the tail boundary layer (*8*). Recent Venus Express data (*9*) reveal escape through the plasma sheet of the magnetotail and the tail boundary layer. Here, we show that reconnection is another acceleration mechanism, a situation not expected in the induced tail of Venus.

[1]Chinese Academy of Sciences Key Laboratory of Geospace Environment, University of Science and Technology of China, Hefei 230026, China. [2]Space Research Institute, Austrian Academy of Sciences, Graz 8042, Austria. [3]Institute of Geophysics and Planetary Physics, University of California, Los Angeles (UCLA), CA 90095–1567, USA. [4]Centre d'Etude Spatiale des Rayonnements, Toulouse 31028, France. [5]Swedish Institute of Space Physics, Kiruna 98128, Sweden. [6]Mullard Space Science Laboratory, University College London, London RH5 6NT, UK. [7]Institute of Geology and Geophysics, Chinese Academy of Sciences, Beijing 100029, China. [8]Space Science Institute, Beihang University, Beijing 100191, China. [9]Institut für Geophysik und Extraterrestrische Physik, Technischen Universität Braunschweig, Braunschweig 38106, Germany. [10]Department of Automatic Control and Systems Engineering, University of Sheffield, Sheffield S1 3JD, UK.

*To whom correspondence should be addressed. E-mail: tielong.zhang@oeaw.ac.at

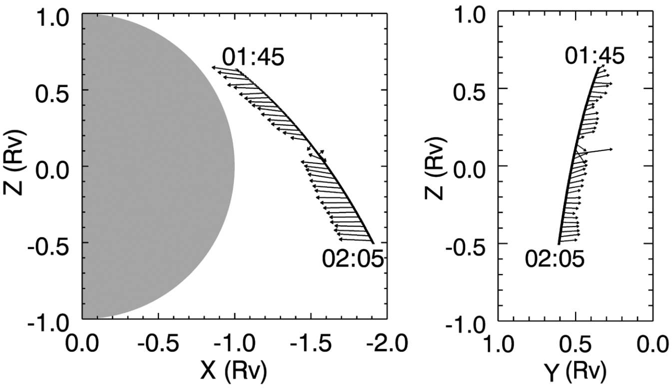

Fig. 1. A rotational magnetic field structure in the Venus magnetotail based on magnetic field measurements by Venus Express on 15 May 2006. The measurements (*22*) are in the planet-centered Venus Solar Orbital (VSO) coordinate system, with X sunward and Z toward orbital north, similar to the Geocentric Solar Ecliptic coordinate system at Earth. The shaded area represents Venus.

On 15 May 2006, a rotational magnetic field structure was observed by Venus Express when crossing the Venusian magnetotail (Fig. 1). The structure was located ~1.5 R_V (1 R_V = 6051 km, one Venus radius) down the tail and lasted ~3 min (0153 to 0156 UT). The event occurred during a time of enhanced interplanetary magnetic field (IMF) strength with small directional variation.

Because Venus has no intrinsic magnetic field, the configuration of its induced magnetosphere is controlled by the upstream IMF orientation and its draping around the highly conducting ionosphere. When we rotate the magnetic field observations from the measurement system to a system oriented with the expected electric field

Fig. 2. Plasmoid flux rope observed with magnetic field and plasma measurements on 15 May 2006. (**A** to **D**) The magnetic field data were rotated into a natural coordinate system with *x* along the ambient magnetic field before and after the events, *y* containing the bimodal perturbation, and *z* along the unimodal perturbation. The rotated coordinates are *x* = (0.863 –0.500 0.075), *y* = (0.213 0.224 –0.951), and *z* = (0.459 0.837 0.300). The dashed vertical lines are the edges of the plasmoid defined by the diamagnetic field minima at 0153:45 UT and 0155:19 UT. (**E** and **F**) The total counts of energetic electrons measured by the Electron Spectrometer (ELS) sensor and the total counts of the proton of the Ion Mass Analyzer (IMA) sensor (*23*), respectively. In these spectrograms, the IMA has 12 s time resolution, and the ELS has 4 s resolution. The termination of the ion counts at 0154:17 is due to a rotation of the spacecraft, which moved the look-direction of the ion sensor. The electron sensor is not as sensitive to spacecraft rotation as the ion sensor.

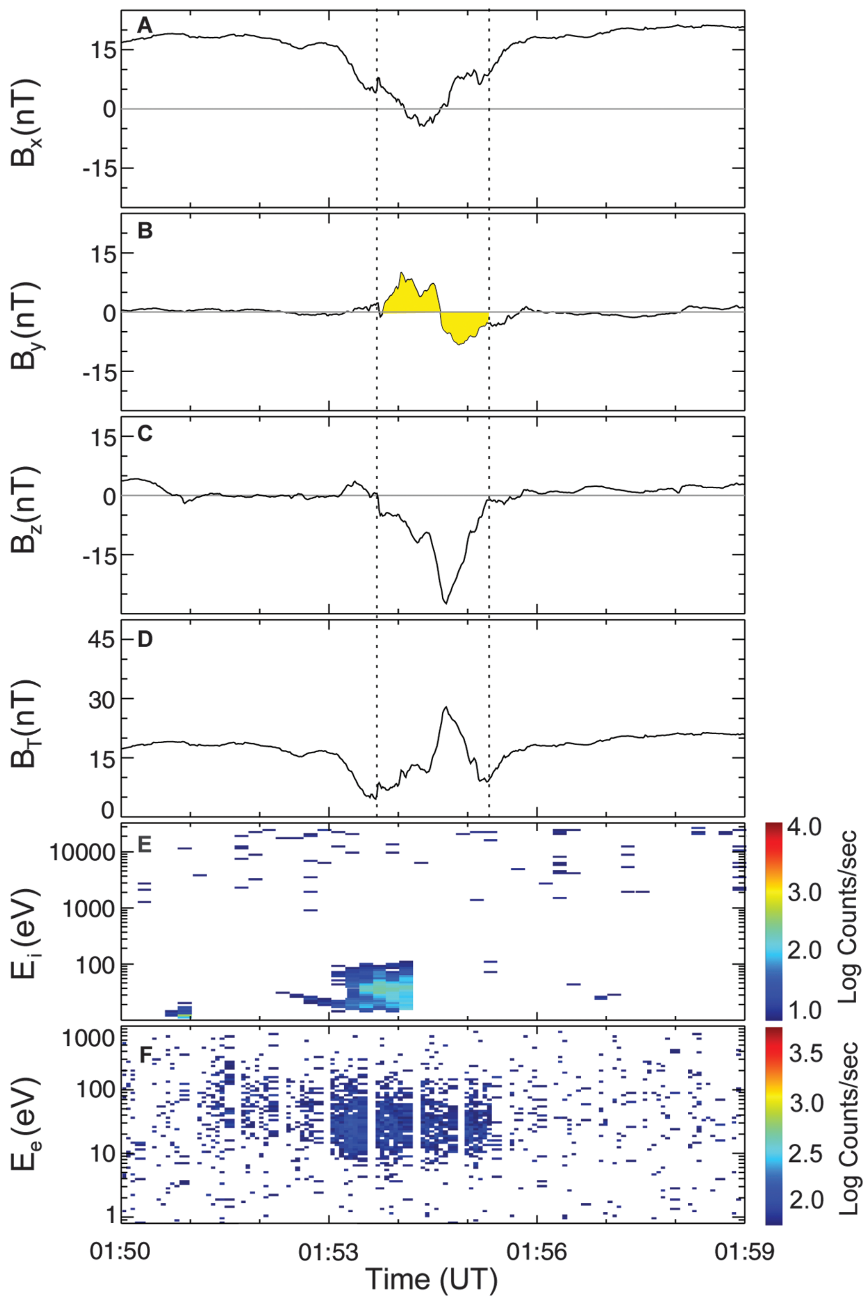

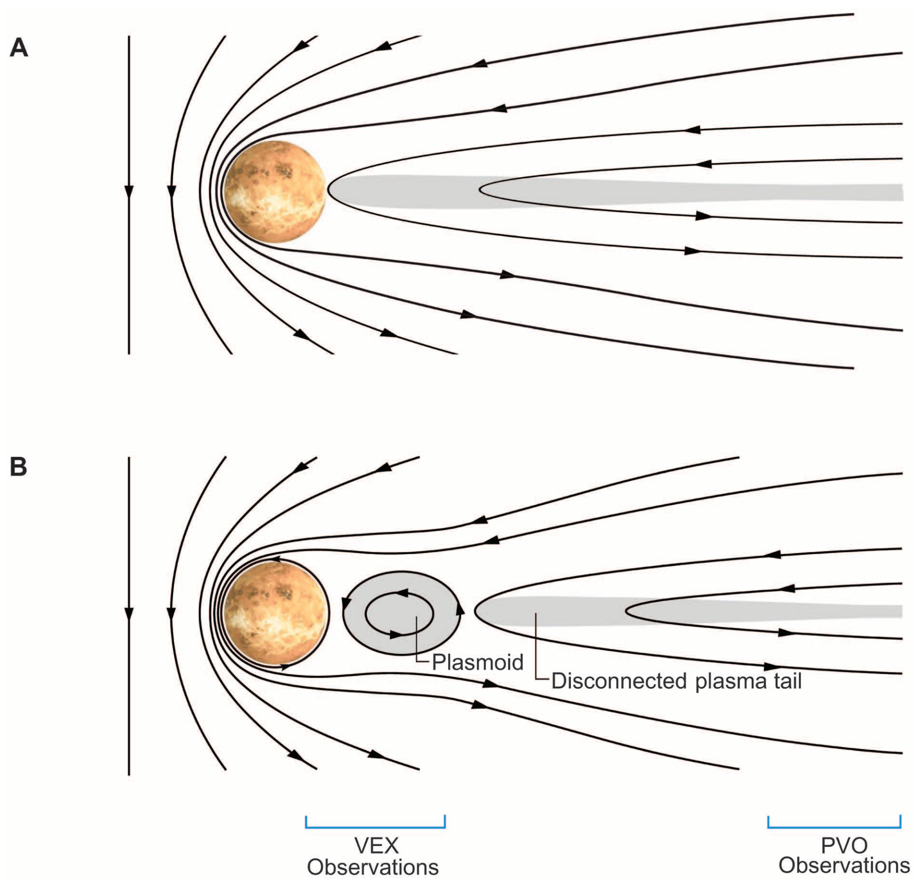

Fig. 3. Schematic illustration of the plasmoid formation and disconnected plasma tail events during the magnetic reconnection observed in the near Venusian tail. Field lines are indicated by solid lines. (**A**) Venusian magnetotail before magnetic reconnection and plasmoid formation. (**B**) The ionosphere was magnetized with a field line going all the way around the planet. The flux rope/O-line (plasmoid) was separated from the nightside magnetized ionosphere by a magnetic X-line. The more distant side of the O-line was separated from the disconnected plasma sheet by another X-line. The tail plasma sheet shedded O-lines toward the planet. The O-lines ran into the magnetized nightside, magnetically connected with it, and created first oval field lines and then circular field lines in the lower ionosphere. Later arriving O-lines reinforced the field. The region of observations by the Pioneer Venus mission (PVO) was in the distant tail, in contrast to Venus Express (VEX), which observed the near tail.

and the ambient magnetic directions (Fig. 2), the magnetic temporal variation is that of a well-defined flux rope plasmoid moving over the spacecraft. The structure has a bipolar-like rotation of the field and magnetic field maximum centered near the inflection point of the bipolar signature (*10*). The edges of the flux rope are well defined by diamagnetic field minima at 01:53:45 UT and 01:55:19 UT. A very strong plasmoid core field peaked at 27.8 nT, which is 46% higher than the neighboring lobe field of 19 nT. The enhanced ion and electron flux signatures were coincident with the plasmoid structure (Fig. 2, E and F). Simple integration as a moment of distribution function gives a bulk velocity of (31, –18, 7) km/s in VSO coordinates, revealing the Venus-ward motion of the plasmoid structure. The plasmoid duration was 94 s (from magnetic field measurements), implying its size was 3400 km, assuming the bulk velocity was the same as the plasmoid speed.

A plasmoid is a transient magnetic loop structure formed by magnetic reconnection in a planetary magnetotail. It is ubiquitous in planets with an intrinsic magnetic field such as Earth, Jupiter, Saturn, and Mercury (*2*–*5*), but it is not expected in the magnetotail of an unmagnetized planet such as Venus. We further looked through the Venus Express magnetic field data, identifying the negative B_Y in the current sheet in the magnetic field coordinate system. In this system, the current sheet is in the *xz* plane and IMF in the *xy* plane pointing to +*y* direction, thus a negative B_Y in the current sheet can be regarded as the signature of reconnection, which is similar to the indication by a negative B_Z in the Earth's magnetotail plasma sheet. We found that the negative B_Y in the current sheet occurs quite frequently, predominantly in the –E hemisphere, where the magnetic field draping pattern is more wrapped around the planet and the field reversal is dominant (*11*). Furthermore, the Venus-ward bulk flows are found mostly within 2 R_V down the tail. Observations of Venus Express data imply that reconnection can operate in a quasi-steady-state in the near tail at Venus, at least during current conditions. Thus, the magnetic field is not just a buffer between the solar wind flow and the planetary atmosphere and ionosphere; rather, it provides a pathway for channelling a fraction of the incident energy flux of the solar wind into the night side atmosphere much like the situation in the terrestrial magnetotail.

The plasmoid in the Venus magnetotail as observed in this study is illustrated schematically in Fig. 3. When the magnetic record shown in Fig. 2 began, the spacecraft was between the planet and the magnetic island and the "rope" contained within it. As the event proceeded, the rope moved toward Venus and across the spacecraft (*12*). Venus' induced magnetosphere serves as an obstacle to the solar wind in the same way the Earth's magnetosphere does (*13*), but it occupies much smaller space volume, with a scaling factor of ~10. Magnetic reconnection occurs in the Earth's magnetotail and plasma sheet at ~10 to 30 Earth radii in the antisolar direction. By simple scaling, the equivalent region at Venus would be 1 to 3 R_V down the tail. That is exactly the region where Venus Express detected reconnection events. Because of its orbital geometry, the earlier Pioneer Venus mission (PVO) observed mainly the distant tail region at 8 to 12 R_V (*14*, *15*) and was thus unable to sample the right region.

The first observational estimate of the atmospheric loss of Venus was obtained by integrating the outflow plasma in the magnetotail on the basis of Venus Express observations (*16*). In this analysis, based on the reconstruction of the full distribution function, only regions in which the outward flux becomes stable were considered, and only the total outward flux regardless of the acceleration mechanism was taken into account. Any inward flux will not affect the total escape rate. However, if the plasma reaches the ionosphere and becomes deposited there, this interaction should lead to greater magnetization of the nightside ionosphere as well as heating and plasma transport. In this case, the plasma circulation may be like that recently considered for the Earth magnetosphere (*17*). Thus, despite their very different magnetic envelopes, the plasma dynamics of Venus and Earth display many similar characteristics.

References and Notes

1. P. F. Chen, *Liv. Rev. Sol. Phys.* **8**, 1 (2011).
2. C. T. Russell, in *Correlated Interplanetary and Magnetospheric Observations*, D. E. Page, Ed. (Reidel, Dordrecht, Netherlands, 1974), pp. 3–47.
3. C. T. Russell, K. K. Khurana, D. E. Huddleston, M. G. Kivelson, *Science* **280**, 1061 (1998).
4. C. M. Jackman *et al.*, *Geophys. Res. Lett.* **34**, L11203 (2007).
5. J. A. Slavin *et al.*, *Science* **324**, 606 (2009).
6. C. T. Russell, M. A. Saunders, J. L. Phillips, J. A. Fedder, *J. Geophys. Res.* **91**, (A2), 1417 (1986).
7. Y. D. Jia *et al.*, *Astrophys. J.* **696**, L56 (2009).

8. H. Lammer *et al.*, *Planet. Space Sci.* **54**, 1445 (2006).
9. S. Barabash *et al.*, *Nature* **450**, 650 (2007).
10. The bipolar signature in our rotated coordinate system is in the B_Y component here instead of the B_Z component, as it would be in the usual coordinate system used for a terrestrial magnetotail plasmoid (*18*).
11. T. L. Zhang *et al.*, *Geophys. Res. Lett.* **37**, L14202 (2010).
12. An earlier study found a flux rope in the Venus tail, but reconnection was rejected as a possible source because of the inconsistent orientation of the rope axis (*19*). In our case, the axis is consistent with reconnection. Flux ropes that have been seen on the nightside of Venus are much larger than those in the dayside ionosphere (*20*) and cannot explain these micro-ropes, which appear not to have a magnetic reconnection source (*21*).
13. T. L. Zhang *et al.*, *Nature* **450**, 654 (2007).
14. C. T. Russell, O. Vaisberg, in *Venus*, D. M. Hunten, L. Colin, T. M. Donahue, V. I. Moroz, Eds. (Univ. of Arizona Press, Tucson, AZ, 1983), pp. 873–940.
15. J. L. Phillips, D. L. McComas, *Space Sci. Rev.* **55**, 1 (1991).
16. A. Fedorov *et al.*, *J. Geophys. Res.* **116**, (A7), A07220 (2011).
17. V. Angelopoulos *et al.*, *Science* **321**, 931 (2008).
18. M. B. Moldwin, W. J. Hughes, *J. Geophys. Res.* **96**, (A8), 14051 (1991).
19. J. A. Slavin *et al.*, *Geophys. Res. Lett.* **36**, L09106 (2009).
20. C. T. Russell, R. C. Elphic, *Nature* **279**, 616 (1979).
21. H. Y. Wei, C. T. Russell, T. L. Zhang, M. K. Dougherty, *Icarus* **206**, 174 (2010).
22. T. L. Zhang *et al.*, *Planet. Space Sci.* **54**, 1336 (2006).
23. S. Barabash *et al.*, *Planet. Space Sci.* **55**, 1772 (2007).

Acknowledgments: The work in China was supported by National Natural Science Foundation of China grants 41121003 and 41174156. The work at Graz was supported by Austrian Science Fund (FWF: I429-N16). The work at UCLA was supported by NASA under research grant NNX10AV29G.

23 November 2011; accepted 8 March 2012
Published online 5 April 2012;
10.1126/science.1217013

Ancient Impact and Aqueous Processes at Endeavour Crater, Mars

S. W. Squyres,[1]* R. E. Arvidson,[2] J. F. Bell III,[3] F. Calef III,[4] B. C. Clark,[5] B. A. Cohen,[6] L. A. Crumpler,[7] P. A. de Souza Jr.,[8] W. H. Farrand,[5] R. Gellert,[9] J. Grant,[10] K. E. Herkenhoff,[11] J. A. Hurowitz,[4] J. R. Johnson,[12] B. L. Jolliff,[2] A. H. Knoll,[13] R. Li,[14] S. M. McLennan,[15] D. W. Ming,[16] D. W. Mittlefehldt,[16] T. J. Parker,[4] G. Paulsen,[17] M. S. Rice,[1] S. W. Ruff,[3] C. Schröder,[18] A. S. Yen,[4] K. Zacny[17]

The rover Opportunity has investigated the rim of Endeavour Crater, a large ancient impact crater on Mars. Basaltic breccias produced by the impact form the rim deposits, with stratigraphy similar to that observed at similar-sized craters on Earth. Highly localized zinc enrichments in some breccia materials suggest hydrothermal alteration of rim deposits. Gypsum-rich veins cut sedimentary rocks adjacent to the crater rim. The gypsum was precipitated from low-temperature aqueous fluids flowing upward from the ancient materials of the rim, leading temporarily to potentially habitable conditions and providing some of the waters involved in formation of the ubiquitous sulfate-rich sandstones of the Meridiani region.

After more than 7 years in operation and 33 km of traversing, the Mars Exploration Rover Opportunity has reached Endeavour Crater. Endeavour is ~22 km in diameter and formed in Noachian (*1*) materials that predate the sulfate-rich sedimentary rocks explored by Opportunity for most of its mission (*2*, *3*). Endeavour was chosen as a target because the rocks there record an ancient epoch in martian history, and because orbital infrared data show that phyllosilicate minerals are present in portions of the crater rim (*4*).

Opportunity arrived at Endeavour Crater on sol 2681 (*5*) of its mission, at a low-lying segment of the rim, ~700 m in length, named Cape York (Fig. 1). Shoemaker Ridge (*6*) forms the spine of Cape York and is the type locality for the Noachian materials of the rim, which we call the Shoemaker formation. Opportunity first arrived at Spirit Point, the southern tip of Cape York, and then traversed northward 851 m before stopping at Greeley Haven (*7*) at the northern end of Cape York to spend the martian winter.

Instruments of Opportunity's Athena payload (*8*, *9*) were used to investigate materials within the Shoemaker formation, including the bedrock outcrop Chester Lake (Fig. 2) near the southern end of Shoemaker Ridge, and several bedrock targets near Greeley Haven at the northern end. Although separated by more than half a kilometer, these outcrops are similar in physical appearance and elemental chemistry; we interpret them to represent the dominant surface rock type of Cape York.

Chester Lake and all the rocks near Greeley Haven have similar textures. They are brecciated, with dark, relatively smooth angular clasts up to ~10 cm in size embedded in a brighter, fractured, fine-grained matrix. Some outcrops, notably Chester Lake, show fine-scale lineations in the matrix and alignment of some clasts (Fig. 2). Pancam spectra of the matrix exhibit a gradual decrease in reflectance toward 1000 nm. The clasts can show specular reflections, have a relatively deep absorption at 934 nm, and have a shallower 535-nm absorption than the matrix materials, consistent with relatively unoxidized basaltic material containing low-Ca pyroxene.

The matrix of Chester Lake is easily abraded. A portion of Chester Lake dominated by matrix was abraded to a depth of ~2.5 mm with the rover's Rock Abrasion Tool (RAT). Resistance to abrasion is quantified using specific grind energy, the energy required to abrade away a unit volume of rock. The specific grind energy for Chester Lake was ~1.5 J mm^{-3}. Representative values for weak terrestrial materials are 0.7 to 0.9 J mm^{-3} for chalk and 4.8 to 5.3 J mm^{-3} for gypsum (*10*). Chester Lake is substantially weaker than all but 1 of the 14 diverse rocks abraded by Spirit at Gusev Crater (*11*) but is comparable to the sulfate-rich sandstones at Opportunity's landing site (*12*).

At Chester Lake, we used the Alpha Particle X-Ray Spectrometer (APXS) to measure the elemental composition of both the matrix (after abrasion by the RAT) and one of the clasts. Measurements were also made of three targets near Greeley Haven: Transvaal and Boesmanskop (both matrix) and Komati (a clast). All are similar to one another in composition, and all are similar to the basaltic sand typical of the Meridiani region (Table 1). The major elements (Na, Mg, Al, Si, Ca, and Fe) are mostly within 10 weight percent (wt %) of the basaltic sand composition, and all but a few are within 20 wt %.

Fe/Mn ratios of the matrix range from 40 to 44, and "Mg numbers" [100 × molar Mg/(Mg + Fe)] of all samples range from 41 to 48. These are within the ranges of basaltic meteorites from Mars [Fe/Mn ratios, 36 to 45; Mg numbers, 24 to 68 (fig. S1)] and indicate that any alteration of the protolith of these rocks did not substantially mobilize Mg, Mn, or Fe. P contents are higher than

[1]Department of Astronomy, Cornell University, Ithaca, NY 14853, USA. [2]Department of Earth and Planetary Sciences, Washington University, St. Louis, MO 63031, USA. [3]School of Earth and Space Exploration, Arizona State University, Tempe, AZ 85287, USA. [4]Jet Propulsion Laboratory, California Institute of Technology, Pasadena, CA 91109, USA. [5]Space Science Institute, Boulder, CO 80301, USA. [6]NASA Marshall Space Flight Center, Huntsville, AL 35812, USA. [7]New Mexico Museum of Natural History & Science, Albuquerque, NM 87104, USA. [8]Human Interface Technology Laboratory, University of Tasmania, Launceston TAS 7250, Australia. [9]Department of Physics, University of Guelph, Guelph, Ontario N1G 2W1, Canada. [10]Center for Earth and Planetary Studies, Smithsonian Institution, Washington, DC 20560, USA. [11]U.S. Geological Survey, Astrogeology Science Center, Flagstaff, AZ 86001, USA. [12]Applied Physics Laboratory, Johns Hopkins University, Laurel, MD 20723, USA. [13]Botanical Museum, Harvard University, Cambridge, MA 02138, USA. [14]Department of Civil, Environmental, and Geodetic Engineering, Ohio State University, Columbus, OH 43210, USA. [15]Department of Geosciences, State University of New York, Stony Brook, NY 11794, USA. [16]Astromaterials Research and Exploration Science (ARES), NASA Johnson Space Center, Houston, TX 77058, USA. [17]Honeybee Robotics & Spacecraft Mechanisms Corporation, Pasadena, CA 91103, USA. [18]Universität Bayreuth und Eberhard Karls Universität, 72076 Tübingen, Germany.

*To whom correspondence should be addressed. E-mail: squyres@astro.cornell.edu

those of basaltic sand, and Cr contents are lower. However, these minor elements follow trends of martian basaltic and lherzolitic meteorites (fig. S1), which suggests that igneous fractionation established the major and minor element concentrations.

We interpret all of these rocks to be breccias formed during the Endeavour impact. The compositional similarity to Meridiani basaltic sand is consistent with the view that both materials broadly reflect the composition of the surficial crust in this region.

Although we cannot assess the degree of shock metamorphism of the clasts or the presence of glass in the matrix, we note that the texture of these rocks is similar to the typical texture of suevite breccias (*13*) common in impact settings on Earth and the Moon. For terrestrial suevites, particle shape fabrics have been reported that are oriented radial to the impact point and consequently have been related to the emplacement flow (*14*). The linear fabric in Chester Lake is oriented within ~5° of radial to the center of Endeavour, although we cannot rule out the possibility that this texture is erosional rather than primary.

Near the southern end of Shoemaker Ridge, Opportunity encountered Odyssey crater (Fig. 1). Odyssey is elliptical, ~23 m by 19 m, with its major axis oriented orthogonal to a field of ejecta blocks that extends to the southeast. The ejecta block Tisdale was investigated in detail. Tisdale differs texturally and compositionally from Chester Lake and Greeley Haven rocks. Because it was excavated from Odyssey crater, Tisdale may represent a deeper unit within the Shoemaker formation. Tisdale and other Odyssey ejecta blocks are breccias, with poorly sorted, closely packed, angular to rounded clasts up to several centimeters in size (Fig. 3). Tisdale lacks the extensive fine-grained matrix of Chester Lake and other rocks, and contains lithic fragments over a wide range of grain sizes.

The clasts in Tisdale exhibit spectral variability beyond that expected from discontinuous dust coatings, including positive and negative near-infrared spectral slopes and some 903-nm absorptions. Small, localized spots in Tisdale and nearby rocks exhibit 860- and 535-nm absorptions possibly consistent with a ferric phase and/or minor hydrated Mg/Fe silicates. On the basis of its textural and color properties, we interpret Tisdale as a lithic breccia that is possibly polymict.

APXS measurements of Tisdale were made at three locations on a relatively dust-free vertical face (Table 1). The results are similar to Chester Lake and the Greeley Haven outcrops; however, concentrations of Mg are lower, and concentrations of P and the trace elements Ni, Zn, and Br are higher and quite variable. One location has the highest Zn concentration (~6300 μg g^{-1}) of all analyses from Mars. The Zn and Ni elemental trends are similar to trends in hydrothermally altered rocks around Home Plate in Gusev crater (*15*). Variable P enrichment may result from metasomatism of silicate materials by P-rich hydrothermal solutions (*16*) or acidic solutions dissolving P from source rocks and reprecipitating it (*17*). It is unlikely, however, that the high P content simply reflects an igneous composition different from that of the Chester Lake target material, as the Tisdale targets do not follow typical igneous fractionation trends, such as that defined by martian meteorites (fig. S1C).

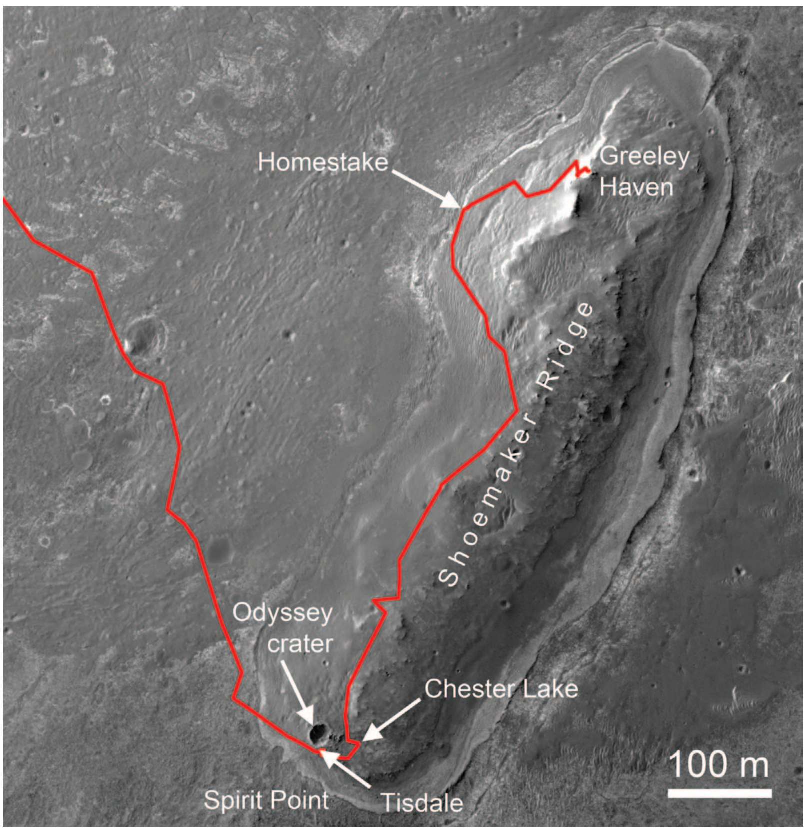

Fig. 1. Opportunity's traverse along the rim segment of Endeavour Crater named Cape York. Major features discussed in the text are indicated. Image was acquired by the Mars Reconnaissance Orbiter HiRISE camera. North is at the top.

It is instructive to compare the rim deposits of Endeavour Crater to those of the comparably sized Ries impact structure in Germany (*18*). At Ries, thin deposits of surficial suevite (*19*), often just a few meters thick, overlie the Bunte Breccia that dominates the impactites of the rim (*20*). The Bunte Breccia is a poorly sorted polymict lithic breccia. It represents the continuous ballistic ejecta deposit and is derived primarily from the uppermost lithologies of the target (*21*). Rounded clasts are common. The surficial suevite that overlies it was deposited late in the impact process, either via fallout from a gaseous ejecta plume (*22*) or as a surface-hugging flow (*23*). We suggest that a similar relationship may hold at Endeavour, with Tisdale representing the main breccia unit of the rim, and Chester Lake and the rocks near Greeley Haven emplaced later in the impact flow.

Tisdale's Zn abundances correlate with both S and P, which suggests that Zn sulfides, sulfates, and/or phosphates could be present. High-Zn materials on Earth are common in settings such as volcanogenic massive sulfide deposits, where hydrothermal circulation has mobilized Zn and caused precipitation of Zn sulfides and development of associated alteration products (*24*). The heating caused by an impact the size of Endeavour is sufficient to cause hydrothermal circulation if water is present (*25*). We suggest that the Zn enrichment in Tisdale could have resulted from such activity. Enrichments of trace metal mineralization by hydrothermal fluids will naturally be localized where fluids readily flow, including fractures, zones with increased permeability, and other void spaces. Highly heterogeneous distribution of secondary mineralization is therefore expected.

When normalized to the average composition of the sulfate-rich sandstones that constitute the Burns formation of the Meridiani plains (*2*, *3*), all rocks of the Shoemaker formation show fractionations among the major elements—for example, high Na/Mg and Al/Mg ratios (fig. S2). Either the Shoemaker formation is not representative of the feedstock for the sulfate-rich grains of the Burns formation, or the alteration process that formed those grains resulted in major compositional changes.

The composition of Shoemaker formation rocks is also not a good match to either Bounce Rock (*26*) or Marquette Island (*27*), two basaltic rocks encountered earlier in Opportunity's mission that lie atop Burns formation sandstones. These must be ejecta blocks from distant craters that postdate Endeavour, sampling different crustal materials.

Cape York is encircled by a gently outward-sloping topographic bench ~6 m wide on the west and up to 20 m wide on the east (Fig. 1). The outer part of the bench on the western side exposes bright, thinly bedded sandstones with bedding that dips shallowly toward the plains. These sandstones lie directly above darker granular sedimentary rocks that form the inner portion of the bench. This stratigraphic relationship is interpreted as the unconformable onlapping contact of the Burns formation onto older sedimentary materials shed from the Shoemaker formation. The inner bench materials, in turn, overlie the Noachian breccias that form the lower slopes of Cape York.

Bench materials are cut in many places by bright linear veins. Veins are prominent in the poorly exposed dark sedimentary materials of the inner bench, but occur within the bright outcrops of the basal Burns sandstone as well. Measurements of 37 veins yielded a mean width of 2 cm and a mean exposed length of 33 cm. Most vein orientations lie subparallel to the margins of Cape York.

Opportunity investigated one of these veins, named Homestake (Fig. 4), near the northern end of Cape York. Homestake forms a discontinuous, flat-topped ridge 1 to 1.5 cm wide and ~50 cm long. It stands up to ~1 cm above the surrounding bedrock, which suggests that it is more erosion-resistant than the material into which it was emplaced. Microscopic Imager (MI) images reveal a fine linear texture perpendicular to the trend of the vein (Fig. 4B).

Three separate APXS analyses were conducted on Homestake. All were similar (Table 1), with high abundances of SO_3 and CaO. The SO_3/CaO ratio is within a few percent of stoichiometry for $CaSO_4$, with a possible slight excess of sulfate. Other cations such as Mg, K, Al, and Fe do not show positive correlation with S, but Na does, so a small amount of Na sulfate could be present.

The nonsalt portion of the APXS measurement of Homestake is dominated by Si and Al, which are highly correlated with each other (R^2 = 0.89) and are anticorrelated with S (R^2 = 0.97 to 0.99). MI images (Fig. 4B) show, however, that contaminants must be present in this measurement. Homestake does not fill the ~3.8-cm circular field of view of the APXS, so contamination by background material (mostly dark sand in the MI images) must be present. MI images of Homestake show a mottled upper surface, also suggesting surface contamination.

Modeling the composition of Homestake as a three-component mixture of calcium sulfate,

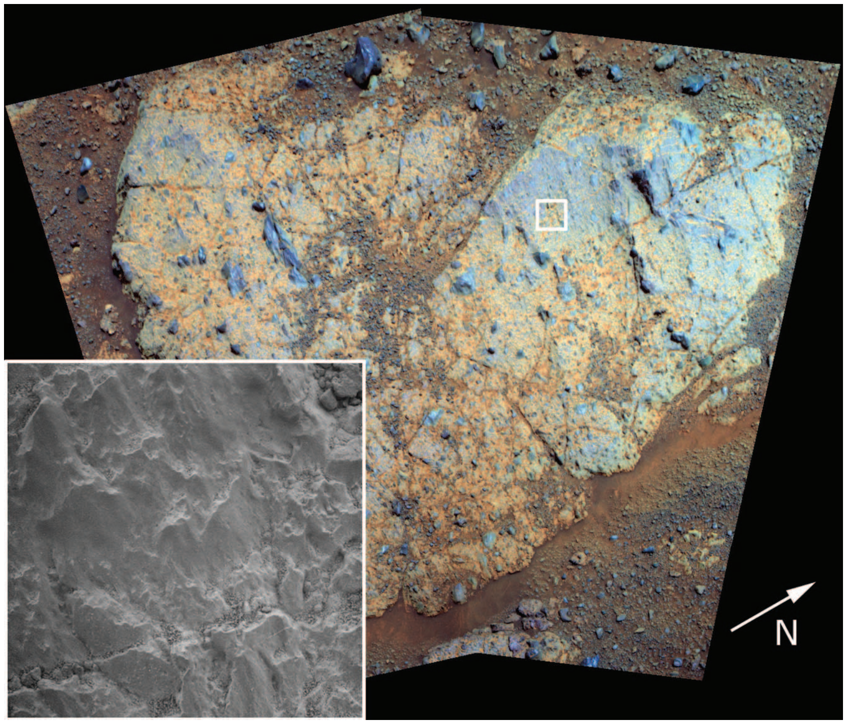

Fig. 2. Pancam false-color mosaic of the rock Chester Lake acquired on sol 2709 using the 753-, 535-, and 432-nm filters, sequence p2394. Scale across the image is ~1 m. Square shows location of MI image (inset) acquired on sol 2713. Scale across MI image is ~3 cm. Clasts in Chester Lake, which stand out in relief, are poorly sorted and irregularly shaped. The MI image shows irregular to cuspate fluting that is aligned with the orientations of elongate clasts.

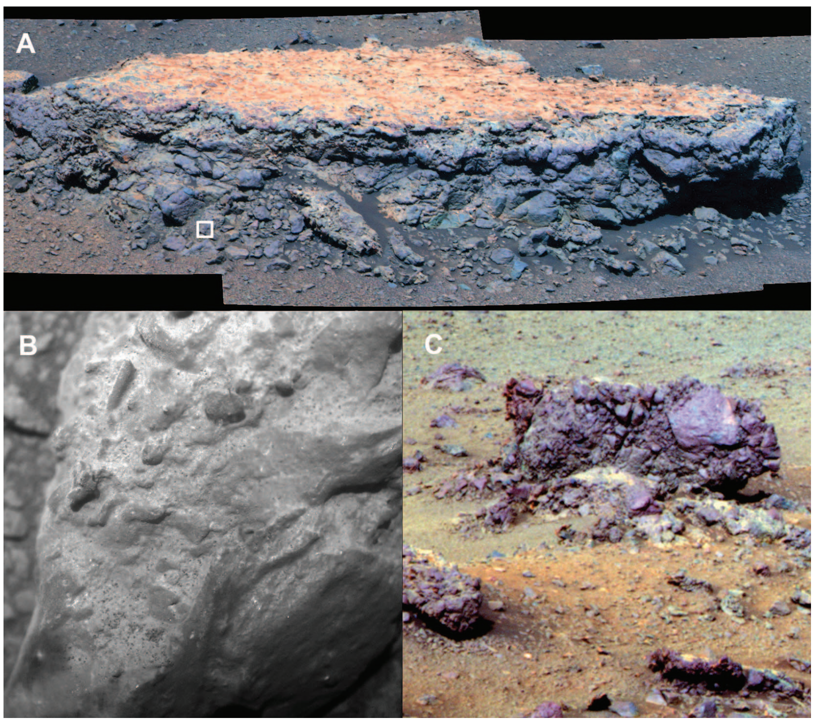

Fig. 3. Ejecta blocks from Odyssey crater. (**A**) Pancam false color image of the block Tisdale acquired on sol 2690 using the 753-, 535-, and 432-nm filters, sequence p2387. Height of Tisdale is ~30 cm. Square shows location of image in (B). (**B**) MI image acquired on sol 2696. Scale across the image is ~2.5 cm. (**C**) Pancam false-color image of the ejecta block Kidd Creek acquired on sol 2694 using the 753-, 535-, and 432-nm filters, sequence p2593. Scale across Kidd Creek is ~1 m. All images show a lithic breccia texture, with clasts ranging in size from tens of centimeters to near the resolution limit of MI images.

typical Meridiani basaltic sand, and typical martian dust, and accounting for the energy dependence of the signal from a thin dust layer, we find that the composition in Table 1 is matched by a mixture of 43% $CaSO_4$, 29% sand, and 28% dust 4 μm thick (*28*). Because the MI images are consistent with these amounts of background sand and surface dust contamination, we conclude that the vein material itself is predominantly $CaSO_4$, with perhaps minor Na_2SO_4, phosphate, and a Cl-containing salt.

Calcium sulfates can have a range of hydration states. APXS data do not constrain the hydration

Table 1. Elemental chemistry as determined by the APXS instrument, under the standard assumption of a homogeneous matrix. Chester Lake is a suevite-like breccia near Spirit Point (Fig. 1), and Transvaal and Boesmanskop are similar rocks near Greeley Haven. Tisdale is a lithic breccia with variable composition. Homestake is the vein in Fig. 4, and Deadwood is the material in which Homestake is emplaced.

	Chester Lake		Transvaal (matrix)	Boesmanskop (matrix)†	Komati (clast)	Tisdale‡	Homestake§	Deadwood	Basaltic sand‖	Dust#	Effective dust**
	Matrix*	Clast									
Weight percent											
Na_2O	2.7 ± 0.2	2.7 ± 0.2	2.3 ± 0.3	2.4 ± 0.4	2.4 ± 0.2	1.8 ± 0.3	1.6 ± 0.2	2.2 ± 0.2	2.34	2.31	2.28
						2.2 ± 0.3					
						2.5 ± 0.4					
MgO	8.8 ± 0.1	7.4 ± 0.1	7.5 ± 0.2	8.9 ± 0.2	8.4 ± 0.1	6.2 ± 0.1	4.7 ± 0.1	5.7 ± 0.1	7.33	7.62	7.18
						6.0 ± 0.1					
						6.2 ± 0.2					
Al_2O_3	8.8 ± 0.1	10.1 ± 0.2	9.2 ± 0.2	9.5 ± 0.2	9.3 ± 0.2	8.9 ± 0.2	4.8 ± 0.1	8.3 ± 0.2	9.65	9.21	7.99
						10.0 ± 0.2					
						10.1 ± 0.2					
SiO_2	45.5 ± 0.4	46.1 ± 0.5	45.9 ± 0.5	45.6 ± 0.5	44.7 ± 0.4	42.6 ± 0.5	25.3 ± 0.3	44.0 ± 0.5	46.97	45.33	35.29
						46.2 ± 0.5					
						45.4 ± 0.5					
P_2O_5	1.00 ± 0.08	1.13 ± 0.09	1.04 ± 0.10	1.21 ± 0.09	1.16 ± 0.09	3.14 ± 0.13	0.78 ± 0.11	1.13 ± 0.10	0.85	0.91	0.73
						1.22 ± 0.10					
						1.20 ± 0.10					
SO_3	3.1 ± 0.1	4.8 ± 0.1	6.3 ± 0.1	5.6 ± 0.1	5.8 ± 0.1	8.6 ± 0.2	32.7 ± 0.4	9.2 ± 0.1	4.68	7.23	5.02
						6.0 ± 0.1					
						6.5 ± 0.1					
Cl	0.9 ± 0.0	1.0 ± 0.0	1.0 ± 0.0	1.0 ± 0.0	0.9 ± 0.0	1.2 ± 0.0	1.0 ± 0.0	1.1 ± 0.0	0.59	0.81	0.48
						0.9 ± 0.0					
						1.0 ± 0.0					
K_2O	0.41 ± 0.06	0.46 ± 0.06	0.49 ± 0.06	0.51 ± 0.06	0.58 ± 0.06	0.43 ± 0.07	0.27 ± 0.06	0.62 ± 0.07	0.51	0.5	0.19
						0.50 ± 0.07					
						0.53 ± 0.07					
CaO	6.8 ± 0.1	7.1 ± 0.1	6.6 ± 0.1	5.7 ± 0.1	6.1 ± 0.1	7.1 ± 0.1	22.0 ± 0.2	6.7 ± 0.1	7.38	6.66	2.03
						6.8 ± 0.1					
						5.9 ± 0.1					
TiO_2	1.09 ± 0.08	1.15 ± 0.08	1.11 ± 0.08	1.03 ± 0.08	1.08 ± 0.07	0.99 ± 0.08	0.27 ± 0.06	0.98 ± 0.08	0.9	0.99	0.22
						1.05 ± 0.10					
						1.05 ± 0.09					
Cr_2O_3	0.25 ± 0.03	0.27 ± 0.04	0.28 ± 0.04	0.25 ± 0.04	0.18 ± 0.03	0.16 ± 0.04	0.13 ± 0.04	0.30 ± 0.04	0.39	0.34	0.05
						0.27 ± 0.04					
						0.23 ± 0.04					
MnO	0.48 ± 0.02	0.63 ± 0.02	0.41 ± 0.02	0.41 ± 0.02	0.59 ± 0.01	0.38 ± 0.02	0.15 ± 0.01	0.22 ± 0.02	0.39	0.36	0.04
						0.38 ± 0.02					
						0.23 ± 0.02					
FeO	20.1 ± 0.1	17.0 ± 0.2	17.8 ± 0.2	17.6 ± 0.2	18.7 ± 0.1	17.6 ± 0.2	6.4 ± 0.1	19.4 ± 0.2	17.57	17.59	1.62
						18.0 ± 0.2					
						18.8 ± 0.2					
Concentration (μg g^{-1})											
Ni	482 ± 54	461 ± 65	565 ± 64	615 ± 65	461 ± 48	950 ± 84	36 ± 83	410 ± 62	349	486	53
						1405 ± 95					
						2030 ± 108					
Zn	246 ± 18	244 ± 23	294 ± 23	350 ± 25	266 ± 15	6267 ± 108	121 ± 20	521 ± 29	199	390	29
						1798 ± 58					
						710 ± 42					
Br	124 ± 18	68 ± 19	139 ± 21	153 ± 22	229 ± 19	779 ± 35	68 ± 19	301 ± 25	24	31	1
						722 ± 34					
						377 ± 29					

*Sample abraded with the RAT. †Sample brushed with the RAT. ‡Measurements at three different locations on a relatively dust-free vertical face. §Average of three measurements. ‖Typical Meridiani basaltic sand composition. #Typical martian dust used in geochemical modeling of Homestake. **Effective composition of a layer of dust 4 μm thick, taking into account the energy dependence of the APXS signal.

state of Homestake because of the instrument's inability to detect H and the confounding effects of background and contamination discussed above. However, Pancam's longest-wavelength filter (1009 ± 19 nm) provides the ability to detect remotely and map spatially certain hydrated minerals, based on the presence of the $2\nu_1 + \nu_3$ H_2O combination absorption band and/or the $3\nu_{OH}$ overtone absorption band centered near ~1000 nm in many minerals containing bound H_2O and/or OH^- (*29*, *30*).

Figure 5A shows that hydrated mineral signatures [characterized by four total spectral parameters (*30*), including steeply negative slopes from 934 to 1009 nm] are detected in Homestake. These spectral features occur in three separate unsaturated Pancam observations acquired at different viewing geometries and incidence angles, convincing us that the signature is due to hydration in Homestake rather than any instrumental, calibration, or viewing geometry artifact (*30*). The magnitude of the hydration signature and the albedo both increased after Opportunity drove over and exposed fresh crushed parts of Homestake; this suggests that the hydrated material is not a superficial coating or rind, but rather a component of the bulk volume of the vein material.

Laboratory reflectance spectra of calcium sulfates convolved to Pancam bandpasses (Fig. 5B) suggest that the hydration signature is consistent with gypsum ($CaSO_4$•$2H_2O$), but not anhydrite ($CaSO_4$) or bassanite ($CaSO_4$•$0.5H_2O$). Anhydrite lacks a hydration band, and the weak bassanite hydration band is centered near ~950 nm, between Pancam's two longest-wavelength band centers.

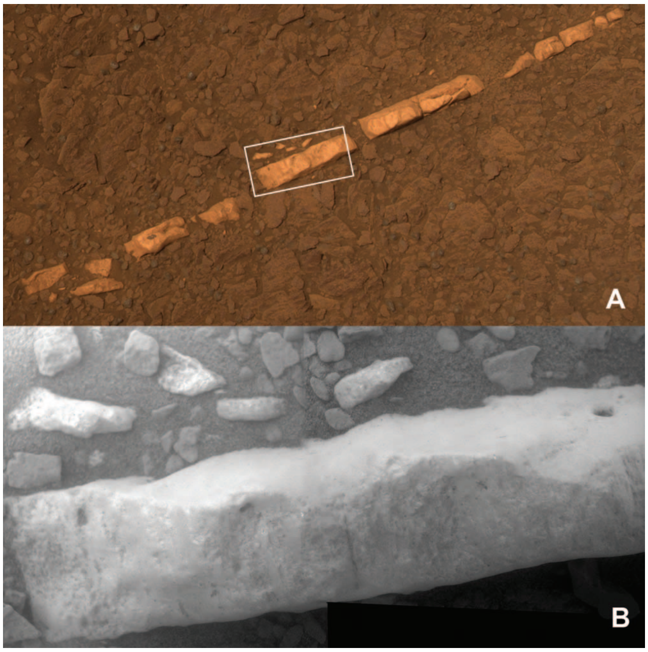

Fig. 4. (**A**) Pancam approximate true-color image of the vein Homestake acquired on sol 2769 using the 753-, 535-, and 432-nm filters, sequence p2574. Scale across the image is ~40 cm. Rectangle shows location of image in (B). (**B**) MI mosaic acquired on sol 2766.

Gypsum veins have been reported in a variety of settings on Earth, where their formation is invariably attributed to precipitation from relatively low-temperature (less than ~60°C) water in fractures (*31*–*34*). Vein growth is often antitaxial, with nucleation occurring at the vein-wall interface. Crystals precipitated in such settings are commonly fibrous, with long axes that track the opening trajectory of the fracture (*34*–*36*); fibers therefore form perpendicular to the vein axis when vein growth occurs in extension fractures. We suggest that the transverse lineations seen in MI images of Homestake are remnants of such a texture. The orientations of the veins themselves suggest that the rocks of the bench surrounding Cape York were subjected to horizontal tension perpendicular to the bench margins at the time of vein emplacement, perhaps related to sediment compaction, dewatering, and settling.

Homestake was emplaced in the darker inner unit of the bench surrounding Cape York. The rock of this unit is platy in appearance, with millimeter-scale layering that is poorly exposed but shows locally varying strikes and dips. Its elemental composition, measured at a location named Deadwood (Table 1), is similar to that of rocks of the Shoemaker formation, although without strong Zn and Ni enrichments. From its elevated Ca and S concentrations, Deadwood also appears to contain a small amount (~10%) of Homestake-like material. Typical Meridiani basaltic sand could constitute up to 30% of the total (MI images suggest 20 to 30% contamination), but not more because the Mn/Fe ratio would become untenably low. We interpret Deadwood to be a clastic sedimentary rock dominated by grains from the Shoemaker formation, with minor

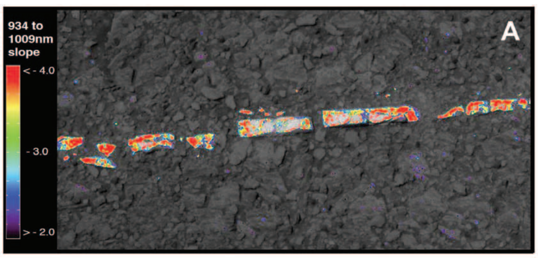

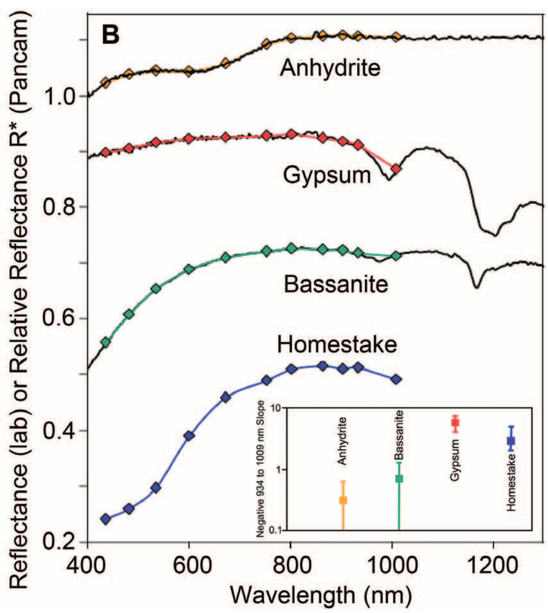

Fig. 5. (**A**) Pancam "hydration signature" data overlain on a 754-nm image of Homestake acquired on sol 2769, sequence p2574. Colors indicate regions where the 934- to 1009-nm spectral slope is negative and where four other hydration signature spectral parameters (*29*) are also met. (**B**) Comparison of Pancam relative reflectance [*R** (*41*)] spectra of Homestake to laboratory reflectance spectra (*42*) of three calcium sulfates with different levels of hydration. Solid lines are full-resolution lab spectra; points indicate lab spectra values convolved to Pancam bandpasses. The anhydrite, gypsum, and bassanite data are offset by +0.2, 0.0, and –0.2 reflectance units, respectively. The inset shows the magnitude of the negative 934- to 1009-nm spectral slope values for these three mineral samples compared to the minimum, average, and maximum Pancam Homestake values. Error bars represent estimated 1σ uncertainties on the laboratory and Pancam ratio values. Logarithmic plot; units are 10^{-4} nm^{-1}.

$CaSO_4$, perhaps as cement. Basaltic sand contaminates the APXS measurement but does not change this interpretation.

The key stratigraphic and crosscutting relationships along the western margin of Cape York are depicted in Fig. 6. We interpret the inner portion of the bench, characterized by Deadwood, to be the first sedimentary unit to form on Endeavour's rim, dominated by material shed from the Cape York breccias. This material, and the basal Burns formation sandstone that unconformably overlies it, were subsequently cut by fractures that were filled by gypsum precipitated from sulfate-rich fluids generated within the nearby Noachian crust. These fluids were likely at a low temperature (if hydrothermal, they were distal), because anhydrite would be expected otherwise. In pure water the gypsum/anhydrite conversion temperature is ~40° to 60°C, and in concentrated brines it can be substantially lower (*37*). Calcium sulfate was precipitated closest to the Noachian source rocks, rather than other sulfates (e.g., $MgSO_4 \cdot nH_2O$; $FeSO_4 \cdot nH_2O$) or chlorides, because of its lower solubility. Some gypsum was also precipitated as cement in the bedrock. Unlike the Burns formation sulfates that dominate the Meridiani plains and are rich in jarosite (*2*, *3*), the gypsum of Homestake did not require acidic fluids for its formation. We suggest, however, that the fluids from which the gypsum was precipitated may have been a contributor to the overall hydrologic budget responsible for formation of the Meridiani sulfate sandstones.

The absence of substantial deformation of the veins suggests that there has been minimal transformation between gypsum and anhydrite since emplacement. The molar volumes of these minerals differ by a factor of ~1.6; in terrestrial settings, such transformations typically produce complex deformation features (*38*). The absence of gypsum-anhydrite transformations further suggests that these rocks remained at relatively low temperatures since vein emplacement.

Development of the materials investigated at Endeavour began with an impact into basaltic rocks, producing breccias with a stratigraphy similar to that observed at some comparably sized terrestrial impact craters. Degradation and shedding of these breccias formed thin sedimentary materials immediately surrounding Cape York, over which the basal Burns formation sandstones were unconformably deposited. Emplacement of the gypsum veins then took place, postdating the earliest Burns formation sandstones but probably predating much of the rest of the Burns formation stratigraphy encountered by Opportunity.

The ubiquity of impact breccia at Cape York contrasts with the only other Noachian terrain explored in situ, the Columbia Hills in Gusev Crater. The rover Spirit encountered great lithologic diversity there, including materials interpreted as impact ejecta (*11*). However, none were breccias, and none had the lateral extent of the Shoemaker formation. We suggest that the difference can be attributed to Opportunity's sampling of the rim deposits of a single large crater, rather than Spirit's sampling of more distal ejecta from multiple impacts.

The gypsum veins at Cape York provide clear evidence for relatively dilute [water activity $a_w \approx 0.98$ (*39*)] water at a moderate temperature, perhaps supporting locally and transiently habitable environments. More broadly, rocks at Cape York appear to record early events in a transition from (commonly) hydrothermal waters that altered basaltic crust to phyllosilicates (*40*) to sulfate-charged ground waters that generated salt-rich sandstones deposited widely over the Meridiani plains and elsewhere.

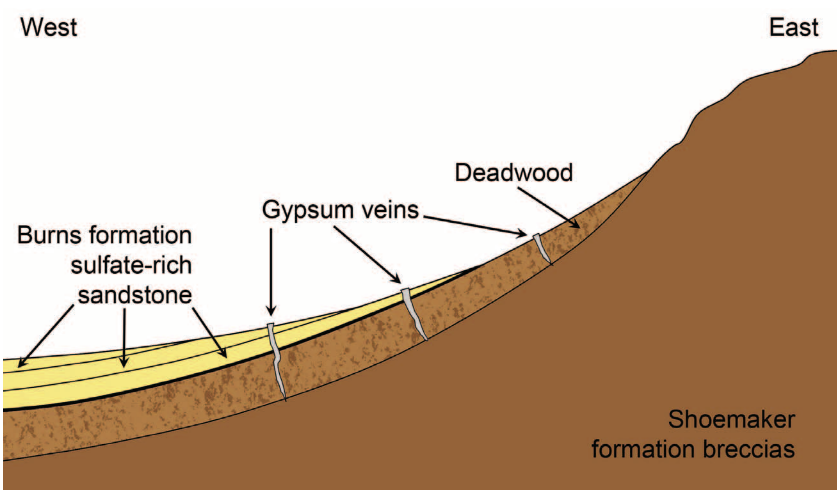

Fig. 6. Schematic east-west cross section, with large vertical exaggeration, through the western flank of Cape York. Materials shed from the Shoemaker formation breccias form the lowest sedimentary unit, which includes Deadwood. This unit is overlain by the sulfate-rich sandstones of the Burns formation; the heavy line separating them represents an unconformity. The Deadwood unit and the basal portion of the Burns formation closest to Cape York are cut by fractures; these fractures are filled with gypsum that was precipitated from waters arising from the underlying breccias.

References and Notes

1. The Noachian is a geologic system on Mars representing the oldest period of the planet's geologic history, characterized by high impact rates.
2. S. W. Squyres *et al.*, *J. Geophys. Res.* **111**, E12S12 (2006).
3. R. E. Arvidson *et al.*, *J. Geophys. Res.* **116**, E00F15 (2011).
4. J. J. Wray *et al.*, *Geophys. Res. Lett.* **36**, L21201 (2009).
5. A sol is defined as one martian solar day.
6. Shoemaker Ridge is named to honor the late Eugene M. Shoemaker, one of the founders of planetary geoscience.
7. Greeley Haven is named to honor the late Ronald Greeley, distinguished planetary scientist and member of the Athena Science Team.
8. S. W. Squyres *et al.*, *J. Geophys. Res.* **108**, 8062 (2003).
9. The Miniature Thermal Emission Spectrometer (Mini-TES) was not used for this investigation because of temperature-related instrument degradation and optically thick dust on its mirrors accumulated during a prior global dust storm. The Mössbauer Spectrometer was not used because of the decay of its ^{57}Co radiation source.
10. T. Myrick *et al.*, in *Proceedings of AIAA Space 2004 Conference and Exhibit* (American Institute of Aeronautics and Astronautics, Reston, VA, 2004), pp. 1–11.
11. S. W. Squyres *et al.*, *J. Geophys. Res.* **111**, E02S11 (2006).
12. R. E. Arvidson *et al.*, *Science* **306**, 1730 (2004).
13. D. Stöffler, R. A. F. Grieve, in *Metamorphic Rocks: A Classification and Glossary of Terms, Recommendations of the International Union of Geological Sciences*, D. Fettes, J. Desmons, Eds. (Cambridge Univ. Press, Cambridge, 2007), chap. 2.11.
14. C. Meyer, M. Jebrak, D. Stoffler, U. Riller, *Geol. Soc. Am. Bull.* **123**, 2312 (2011).
15. M. E. Schmidt *et al.*, *J. Geophys. Res.* **113**, E06S12 (2008).
16. C. G. Wheat, R. A. Feely, M. J. Motti, *Geochim. Cosmochim. Acta* **60**, 3593 (1996).
17. E. S. Deevey Jr., *Sci. Am.* **223**, 148 (1970).
18. J. Pohl *et al.*, in *Impact and Explosion Cratering*, D. J. Roddy, R. O. Pepin, R. B. Merrill, Eds. (Pergamon, New York, 1977), pp. 343–404.
19. W. von Engelhardt *et al.*, *Meteoritics* **30**, 279 (1995).
20. W. von Engelhardt, *Tectonophysics* **171**, 250 (1990).
21. F. Hörz, R. Ostertag, D. A. Rainey, *Rev. Geophys.* **21**, 1667 (1983).
22. W. von Engelhardt, *Meteorit. Planet. Sci.* **32**, 545 (1997).
23. H. E. Newsom, G. Graup, T. Sewards, K. Keil, *J. Geophys. Res.* **91**, E239 (1986).
24. J. M. Franklin, J. W. Lydon, D. F. Sangster, *Econ. Geol.* (75th anniv. volume), 485 (1981).
25. J. A. Rathbun, S. W. Squyres, *Icarus* **157**, 362 (2002).
26. J. Zipfel *et al.*, *Meteorit. Planet. Sci.* **46** (suppl. S1), A1 (2011).
27. D. W. Mittlefehldt *et al.*, *Lunar Planet. Sci.* **41**, 2109 (2009).
28. A 4-μm-thick dust layer is the simplest model that fits the APXS data; the actual dust coating is probably discontinuous and variable in thickness.
29. A. Wang *et al.*, *J. Geophys. Res.* **113**, E12S40 (2008).
30. M. S. Rice *et al.*, *Icarus* **205**, 375 (2010).
31. S. Taber, *J. Geol.* **26**, 56 (1918).
32. T. C. Gustavson *et al.*, *J. Sed. Res. A* **64**, 88 (1994).
33. M. El Tabakh *et al.*, *J. Sed. Res.* **68**, 88 (1998).
34. S. L. Philipp, *Geol. Mag.* **145**, 831 (2008).
35. D. W. Durney, J. G. Ramsay, in *Gravity and Tectonics*, K. A. de Jong, R. Scholten, Eds. (Wiley, New York, 1973), pp. 67–96.
36. P. D. Bons, M. Montenari, *J. Struct. Geol.* **27**, 231 (2005).

37. D. Freyer, W. Voigt, *Monatsh. Chem.* **134**, 693 (2003).
38. W. M. Bundy, *J. Sed. Res* **26**, 240 (1956).
39. N. J. Tosca, A. H. Knoll, S. M. McLennan, *Science* **320**, 1204 (2008).
40. B. L. Ehlmann *et al.*, *Nature* **479**, 53 (2011).
41. J. F. Bell III *et al.*, *J. Geophys. Res.* **108**, 8063 (2003).
42. R. N. Clark *et al.*, U.S. Geological Survey, USGS Digital Spectral Library 06 (2007); http://speclab.cr.usgs.gov/spectral.lib06.

Acknowledgments: This research was carried out for the Jet Propulsion Laboratory, California Institute of Technology, under a contract with NASA.

Supplementary Materials
www.sciencemag.org/cgi/content/full/336/6081/570/DC1
Figs. S1 and S2
References (*43–96*)

13 February 2012; accepted 3 April 2012
10.1126/science.1220476

21st-Century Evolution of Greenland Outlet Glacier Velocities

T. Moon,[1,2]* I. Joughin,[2] B. Smith,[2] I. Howat[3,4]

Earlier observations on several of Greenland's outlet glaciers, starting near the turn of the 21st century, indicated rapid (annual-scale) and large (>100%) increases in glacier velocity. Combining data from several satellites, we produce a decade-long (2000 to 2010) record documenting the ongoing velocity evolution of nearly all (200+) of Greenland's major outlet glaciers, revealing complex spatial and temporal patterns. Changes on fast-flow marine-terminating glaciers contrast with steady velocities on ice-shelf–terminating glaciers and slow speeds on land-terminating glaciers. Regionally, glaciers in the northwest accelerated steadily, with more variability in the southeast and relatively steady flow elsewhere. Intraregional variability shows a complex response to regional and local forcing. Observed acceleration indicates that sea level rise from Greenland may fall well below proposed upper bounds.

Changes in glacier dynamics contribute to roughly half of the Greenland Ice Sheet's current mass loss (~250 Gt/year, equivalent to 0.6 mm/year sea level rise) (*1*, *2*), largely through thinning and increased calving as glaciers have sped up. Large changes in ice dynamics have been observed (*3*), but were not accounted for in early models and led to the inability to quantify uncertainty of 21st-century sea level rise in the Intergovernmental Panel on Climate Change's (IPCC's) Fourth Assessment (*4*). Although multiglacier speedups have been linked to recent warming in Greenland (*5*–*7*), the exact connection to climate change is poorly known, but may be related to processes controlled by ice-ocean interaction (*8*–*10*). A firm understanding of the processes driving recent change, which is needed to improve predictions of sea level rise, requires a better characterization of the temporal and spatial patterns of ice flow across the ice sheet.

Despite the need for comprehensive data, recent studies of glacier velocity in Greenland are limited in spatial and temporal resolution. For Jakobshavn Isbræ, Helheim Gletscher, and Kangerdlugssuaq Gletscher, three of Greenland's fastest outlet glaciers, velocity is relatively well documented (*3*, *11*, *12*). For most of Greenland's other 200+ outlet glaciers, however, observation has been limited to ~5-year sampling on an ice-sheet–wide scale (*13*, *14*) or smaller regions with more frequent sampling (*7*). Where comprehensive records exist, they have been used to focus on aggregate discharge rather than regional variability (*2*). We present a decade-long record, with annual sampling for the latter half, to examine decadal-scale trends and regional and local interannual variation, and to inform predictions of sea level rise.

To create this record, we produced velocity maps for winter 2000 to 2001 (referred to as 2000) and annually for each winter from 2005 to 2006 through 2010 to 2011 (referred to using the earlier year for the map), using synthetic aperture radar data from the Canadian Space Agency's RADARSAT-1, German TerraSAR-X, and Japanese Advanced Land Observation Satellite (ALOS) (table S1). We used a combination of speckle-tracking and interferometric algorithms to estimate ice-flow velocity (*14*, *15*). Coverage for each year is almost complete, with some unavoidable gaps, primarily in the south, due to satellite acquisition limits.

Of the 206 largest Greenland outlet glaciers, 178 have adequate temporal coverage for 2000 to 2005, and 195 have sufficient data for 2005 to 2010 (Fig. 1) (*16*). We divided these glaciers into several categories. First, we identified land-terminating, ice-shelf–terminating (ice shelf >10 km long), and low-velocity marine-terminating (mean velocity <200 m/year) glaciers (55 total). Next, glaciers with highly variable behavior were separated to avoid misrepresenting large variations as consistent trends (*16*). This included glaciers such as Harald Moltke Bræ (fig. S1), where apparent surge behavior produces erratic changes (*17*). The final group consisted of fast-flow marine-terminating glaciers that we fit with linear regressions for all available data for 2000 to 2005 (111 glaciers) and 2005 to 2010 (123 glaciers) to evaluate trends and fill data gaps (figs. S2 and S3).

Our record reveals the complexity of Greenland's ice flow. Greenland's largest land-terminating glaciers are located primarily along the southwest coast, with a few in the northeast (Fig. 1). Nearly all flow at peak velocities between 10 and 100 m/year, so that annual changes of 10 to 30 m/year produce large long-term trends (>15% change over 5 years). Most (70%) of the land-terminating glaciers with a notable trend slowed during 2005 to 2010—a continuing trend for half of them. The scale of these changes, however, is close to the measurement error and seasonal variability (*11*) and orders of magnitude smaller than changes seen on many fast-flowing glaciers. The one outlier, Frederikshab Isblink (fig. S1), has a large lobe-shaped terminus that is primarily land-terminating, but with one segment of lake-terminating ice front. The velocity field suggests that this segment helps the glacier maintain a higher peak velocity (~270 m/year) than other land-terminating glaciers and hints at the importance of a calving terminus in maintaining fast ice flow.

Ice-shelf–terminating glaciers (Fig. 1) have mean velocities (300 to 1670 m/year) that are generally slower than those of other marine-terminating glaciers (total mean: 1890 m/year), but most show negligible change for 2000 to 2010. The most notable change occurred on Hagen Bræ (from 50 m/year in 2000 to 650 m/year in 2007), a previously identified surge-type glacier (*18*).

Surge-type glaciers occur mostly in the northwest, north, and east (*18*, *19*). In several cases, 1- or 2-year velocity changes suggest surge-type behavior, as observed on Harald Moltke Bræ (high speed in 2005), where surges have been recorded before, and Adolf Hoel Gletscher (low speed in 2007) (fig. S1) and Kangilerngata sermia (low speed in 2005), where earlier surges have not been recorded. Other glaciers where surges have been observed previously, including Storstrommen and L. Bistrup Bræ (*18*) and Sortebræ (*20*), maintained quiescent speeds over the past decade.

Most glaciers in east Greenland are marine-terminating, but have substantially slower mean velocities (1040 m/year) relative to southeast (2830 m/year) or northwest (1630 m/year) marine-terminating glaciers. This is consistent with the lower regional discharge from this low accumulation area (*21*). As a group, eastern glaciers showed only negligible changes from 2000 to

[1]Earth and Space Sciences, University of Washington, Seattle, WA 98195, USA. [2]Polar Science Center, Applied Physics Lab, University of Washington, Seattle, WA 98105, USA. [3]School of Earth Sciences, Ohio State University, Columbus, OH 43210, USA. [4]Byrd Polar Research Center, Ohio State University, Columbus, OH 43210, USA.

*To whom correspondence should be addressed. E-mail: twilap@uw.edu

2010. The low decadal-scale variability may be related to colder surface and subsurface ocean temperatures north of ~69°N (*22*). Of the few glaciers where we did detect a trend, at least half were slowing in each period (Fig. 1). The predominance of surge-type glaciers in the east (*19*) also suggests that the few notable trends may result from surge-related dynamics, which represent velocity changes that are not necessarily linked to climate (*23*, *24*).

Fast-flow marine-terminating glaciers are the dominant type in the northwest, and regional speed increased there by 8% from 2000 to 2005 (Fig. 2). This was followed by a larger increase (18%) from 2005 to 2010, with most of the speedup during 2007 to 2010 (14%). This trend results from a number of glaciers speeding up and is not driven by the acceleration of any particular glacier (supplementary materials). Despite the overall increase, however, there is not a uniform pattern of synchronous intraregional acceleration (fig. S2). A third of northwest glaciers steadily increased over the whole decade, whereas ~15% slowed from 2000 to 2005 and then accelerated substantially from 2005 to 2010. Another third of the glaciers showed no trend, and a quarter of the region's glaciers slowed over the decade (Fig. 1).

Greenland's southeast sector also has a high concentration of marine-terminating glaciers. Satellite coverage is more limited in this region, which allowed us to sample 35 of 47 glaciers for the whole decade (Fig. 1). Many (43%) of these glaciers sped up substantially over the first half of the decade, but most did not maintain their rate of acceleration to 2010, and a third dropped below their 2005 speed. Across the region, a quarter of the glaciers slowed by more than 15% from 2005 to 2010 (none did during 2000 to 2005). As a result, the southeast's mean velocity in 2010 (3120 m/year) was less than 200 m/year higher than its 2005 mean (2980 m/year) (Fig. 2)—the result of a 2005 to 2006 slowdown followed by a sluggish 2006 to 2010 speedup (50 to 110 m/year average annual speedup). The pattern is similar when excluding the three fastest 2010 glaciers, though the annual speedup after 2005 is lower (20 to 60 m/year average annual speedup). Like the northwest, however, the regional trend in the southeast does not describe most individual glaciers (fig. S3). Instead, large speedups on many glaciers during 2005 to 2010 are balanced by considerable slowing on others (Fig. 1).

Despite some consistency in regional trends, the data show a marked degree of overall variability. Substantial acceleration (28%) in the southeast and on Jakobshavn Isbræ (32%) from 2000 to 2005 garnered much attention (*7*, *13*, *25*) and raised concern about the climate sensitivity of the Greenland Ice Sheet, particularly because these changes were not included in IPCC sea level rise predictions (*4*). Subsequent studies found that acceleration was not sustained on the southeast's largest glaciers, but continued on Jakobshavn (*3*). Our expanded record shows

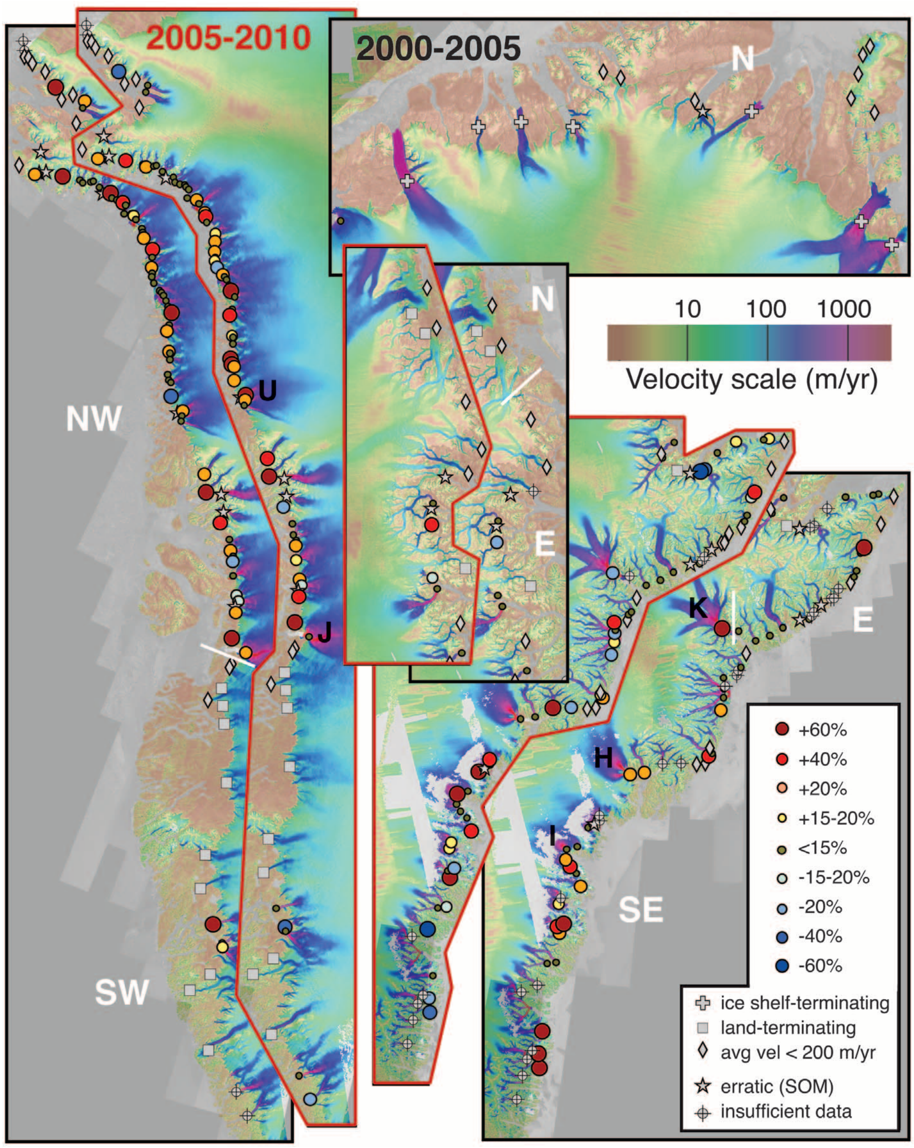

Fig. 1. Outlet glacier categories and rates of velocity change (percentage change from beginning of 5-year period). Black-outlined images show 2000 to 2005 results, and red-outlined images are 2005 to 2010 results. The background velocity map for both periods is a 2007 to 2010 composite, with the five ice-sheet regions indicated: north (N), northwest (NW), southwest (SW), southeast (SE), and east (E). There was no change for the north during 2005 to 2010. Jakobshavn (J), Upernavik North (U), Helheim (H), Kangerdlugssuaq (K), and Ikeq Fjord (I) glaciers are indicated.

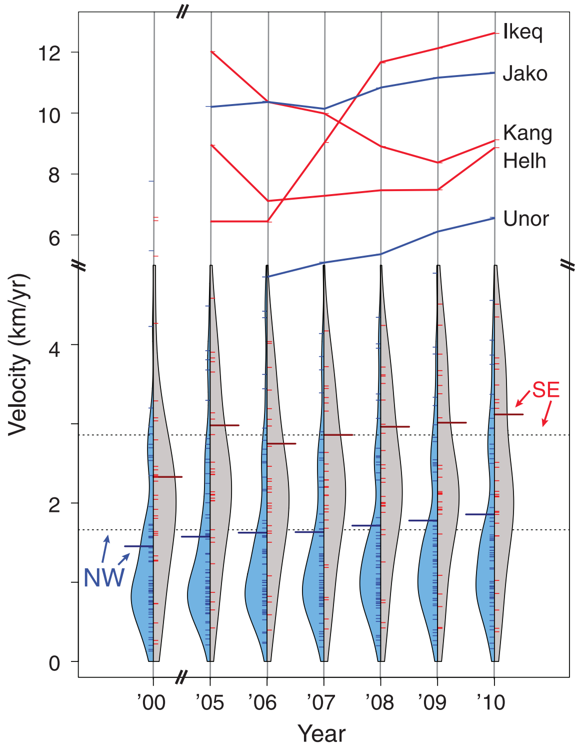

Fig. 2. Bottom: Distribution of glacier speeds (short ticks), smoothed speed density (colored bars), and mean speeds (long ticks) for 7 years' data. The northwest region is shown in blue with blue tick marks (left side) and the southeast region in gray with red tick marks (right side). Dashed black lines indicate regional mean speed over the entire decade (top for southeast, bottom for northwest). Only glaciers with sufficient data for both 2000 to 2005 and 2005 to 2010 are included. **Top:** Velocity plots for Jakobshavn (Jako), Upernavik North (Unor), Kangerdlugssuaq (Kang), Helheim (Helh), and Ikeq Fjord (Ikeq).

that these patterns are truly region-wide: Early acceleration in the southeast decreased, with little change from 2005 to 2010, whereas the northwest overall maintained relatively steady acceleration throughout the decade. As a result, 2000 to 2010 acceleration in the northwest (28%) is comparable to that in the southeast (34%).

Differences in the regional velocity patterns for the northwest and southeast may be connected to ice-sheet environment; many northwest glaciers are embedded within the surrounding ice sheet so that strongly convergent flow may limit rapid thinning, whereas southeast glaciers tend to flow through long fjords where along-flow stretching can produce rapid thinning as a glacier speeds up, potentially creating faster and larger fluctuations in speed (*3*). Ocean water characteristics may also affect regional trends. Both southeast and northwest glaciers respond to changes in warm North Atlantic waters, but geography and atmospheric and ocean circulation patterns control when and how these warm waters reach the separate sectors (*8*, *26*, *27*).

Although ocean and climate factors seem to exert a regional influence (*7*, *22*, *26*), the effect on any particular glacier is highly variable and may be primarily affected by a wide range of local factors (*28*, *29*). We observe many instances of asynchronous behavior on neighboring glaciers on annual (fig. S2 and S3) and decadal (Fig. 1) time scales. Influencing factors likely include fjord, glacier, and bed geometry (*3*); local climate (*30*); and small-scale ocean water flow and terminus sea ice conditions (*31*, *32*). The scale of many of Greenland's glaciers (<5 km width) suggests that high-resolution models with detailed topography and local conditions may be necessary to resolve this complex behavior—a challenge that remains from individual glacier to full ice-sheet simulations. Despite the extent of our observations, this remains a glaciologically short record, and efforts in modeling and statistical extrapolation will benefit as the period of observation lengthens.

Finally, our observations have implications for recent work on sea level rise. Earlier research (*33*) used a kinematic approach to estimate upper bounds of 0.8 to 2.0 m for 21st-century sea level rise. In Greenland, this work assumed ice-sheet–wide doubling of glacier speeds (low-end scenario) or an order of magnitude increase in speeds (high-end scenario) from 2000 to 2010. Our wide sampling of actual 2000 to 2010 changes shows that glacier acceleration across the ice sheet remains far below these estimates, suggesting that sea level rise associated with Greenland glacier dynamics remains well below the low-end scenario (9.3 cm by 2100) at present. Continued acceleration, however, may cause sea level rise to approach the low-end limit by this century's end. Our sampling of a large population of glaciers, many of which have sustained considerable thinning and retreat, suggests little potential for the type of widespread extreme (i.e., order of magnitude) acceleration represented in the high-end scenario (46.7 cm by 2100). Our result is consistent with findings from recent numerical flow models (*34*).

References and Notes

1. M. van den Broeke *et al.*, *Science* **326**, 984 (2009).
2. E. Rignot, I. Velicogna, M. Van Den Broeke, A. Monaghan, J. Lenaerts, *Geophys. Res. Lett.* **38**, L05503 (2011).
3. I. M. Howat, I. Joughin, T. A. Scambos, *Science* **315**, 1559 (2007).
4. IPCC, *Climate Change 2007: The Physical Science Basis. Contribution of Working Group I to the Fourth Assessment Report of the Intergovernmental Panel on Climate Change*, S. Solomon *et al.*, Eds. (Cambridge Univ. Press, Cambridge, 2007).
5. R. S. van de Wal *et al.*, *Science* **321**, 111 (2008).
6. H. J. Zwally *et al.*, *J. Glaciol.* **57**, 88 (2011).
7. I. Howat, I. Joughin, M. Fahnestock, B. Smith, T. Scambos, *J. Glaciol.* **54**, 646 (2008).
8. D. M. Holland, R. H. Thomas, B. de Young, M. H. Ribergaard, B. Lyberth, *Nat. Geosci.* **1**, 659 (2008).
9. E. Rignot, M. Koppes, I. Velicogna, *Nat. Geosci.* **3**, 187 (2010).
10. C. S. Andresen *et al.*, *Nat. Geosci.* **5**, 37 (2011).
11. I. Joughin *et al.*, *Science* **320**, 781 (2008).
12. I. Howat *et al.*, *Geophys. Res. Lett.* **38**, L12501 (2011).
13. E. Rignot, P. Kanagaratnam, *Science* **311**, 986 (2006).
14. I. Joughin, B. Smith, I. Howat, T. Scambos, T. Moon, *J. Glaciol.* **56**, 415 (2010).
15. I. Joughin, *Ann. Glaciol.* **34**, 195 (2002).
16. Materials and methods are available on *Science* Online as supplementary materials.
17. S. J. Mock, *J. Glaciol.* **6**, 369 (1966).
18. E. Rignot, S. Gogineni, I. Joughin, W. Krabill, *J. Geophys. Res.* **106**, 34007 (2001).
19. H. Jiskoot, T. Murray, A. Luckman, *Ann. Glaciol.* **36**, 142 (2003).
20. T. Murray, T. Strozzi, A. Luckman, H. Pritchard, H. Jiskoot, *Ann. Glaciol.* **34**, 323 (2002).
21. J. E. Box *et al.*, *J. Clim.* **19**, 2783 (2006).
22. A. Seale, P. Christoffersen, R. I. Mugford, M. O'Leary, *J. Geophys. Res.* **116**, F03013 (2011).
23. B. Kamb *et al.*, *Science* **227**, 469 (1985).
24. T. Murray, T. Strozzi, A. Luckman, H. Jiskoot, P. Christakos, *J. Geophys. Res.* **108**, 2237 (2003).
25. I. Joughin, W. Abdalati, M. Fahnestock, *Nature* **432**, 608 (2004).
26. T. Murray *et al.*, *J. Geophys. Res.* **115**, F03026 (2010).
27. F. Straneo *et al.*, *Nat. Geosci.* **3**, 182 (2010).
28. F. Nick *et al.*, *J. Glaciol.* **58**, 229 (2012).
29. I. Howat, I. Joughin, S. Tulaczyk, S. Gogineni, *Geophys. Res. Lett.* **32**, L22502 (2005).
30. A. Shepherd *et al.*, *Geophys. Res. Lett.* **36**, L01501 (2009).
31. F. Straneo *et al.*, *Nat. Geosci.* **4**, 322 (2011).
32. J. Amundson *et al.*, *J. Geophys. Res.* **115**, F01005 (2010).
33. W. T. Pfeffer, J. T. Harper, S. O'Neel, *Science* **321**, 1340 (2008).
34. S. F. Price, A. J. Payne, I. M. Howat, B. E. Smith, *Proc. Natl. Acad. Sci. U.S.A.* **108**, 8978 (2011).

Acknowledgments: Velocity products were processed under NASA MEaSUREs (NNX08AL98A). Analysis was funded by an NSF Graduate Research Fellowship (T.M.) and grants NSF ANT-0852697 (I.J.) and NNX08AQ83G (B.S. and I.H.). Velocity data maps are or will be available via the MEaSUREs Earth Science Data Record at the National Snow and Ice Data Center, Boulder, CO (http://nsidc.org/data/nsidc-0478.html). We acknowledge the contributions of synthetic aperture radar data from the Canadian (CSA), German (DLR), and Japanese (JAXA) space agencies. We thank three anonymous reviewers and J. Carmichael for comments that improved the manuscript.

Supplementary Materials
www.sciencemag.org/cgi/content/full/336/6081/576/DC1
Materials and Methods
Figs. S1 to S3
Table S1
Reference (*35*)

2 February 2012; accepted 28 March 2012
10.1126/science.1219985

Imaginal Discs Secrete Insulin-Like Peptide 8 to Mediate Plasticity of Growth and Maturation

Andres Garelli,* Alisson M. Gontijo,* Veronica Miguela, Esther Caparros, Maria Dominguez†

Developing animals frequently adjust their growth programs and/or their maturation or metamorphosis to compensate for growth disturbances (such as injury or tumor) and ensure normal adult size. Such plasticity entails tissue and organ communication to preserve their proportions and symmetry. Here, we show that imaginal discs autonomously activate DILP8, a *Drosophila* insulin-like peptide, to communicate abnormal growth and postpone maturation. DILP8 delays metamorphosis by inhibiting ecdysone biosynthesis, slowing growth in the imaginal discs, and generating normal-sized animals. Loss of *dilp8* yields asymmetric individuals with an unusually large variation in size and a more varied time of maturation. Thus, DILP8 is a fundamental element of the hitherto ill-defined machinery governing the plasticity that ensures developmental stability and robustness.

Animal size is remarkably constant within species. This constancy is even more striking within the animal, such as in comparing the left and right sides of bilaterian organisms—for example, the symmetry of a human face or the coincidence in size of the left and right hand. Such precision requires growing organs to communicate and coordinate their final sizes, processes that have long remained poorly understood (*1*).

The imaginal disc epithelia that generate the adult *Drosophila* structures have a remarkable capacity to regulate their size, although only in larvae (*2*). The onset of the larval-pupal transition is controlled by pulses of the steroid hormone 20-hydroxyecdysone (20HE), as initiated by brain-derived prothoracicotropic hormone (PTTH), and this transition marks the end of imaginal disc growth (*3*, *4*). Typically, the time of pupariation adapts to accommodate imaginal disc growth (*4*), and indeed, pupariation is delayed when imaginal discs suffer lesions to allow the missing parts to be restituted (*5*–*7*). The length of the delay correlates with the amount of tissue to be regenerated (*6*), indicating that the endocrine system fine-tunes organ growth (or regeneration) and adjusts maturation accordingly. Tumor growth in imaginal discs also delays or blocks metamorphosis [(*8*) and citations therein]. Moreover, larvae with imaginal discs that are damaged or contain tumors metamorphose at the correct size (*9*). Thus, we speculated that tumors and regenerating discs might emit a common signal to adapt growth and maturation.

We attempted to identify such a signal in oligonucleotide microarrays (fig. S1) by screening for genes encoding signal peptides that are up-regulated in association with tumors in eye discs induced by an oncogenic combination of the Notch ligand *Delta* and two neighboring epigenetic repressors, *pipsqueak* and what are collectively called "eyeful" (*10*), which causes massive overgrowth and metastasis. *CG14059* was the most consistently enriched putatively secreted gene product in tumor discs (Fig. 1A and table S1) and was also enriched during transdetermination (*11*),

Instituto de Neurociencias, Consejo Superior de Investigaciones Científicas–Universidad Miguel Hernández de Elche, Sant Joan d'Alacant, 03550 Alicante, Spain.

*These authors contributed equally to this work.

†To whom correspondence should be addressed. E-mail: m.dominguez@umh.es

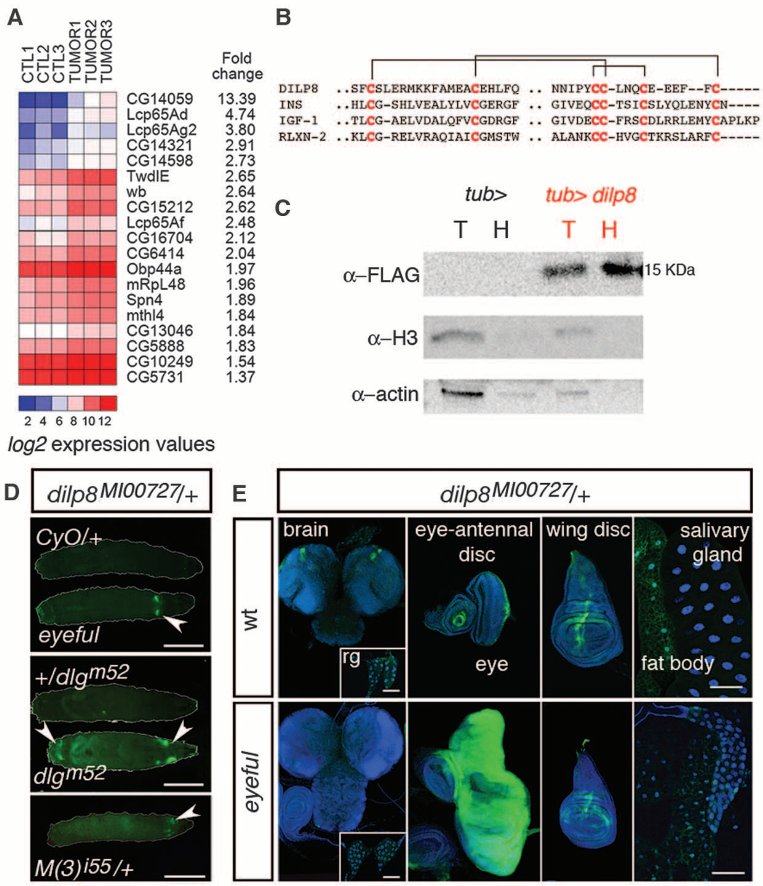

Fig. 1. Tumor discs produce DILP8, a divergent insulin/relaxin-like peptide. (**A**) Heat map of putatively secreted genes up-regulated in eyeful tumor eye discs from three independent replicates (1 to 3) of microarray experiments in which expression is color-coded. Relative gene expression levels are color-coded to range from blue (lower levels of gene expression), through white (medium expression), to red (higher levels of expression). CTL, control non-tumor eye discs [*+/UAS-Dl GS(2)88A8$^{lola\ pipsqueak}$*]; TUMOR, eyeful tumor eye discs [*+/ey-Gal4 UAS-Dl GS(2)88A8$^{lola\ pipsqueak}$*]. (**B**) Alignments of CG14059/DILP8 with representative members of the human insulin-like family of peptides. Alignments of DILP8 with the seven *Drosophila* ILPs characterized previously are shown in fig. S1. (**C**) DILP8 is readily detected in the cell-free hemolymph (H) of *tub>dilp8::3x-FLAG* larvae in Western blots probed with anti-FLAG antibodies. Total (T) hemolymph extract serve as loading controls. Samples are free of cell contamination, as shown by actin and histone H3 controls. (**D**) Responses of eGFP trap *dilp8^{MI00727}* to abnormal imaginal disc growth (arrowheads). Scale bars, 1 mm. Controls (top images in top two panels) are sibling larvae that were either CyO/+ (wild type; top) or heterozygous *+/dlg^{m52}* (middle). Representative heterozygous third chromosome Minute mutant, M(3)^{i55}, is shown at bottom. (**E**) Confocal images show GFP (green) and 4′,6-diamidino-2-phenylindole (DAPI) (blue) staining in wild type (top) and eyeful (bottom) larvae heterozygous for *dilp8^{MI00727}*. Brain expression is delayed in the eyeful tumor model. rg, ring gland.

another process that delays pupariation. Because the gene product had an invariant 6-cysteine motif typical of the insulin-relaxin peptide family (Fig. 1B and figs. S1 and S2), we named this gene *Drosophila* insulin-like peptide 8 (*dilp8*). This is the only DILP differentially expressed in tumors (fig. S3). The secretion of DILP8 was confirmed by expressing a carboxy-terminal FLAG-tagged construct, which, consistent with its hormonal nature, was detected in larval hemolymph (Fig. 1C) and in the medium of transfected Schneider (S2) cells (fig. S4).

We examined the native and induced expression of *dilp8* using an enhanced green fluorescent protein (eGFP) trap in the gene's first intron [*Mi{MIC}CG14059*^{MI00727} (*12*), hereafter *dilp8*^{MI00727} (fig. S5)]. Larval eGFP expression was assessed in mutants with different growth perturbations in the imaginal discs that delay pupariation: fast-growing tumors induced by oncogene activation (*10*); slow-growing tumors, exemplified by a recessive mutation in the tumor-suppressor gene *discs large* [*dlg*^{m52} (*13*)]; and slow growth of imaginal discs due to *Minute* mutations (*9*). In all cases, there was cell-autonomous induction of eGFP in the affected third-instar imaginal discs (Fig. 1, D and E, and fig. S6), as well as weak and dynamic signals in the normally growing discs and brain (Fig. 1E). Hence, DILP8 is a common response to abnormal imaginal disc growth, and the response is conserved in other *Drosophila spp.* (fig. S7).

Using the homozygous *dilp8*^{MI00727} insertional mutation that reduces *dilp8* mRNA expression by 99.4% (Fig. 2A), we investigated whether *dilp8* influences pupariation. In synchronous larvae, loss of *dilp8* reverted the delay in pupariation caused by eye disc tumors from 26.6 ± 7.5 hours to 5.9 ± 7.1 hours (mean ± SD pupariation time, $P = 0.026$) (Fig. 2B).

To determine whether the *dilp8* response is tumor-selective or broadly used, we assayed

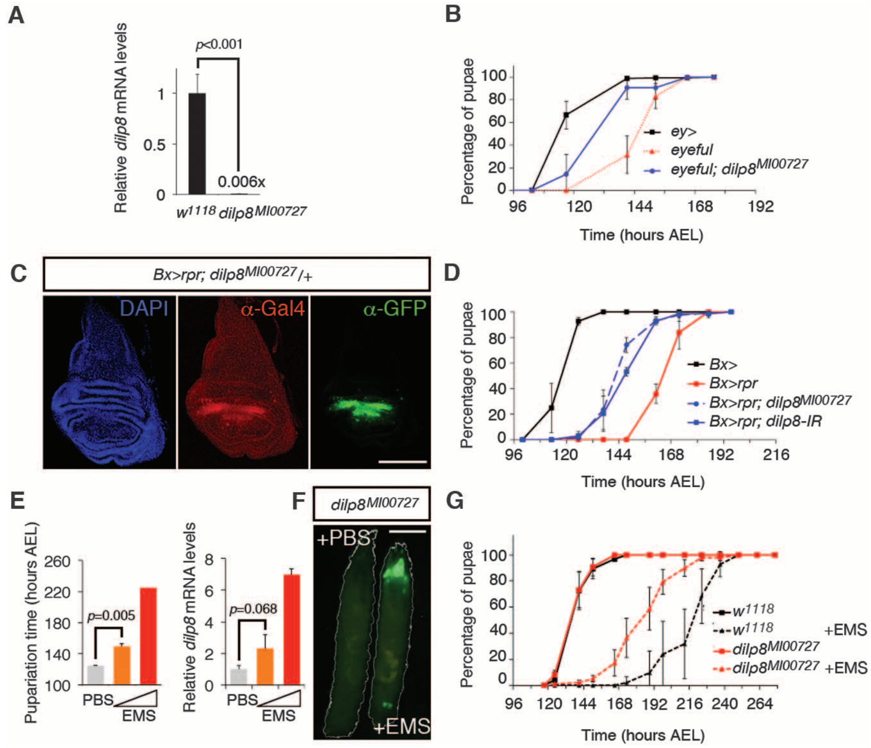

Fig. 2. DILP8 is required for adaptive developmental plasticity in imaginal discs growing abnormally. (**A**) *dilp8* expression relative to *rp49* analyzed by means of quantitative reverse transcription polymerase chain reaction (RT-PCR) in virgin females of the wild type (*w*^{1118}) or homozygous *dilp8*^{MI00727} mutant (mean ± SD of three or four independent replicates) (fig. S5). (**B**) Loss of *dilp8* in the eyeful tumor background rescues delayed pupariation. Three replicates were scored, each with two to five tubes containing ~30 larvae. (**C**) Confocal images of GFP (green) and GAL4 (red) staining in *Bx>rpr;dilp8*$^{MI00727/+}$ wing discs (DAPI, blue). Scale bar, 100 μm. (**D**) Depletion of *dilp8* in *Bx>rpr* animals partially rescues the delay in pupariation ($n = 5$ replicates of two to five tubes of ~25 larvae per genotype scored). (**E**) Pupariation time and *dilp8* expression analyzed by means of quantitative RT-PCR in animals fed with phosphate-buffered saline or two doses of EMS (10 to 20 mM). (**F**) EMS (10 mM) activated the eGFP reporter in damaged discs. Scale bar, 1 mm. (**G**) *dilp8*^{MI00727} reduced the delay in pupariation in EMS-fed larvae (four tubes of ~25 larvae were scored per genotype and treatment). *ey>* and *Bx>* indicate *eyeless (ey)-Gal4/+* and *P{GawB}Bx*^{MS109}*/+* and serve as genetic background controls.

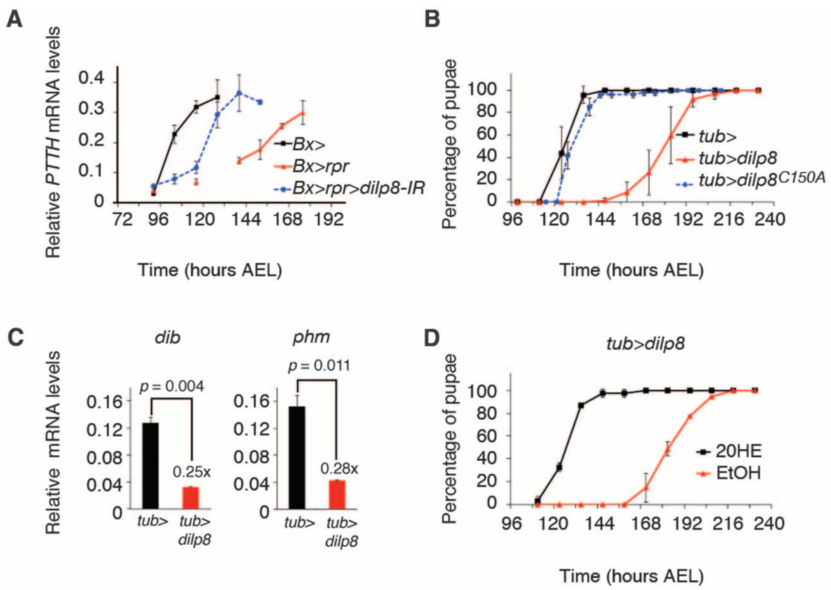

Fig. 3. DILP8 delays metamorphosis by regulating the expression of ecdysone biosynthetic genes. (**A**) PTTH expression relative to *rp49* analyzed by means of quantitative RT-PCR in synchronous *Bx>rpr* larvae with or without *dilp8* RNAi silencing induced by expression of inverted repeat (IR) transgene. The mRNA was isolated from approximately five larvae per time point and genotype. (**B**) *dilp8* overexpression delayed pupariation ($n = 3$ to 4 tubes of ~20 larvae each per genotype). The cysteine-to-alanine mutation at residue 150 (C150A) renders a biologically inactive DILP8 protein. (**C**) *dib* (left) and *phm* (right) expression analyzed by means of quantitative RT-PCR in mRNA isolated from ring gland/brain complexes from synchronous larvae (118 hours AEL; $n = 3$ replicates, each with RNA isolated from ~20 ring gland/brains, mean ± SD two-tailed unpaired *t* test). (**D**) Pupariation time of *tub>dilp8* larvae fed 20HE (0.5 mg/mL) or the ethanol (EtOH) as vehicle ($n > 40$ larvae per treatment). *tub>* indicates *tubulin-Gal4/+* and serves as background control.

dilp8 expression and activity during regeneration induced by two forms of damage. First, cell death was induced by overexpressing the proapoptotic gene *reaper* (*rpr*) by using *Beadex-Gal4* (*Bx>rpr*), which provokes continuous intrinsic damage and regenerative growth in the wing pouch, and a pupariation delay (*14*). *dilp8* transcripts were up-regulated in third-instar *Bx>rpr* larvae (fig. S8), and the $dilp8^{MI00727}$ reporter was activated cell-autonomously in damaged/regenerating cells (Fig. 2C and fig. S8). When *dilp8* was diminished in whole *Bx>rpr* larvae by $dilp8^{MI00727}$ mutation or by tissue-specifically reducing *dilp8* mRNA by 71% through RNA interference (RNAi) (*Bx>rpr>dilp8-IR*) (fig. S9), the delay in pupariation reverted from 46.2 ± 1.3 hours to 27.8 ± 2.9 hours ($P < 0.001$) and 29.1 ± 2.5 hours ($P < 0.001$), respectively (Fig. 2D).

Secondly, synchronized larvae were fed with the genotoxic agent ethyl methanosulfonate (EMS) administered from 72 hours after egg-laying (AEL), which produced a dose-dependent delay in pupariation (Fig. 2E), strong caspase activation in imaginal discs, yet only mild defects in adult structures (fig. S10), which is similar to that caused by DNA damage and repair following irradiation (*14*, *15*). In imaginal discs of $dilp8^{MI00727}$ larvae, eGFP highlighted the damage produced by EMS (Fig. 2F), and this response of *dilp8* was dose-dependent (Fig. 2E), indicating that *dilp8* is tightly associated with the extent of damage/regeneration. The endogenous $dilp8^{MI00727}$ mutation shortened the delay induced by EMS by 44.03% ± 13.24 ($P <$ 0.0001) (Fig. 2G), and *dilp8* RNAi (*tub>dilp8-IR*) reduced this delay by 43.24% ± 9.36 ($P = 0.0063$) (fig. S11). Moreover, *dilp8* depletion augmented the pupal lethality associated with exposure to EMS (fig. S11). Thus, DILP8 regulates the timing of pupariation in response to tumor and regenerative growth and increases survival after tissue insult.

We examined the expression of hormone genes regulating the larval-to-pupal transition in relation to DILP8. Cell death–induced damage by *Bx>rpr* delays metamorphosis inhibiting PTTH synthesis in the brain, a delay that is enhanced by the consumption of provitamin A (ß-carotenoids) in the diet (*14*). Down-regulating *dilp8* attenuated the PTTH delay by some 12 to 24 hours (Fig. 3A), independently of retinoids (fig. S12), indicating that DILP8 is required to delay PTTH synthesis in damaged/regenerating tissues.

We next assessed whether DILP8 is sufficient to delay pupariation in the absence of growth abnormalities. Synchronized larvae overexpressing *dilp8* driven by *tub-Gal4* (*tub>dilp8*) initiated pupariation 55.9 ± 7.6 hours later than did control *tub>* or $tub>dilp8^{C150A}$ larvae that overexpress *dilp8* mutated at a conserved cysteine ($P < 0.001$) (Fig. 3B). Compared with the damaged *Bx>rpr* animals, *dilp8* overexpression caused delayed induction of transcription of the *disembodied* (*dib*) and *phantom* (*phm*) genes in the ecdysone synthesis cascade (Fig. 3C and fig. S13) without delaying PTTH (fig. S13). The delay in pupariation induced by DILP8 was overcome by feeding larvae 20HE (Fig. 3D), confirming that the effects of DILP8 were a consequence of reduced ecdysone production.

Damaged and regenerating larvae, or those with tumor discs, attain a wild-type size. Similarly, although *tub>dilp8* larvae prolong their feeding (longer than the controls), they were no larger (Fig. 4A and fig. S14). However, this extended feeding made *tub>dilp8* adults weigh more than controls (Fig. 4B and fig. S15).

To attain correct final size despite their prolonged larval life span, DILP8 overexpression may also exert control on growth rates to prevent overgrowth. Hence, we quantified the transcription of *Thor* (*d4E-BP*), a direct target of the growth inhibitor FOXO, as surrogate measure for imaginal disc growth (*16*–*18*). *Thor* expression was selectively up-regulated in *tub>dilp8* imaginal discs (Fig. 4C), which is consistent with a slower imaginal disc growth. In contrast, *Thor* expression in the fat body (fig. S15) showed that insulin/insulin-like growth factor 1 (IGF-1) signaling was not generally impaired, as also evident through the analysis of *dilp2* and *dilp3* expression (fig. S16). Thus, DILP8 exerts a fundamental influence on an adaptive plasticity of both growth and maturation, either directly or via secondary signals.

In the absence of such plasticity, organisms would be incapable of adjusting the growth of distinct body parts to maintain their overall proportionality and left-right symmetry. Indeed, $dilp8^{MI00727}$ animals pupate over an extended time scale and are more varied in size than controls sharing the same genetic background

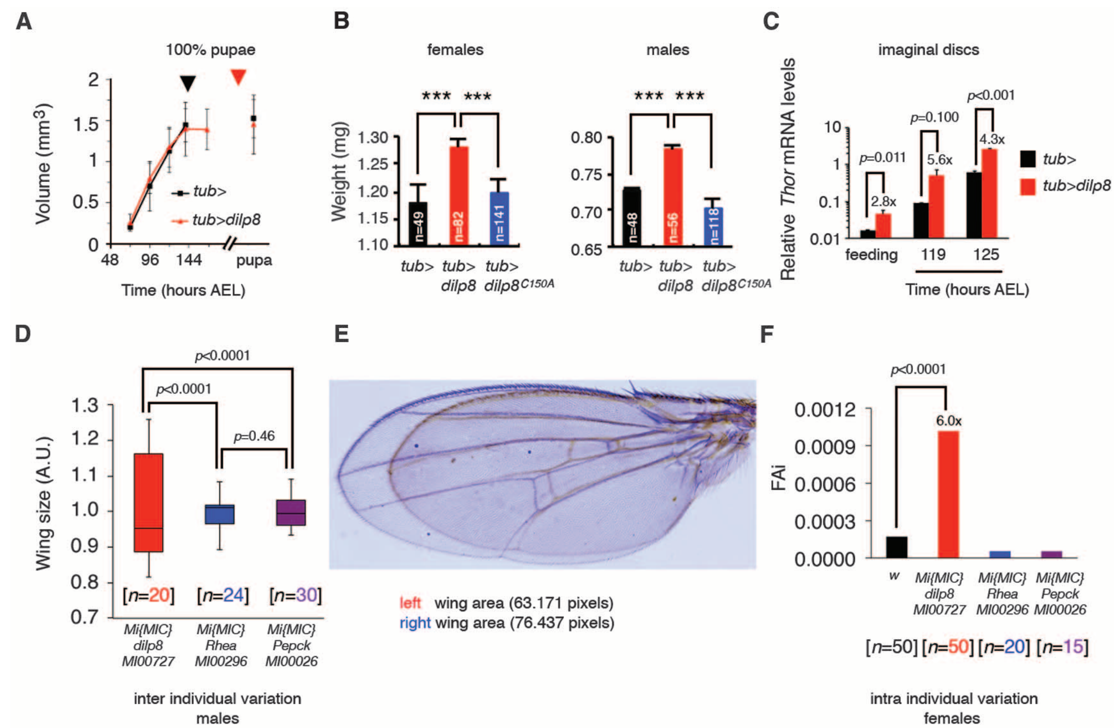

Fig. 4. DILP8 reduces inter- and intra-individual phenotypic variations, reflecting greater developmental stability and robustness. (**A**) Growth rate curve derived by scoring >10 animals of each genotype and time point. Multiple pair-wise two-tailed unpaired *t* tests with Bonferroni correction showed no significant differences ($P >$ 0.10). Arrowheads indicate the time of 100% pupation for each genotype. (**B**) Virgin female and male adults overexpressing *dilp8* weigh more than controls (***$P < 0.001$, mean ± SD two-tailed unpaired *t* test with Bonferroni correction), although their overall size is the same (fig. S14). (**C**) *Thor* expression in imaginal discs from synchronous *tub>* or *tub>dilp8* third-instar larvae relative to *rp49* and *dUba2*, analyzed by means of quantitative RT-PCR (feeding larvae, ~115 hours AEL, $n = 3$ biological replicates, each with RNA isolated from imaginal discs of ~20 larvae per genotype, mean ± SD two-tailed unpaired *t* test). (**D**) Box-and-whiskers plot of the wing area of $dilp8^{MI00727}$ and control of genetic background ($Rhea^{MI00296}$ and $Pepck^{MI00026}$) males ($P < 0.0001$, *f* test for unequal distributions). The three Mi{MIC} insertions were generated in the same genetic background (*12*). (**E**) Comparisons of the left and right wings of a $dilp8^{MI00727}$ female. (**F**) Bar graphs of the FAi of the left and right wings of the genotypes indicated (*20*). Numbers in brackets in (D) and (F) are the wing pairs scored.

(Fig. 4D and fig. S17). Individually, *dilp8*^{MI00727} flies reared at 26.5°C display imperfect bilateral symmetry (Fig. 4E), and when intra-individual variation between the left and right wings was assessed by using the fluctuating asymmetry index (FAi) (*19*, *20*), wing FAi was statistically significantly higher in *dilp8*^{MI00727} females than in w^{1118} (Fig. 4F). This higher asymmetry reflects lesser stability (*19*).

Collectively, our results suggest that DILP8—an insulin/IGF/relaxin–like hormone peptide (Fig. 1)—provides a signal that communicates the growth status of peripheral tissues in order to regulate developmental timing, population robustness, and individual developmental stability [detected by fluctuating asymmetry analysis (*19*)], as well as local responses to processes such as regeneration and cancer.

References and Notes

1. H. F. Nijhout, *Dev Biol* **261**, 1 (2003).
2. P. J. Bryant, O. Schmidt, *J. Cell Sci. Suppl.* **13**, 169 (1990).
3. J. M. Tennessen, C. S. Thummel, *Curr. Biol.* **21**, R750 (2011).
4. A. W. Shingleton, *Organogenesis* **6**, 76 (2010).
5. C. A. Poodry, D. F. Woods, *Rouxs Arch. Dev. Biol.* **199**, 219 (1990).
6. P. Simpson, P. Berreur, J. Berreur-Bonnenfant, *J. Embryol. Exp. Morphol.* **57**, 155 (1980).
7. R. K. Smith-Bolton, M. I. Worley, H. Kanda, I. K. Hariharan, *Dev. Cell* **16**, 797 (2009).
8. L. Menut *et al.*, *Genetics* **177**, 1667 (2007).
9. B. C. Stieper, M. Kupershtok, M. V. Driscoll, A. W. Shingleton, *Dev. Biol.* **321**, 18 (2008).
10. D. Ferres-Marco *et al.*, *Nature* **439**, 430 (2006).
11. A. Klebes *et al.*, *Development* **132**, 3753 (2005).
12. K. J. Venken *et al.*, *Nat. Methods* **8**, 737 (2011).
13. D. F. Woods, P. J. Bryant, *Dev. Biol.* **134**, 222 (1989).
14. A. Halme, M. Cheng, I. K. Hariharan, *Curr. Biol.* **20**, 458 (2010).
15. L. A. Abbott, *Radiat. Res.* **96**, 611 (1983).
16. M. A. Jünger *et al.*, *J. Biol.* **2**, 20 (2003).
17. M. Miron *et al.*, *Nat. Cell Biol.* **3**, 596 (2001).
18. V. Hietakangas, S. M. Cohen, *Annu. Rev. Genet.* **43**, 389 (2009).
19. A. R. Palmer, C. Strobeck, *Annu. Rev. Ecol. Syst.* **17**, 391 (1986).
20. Materials and methods are available as supplementary materials on *Science* Online.

Acknowledgments: We thank E. Hafen, L. Garcia-Alonso, B. Lakowski, and F. Heredia for their comments and suggestions; J. Colombani, D. S. Andersen, and P. Léopold for sharing unpublished data; and I. Gutierrez and E. Ballesta for technical help. V.M. is a Generalitat Valenciana fellow, and A.M.G. was supported by a Marie Curie Fellowship. This work was supported by grants from the Fundación Botin, the Ministerio de Ciencia e Innovación (BFU2009-09074 and MEC-CONSOLIDER/CSD2007-00023), Generalitat Valenciana (PROMETEO/2008/134), and the European Commission (HEALTH-F2-2008-201666) to M.D. The microarray data are deposited in the Gene Expression Omnibus (GEO) repository (accession GSE35471). A.M.G. and M.D. designed the research; A.G., A.M.G., V.M., E.C., and M.D. performed the experiments and analyzed the data. A.G., A.M.G., and M.D. wrote the manuscript.

Supplementary Materials

www.sciencemag.org/cgi/content/full/336/6081/579/DC1
Materials and Methods
Figs. S1 to S17
Table S1
References (*21–27*)

16 November 2011; accepted 30 March 2012
10.1126/science.1216735

Secreted Peptide Dilp8 Coordinates *Drosophila* Tissue Growth with Developmental Timing

Julien Colombani,* Ditte S. Andersen,*† Pierre Léopold†

Little is known about how organ growth is monitored and coordinated with the developmental timing in complex organisms. In insects, impairment of larval tissue growth delays growth and morphogenesis, revealing a coupling mechanism. We carried out a genetic screen in *Drosophila* to identify molecules expressed by growing tissues participating in this coupling and identified *dilp8* as a gene whose silencing rescues the developmental delay induced by abnormally growing tissues. *dilp8* is highly induced in conditions where growth impairment produces a developmental delay. *dilp8* encodes a peptide for which expression and secretion are sufficient to delay metamorphosis without affecting tissue integrity. We propose that Dilp8 peptide is a secreted signal that coordinates the growth status of tissues with developmental timing.

Classical regeneration experiments in insects have demonstrated an important role for imaginal tissues (also called "discs," the larval tissues that give rise to the adult appendages) in coupling tissue growth, maturation, and patterning during development (*1*). When disc growth is impaired, the duration of the larval period is extended, allowing tissues to regenerate and/or grow to their target size before entering metamorphosis (*2*–*9*). However, when discs are strongly reduced or absent, larvae enter metamorphosis with normal timing (*5*). This suggests that discs that have not yet completed a certain amount of growth are able to inhibit the developmental transition leading to metamorphosis. We have used a genetic approach in *Drosophila* to identify signals emanating from growing larval discs that inhibit the onset of metamorphosis.

We first sought to identify conditions for which modification of disc growth would give rise to substantial developmental delay. We used the *rotund-Gal4* driver (*Rn>*) for disc-targeted RNA interference (RNAi) silencing of the *avalanche* gene (*avl*; *Rn>avl-RNAi*), encoding a syntaxin that functions in the early endocytic machinery (*10*), or the ribosomal protein L7-encoding gene (*rpl7*; *Rn>rpl7-RNAi*). Both conditions induced robust developmental delays of larva-to-pupa transition of about 2 to 3 and 3 to 5 days, respectively (Fig. 1A). *Rn>avl-RNAi* discs reach near -normal size after 5 days of development, then undergo unrestricted neoplastic growth (*10*) (Fig. 1, C to F). *Rn>rpl7-RNAi* animals grow at the same rate as control animals but fail to puariate at the normal time, giving rise to giant larvae and pupae after 2 to 3 days of extra growth (Fig. 1B and fig. S1E). In contrast, *Rn>rpl7-RNAi* discs grow and mature significantly slower than control discs and reach normal size after an extended period of growth (Fig. 1, C and G to I). Accordingly, *Rn>rpl7-RNAi* larvae grow at a slower rate and reach normal larvae and pupa sizes after an extended period of growth, as described for *Minute* mutants (Fig. 1B and fig. S1F) (*11*). In both conditions, the expression peaks of *phm* and *dib* [two genes involved in ecdysone biosynthesis (*12*)] were delayed (fig. S1, A and B), as was the activity peak of ecdysone (as measured by expression levels of its target gene, *E75B*) (fig. S1C) (*13*). The rise of expression of the prothoracicotropic hormone (PTTH) gene normally observed at the end of third larval instar was only slightly delayed (fig. S1D), indicating that *PTTH* expression is not limiting for pupariation in these conditions. Thus, in both conditions, altered disc growth acts upstream of ecdysone production to delay metamorphosis.

For our genome-wide approach, we used the *Rn>avl-RNAi* tester line to screen a collection of RNAi lines for their abilities to rescue the delay at pupariation (fig. S1G). Of the 10,100 lines tested, 121 significantly rescued the delay in *Rn>avl-RNAi* larvae. To eliminate candidates rescuing specifically the *Rn>avl-RNAi* condition, we rescreened the 121 lines by using the *Rn>rpl7-RNAi* tester line (fig. S1G). Of the 121 candidates, only one rescued both conditions efficiently (Fig. 1J). This RNAi line targets a previously uncharacterized gene, *CG14059*, which encodes a small peptide of about 150 amino acids, with a signal peptide followed by a cleavage site at its N terminus, and is therefore predicted to be secreted (fig. S5A). The peptide encoded by *CG14059* is characterized by a conserved code of cysteins found in many insulin-like peptides (*14*), and hence we called this gene *Drosophila insulin-like peptide 8* (*dilp8*). *dilp8* loss of function does not suppress the overgrowth phenotype observed in

Université de Nice, INSERM 1091, CNRS 7277, and France Institute of Biology, Parc Valrose, 06108 Nice, France.

*These authors contributed equally to this work.
†To whom correspondence should be addressed. E-mail: leopold@unice.fr (P.L.); andersen@unice.fr (D.S.A.)

Rn>avl-RNAi discs (fig. S2, A and B), consistent with its function being downstream of neoplastic growth.

Microarray analyses identified *dilp8* in a list of 52 genes differentially expressed in control and *Rn>avl-RNAi* discs (fig. S3). Quantitative reverse transcription polymerase chain reaction (qRT-PCR) analysis confirmed that *dilp8* mRNA levels are strongly up-regulated in *Rn>avl-RNAi*

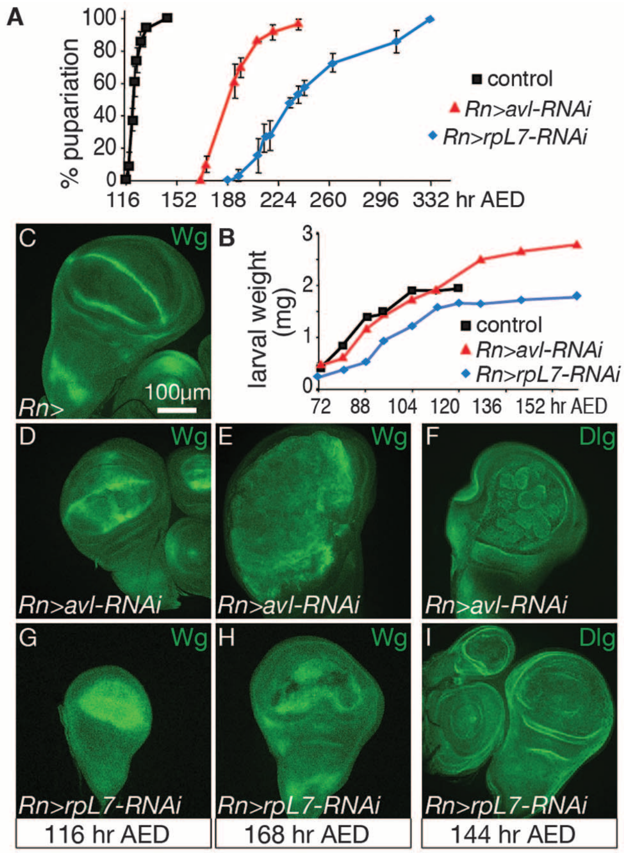

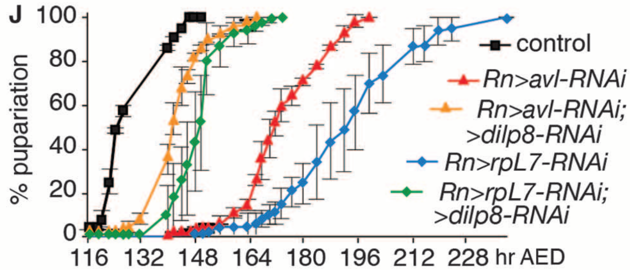

Fig. 1. A genome-wide screen for molecules coordinating disc growth with the developmental clock. Effects on the developmental timing (**A**), measured as % larvae that have pupariated, and larval weight (**B**) (n = 10) after silencing *avl* or *rpl7* in the imaginal discs. (**C** to **I**) Wing discs dissected from indicated genotypes at the indicated time AED, stained for Wingless [Wg; (C) to (E), (G), and (H)] or Disc large (Dlg) [(F) and (I)]. (**J**) Rescue of the pupariation delays upon *dilp8* silencing in the indicated genotypes. Error bars represent SEM (standard error of the mean).

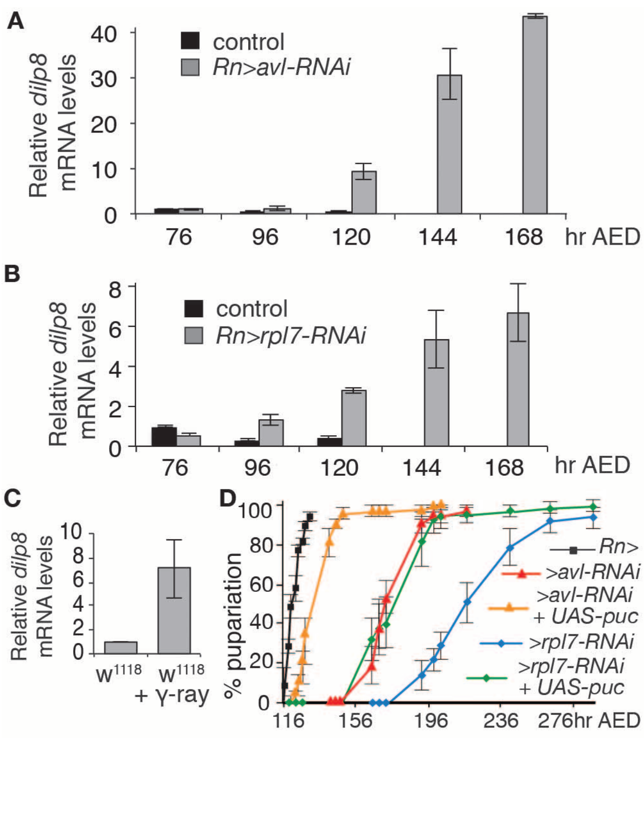

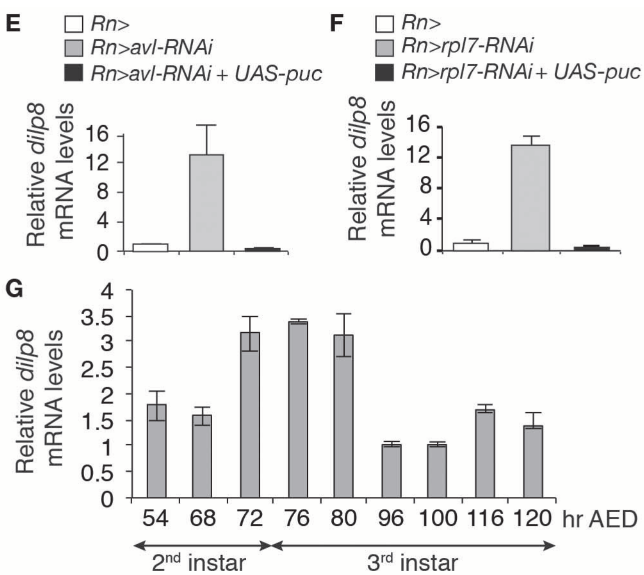

Fig. 2. *dilp8* expression is up-regulated in response to a variety of disc growth alterations. (**A** and **B**) Larval *dilp8* transcript levels measured by qRT-PCR in the indicated genotypes. Fold changes are relative to control animals at 76 hours AED. (**C**) *dilp8* transcript levels (qRT-PCR) in isogenic w^{1118} (control) and irradiated (γ-rays, 40 Gy) larvae at 120 hours AED. (**D** to **F**) Coexpression of *puckered* (*UAS-puc2A*) rescues the pupariation delays (D) and *dilp8* expression levels [(E) and (F)]. (**G**) Time course of *dilp8* expression in whole larvae (qRT-PCR). Fold changes are relative to *dilp8* levels at 96 hours AED.

and *Rn>rpl7-RNAi* larvae (Fig. 2, A and B). In addition, *dilp8* mRNA levels were elevated in other tumorlike tissues (fig. S6H) and in response to γ-ray irradiation (Fig. 2C), a condition previously shown to induce regenerative growth in the discs (*6*, *7*). This suggests a more general role for *dilp8* in regulating developmental timing in response to a range of conditions that alter disc growth. Consistent with this, *dilp8* was previously found up-regulated in areas of discs undergoing leg-to-wing transdetermination (*15*).

The c-Jun N-terminal kinase (JNK) pathway is activated in response to various types of tissue stress, including wound healing and regeneration (*16*, *17*). We observed an induction of the JNK pathway in *Rn>avl-RNAi and Rn>rpl7-RNAi* conditions (fig. S2, C to G). Accordingly, reducing the activity of JNK signaling by coexpression of the JNK phosphatase gene, *puckered*, suppressed the up-regulation of *dilp8* mRNA levels observed in *Rn>avl-RNAi* and *Rn>rpl7-RNAi* animals (Fig. 2, E and F) and rescued the delay in metamorphosis (Fig. 2D).

In wild-type conditions, *dilp8* transcript levels peak at the transition from second to third larval instar and is maintained during early third instar (Fig. 2G). This modest increase in *dilp8* expression is comparable to that observed in the *Rn>rpl7-RNAi* tester line at 120 hours after egg deposition (AED) (Fig. 2B), where it is sufficient to delay metamorphosis (Fig. 1A). Therefore, the developmental reduction of *dilp8* levels in mid–third instar is likely to be a prerequisite for the initiation of pupariation. What regulates *dilp8* levels during normal development is unclear. The JNK pathway represents an unlikely candidate because its activity levels remain low in healthy discs.

Consistent with *dilp8* being transcriptionally regulated, ectopic expression of *dilp8* in the discs (*Rn>dilp8*) delayed pupariation by 2 to 3 days (Fig. 3A). As in the case of *Rn>avl-RNAi* and *Rn>rpl7-RNAi*, this delay was accompanied by a modest delay in *PTTH* expression and a suppression of ecdysone activity normally peaking at 5 days AED in control animals (fig. S4, A to D). However, misexpression of *dilp8* affected neither disc patterning nor general disc morphology (fig. S4, F to I), JNK activity (fig. S4E), or apoptosis (fig. S4, J to L), suggesting an absence of tissue stress. Altogether, this indicates that *dilp8* acts downstream of disc growth checkpoints but upstream of the hormonal events controlling pupariation.

We observed a slight but consistent growth retardation of *Rn>dilp8* discs, which reach normal pupariation sizes with a 6-hour delay (Fig. 3B). Importantly, *Rn>dilp8* animals pupariate with a 2- to 3-day delay, giving rise to 20% heavier adults (Fig. 3, C and D). This indicates that the growth reduction observed in *Rn>dilp8* animals is not responsible for their developmental delay. Upon tissue damage, nondamaged tissues coordinate with regenerating tissues and do not overgrow during the prolonged larval period (*9*, *18*). Therefore, in addition to its role in developmental timing, Dilp8 could serve as a growth inhibitory endocrine signal that coordinates organ growth rate.

We next generated a small deletion encompassing the *dilp8* locus (*dilp8*^{EX}) and part of the two neighboring genes (fig. S4M). Because *dilp8* overexpression delays pupariation, one might

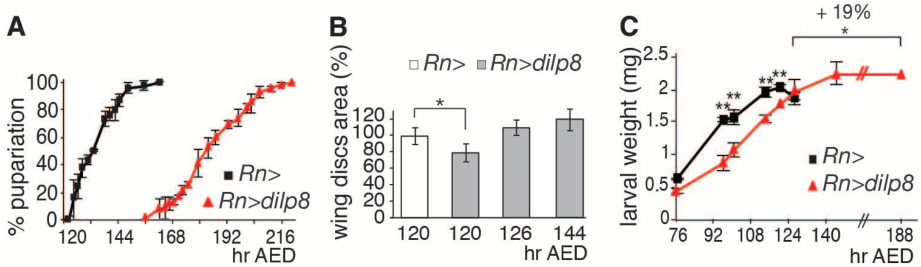

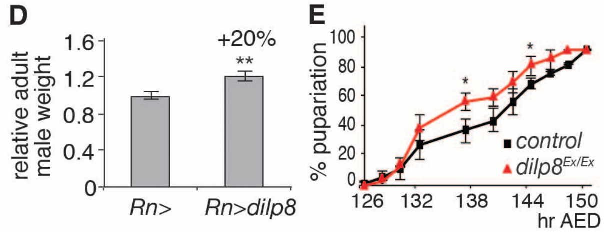

Fig. 3. Misexpression of *dilp8* is sufficient to induce a developmental delay. (**A**) Pupariation curves for control and *Rn>dilp8* larvae. (**B**) Wing disc area of control and *Rn>dilp8* larvae at indicated times. (**C**) Larval growth curves of control and *Rn>dilp8* animals. (**D**) Adult weight of *Rn>dilp8* flies relative to control. (**E**) Pupariation curve for control (precise excision) and *dilp8*$^{EX/EX}$ larvae. (*$P < 0.05$; **$P < 0.01$)

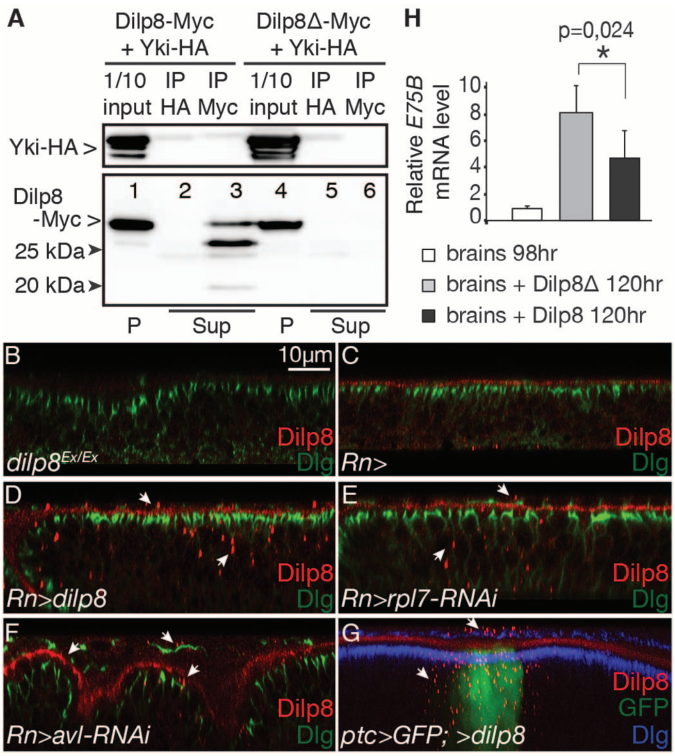

Fig. 4. Dilp8 is secreted from discs to control the developmental timing. (**A**) Immunoprecipitation (IP) from supernatants of S2R+ cells coexpressing hemagglutinin (HA)-Yorkie (Yki, intra cellular control) and Dilp8-Myc (lanes 1 to 3) or Dilp8Δ-Myc (lanes 4 to 6) using antibodies against HA (lanes 2 and 5, negative control) and Myc (lanes 3 and 6) shows that Dilp8-myc, but not Dilp8Δ-Myc, is secreted. Full-length Dilp8-Myc and additional shorter forms are visible (lane 3). (**B** to **F**) Transverse sections of discs from indicated genotypes stained for Dilp8 (red) and Dlg (green). (**G**) Transverse sections of discs expressing Dilp8 (red) in the *patched* (*ptc*) domain labeled by green fluorescent protein (GFP) (Dlg in blue). (**H**) Ex vivo coculture experiments of discs, brains, and ring glands. *E75B* mRNA levels in dissected brains are used as readouts for ecdysone signaling. Incubation with *dilp8*-expressing discs partially prevents *E75B* expression compared with discs expressing *dilp8*Δ ($n = 5$).

expect that its loss of function leads to early pupariation. Homozygous *dilp8*$^{EX/EX}$ animals are viable, and their timing of pupariation is only slightly advanced (~4 hours) compared with that of control animals (Fig. 3E). This modest pupariation phenotype can be explained in the light of earlier genetic experiments showing that *discless* mutant larvae pupariate with normal timing (*5*). It suggests that the onset of metamorphosis relies on additional signals provided by other larval organs.

Our experiments suggest that Dilp8 relays the growth status of the discs to the central control of metamorphosis. This raises the possibility that Dilp8 travels from the discs, where it is emitted, to its target tissues. Consistent with this, when expressed in S2R+ cells, a myc-tagged full-length form of Dilp8 is recovered in the culture medium but not a truncated form lacking the signal peptide (Dilp8Δ-myc) (Fig. 4A and fig. S5A). Moreover, by using a specific Dilp8 antibody, we could observe Dilp8 in vesicular particles apical to the wing pouch as well as in the lumen separating the columnar epithelium from the peripodial cells in discs from *Rn>dilp8*, *Rn>avl-RNAi*, and *Rn>rpl7-RNAi* animals (Fig. 4, D to F, white arrows, and fig. S6, C to F) but not in *Rn>* discs where low levels of Dilp8 were only detectable in the lumen (Fig. 4C and fig. S6B). By contrast, a nonsecretable form of Dilp8 (Dilp8Δ-myc) is found perinuclear (fig. S5, C, F, and G), suggesting that it fails to enter the secretory pathway. When *dilp8* expression was targeted to a restricted domain of the disc, Dilp8 particles were detected in cells neighboring its expression domain, in the lumen, and in the basal part of the peripodial cells (Fig. 4G and fig. S6G). Therefore, Dilp8 is secreted from the disc epithelium and transits in the lumen and the peripodial cells, from where it may reach the hemolymph.

In addition, the secretion of Dilp8 is essential for its role in controlling developmental timing, because overexpression of the nonsecreted form of Dilp8 (*Rn>dilp8Δ*) is incapable of delaying pupariation (fig. S5, H and I).

What are the target tissues of Dilp8? The hormonal cascade for ecdysone production takes place in the brain (for PTTH production) and in the ring gland (for ecdysone production) (*19*). To test whether these tissues could be direct targets of Dilp8, we cocultured wild-type brains and attached ring glands (brain complexes) with discs expressing *dilp8* or *dilp8Δ* and tested whether Dilp8 produced by the discs could suppress ecdysone production in the brain complexes. As readout for ecdysone activity, we measured expression of *E75B* in brains before (98 hours AED) and after (120 hours AED) incubation with *dilp8* or *dilp8Δ* discs. In brain complexes cocultured with discs expressing nonsecreted Dilp8Δ (serving as a negative control), *E75B* was induced about eightfold, indicating that ecdysone activity can be detected in the brain and therefore that ecdysone production by the ring gland operates ex vivo (Fig. 4H). This induction was significantly suppressed upon coculture with discs expressing the secreted full-length Dilp8 (Fig. 4H). Although these experiments cannot rule out the existence of a secondary relay signal, they suggest that Dilp8 produced by the disc remotely acts on the brain complex to suppress ecdysone production and activity.

We have identified Dilp8 as a signal produced by growing imaginal tissues that controls the timing of metamorphosis. *dilp8* is induced in a variety of conditions that perturb the imaginal disc growth program. We propose that, in conditions of impaired growth, secreted Dilp8 acts on the brain complex to delay metamorphosis, allowing extra time for tissue repair and growth to occur. In addition, Dilp8 might serve to synchronize growth of undamaged tissues with delayed ones.

Our experiments also suggest that Dilp8 participates in a feedback control on growth during normal development, ensuring that animals do not progress to the next developmental stage before organs and tissues have completed adequate growth. Dilp8 shares some features with a distant insulin-like peptide family member, raising the possibility that peptides with similar roles may exist in vertebrates.

References and Notes

1. P. J. Bryant, P. Simpson, *Q. Rev. Biol.* **59**, 387 (1984).
2. M. A. Russell, *Dev. Biol.* **40**, 24 (1974).
3. P. Simpson, H. Schneiderman, *Wilhelm. Rouxs. Arch. Develop. Biol.* **178**, 247 (1975).
4. J. G. Kunkel, *Biol. Bull.* **153**, 145 (1977).
5. P. Simpson, P. Berreur, J. Berreur-Bonnenfant, *J. Embryol. Exp. Morphol.* **57**, 155 (1980).
6. C. A. Poodry, D. F. Woods, *Rouxs Arch. Dev. Biol.* **199**, 219 (1990).
7. A. Halme, M. Cheng, I. K. Hariharan, *Curr. Biol.* **20**, 458 (2010).
8. B. C. Stieper, M. Kupershtok, M. V. Driscoll, A. W. Shingleton, *Dev. Biol.* **321**, 18 (2008).
9. N. F. Parker, A. W. Shingleton, *Dev. Biol.* **357**, 318 (2011).
10. H. Lu, D. Bilder, *Nat. Cell Biol.* **7**, 1232 (2005).
11. G. Morata, P. Ripoll, *Dev. Biol.* **42**, 211 (1975).
12. Z. McBrayer *et al.*, *Dev. Cell* **13**, 857 (2007).
13. K. King-Jones, C. S. Thummel, *Nat. Rev. Genet.* **6**, 311 (2005).
14. A. Garrelli *et al.*, *Science* **336**, 579 (2012).
15. A. Klebes *et al.*, *Development* **132**, 3753 (2005).
16. C. Bergantiños, M. Corominas, F. Serras, *Development* **137**, 1169 (2010).
17. M. Bosch, F. Serras, E. Martín-Blanco, J. Baguñà, *Dev. Biol.* **280**, 73 (2005).
18. F. A. Martín, G. Morata, *Development* **133**, 4421 (2006).
19. L. Riddiford, in *The Development of* Drosophila melanogaster, M. Bate, A. Martinez Arias, Eds. (Cold Spring Harbor Press, Cold Spring Harbor, NY, 1993), vol. 2, pp. 899–939.

Acknowledgments: We thank P. O'Farrell for initial insightful discussions; G. Jarretou and J. Villalba for technical assistance; V. Pantesco and L. Vallar for microarray data and analysis; the Vienna *Drosophila* RNAi Center, *Drosophila* Genetics Resource Center, and Bloomington stock centers; I. Bourget for γ-ray experiments; S. Leevers, N. Tapon, and laboratory members for comments on the manuscript; and M. Dominguez, A. Garelli, and A. Gontijo for communicating unpublished results. This work was supported by the CNRS, INSERM, Agence Nationale de la Recherche, Fondation pour la Recherche Médicale, European Research Council (grant no. 268813), Danish Research Council (grant no. 272-08-0064 for D.S.A.) and Marie Curie Life Long Training (grant no. 252373 for D.S.A.). The microarray data are presented at www.ncbi.nlm.nih.gov/geo/query/acc.cgi?acc=GSE36862 (accession no. GSE36862).

Supplementary Materials
www.sciencemag.org/cgi/content/full/336/6081/582/DC1
Materials and Methods
Figs. S1 to S6

16 November 2011; accepted 30 March 2012
10.1126/science.1216689

Function, Developmental Genetics, and Fitness Consequences of a Sexually Antagonistic Trait

Abderrahman Khila,[1,2,3] Ehab Abouheif,[2] Locke Rowe[1]*

Sexual conflict is thought to be a potent force driving the evolution of sexually dimorphic traits. In the water strider *Rheumatobates rileyi*, we show that elaborated traits on male antennae function to grasp resistant females during premating struggles. Using RNA interference, we uncovered novel roles of the gene *distal-less* (*dll*) in generating these male-specific traits. Furthermore, graded reduction of the grasping traits resulted in a graded reduction of mating success in males, thus demonstrating both selection for elaboration of the traits and the role of *dll* in their evolution. By establishing developmental genetic tools in model systems where sexual selection and conflict are understood, we can begin to reveal how selection can exploit ancient developmental genes to enable the evolution of sexually dimorphic traits.

Sexual conflict, or sexually antagonistic selection, can influence the evolution and elaboration of novel sexually dimorphic traits in two distinct and potentially opposing ways (*1*). First, conflict over any interaction between the sexes (e.g., mating rate) may drive the evolution of novel or exaggerated antagonistic characters such as grasping and antigrasping structures involved in premating struggles (*2*). Second, the resulting sex-biased selection on these traits gen-

erates sexual antagonism if the trait has a shared genetic basis in the two sexes (*3*). This intralocus conflict constitutes a major obstacle to the evolution of sexual dimorphism that can be overcome with the evolution of sex-specific regulatory mechanisms (*3*).

Our understanding of the role of sexually antagonistic selection in driving the evolution of dimorphisms in natural systems is rapidly increasing (*1*, *4*, *5*). However, we have little understanding of the developmental genetic mechanisms underlying these novel traits (*6*). For example, the extent to which highly conserved and pleiotropic developmental genes can evolve to resolve intralocus conflict and enable the evolution of sexual dimorphism remains unclear. In a few cases, such genes have been shown to play a role in the evolution of dimorphic traits (*6*–*9*); however, in no case have gene effects on the fine-scale structure and function of these traits, and their fitness consequences, been determined.

In water striders (Heteroptera: Gerridae), females resist costly superfluous mating through vigorous struggles aimed at rejecting male mating attempts (*2*, *10*). The genus *Rheumatobates* is distinguished by a diverse set of structural modifications of male appendages that are used to overcome this female resistance (*11*, *12*). Here, we focused on *Rheumatobates rileyi*, in which males have evolved spectacular appendage elaborations, particularly in the morphology of their antennae (*11*, *12*). We used fine-scale behavioral and mating performance analyses, coupled with pyrosequencing and RNA interference (RNAi) knockdown, to (i) reveal the structure and function of these traits, (ii) identify genes and genetic modifications underlying their evolution, and (iii) quantify their fitness consequences.

Using a combination of high-speed video (movies S1 to S3), flash-freezing of mating pairs, and scanning electron microscopy, we discovered four composite traits of male antennae that are used to gain a purchase on resistant females during premating struggles (Fig. 1, fig. S1, and movie S1). The first trait is the wrench-like shape of the male antennae that is formed by the curvature of the distal part of the first segment, the second segment, and the proximal part of the third segment (dashed outline in Fig. 1A), which fits precisely around the female eye (Fig. 1, E and F, fig. S1, and movie S1). The second trait is a "spike" formed by a set of 8 to 10 large bristles located on the ventral side of the most proximal segment (green in Fig. 1A). The spike fits in the groove formed by the intersection of the female's head capsule, first thoracic segment, and eye (Fig. 1, C, E, and F, and fig. S1). The third trait is a "pad" with a set of four or five internal setae on the second most distal segment (red in Fig. 1A). The pad rests underneath the female eye, and its internal setae may prevent male antennae from sliding sideways (Fig. 1, D to F). The fourth trait is a "hook" that is located on the most distal segment of male antennae (purple in Fig. 1, A and B). The hook fits into two alternative positions underneath the female's head (referred to as positions 1 and 2 in Fig. 1, D to F). In position 1, the hook fits into a groove at the intersection of the female's eye, head, and first thoracic segment (Fig. 1E), whereas in position 2 the hook sits between the first and second thoracic segments (Fig. 1F). Males alternate their antennae between positions 1 and 2 to leverage their body on top of the female in order to copulate. We found that the hook is equipped with a row of button-like structures (red in Fig. 1B), which may increase friction, enhancing the hook's grip. Thus, these elaborate traits are not simply generalized grasping structures, but are exquisitely shaped to the structural detail of the female head.

Male antennal traits begin to appear in the third instar and are elaborated during the fourth and fifth instars (Fig. 2), followed by the most substantive change at final molt, where all four traits are completed (compare Fig. 2, E and F). In contrast to males, female antennae (Fig. 2, H to L) grow uniformly throughout development and are not elaborated. To identify candidate genes responsible for the development of these male grasping characters, we performed a small-scale sequencing of the transcriptomes of appendages from third-, fourth-, and fifth-instar males and females. Among these sequences, we found a transcript that corresponds to the *distal-less* (*dll*) gene. *dll* is known to play important roles in controlling appendage growth and patterning, as well as bristle formation throughout development (*13*–*16*). Furthermore, we found that *dll* transcripts in *R. rileyi* are shorter than those of other hemipterans (*17*) [including other closely related water striders (*18*)] in which male antennae are not elaborated (Fig. 3A and figs. S2 and S3). We therefore analyzed the expression and function of *dll* in developing male and female antennae.

We discovered that, although *dll* is expressed in both male and female antennae (fig. S4), it functions only in the males to generate all four antennal grasping traits (Fig. 3). *dll* RNAi also causes a subtle (2 to 9%) shortening of the legs in males (fig. S5A). Several other male grasping

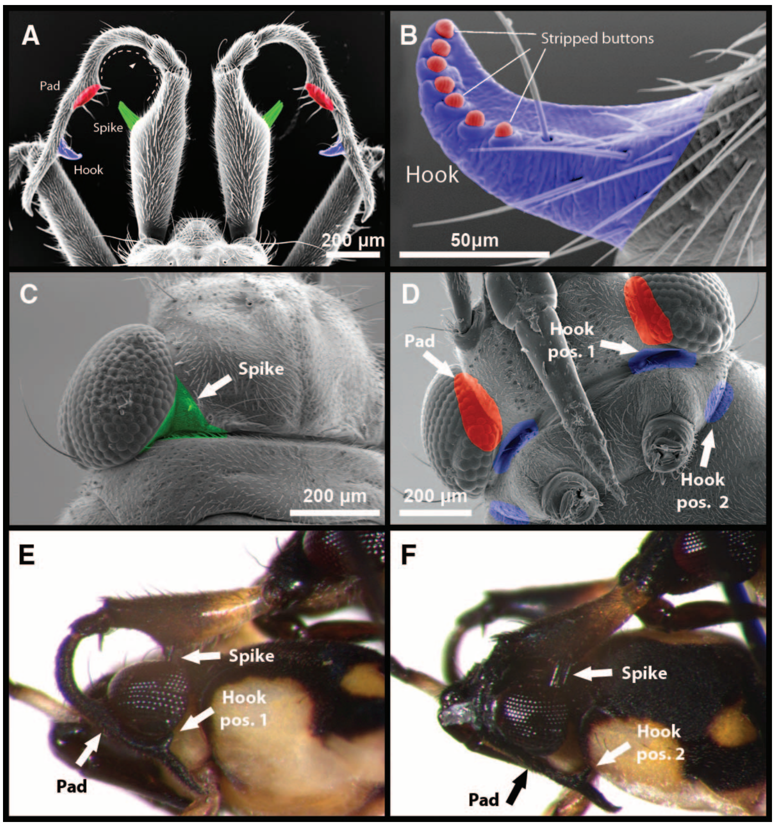

Fig. 1. Male and female structures involved in premating struggles. (**A**) Dorsal view of male antennae. (**B**) Close-up of the distal hook. (**C** and **D**) Dorsal (C) and ventral (D) views of female's head. (**E** and **F**) Positioning of antennae when males grasp females. In (A) to (D), the grasping structures in male antennae and the corresponding grasped structures on the female head are represented by the same colors.

[1]Department of Ecology and Evolutionary Biology, University of Toronto, Toronto, Ontario M5S 3B2, Canada. [2]Department of Biology, McGill University, Montreal, Quebec H3A 1B1, Canada. [3]Institut de Genomique Fonctionnelle de Lyon, Ecole Normale Supérieure, CNRS UMR 5242, 46 allée d'Italie, 69364 Lyon Cedex 07, France.

*To whom correspondence should be addressed. E-mail: locke.rowe@utoronto.ca

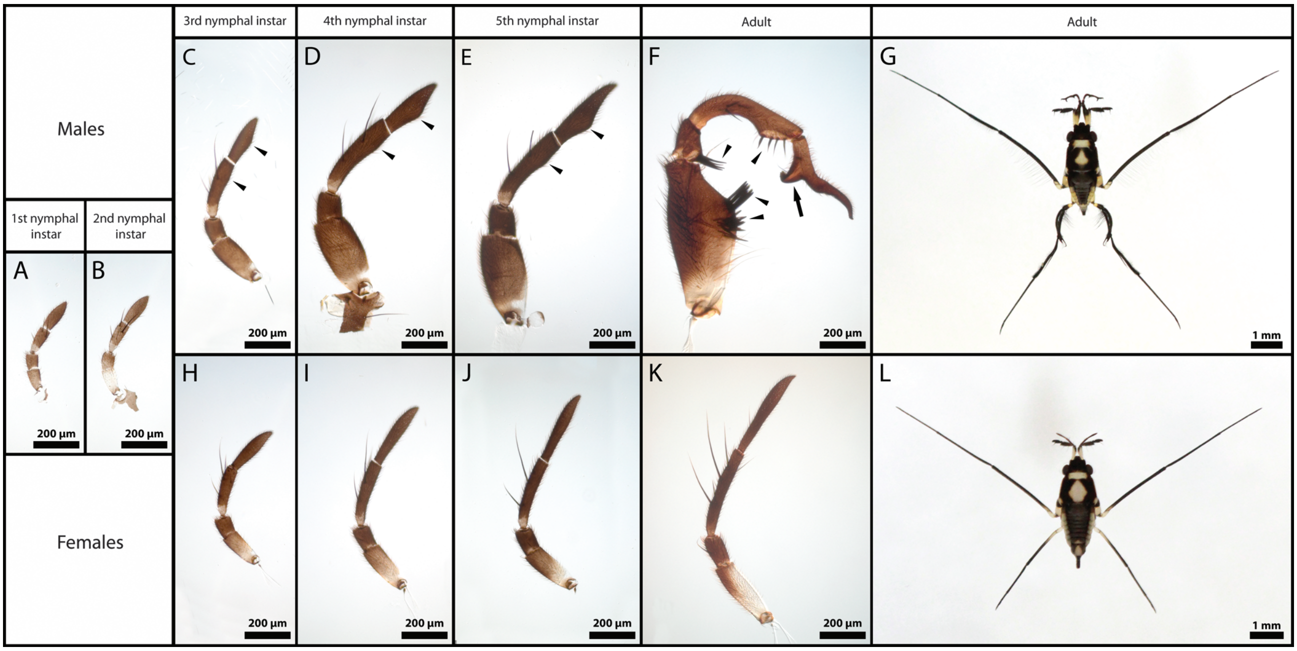

Fig. 2. Morphogenesis of male and female antennae. (**A** and **B**) Antennae of first and second nymphal instars. (**C** to **L**) Male [(C) to (F)] and female [(H) to (K)] antennae from third nymphal instar through adult; (G), adult male; (L), adult female.

A

```
Rr_Dll    YPFPPMHHNTYPSYHLAPYPQPCPSPPKD-EKCGEEGG-LRVNGKGKKMRKPRTIYSSLQLQQLNRRFQRTQYLALPERAELAASLGLTQTQVKIWFQN
Ld_Dll    YPFPPMHHNTYTGYHLASYAPQCPSPPKD-EKCGEEGG-LRVNGKGKKMRKPRTIYSSLQLQQLNRRFQRTQYLALPERAELAASLGLTQTQVKIWFQN
Ph_Dll    YPFPPMHQNSYSSYHLGGYGPQSPPKESELDKIGVEDGPLRVNGKGKKMRKPRTIYSSLQLQQLNRRFQRTQYLALPERAELAASLGLTQTQVKIWFQN
          *******:*:*..***. *   .*.  .: :* * *.* ************************************************************

Rr_Dll    RRSKYKKMMKA---------------------------------------------------------------------------------------
Ld_Dll    RRSKYKKMMKAAQQGGGGGGQGGGAPHMLGGLPPQSPPPAAAILQGSGGSSSGSSQQHSPGGGGGGGGPGYMSHVGTPTPSSTPQSDVSPHGM--SP
Ph_Dll    RRSKYKKMMKAAQNTGPGGQNNNGGGN--------GSPAPPGGATVGILGGNNSTGSQNSPNYG-------HHNQNQTSPSPSSTPVSDMSPHGLSGSP
          ***********

Rr_Dll    ----------------------------------PPHTAYMPQYSWYQTGAPPSEPNTAPGLLTVWPSV
Ld_Dll    PAA-WDMKP------VGPPAHPP-----HSAPPPPPHTAYMPQYSWYQAGPPPSEPNSTTGLLTVWPSV
Ph_Dll    PTMNWDMKPNINNLGVTPTHHTTGHPHHTPTHHHPTHHSYMPQYSWYNADT-ANQP-----LLTVWPAV
                                            *.* :********::.. ..:*     ******:*
```

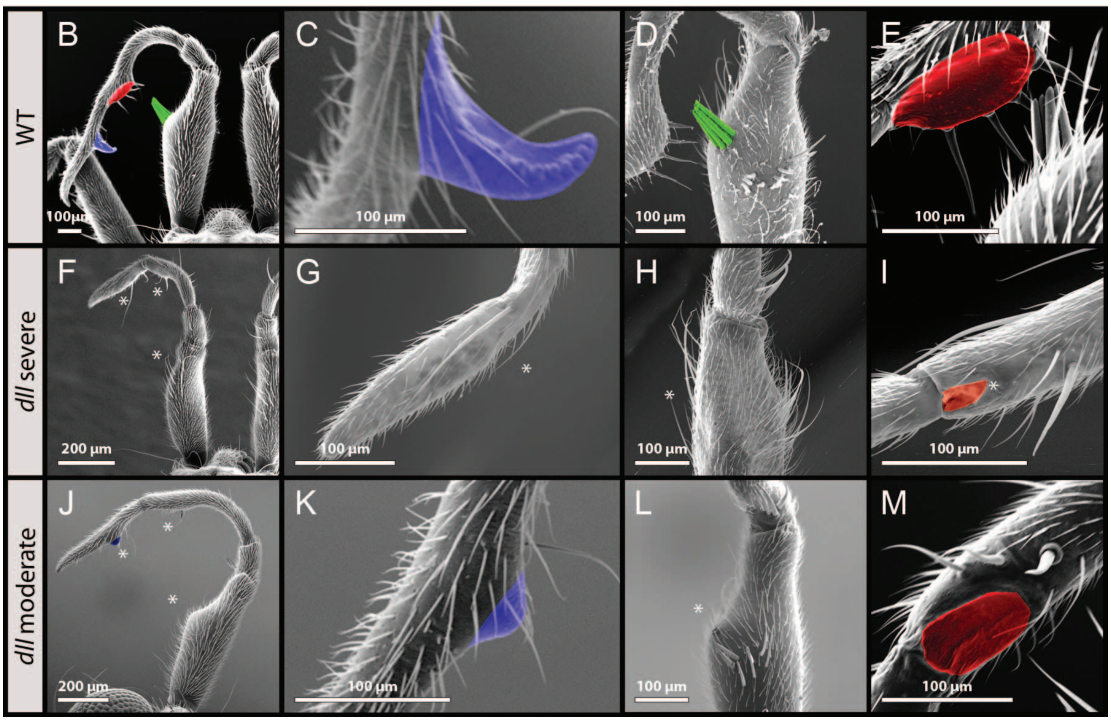

Fig. 3. (**A**) Comparison of Dll protein sequence in *R. rileyi* (Rr_Dll), *Limnoporus dissortis* (Ld_Dll), and the human louse *Pediculus humanus* (Ph_Dll) (*18*). Note that Rr_Dll is shorter; missing sequence (dashes) is immediately downstream of the homeodomain (in bold). Black asterisks indicate sequence identity among the three species. Motifs conserved between Ld_Dll and Ph_Dll are highlighted in green. (**B** to **M**) Effect of *dll* RNAi on *R. rileyi* male antennae. (B) to (E): Normal male antennae with close-ups of the hook (C), spikes (D), and pad (E). (F) to (I): Antennae of males showing severe *dll* RNAi effect. (J) to (M): Antennae of males showing moderate *dll* RNAi effect. White asterisks indicate traits affected by *dll* RNAi treatment. Colors are as in Fig. 1.

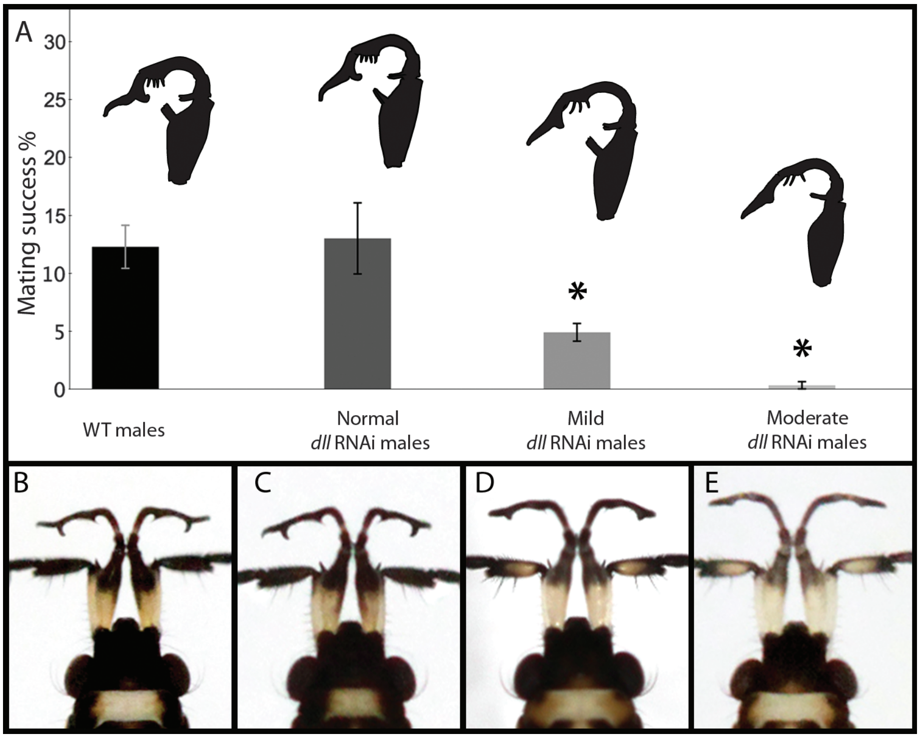

Fig. 4. Effect of *dll* RNAi on male antennae and its consequences for mating performance. (**A**) Graded reduction of antennal grasping structures results in a graded reduction in male mating performance. Mating success is measured as the percentage of the total number of premating struggles in which the male immobilizes and successfully copulates with the female. There is a significant overall effect of treatment (analysis of variance; $F = 32.6$, df = 3, $*P < 0.001$) on mating success, and post hoc contrasts reveal that mating success differences in the treatments can be summarized as wild type = normal > mild > moderate (Tukey's honestly significant difference, $\alpha = 0.05$). Mean numbers of mating attempts per male: wild type, 11.02 ± 6.85 (SE); normal, 13.00 ± 1.04; mild, 16.6 ± 5.49; moderate, 36.91 ± 12.55. Antennal diagrams for each treatment illustrate the degree of *dll* RNAi effect on antennal grasping structures. (**B**) Untreated male showing antennae morphology. (**C** to **E**) *dll* RNAi males with varying degrees of trait reduction: normal (no obvious reduction) (C), mild (D), and moderate (E).

structures, like those on the rear legs, are elaborated at developmental stages similar to those seen with the antennae (fig. S6, A to F) but are not affected by *dll* RNAi (compare fig. S6, F and G). This indicates that *dll* is not responsible for elaborating male grasping structures on other appendages, which suggests that they have a different genetic basis. Finally, we observed no effect on female appendages other than a small (2 to 4%) and insignificant reduction in appendage length, similar to what we saw in males (fig. S5B). Therefore, *dll* has evolved a novel function during late nymphal development to generate grasping traits specifically on male antennae.

The *dll* RNAi phenotypes we obtained range from complete loss to a subtle reduction of male antennal grasping traits (Fig. 3, Fig. 4, and fig. S7). We categorized these male antennal phenotypes into four broad classes: (i) "severe," in which all four antennal grasping traits are lost or nearly lost, such that male antennae become similar to those of females (Fig. 3, F to I, and fig. S4); (ii) "moderate" (Fig. 3, J to M, and Fig. 4E); (iii) "mild" reduction of antennal grasping traits (Fig. 4D and fig. S7); and (iv) "normal" antennal grasping traits (Fig. 4C and fig. S7). All classes of *dll* RNAi males are fully viable and repeatedly attempt to mate with females, which suggests that there are no deleterious pleiotropic effects when *dll* RNAi is applied at late nymphal development. The observed graded reduction of antennae and viability of *dll* RNAi males provided us with a unique opportunity to determine the consequence of their reduction on mating performance.

In mating performance tests, the experimentally graded reduction of antennal grasping structures resulted in a corresponding graded reduction in mating success. The mating success of males with moderate trait reduction was significantly reduced below that of wild-type males (Fig. 4). Examination of premating struggles revealed that these moderate males tended to fail during the initial flip of the female because their antennae failed to maintain their position around the female's head (fig. S8 and movie S2). The mating success of males with a mild reduction of antennal traits was significantly higher than for moderate males but lower than for wild-type males (Fig. 4). Males with mild reduction tended to fail later in the behavior sequence (movie S3) than did moderately reduced males. In contrast to both mild and moderate males, the mating success of *dll* RNAi males with normal antennae was not significantly different from that of wild-type males (Fig. 4). *dll* RNAi males, including those with normal antennae, tended to have mild reductions in leg length (fig. S7). Although we cannot exclude the possibility that the mild reduction in leg length contributes to the reduced mating success of *dll* RNAi males, we could not detect any effect on leg grasping structures (figs. S6 and S7) or any failure of their function in the videos. Even in wild-type males, only 12% of mating attempts were successful (Fig. 4). Such a large proportion of failures is a measure of the effectiveness of female resistance, which in turn accounts for the remarkable elaboration of antennae (*19*). Therefore, these data demonstrate both selection for elaborating male antennal grasping traits and the role of *dll* in their evolution.

Collectively, our results link an evolutionary change in morphology, the fitness advantage of this change, and its underlying genetic basis. The co-option of Dll late in development, after all the appendages have been specified (*20*, *21*), may have been an important factor that facilitated the evolution of male antennae elaboration without any apparent deleterious pleiotropic consequences (*22*). It remains unclear, however, how Dll function in elaborating the antennae is restricted to males. It is possible that proteins differentially expressed between the sexes, such as those encoded by sex determination genes, may act as cofactors to limit Dll's role to males (*9*, *23*–*25*). Furthermore, *R. rileyi dll* transcripts are shorter than those of other insects, including close relatives whose antennae are not sexually dimorphic (Fig. 3 and figs. S2 to S4). In these species, Dll does not seem to play any role in elaborating nymphal antennae (*20*) (fig. S9), raising the possibility that changes in *R. rileyi dll* coding sequence may be associated with the evolution of its novel function.

The graded effect of *dll* RNAi on male antennal grasping traits and its graded consequence on male mating performance suggests that even a slight elaboration of these traits from an unmodified ancestral state would be favored by female premating struggles. Therefore, in *R. rileyi*, selection resulting from female resistance may have favored the continuous elaboration of male antennae through this novel function of Dll. The elaboration of male antennae into grasping structures is not unique to *R. rileyi* but has evolved repeatedly within the genus *Rheumatobates* (*11*, *12*). This raises the possibility that variation in *dll* expression and function may underlie the diversity and degree of modification observed in the clade (*11*, *12*). By combining an understanding of the elaborated morphologies generated through sexual antagonism with the power of developmental

genetics and genomics tools, water striders provide a model to reconstruct the genetic and adaptive paths to morphological diversity.

References and Notes

1. G. Arnqvist, L. Rowe, *Sexual Conflict* (Princeton Univ. Press, Princeton, NJ, 2005).
2. G. Arnqvist, L. Rowe, *Nature* **415**, 787 (2002).
3. R. Bonduriansky, S. F. Chenoweth, *Trends Ecol. Evol.* **24**, 280 (2009).
4. D. Hosken, R. Snook, *Am. Nat.* **165** (suppl. 5), S1 (2005).
5. T. Tregenza, N. Wedell, T. Chapman, *Philos. Trans. R. Soc. London Ser. B* **361**, 229 (2006).
6. T. M. Williams, S. B. Carroll, *Nat. Rev. Genet.* **10**, 797 (2009).
7. D. J. Emlen, L. Corley Lavine, B. Ewen-Campen, *Proc. Natl. Acad. Sci. U.S.A.* **104** (suppl. 1), 8661 (2007).
8. A. P. Moczek, D. J. Rose, *Proc. Natl. Acad. Sci. U.S.A.* **106**, 8992 (2009).
9. T. M. Williams *et al.*, *Cell* **134**, 610 (2008).
10. L. Rowe, G. Arnqvist, *Evolution* **56**, 754 (2002).
11. L. Rowe, K. Westlake, D. C. Currie, *Can. Entomol.* **138**, 568 (2006).
12. K. P. Westlake, L. Rowe, D. C. Currie, *Syst. Entomol.* **25**, 125 (2000).
13. A. Beermann *et al.*, *Development* **128**, 287 (2001).
14. A. Khila, M. Grbić, *Dev. Genes Evol.* **217**, 241 (2007).
15. G. Panganiban, *Dev. Dyn.* **218**, 554 (2000).
16. G. Panganiban *et al.*, *Proc. Natl. Acad. Sci. U.S.A.* **94**, 5162 (1997).
17. E. F. Kirkness *et al.*, *Proc. Natl. Acad. Sci. U.S.A.* **107**, 12168 (2010).
18. J. Damgaard *et al.*, *Syst. Entomol.* **30**, 289 (2005).
19. L. Rowe, G. Arnqvist, A. Sih, J. J. Krupa, *Trends Ecol. Evol.* **9**, 289 (1994).
20. D. R. Angelini, T. C. Kaufman, *Dev. Biol.* **286**, 57 (2005).
21. A. Khila, E. Abouheif, L. Rowe, *PLoS Genet.* **5**, e1000583 (2009).
22. T. Werner, S. Koshikawa, T. M. Williams, S. B. Carroll, *Nature* **464**, 1143 (2010).
23. F. W. Buaas, P. Val, A. Swain, *Hum. Mol. Genet.* **18**, 2989 (2009).
24. R. Clifford *et al.*, *Development* **127**, 5265 (2000).
25. K. Tanaka, O. Barmina, L. E. Sanders, M. N. Arbeitman, A. Kopp, *PLoS Biol.* **9**, e1001131 (2011).

Acknowledgments: Supported by the Canada Research Chairs program and the Natural Sciences and Engineering Research Council of Canada (L.R. and E.A.) and by ATIP-Avenir program CNRS France (A.K.). We thank G. Arnqvist, A. Bruce, and M. Sokolowski for comments; H. Rodd and A. Agrawal for sharing their high-speed camera; and S. B. Carroll for the Dll antibody. DNA sequences were deposited in GenBank (accession nos. JQ639098, JQ639093, JQ639097, JQ639094, JN936863, JQ639092, JQ639096, and JQ639095).

Supplementary Materials
www.sciencemag.org/cgi/content/full/336/6081/585/DC1
Materials and Methods
Figs. S1 to S9
Table S1
Movies S1 to S3
References (*26*, *27*)

30 November 2011; accepted 23 March 2012
10.1126/science.1217258

Impacts of Biodiversity Loss Escalate Through Time as Redundancy Fades

Peter B. Reich,[1,2] David Tilman,[3,4] Forest Isbell,[3] Kevin Mueller,[3] Sarah E. Hobbie,[3] Dan F. B. Flynn,[5] Nico Eisenhauer[1,6]

Plant diversity generally promotes biomass production, but how the shape of the response curve changes with time remains unclear. This is a critical knowledge gap because the shape of this relationship indicates the extent to which loss of the first few species will influence biomass production. Using two long-term (≥13 years) biodiversity experiments, we show that the effects of diversity on biomass productivity increased and became less saturating over time. Our analyses suggest that effects of diversity-dependent ecosystem feedbacks and interspecific complementarity accumulate over time, causing high-diversity species combinations that appeared functionally redundant during early years to become more functionally unique through time. Consequently, simplification of diverse ecosystems will likely have greater negative impacts on ecosystem functioning than has been suggested by short-term experiments.

Experiments in grasslands regularly indicate strong plant diversity effects on biomass production (*1*–*16*), and some analyses indicate that relatively few of the species in any diverse mixture promote productivity (*1*, *5*). However, many important temporal aspects of the diversity-productivity relationship remain obscure, including whether and how its shape changes over time, because most biodiversity experiments have been short (≤4 years typically, median ≈2 years) (*10*).

Prior studies have characterized the response of plant biomass to species richness as saturating (*1*, *7*) or as continuously increasing, but in a decelerating manner (*6*, *8*, *9*). A recent meta-analysis (*1*) showed that saturating Michaelis-Menten curves were often the best statistical fit to the diversity-productivity relationship, suggesting losses of one or a few species at high richness levels could have minimal consequences for productivity.

Several experiments showed that the positive effects of species richness on biomass and productivity increased over time (*6*, *8*, *10*, *12*–*15*), but implications of such changes for the shape of the diversity-productivity relationship are unknown. Two possibilities can be distinguished: (i) differences between low and intermediate diversity levels grow, resulting in an elevated but saturating response curve (fig. S1, scenario I); or (ii) diversity effects become progressively greater at higher diversity, resulting in an elevated and more linear response curve (fig. S1, scenario II, nonsaturating response curve). These scenarios have fundamentally different implications for the consequences of biodiversity loss. If response curves become less saturating over time, losses of even very few species from diverse assemblages could cause substantial declines in productivity.

Several studies have assessed how biodiversity influences multiple functions within 1 year or across multiple years (*2*, *4*, *5*), but identifying what proportion of the available species pool contributes to multifunctionality does not address the question of whether species are redundant with respect to a single function, such as productivity, in a single year, let alone how that changes with time. We examined this latter issue by considering how the influence of biodiversity on productivity within each year changes from the early to the late years of two long-term experiments.

We present data from two long-running (≥13 years) grassland biodiversity experiments in Minnesota, USA: the "Cedar Creek Biodiversity Experiment" (BioDIV), planted in 1994–1995, and the "Biodiversity, CO_2, and N Experiment" (BioCON), planted in 1997 (*6*, *17*–*21*). These independent, comparable experiments allow us to assess temporal variation in the response of biomass to planted and realized species richness. Species pools differed somewhat in the two experiments, although both include many of the same C3 and C4 grasses, and nitrogen (N)–fixing and nonfixing dicotyledonous herbs. BioCON included elevated carbon dioxide and enriched N treatments (*18*, *19*), but only the ambient plots are considered here to facilitate comparison with BioDIV. In both experiments, the species richness across treatments ranged from 1 to 16 species, spanning the typical range observed from disturbed to native grassland (*17*).

In both experiments, the number of planted species explained an increasingly greater fraction of the variance in total plant biomass over time and had a larger effect on total plant biomass over time (Fig. 1, Table 1, and table S1). More-

[1]Department of Forest Resources, University of Minnesota, St. Paul, MN 55108, USA. [2]Hawkesbury Institute for the Environment, University of Western Sydney, Penrith NSW 2753, Australia. [3]Department of Ecology, Evolution, and Behavior, University of Minnesota, St. Paul, MN 55108, USA. [4]Bren School of the Environment, University of California, Santa Barbara, CA 93106, USA. [5]Institute of Evolutionary Biology and Environmental Studies, University of Zurich, Zurich 8057, Switzerland. [6]Department of Ecology and Ecosystem Management, Technische Universität München, Hans-Carl-von-Carlowitz-Platz 2, 85354 Freising, Germany.

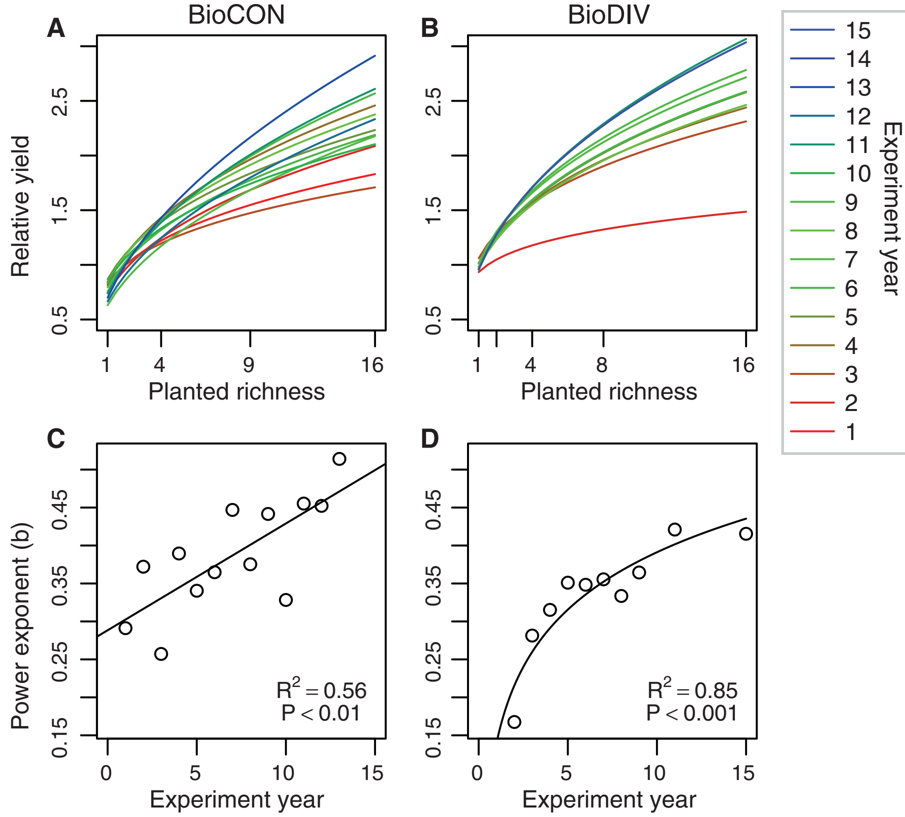

Fig. 1. (**A** and **B**) The power function of the relative yield of total biomass (above- plus belowground, 0 to 20 or 0 to 30 cm depth, respectively) in relation to planted species richness, across years in the BioCON and BioDIV experiments. Relative yield was defined by dividing plot-level values by the mean monoculture yield, averaged across all monoculture plots within each year. Details of all fits are provided in Table 1. (**C** and **D**) The exponent of the power function in relation to experimental years.

over, the relationship became increasingly nonsaturating (*17*) over the range of species richness levels used (Fig. 1 and Table 1). The increasing linearity is illustrated first by comparing the Akaike Information Criterion (AIC) values of saturating functions (Michaelis-Menten) with decelerating functions. The saturating function is the best model by AIC only in the first few years in BioCON and is a poorer model than decelerating functions (especially the power function) in most years late in both experiments (table S1). Second, the exponent from the power function fits ("b") increased over time in both experiments (Fig. 1 and Table 1), with increases from 0 toward 1, indicating that the diversity-productivity relationship is becoming more linear and less strongly decelerating. Consequently, we also observed increases over time for estimates of the number of planted species required to yield 90% of the biomass in 16 species plots (the number of species required to generate most of the diversity effect on biomass in a given year) (fig. S2). Results were similar when we considered aboveground or belowground biomass separately, when we considered absolute biomass, and when we considered observed richness instead of planted richness (figs. S3 to S5 and tables S2 and S3).

Because the statistical fits for the biodiversity functions are imperfect at establishing the precise shape of the relations, directly comparing across species-richness treatments illuminates the role

Table 1. Model fit statistics for the power function describing the relationship between relative biomass yield (Y) and planted richness (S). Relative biomass yield was defined by dividing plot-level values by the mean monoculture yield, averaged across all monoculture plots within each year.

Study	DF	Year	Power: $\ln(Y) = a + b \times \ln(S)$			
			R^2	P value	a	b
BioCON	71	1998	0.24	1.3×10^{-5}	−0.20	0.29
	72	1999	0.24	9.0×10^{-6}	−0.30	0.37
	72	2000	0.19	1.2×10^{-4}	−0.18	0.26
	71	2001	0.34	5.1×10^{-8}	−0.18	0.39
	72	2002	0.38	5.9×10^{-9}	−0.14	0.34
	72	2003	0.34	6.3×10^{-8}	−0.23	0.36
	70	2004	0.23	2.3×10^{-5}	−0.46	0.45
	70	2005	0.40	2.9×10^{-9}	−0.18	0.38
	71	2006	0.34	6.1×10^{-8}	−0.28	0.44
	64	2007	0.35	1.4×10^{-7}	−0.17	0.33
	64	2008	0.39	1.7×10^{-8}	−0.30	0.46
	64	2009	0.31	1.2×10^{-6}	−0.41	0.45
	63	2010	0.39	2.2×10^{-8}	−0.36	0.51
BioDIV	150	1997	0.08	3.3×10^{-4}	−0.07	0.17
	150	1998	0.24	2.3×10^{-10}	0.06	0.28
	150	1999	0.31	1.2×10^{-13}	0.02	0.32
	150	2000	0.37	6.5×10^{-17}	−0.03	0.35
	150	2001	0.39	8.3×10^{-18}	−0.02	0.35
	150	2002	0.43	6.3×10^{-20}	0.01	0.36
	150	2003	0.38	2.1×10^{-17}	−0.02	0.33
	150	2004	0.45	5.6×10^{-21}	0.01	0.36
	150	2006	0.48	2.8×10^{-23}	−0.05	0.42
	150	2010	0.52	1.3×10^{-25}	−0.04	0.42

that different levels of richness played in biodiversity effects at different times during the experiments (Fig. 2 and figs. S6 and S7). In the first 4 years of both experiments, the effect on biomass (shown as $\log_{10}$[biomass ratios]) of an increase in richness from one to four species was strong (Fig. 2C), whereas the increase in richness from medium (eight or nine species) to high (16 species) diversity was negligible (Fig. 2B). However, over time the log of the ratio of biomass in plots with four versus one species remained stable but became progressively larger for plots with 16 versus 1 species (Fig. 2, A and C). The latter result was because the difference in biomass between plots with highest richness (16 species) versus medium richness (eight or nine species) grew over time (Fig. 2B and fig. S8). Because the 16-, 9-, and 8-species plots were all planted with similar proportions of legumes, the increase over time in the biomass differences between them is not a result of differences in legume presence in their original species pools (fig. S7). Additionally, although the shifts in biomass in different diversity treatments occurred in different ways in the two studies (*17*), the results in aggregate suggest that all species contribute to increasing biomass at higher diversity, especially so over time. Hence, simplification of even diverse ecosystems should be considered a possible threat to their long-term productivity.

What caused the diversity-biomass function to grow larger and less saturating over time? Evidence suggests this was due to the accumulating effects of complementarity of resource acquisition and use and of ecosystem feedback effects, such as on soil N cycling. By partitioning diversity effects into those associated with species complementarity versus selection (*10*, *12*, *22*), we show that the substantial and rising diversity effect is due largely to complementarity (Fig. 3, A to D). The complementarity effect may be driven by increasing functional diversity (FD) (*23*, *24*) and/or the replacement of species by functionally dissimilar ones (*25*). Within each level of species richness in BioCON, an abundance-weighted index of FD (FDA) increased over time (Fig. 3E). An alternative abundance-weighted functional diversity metric, Rao's Q, yields similar results, with less increase over time but greater separation across richness levels (fig. S9).

Complementarity can involve many traits, but important ones in an N-limited system might involve N cycling and availability. If diverse plots gradually accumulated more N in soil organic matter and plant biomass than less diverse plots, and this additional N subsequently becomes available through decomposition of plant litter and soil organic matter (*13*), then the diversity-productivity relationship could be boosted by in-

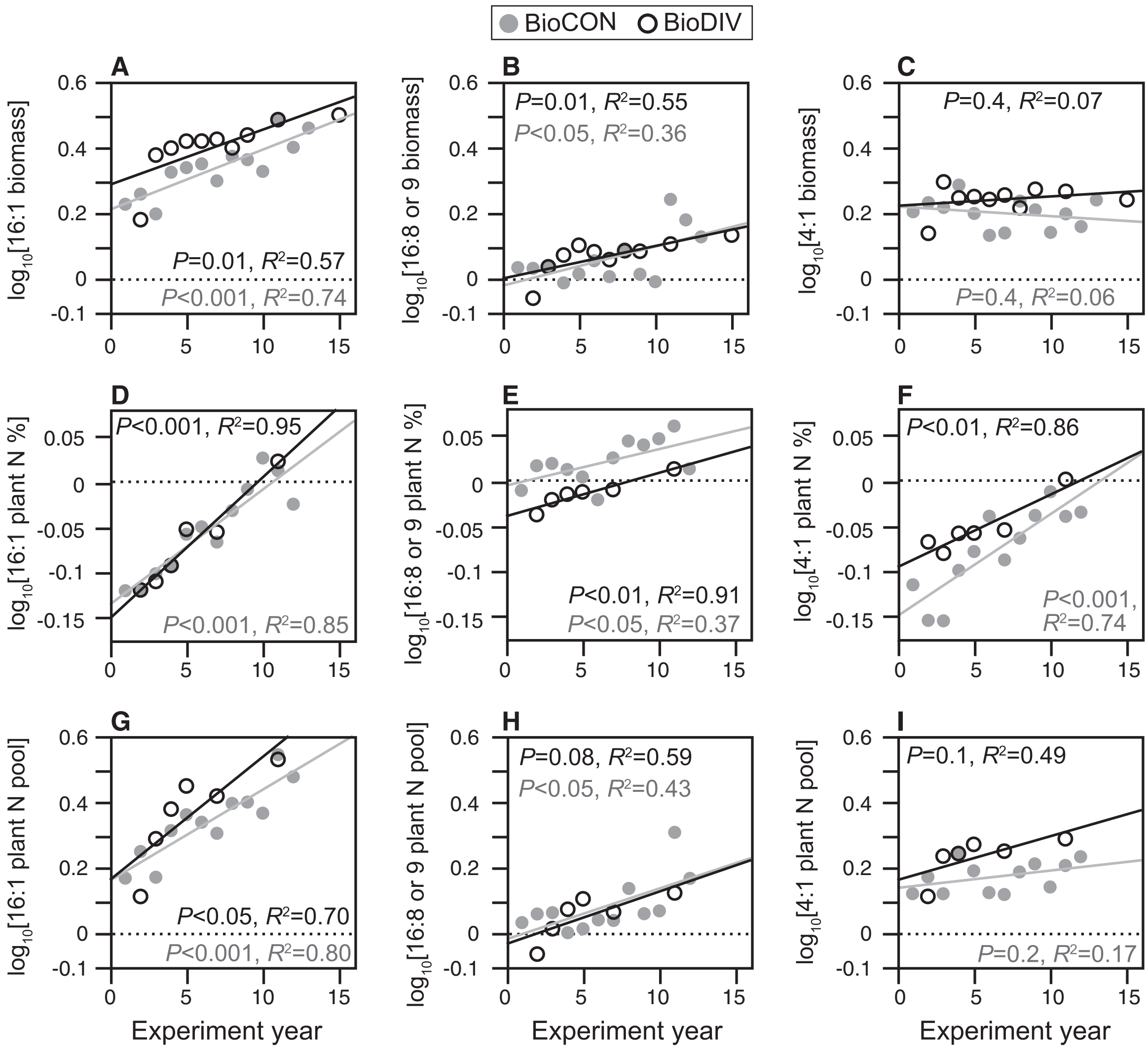

Fig. 2. The $\log_{10}$ ratio of total biomass, tissue nitrogen concentration (plant N percent), and plant N pools (all above- and belowground, 0 to 20 or 0 to 30 cm depth), comparing means from treatments planted with different numbers of species [(**A**), (**D**), and (**G**), 16:1; (**B**), (**E**), and (**H**), 16:8 or 16:9; and (**D**), (**F**), and (**I**), 4:1], across years, in the BioCON and BioDIV experiments. Values above zero represent a positive diversity effect; values below zero a negative effect [following (*10*)]. Similar trends were observed when comparing trends in absolute differences between species-richness levels instead of log ratios (not shown).

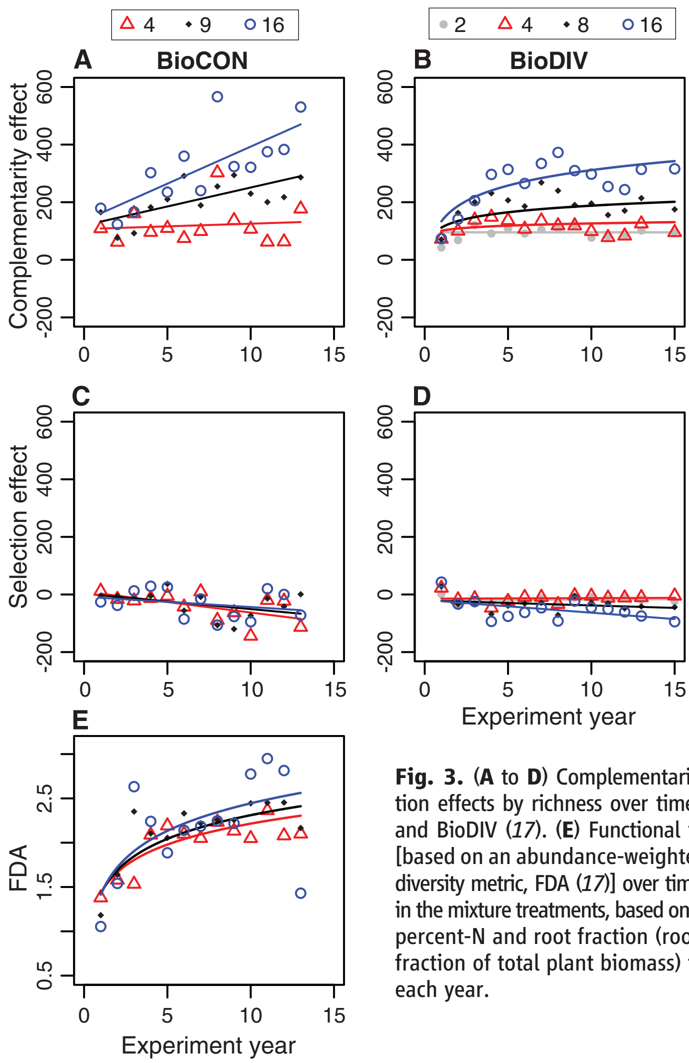

Fig. 3. (**A** to **D**) Complementarity and selection effects by richness over time for BioCON and BioDIV (*17*). (**E**) Functional trait diversity [based on an abundance-weighted functional diversity metric, FDA (*17*)] over time for BioCON in the mixture treatments, based on aboveground percent-N and root fraction (root biomass as fraction of total plant biomass) trait data for each year.

creased N availability in later years. Other biotic effects of diversity, including reduced disease (*7*, *26*) and decreased abundances of herbivores (*27*), could also change over time and contribute to the growing diversity effects on productivity and nutrient cycling.

Species-rich plots became more N-rich over time relative to species-poor plots. Data from BioCON show an increasingly positive effect of diversity over time on rates of net N mineralization and concentrations of ammonium in soil (fig. S6; similar data are not available for BioDIV). For both experiments, diversity effects on community plant tissue N concentrations and plant N pools (Fig. 2) also became more positive, indicating an increase in N stocks, uptake, and/or supply rates in species-rich plots. Earlier reports showed only negative impacts of diversity on tissue percent-N (*12*, *19*), but here we show diversity effects switched to neutral or slightly positive after ≈10 years (Fig. 2, D to F). In addition, variation among species in leaf percent-N, but not root fraction (root biomass as a fraction of total plant biomass), increased in higher-diversity plots. These observations indicate that in species-rich plots, communities became more differentiated in their spread along the leaf economics spectrum (*28*). Last, the increasingly positive effects of diversity on N availability over time were not due solely to the presence of N-fixers. Soil N cycling and tissue percent-N were increasingly enhanced by higher species richness (16 versus 4 planted species) when legume presence was accounted for by examining only plots in which legumes were one-fourth of the original seed pool (fig. S8).

Over ≥13 years, both BioCON and BioDIV showed increasingly positive and nonsaturating relationships between biomass and species richness. These findings suggest that shorter-term studies could be misleading by incorrectly indicating functional redundancy and therefore undervaluing biodiversity. In BioCON and BioDIV, the relationship of biomass to species richness became stronger and less asymptotic as a result of increasing complementarity among species (for example, via increasing functional trait diversity) and increasingly positive impacts of diversity on soil N availability and plant N pools and tissue percent-N. Our long-term results show that changes in diversity at high levels of richness have much larger effects than those shown by short-term studies. Thus, diversity matters for productivity not just in species-depauperate contexts (as in comparing monocultures to two- or four-species mixtures), but also, and increasingly over time, at high plant species richness. Hence, because of reduced cumulative feedback and complementarity effects, even the loss of a few species from mature diverse communities could lead in the long term to decreases in biomass production and the sustainability of ecosystem functioning.

References and Notes

1. B. J. Cardinale *et al.*, *Am. J. Bot.* **98**, 572 (2011).
2. E. S. Zavaleta, J. R. Pasari, K. B. Hulvey, G. D. Tilman, *Proc. Natl. Acad. Sci. U.S.A.* **107**, 1443 (2010).
3. P. Balvanera *et al.*, *Ecol. Lett.* **9**, 1146 (2006).
4. F. Isbell *et al.*, *Nature* **477**, 199 (2011).
5. A. Hector, R. Bagchi, *Nature* **448**, 188 (2007).
6. D. Tilman *et al.*, *Science* **294**, 843 (2001).
7. S. A. Schnitzer *et al.*, *Ecology* **92**, 296 (2011).
8. E. Marquard *et al.*, *Ecology* **90**, 3290 (2009).
9. A. Hector *et al.*, *Science* **286**, 1123 (1999).
10. B. J. Cardinale *et al.*, *Proc. Natl. Acad. Sci. U.S.A.* **104**, 18123 (2007).
11. A. Hector *et al.*, *PLoS ONE* **6**, e17434 (2011).
12. J. Fargione *et al.*, *Proc. Biol. Sci.* **274**, 871 (2007).
13. D. A. Fornara, D. Tilman, *Ecology* **90**, 408 (2009).
14. F. I. Isbell, H. W. Polley, B. J. Wilsey, *Ecology* **90**, 1821 (2009).
15. J. van Ruijven, F. Berendse, *Oikos* **118**, 101 (2009).
16. J. van Ruijven, F. Berendse, *Proc. Natl. Acad. Sci. U.S.A.* **102**, 695 (2005).
17. Materials and methods are available as supplementary materials on *Science* Online.
18. P. B. Reich *et al.*, *Nature* **440**, 922 (2006).
19. P. B. Reich *et al.*, *Nature* **410**, 809 (2001).
20. D. Tilman *et al.*, *Science* **278**, 1866 (1997).
21. D. Tilman, P. B. Reich, J. M. H. Knops, *Nature* **441**, 629 (2006).
22. M. Loreau, A. Hector, *Nature* **412**, 72 (2001).
23. D. U. Hooper, P. M. Vitousek, *Ecol. Monogr.* **68**, 121 (1998).
24. A. Kahmen, C. Renker, S. B. Unsicker, N. Buchmann, *Ecology* **87**, 1244 (2006).
25. E. Allan *et al.*, *Proc. Natl. Acad. Sci. U.S.A.* **108**, 17034 (2011).
26. J. S. Petermann, A. J. F. Fergus, L. A. Turnbull, B. Schmid, *Ecology* **89**, 2399 (2008).
27. N. M. Haddad, G. M. Crutsinger, K. Gross, J. Haarstad, D. Tilman, *Ecol. Lett.* **14**, 42 (2011).
28. I. J. Wright *et al.*, *Nature* **428**, 821 (2004).

Acknowledgments: We thank the U.S. Department of Energy Program for Ecosystem Research (DE-FG02-96ER62291) and the National Institute for Climatic Change Research (DE-FC02-06ER64158); the National Science Foundation Long-Term Ecological Research (DEB-9411972, DEB-0080382, and DEB-0620652), Biocomplexity Coupled Biogeochemical Cycles (DEB-0322057) and Long-Term Research in Environmental Biology Programs (DEB-0716587), and the University of Minnesota for supporting this research. The data sets used in this study are available at the Cedar Creek Ecosystem Science Reserve Web site. The authors declare no conflicts of interest.

Supplementary Materials

www.sciencemag.org/cgi/content/full/336/6081/589/DC1
Materials and Methods
Figs. S1 to S9
Tables S1 to S3
References (*29*–*40*)

14 December 2011; accepted 15 March 2012
10.1126/science.1217909

Removal of Shelterin Reveals the Telomere End-Protection Problem

Agnel Sfeir* and Titia de Lange†

The telomere end-protection problem is defined by the aggregate of DNA damage signaling and repair pathways that require repression at telomeres. To define the end-protection problem, we removed the whole shelterin complex from mouse telomeres through conditional deletion of TRF1 and TRF2 in nonhomologous end-joining (NHEJ) deficient cells. The data reveal two DNA damage response pathways not previously observed upon deletion of individual shelterin proteins. The shelterin-free telomeres are processed by microhomology-mediated alternative-NHEJ when Ku70/80 is absent and are attacked by nucleolytic degradation in the absence of 53BP1. The data establish that the end-protection problem is specified by six pathways [ATM (ataxia telangiectasia mutated) and ATR (ataxia telangiectasia and Rad3 related) signaling, classical-NHEJ, alt-NHEJ, homologous recombination, and resection] and show how shelterin acts with general DNA damage response factors to solve this problem.

Aspects of the end-protection problem have been revealed in yeast, plant, and mammalian cells based on adverse events at telomeres lacking certain telomeric proteins (*1*). However, the fate of telomeres devoid of all protective factors is unknown, and hence the end-protection problem remained undefined. Mammals solve the end-protection problem through the agency of shelterin (*2*), a multisubunit protein complex anchored onto duplex telomeric DNA by the TTAGGG repeat binding factors TRF1 and TRF2 (fig. S1). Both TRF1 and TRF2 interact with TIN2 (TRF1-interacting nuclear factor 2), which in turn links the heterodimer formed by TPP1 (TINT1/PTOP1/PIP1) and POT1 (protection of telomeres 1; POT1a and POT1b in mouse) to telomeres. TPP1/POT1 interacts with the single-stranded TTAGGG repeats present at mammalian chromosome ends in the form of a

Laboratory for Cell Biology and Genetics, The Rockefeller University, 1230 York Avenue, New York, NY 10065, USA.

*Present address: Developmental Genetics Program and Department of Cell Biology, Skirball Institute, New York University School of Medicine, New York, NY 10016, USA.
†To whom correspondence should be addressed. E-mail: delange@mail.rockefeller.edu

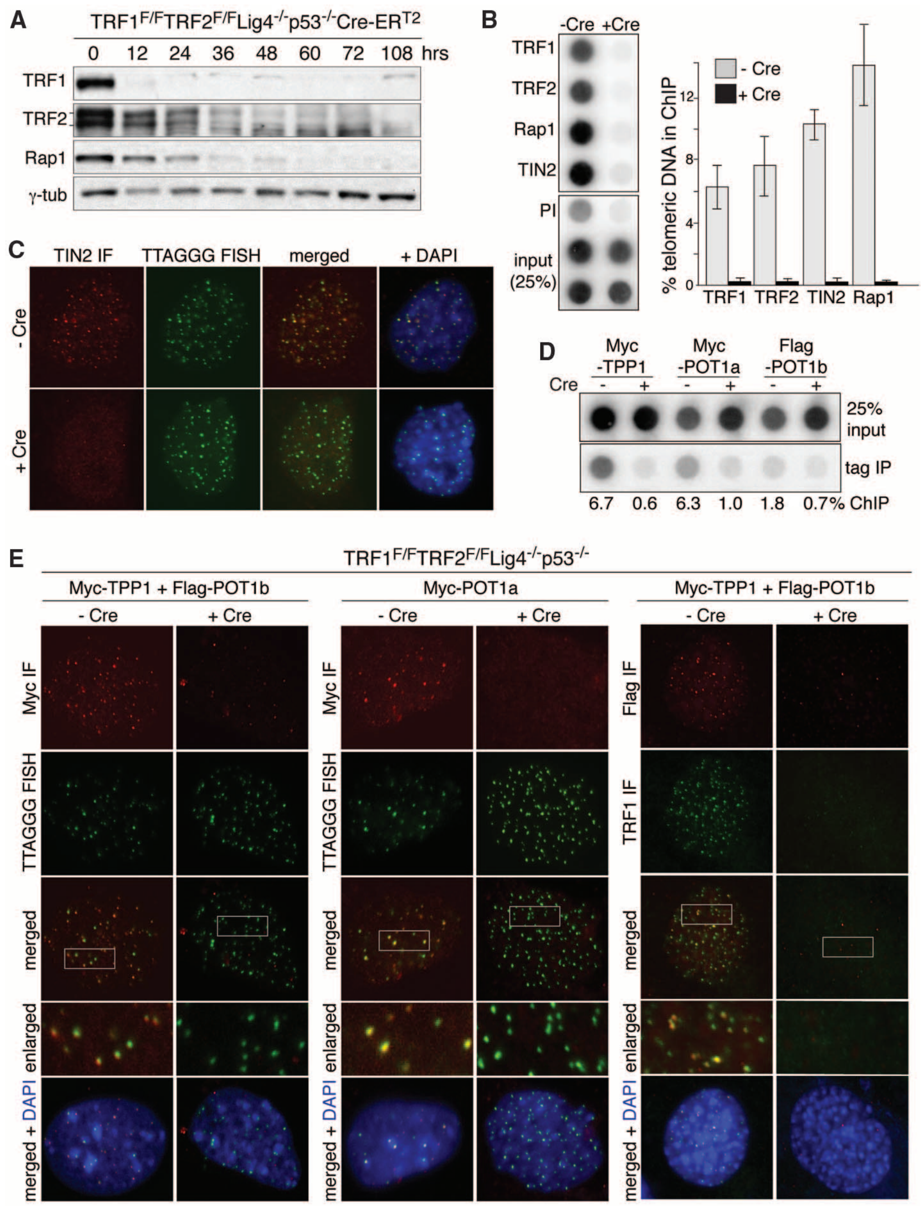

Fig. 1. Shelterin-free telomeres. (**A**) Immunoblots for TRF1, TRF2, and Rap1 after 4-OHT–induced TRF1/2 DKO from $Lig4^{-/-}p53^{-/-}$Cre-ERT2 MEFs. (**B**) ChIP for telomeric DNA associated with shelterin proteins in $TRF1^{F/F}TRF2^{F/F}p53^{-/-}Lig4^{-/-}$ MEFs (day 5 after H&R-Cre). Bars average percentage of telomeric DNA recovered in two independent experiments, ± SEMs. (**C**) IF-FISH for TIN2 at telomeres in $TRF1^{F/F}TRF2^{F/F}p53^{-/-}Lig4^{-/-}$ MEFs day 5 after H&R-Cre. TIN2 IF (red); telomeric PNA probe [fluorescein isothiocyanate (FITC), green]. (**D**) ChIP for telomeric DNA associated with Myc-TPP1, Myc-POT1a, and Flag-POT1b in $TRF1^{F/F}TRF2^{F/F}p53^{-/-}$ $Lig4^{-/-}$ cells, with (+) and without (–) H&R-Cre. (**E**) IF for the telomeric localization of Myc-TPP1, Myc-POT1a, and Flag-POT1b (red, MYC or Flag antibodies) in $TRF1^{F/F}TRF2^{F/F}p53^{-/-}Lig4^{-/-}$ MEFs (5 days after H&R-Cre). Green, telomeric PNA probe or TRF1 IF.

50 to 400 nucleotide (nt) 3′ overhang. The sixth shelterin subunit, Rap1, is a TRF2-interacting factor. Deletion of each of the individual shelterin proteins revealed that the end-protection problem minimally involves the repression of ATM (ataxia telangiectasia mutated) and ATR (ataxia telangiectasia and Rad3 related) signaling as well as inhibition of double-strand break (DSB) repair by nonhomologous end-joining (NHEJ) and homology-directed repair (HDR). However, the possibility of redundant repression of additional DNA damage response (DDR) pathways has prevented a definitive description of the end-protection problem in mammalian cells.

We sought to finalize the tally of telomere-threatening pathways by generating telomeres devoid of all shelterin proteins and their associated factors. We set out to remove both TRF1 and TRF2, which is predicted to lead to complete loss of shelterin (fig. S1). In this TRF1/2 double-knockout (DKO), NHEJ of telomeres devoid of TRF2 thwarts detection of potential novel pathways acting on deprotected chromosome ends. We therefore created conditional TRF1/2 DKO mouse embryo fibroblasts (MEFs) with additional deficiencies in DNA ligase IV (Lig4), Ku80, or 53BP1, which are predicted to minimize telomere fusion (*3*–*5*). Cre was expressed from a self-deleting Hit-and-Run (H&R-Cre) retrovirus or from a genetically introduced tamoxifen (4-OHT)–inducible Cre (Cre-ERT2 in the Rosa26 locus). TRF1$^{F/F}$TRF2$^{F/F}$Lig4$^{-/-}$p53$^{-/-}$Cre-ERT2 MEFs rapidly lost TRF1, TRF2, and Rap1 when treated with 4-OHT and telomeric chromatin immunoprecipitation (ChIP) and immunofluorescence (IF) established that TRF1, TRF2, Rap1, and TIN2 disappeared from telomeres (Fig. 1, A to C). Furthermore, using tagged alleles to facilitate analysis, IF and ChIP documented loss of TPP1 and POT1a/b from the telomeres (Fig. 1, D and E, and fig. S2, A and B). Thus, the TRF1/2 DKO generates shelterin-free telomeres. However, the telomeric DNA remained packaged in nucleosomal chromatin (fig. S2C).

As expected from the ATM/ATR signaling elicited by removal of TRF2 and POT1a, respectively (*6*), cells with shelterin-free telomeres showed phosphorylation of Chk2 and Chk1,

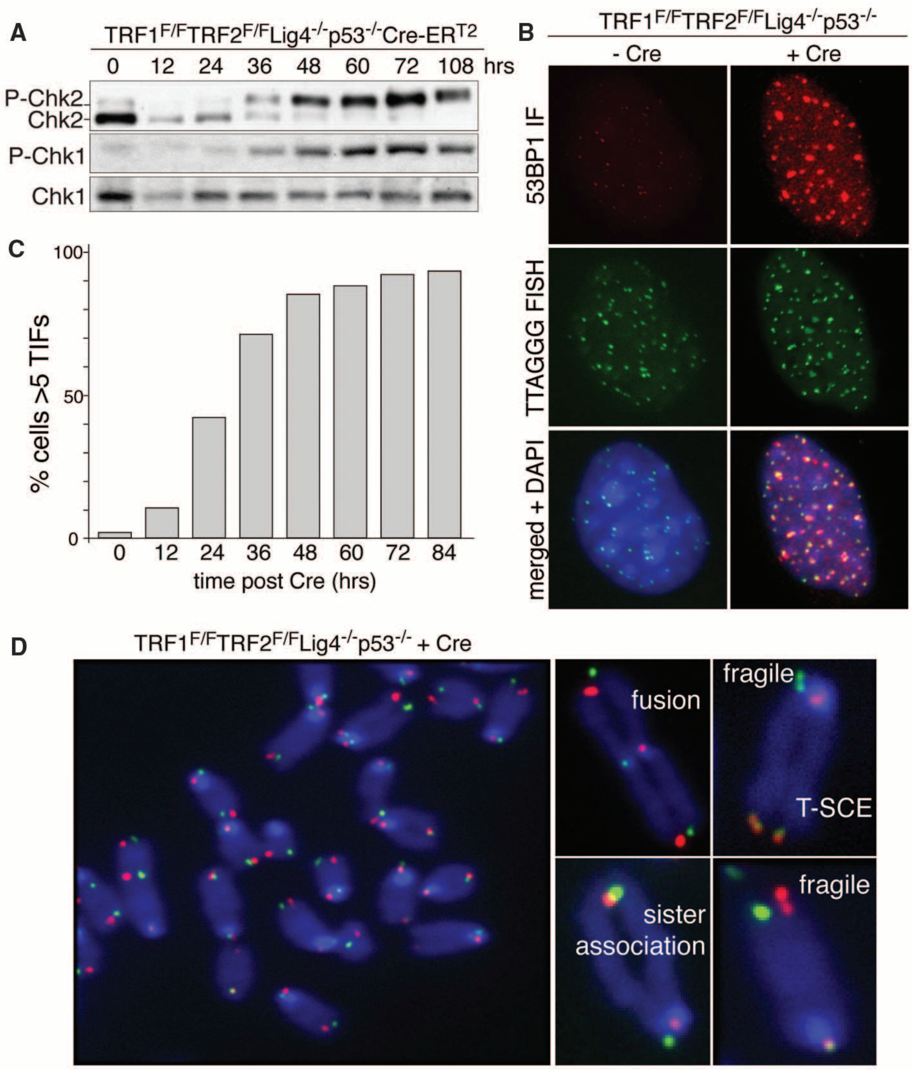

E

TRF1$^{F/F}$TRF2$^{F/F}$ Lig4$^{-/-}$p53$^{-/-}$ MEFs	telomere fusions	T-SCEs	sister telomere associations	fragile telomeres
- Cre (n=3362)	0.1 %	1.1 %	0.4 %	5.4 %
+ Cre (n=4681)	9.5 %	7.4 %	13 %	21 %

Fig. 2. Telomere dysfunction upon shelterin loss. (**A**) Induction of P-Chk1 and P-Chk2 after TRF1/2 codeletion. (**B**) IF-FISH assay for TIFs (telomere dysfunction-induced foci) in TRF1$^{F/F}$TRF2$^{F/F}$Lig4$^{-/-}$p53$^{-/-}$Cre-ERT2 MEFs (5 days after Cre). FISH for telomeres (green), IF for 53BP1 (red), and 4′,6-diamidino-2-phenylindole (DAPI) as DNA counterstain (blue). (**C**) Time course of TIF response as in (B). TIFs were scored in TRF1$^{F/F}$TRF2$^{F/F}$Lig4$^{-/-}$p53$^{-/-}$Cre-ERT2 cells at the indicated time points after 4-OHT. Cells with ≥5 telomeric 53BP1 foci were scored as TIF positive (n > 100 nuclei per time point). (**D**) Metaphase spread from TRF1$^{F/F}$TRF2$^{F/F}$Lig4$^{-/-}$ p53$^{-/-}$ cells at 108 hours after Cre treatment, analyzed by telomeric CO-FISH using a FITC-OO-[CCCTAA]$_3$ PNA probe (green) and a Tamra-OO-[TTAGGG]$_3$ PNA probe (red). Blue, DAPI. Examples of fragile telomeres, chromosome- and chromatid-type fusions, sister telomere associations, and T-SCEs are on the right. (**E**) Quantification of aberrant telomeres in Cre-treated TRF1$^{F/F}$TRF2$^{F/F}$Lig4$^{-/-}$p53$^{-/-}$ MEFs analyzed as in (D).

accumulated telomeric 53BP1 foci, and underwent polyploidization (Fig. 2, A to C, and fig. S2, D and E). Telomeric chromosome-orientation fluorescence in situ hybridization (CO-FISH) revealed a cornucopia of telomeric aberrations in metaphase spreads (Fig. 2, D and E). Telomeres often displayed the fragile telomere phenotype typical of the replication defect induced by TRF1 loss (*7*, *8*). There were frequent sister telomere associations, which were previously noted in cells lacking TRF1, TIN2, TPP1, or POT1a/b (*7*, *9–11*), and ~7.5% of the telomeres showed sequence exchanges between sister telomeres [telomere sister chromatid exchanges (T-SCEs)], indicative of the HDR activated upon loss of either Rap1 or POT1a/b (*12*, *13*).

Because these Lig4 cells were NHEJ deficient, it was unexpected that nearly 10% of the telomeres became fused (Fig. 2E and Fig. 3). Furthermore, TRF1/2 DKO in Ku80-deficient MEFs resulted in fusions involving 65% of telomeres (Fig. 3, A and B, and fig. S3A). These results suggested that the shelterin-free telomeres are processed by alt-NHEJ, which is repressed by Ku70/80 and, to a lesser extent, by Lig4 (*14–18*). Consistent with alt-NHEJ, which is known to be promoted by poly (adenosine diphosphate ribose) polymerase 1 (PARP1) (*16*, *19*), repression of PARP1 with a short hairpin RNA (shRNA) or olaparib (*20*) significantly reduced the fusion of shelterin-free telomeres in Ku-deficient cells (Fig. 3C and fig. S3B). ShRNA knockdown also implicated Lig3 in the alt-NHEJ of telomeres (Fig. 3D and fig. S3C), pointing to microhomology-mediated end-joining (*21*), possibly facilitated by the 2 A-T base pairs per telomeric repeat in annealing 3′ overhangs. Analysis of G0-arrested cells revealed that the alt-NHEJ pathway also operates in nonproliferating cells (Fig. 3E and fig. S3, D and E). Although most telomeres were processed by alt-NHEJ when shelterin was removed in toto, individual deletion of shelterin components from Ku null cells failed to result in frequent telomere fusions (Fig. 3F). The finding that deletion of TPP1 does not elicit alt-NHEJ at telomeres in Ku null cells (Fig. 3F) contrasts with a previous suggestion that TPP1/POT1a/b are required to repress alt-NHEJ at telomeres (*15*). Possibly, the different method used to remove TPP1/POT1a/b in that study had additional effects. We conclude that Lig3/PARP1-dependent alt-NHEJ, is blocked by multiple shelterin components (or their interacting factors) as well as Ku70/80 (Fig. 3G).

We anticipated that fully deprotected, unfused telomeres would be subject to nucleolytic degradation, which is a marked outcome of telomere dysfunction in yeast [reviewed in (*1*)]. However, there was no evidence for overt nucleolytic processing of the shelterin-free telomeres (fig. S4A). In addition, in the absence of Ku70/80, which represses resection at telomeres in other eukaryotes (*22–25*), the overhang signal at the shelterin-free telomeres increased by a factor of <3, even when telomere fusions were repressed by inhibiting PARP1 (fig. S4, A to E).

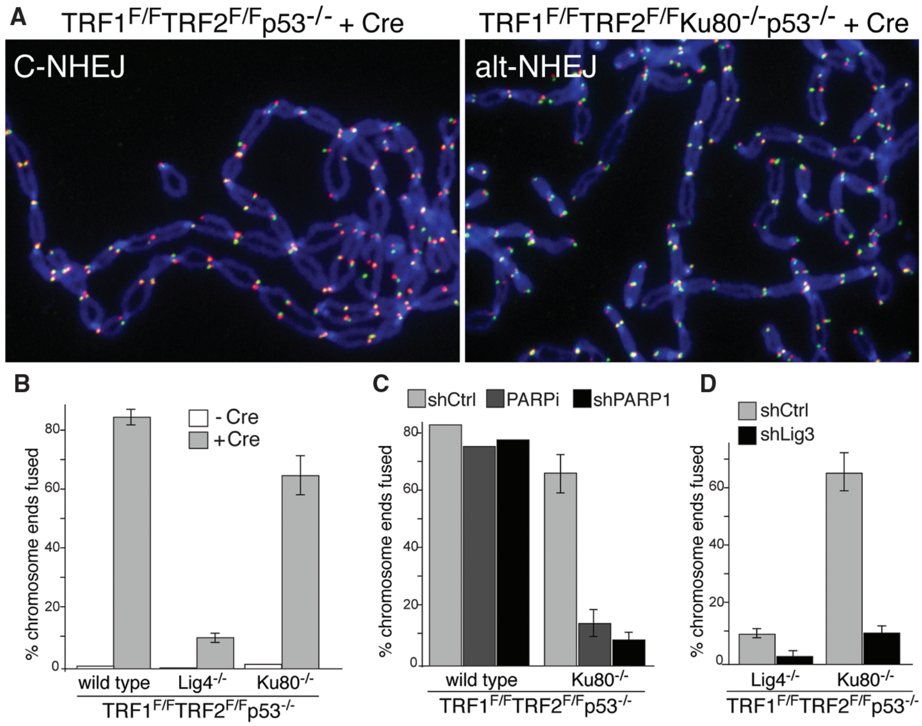

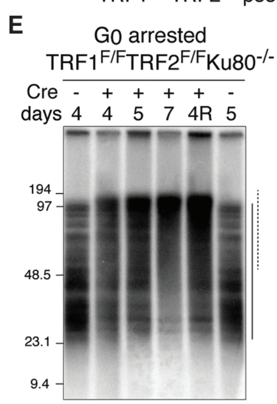

F

Knockout	Fusions
TRF1 TRF2 Ku80	65 %
TRF1 Ku80	5 %
TRF2 Ku80	10 %
TPP1 Ku70	2 %
Rap1 Ku70	0 %
POT1a/b Ku70	0.3 %

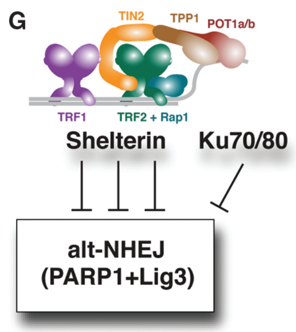

Fig. 3. Lig3- and PARP1-dependent alt-NHEJ in the absence of shelterin. (**A**) Metaphase chromosomes of the indicated MEFs analyzed (as in Fig. 2D) at 108 hours after Cre. (**B**) Quantification of telomere fusions in the indicated MEFs at 108 hours after H&R-Cre. Bars and not error bars means of three independent experiments, ± SDs. (**C**) Quantification of telomere fusions induced by deleting TRF1 and TRF2 [as in (A)] after treatment with PARP1 shRNA or 0.5 μM olaparib. (**D**) Quantification of telomere fusions [as in (**C**)] in cells treated with Lig3 or control shRNA. (**E**) Alt-NHEJ in G0 arrested $TRF1^{F/F}TRF2^{F/F}Ku80^{-/-}p53$+/+Cre-ERT2 MEFs. *Mbo*I and *Alu*I digested DNA resolved on a pulsed-field gel electrophoresis probed with end-labeled $[AACCCT]_4$. Dashed and solid lines: fused and unfused telomeres, respectively. Day 4R: cells released on day 4 and analyzed on day 5. (**F**) Percentage of fused telomeres in Ku-deficient MEFs lacking the indicated shelterin subunit(s). Cells were analyzed at 108 hours after Cre-mediated deletion of the floxed alleles of shelterin. (**G**) Summary of the repression of Lig3- and PARP1-dependent alt-NHEJ by shelterin and Ku70/80.

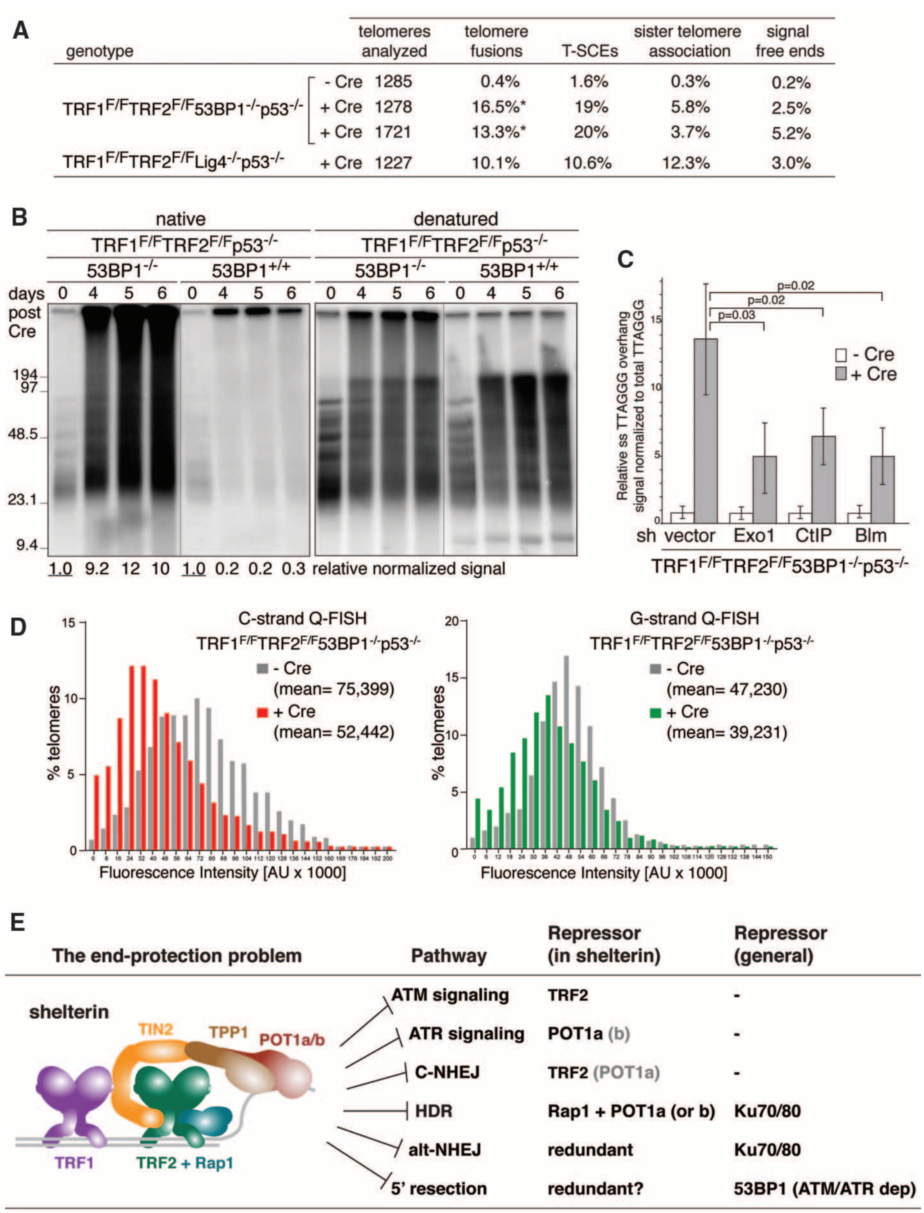

Fig. 4. 53BP1 blocks 5′ end resection and shortening of shelterin-free telomeres. (**A**) Quantification of telomere aberrations in Cre-treated (108 hours) TRF1$^{F/F}$TRF2$^{F/F}$53BP1$^{-/-}$ p53$^{-/-}$ and TRF1$^{F/F}$TRF2$^{F/F}$Lig4$^{-/-}$p53$^{-/-}$ MEFs. *, 93% of the cells had ~12% of chromosome ends fused, whereas 7% of the cells had more than 50% of the chromosome ends fused. (**B**) Representative in-gel 3′ overhang analysis of the indicated MEFs after Cre treatment. Relative overhang signals were normalized to total telomeric DNA (lanes without Cre set to 1). (**C**) Quantification of 3′ overhangs of TRF1$^{F/F}$TRF2$^{F/F}$53BP1$^{-/-}$p53$^{-/-}$ MEFs (+ or – H&R-Cre, 108 hours) treated with Exo1, CtIP, and Blm shRNAs. The ss/total signal ratios of the +Cre samples are expressed relative to the –Cre samples for each shRNA treatment. Means of three independent experiments ± SDs. *P* values: two-tailed student's *t* tests. (**D**) Q-FISH of telomeres in TRF1$^{F/F}$ TRF2$^{F/F}$53BP1$^{-/-}$p53$^{-/-}$ MEFs with or without H&R-Cre (day 5). (**E**) Summary of the end-protection problem.

This modest effect suggested that Ku70/80 does not play a major role in repressing 5′ end resection.

It was recently shown that 5′ end resection at DSBs is minimized by 53BP1, a DDR factor that binds near DSBs and at dysfunctional telomeres in response to ATM or ATR signaling (*26*, *27*). To test the role of 53BP1 at shelterin-free telomeres, we generated TRF1$^{F/F}$TRF2$^{F/F}$53BP1$^{-/-}$p53$^{-/-}$ MEFs. Neither classical nor alt-NHEJ is anticipated at the shelterin-free telomeres of these cells, because 53BP1 is required for Lig4-dependent telomere fusions (*5*) and Ku70/80 impedes alt-NHEJ (Fig. 3). Indeed, TRF1/2 DKO in 53BP1 null cells elicited a modest level of telomere fusions, mediated mainly by Lig3 (Fig. 4A and fig. S5, A and B), and infrequent sister telomere associations (Fig. 4A). The telomeric overhang signal increased by a factor of ~10 after the TRF1/2 DKO, but not when either TRF1 or TRF2 were deleted from 53BP1-deficient cells (Fig. 4, B and C, and fig. S5C). The excessive signal was due to single-stranded DNA at a 3′ end, as it was removed by the *Escherichia coli* 3′ exonuclease Exo1 (fig. S5D). The increase in the overhang signal was maximal in cycling cells, regardless of the cell cycle phase, but also occurred in G0 arrested cells (fig. S6, A to D). Because 5′ end resection at DSBs is mediated by CtIP, Blm, and Exo1 (*28*–*30*), we examined the role of these factors by shRNA knockdown. Depletion of CtIP, Blm, or Exo1 significantly reduced the overhang signal, establishing that 5′ end resection contributes to the phenotype (Fig. 4C and fig. S7, A to E). Furthermore, quantitative FISH (Q-FISH) recorded a 20 to 30% reduction in the length of the telomeric G-rich and C-rich strands, consistent with nucleolytic degradation (Fig. 4D). Thus, telomeres are in danger of excessive 5′ end resection by enzymes involved in DSB processing. This hyperresection is blocked by shelterin and, in the absence of shelterin, by 53BP1 (Fig. 4E and fig. S7F).

The deleterious events at shelterin-free telomeres revealed that six pathways define the end-protection problem (Fig. 4E). Shelterin is the main armor of chromosome ends, providing protection against classical NHEJ and inadvertent activation of the ATM and ATR signaling. In addition to these primary threats, telomeres can fall victim to alt-NHEJ, HDR, and unmitigated resection. However, these pathways are also blocked by either Ku70/80 or 53BP1, providing a second layer of defense. Although 53BP1 can minimize hyperresection, it will only do so at telomeres that elicit a DNA damage signal. Therefore, the protective ability of 53BP1 is limited and shelterin must prevent hyperresection under most conditions. We speculate that the mechanism by which shelterin fulfills this task is related to how it governs the formation of the correct telomeric overhangs after DNA replication. In contrast to 53BP1, Ku70/80 should be available to blocks alt-NHEJ and HDR at telomeres independent of a DNA damage signal. Why, then, should shelterin also repress these pathways? The redundancy may ensure greater protection, or the repression of alt-NHEJ and HDR may be a secondary outcome of the mechanism by which shelterin executes one of its other functions. As the genetic deconstruction of telomeres has illuminated the full spectrum of processing reactions that threaten chromosome ends lacking proper protection, this study provides a framework for the understanding of the consequences of telomere dysfunction arising from telomere attrition in aging and cancer.

References and Notes

1. T. de Lange, *Science* **326**, 948 (2009).
2. W. Palm, T. de Lange, *Annu. Rev. Genet.* **42**, 301 (2008).
3. G. B. Celli, T. de Lange, *Nat. Cell Biol.* **7**, 712 (2005).
4. G. B. Celli, E. L. Denchi, T. de Lange, *Nat. Cell Biol.* **8**, 885 (2006).

5. N. Dimitrova, Y. C. Chen, D. L. Spector, T. de Lange, *Nature* **456**, 524 (2008).
6. E. L. Denchi, T. de Lange, *Nature* **448**, 1068 (2007).
7. A. Sfeir *et al.*, *Cell* **138**, 90 (2009).
8. P. Martínez *et al.*, *Genes Dev.* **23**, 2060 (2009).
9. K. K. Takai, T. Kibe, J. R. Donigian, D. Frescas, T. de Lange, *Mol. Cell* **44**, 647 (2011).
10. T. Kibe, G. A. Osawa, C. E. Keegan, T. de Lange, *Mol. Cell. Biol.* **30**, 1059 (2010).
11. D. Hockemeyer, J. P. Daniels, H. Takai, T. de Lange, *Cell* **126**, 63 (2006).
12. A. Sfeir, *Science* **327**, 1657 (2010).
13. W. Palm, D. Hockemeyer, T. Kibe, T. de Lange, *Mol. Cell. Biol.* **29**, 471 (2009).
14. C. Boboila *et al.*, *J. Exp. Med.* **207**, 417 (2010).
15. R. Rai *et al.*, *EMBO J.* **29**, 2598 (2010).
16. M. Wang *et al.*, *Nucleic Acids Res.* **34**, 6170 (2006).
17. D. Simsek, M. Jasin, *Nat. Struct. Mol. Biol.* **17**, 410 (2010).
18. C. T. Yan *et al.*, *Nature* **449**, 478 (2007).
19. W. Y. Mansour, T. Rhein, J. Dahm-Daphi, *Nucleic Acids Res.* **38**, 6065 (2010).
20. K. A. Menear *et al.*, *J. Med. Chem.* **51**, 6581 (2008).
21. D. Simsek *et al.*, *PLoS Genet.* **7**, e1002080 (2011).
22. P. Baumann, T. R. Cech, *Mol. Biol. Cell* **11**, 3265 (2000).
23. S. Gravel, M. Larrivée, P. Labrecque, R. J. Wellinger, *Science* **280**, 741 (1998).
24. R. M. Polotnianka, J. Li, A. J. Lustig, *Curr. Biol.* **8**, 831 (1998).
25. K. Riha, D. E. Shippen, *Proc. Natl. Acad. Sci. U.S.A.* **100**, 611 (2003).
26. P. Bouwman *et al.*, *Nat. Struct. Mol. Biol.* **17**, 688 (2010).
27. S. F. Bunting *et al.*, *Cell* **141**, 243 (2010).
28. E. P. Mimitou, L. S. Symington, *Nature* **455**, 770 (2008).
29. Z. Zhu, W. H. Chung, E. Y. Shim, S. E. Lee, G. Ira, *Cell* **134**, 981 (2008).
30. S. Gravel, J. R. Chapman, C. Magill, S. P. Jackson, *Genes Dev.* **22**, 2767 (2008).

Acknowledgments: We thank D. White for exceptional dedication to the mouse husbandry involved in this project and members of the de Lange laboratory for comments on this manuscript. This work was supported by grants from the NIH to T.dL. (GM49046 and AG016642). T.dL. is an American Cancer Society Research Professor.

Supplementary Materials
www.sciencemag.org/cgi/content/full/336/6081/593/DC1
Materials and Methods
Figs. S1 to S7
References (*31–41*)

28 December 2011; accepted 9 March 2012
10.1126/science.1218498

Elementary Ca^{2+} Signals Through Endothelial TRPV4 Channels Regulate Vascular Function

Swapnil K. Sonkusare,[1] Adrian D. Bonev,[1] Jonathan Ledoux,[1,2] Wolfgang Liedtke,[3] Michael I. Kotlikoff,[4] Thomas J. Heppner,[1] David C. Hill-Eubanks,[1] Mark T. Nelson[1,5]*

Major features of the transcellular signaling mechanism responsible for endothelium-dependent regulation of vascular smooth muscle tone are unresolved. We identified local calcium (Ca^{2+}) signals ("sparklets") in the vascular endothelium of resistance arteries that represent Ca^{2+} influx through single TRPV4 cation channels. Gating of individual TRPV4 channels within a four-channel cluster was cooperative, with activation of as few as three channels per cell causing maximal dilation through activation of endothelial cell intermediate (IK)- and small (SK)-conductance, Ca^{2+}-sensitive potassium (K^+) channels. Endothelial-dependent muscarinic receptor signaling also acted largely through TRPV4 sparklet-mediated stimulation of IK and SK channels to promote vasodilation. These results support the concept that Ca^{2+} influx through single TRPV4 channels is leveraged by the amplifier effect of cooperative channel gating and the high Ca^{2+} sensitivity of IK and SK channels to cause vasodilation.

Endothelial cells (ECs) line all blood vessels and regulate the smooth muscle contractile state (tone). The concentration of intracellular free calcium ($[Ca^{2+}]_i$) in ECs is increased by influx and by release from intracellular stores through inositol trisphosphate receptors (IP_3Rs) in the membrane of the endoplasmic reticulum. Although Ca^{2+}-influx pathways are incompletely characterized, members of the transient receptor potential (TRP) family of nonselective cation channels have been implicated in this function. In particular, results from gene-knockout studies suggest that the vanilloid (TRPV) family member TRPV4 is involved in endothelium-dependent vascular dilation in response to flow and acetylcholine (ACh) (*1*–*5*).

[1]Department of Pharmacology, College of Medicine, University of Vermont, Burlington, VT 05405, USA. [2]Research Center, Montreal Heart Institute, and Department of Medicine, Université de Montréal, Montreal, QC H1T 1C8, Canada. [3]Department of Medicine and Neurobiology, and Center for Translational Neuroscience, Duke University Medical Center, Durham, NC 27710, USA. [4]Department of Biomedical Sciences, College of Veterinary Medicine, Cornell University, Ithaca, NY 14853, USA. [5]Institute of Cardiovascular Sciences, University of Manchester, Manchester M13 9NT, UK.

*To whom correspondence should be addressed. E-mail: mark.nelson@uvm.edu

Increases in endothelial $[Ca^{2+}]_i$ activate EC pathways that terminate in the release of soluble factors or initiation of processes that hyperpolarize the membrane of adjacent vascular smooth muscle cells, and thus promote dilation. These Ca^{2+}-dependent vasodilatory influences fall into three broad categories: (i) nitric oxide (NO), a tissue-permeable gas generated as a by-product of the oxidation of arginine to citrulline catalyzed by endothelial nitric oxide synthase (eNOS) (*6*); (ii) prostaglandins, produced through phospholipase A_2–dependent activation of cyclooxygenase (COX) (*7*); and (iii) endothelial-derived hyperpolarizing factor (EDHF), characterized by its strict dependence on the activity of EC intermediate-conductance (IK; $K_{Ca}3.1$) and small-conductance (SK; $K_{Ca}2.3$), Ca^{2+}-sensitive potassium (K^+) channels (*8*). Although a number of factors have been suggested as EDHF, accumulating evidence points to the importance of electrotonic spread of EC IK and/or SK channel–mediated hyperpolarizing current to smooth muscle cells through gap junctions (*8*, *9*).

Studies of Ca^{2+} signaling in ECs using conventional Ca^{2+}-binding fluorescent dyes (e.g., Fluo-4) are limited by interference from the vigorous Ca^{2+}-signaling activity of adjacent smooth muscle cells, which also readily take up such dyes. A recently developed alternative is a transgenic mouse that expresses a genetically encoded Ca^{2+} biosensor (GCaMP2) exclusively in the endothelium of the vascular wall (*10*, *11*). GCaMP2 is a fusion protein of the Ca^{2+}-binding protein calmodulin and a circularly permutated enhanced green fluorescent protein (EGFP) that fluoresces when Ca^{2+} binds to calmodulin. The GCaMP2 protein is homogeneously expressed throughout the EC (*10*) and allows long, stable recordings of intracellular Ca^{2+} in ECs in the intact blood vessel wall, without contamination of signals from smooth muscle. Using this model, we previously identified local, IP_3R-mediated Ca^{2+} events in ECs, termed Ca^{2+} pulsars (*10*), that had previously gone undetected with conventional imaging protocols.

To identify Ca^{2+}-influx pathways in the ECs of resistance arteries (i.e., arteries important in regulating peripheral resistance and blood pressure), we imaged Ca^{2+} fluorescence in isolated, small (100 μm diameter) mesenteric arteries from GCaMP2 mice using confocal microscopy (*12*). Isolated arteries were surgically opened and pinned down with the EC surface facing up (en face preparation) to improve optical resolution (*10*). In a single field of view, local Ca^{2+} signals in ~14 individual ECs could be recorded simultaneously with high spatial (0.3 μm) and temporal (15 ms) resolution. Events were analyzed offline by measuring the fluorescence intensity over time within defined 1.7-μm^2 regions of interest on images corresponding to active sites.

With IP_3R-mediated signaling eliminated by pretreatment with the sarcoplasmic reticulum/endoplasmic reticulum Ca^{2+}-ATPase (SERCA) inhibitor, cyclopiazonic acid (CPA), or the

phospholipase C (PLC) blocker, U73122 (*10*), local Ca^{2+} signals distinct from pulsars could be detected [Fig. 1, A (left) and B (upper left); fig. S2A (left); and movie S1], albeit at a very low frequency [2.8 ± 0.8 (SEM) event sites per field per 2 min; $n = 5$], possibly reflecting extracellular Ca^{2+} influx. Exposure of the endothelial surface to the potent, selective TRPV4 channel agonist GSK1016790A (GSK; 10 nM) (*13*, *14*) induced a marked increase [30.4 ± 2.5 (SEM)–fold, $n = 5$] in the activity of these Ca^{2+} signals [Fig. 1, A (right) and B (upper right); fig. S2, A and B; and movie S2], without increasing global $[Ca^{2+}]_i$ (Fig. 1B and movies S1 to S4).

Unlike Ca^{2+} pulsars, which are brief (<300 ms), spikelike signals, GSK-induced Ca^{2+} events exhibited a plateau phase with discrete amplitudes (Fig. 1C). Their spatial spread within an EC was 11.2 ± 0.4 (SEM) μm^2 (50 sites, $n = 5$ arteries), or about 0.6% of the total cell surface area, and they occurred repetitively at the same sites (Fig. 1, A and B). Also in contrast to Ca^{2+} pulsars, which predominantly occur at "holes" in the internal elastic lamina (IEL) corresponding to the locations of endothelial projections to smooth muscle (*10*), TRPV4-mediated Ca^{2+} signals were approximately evenly distributed between such holes (39%) and the ends of cells (31%; fig. S2B).

4α-Phorbol 12,13-didecanoate (4α-PDD), a pharmacological activator of TRPV4 channels, and 11,12-epoxyeicosatrienoic acid (11,12-EET), an endogenous activator of TRPV4 channels, induced IP_3R-independent Ca^{2+} signals comparable to GSK-induced events (Fig. 1D and fig. S3C). The selective TRPV4 channel antagonist HC-067047 (HC; 1 μM) (*13*, *15*), and the non-selective TRPV pore blocker ruthenium red (RuR; 5 μM), inhibited GSK (10 nM)–induced Ca^{2+} signals by about 93%, reducing both the number of sites and the activity per site (Fig. 1E and figs. S2D and S3B). Moreover, GSK had no effect on arteries from $TRPV4^{-/-}$ mice [$P = 0.88$, $n = 5$; paired two-sample t test (*12*)]. Notably, rapid removal of external Ca^{2+} eliminated GSK-induced Ca^{2+} events ($n = 4$; fig. S2C). Thus, these IP_3R-independent optical signals reflect Ca^{2+} influx through plasmalemmal TRPV4 channels.

TRPV4-mediated Ca^{2+} signals exhibited characteristics of single channels, including square, discrete amplitudes (Fig. 1, A to C; fig. S2, A, C, and D; and fig. S3, A to C). Such fluorescence signals can be inferred to represent Ca^{2+} influx through single channels if they meet the following criteria (*16*): (1) Recording volume is very small (<1 fL); (2) events are quantal (i.e., exhibit fixed amplitude steps); (3) amplitude steps depend on the Ca^{2+} electrochemical gradient; (4) amplitude steps do not depend on the concentration or nature of the agonist or antagonist; (5) durations of events are exponentially distributed; and (6) channels have high Ca^{2+} permeability and single-channel conductance. The first criterion may exist naturally for native ECs, which are about 0.5 μm thick (yielding an approximate recording volume of 0.8 fL), and satisfaction of the last criterion has been demonstrated for TRPV4 channels (*17*). A fit of multiple Gaussians to an all-points histogram of fluorescence signals (Fig. 2A) (*12*) revealed quantal amplitudes (criterion 2), with evenly spaced $\Delta F/F_0$ increments ($\Delta F/F_0$: change in fluorescence relative to baseline fluorescence) of 0.19 with 2 mM extracellular Ca^{2+}. Increasing extracellular Ca^{2+} from 2 to 10 mM increased the amplitude of these events (Fig. 2A), and membrane depolarization with 100 mM K^+ decreased their amplitude (Fig. 2B), indicating a dependence on the Ca^{2+} electrochemical gradient (criterion 3). Moreover, these events were independent of the concentration and nature of the agonist or antagonist used (criterion 4): Increasing GSK concentration from 3 to 10 nM increased activity (fluorescence integral) 3.7 ± 0.8 (SEM)–fold ($n = 3$ arteries; fig. S3A, left), but did not increase amplitude (fig. S3A, right); the specific TRPV4 inhibitor HC reduced activity, but not amplitude (fig. S3B); and other TRPV4 channel activators (4α-PDD and 11,12-EET) did not differentially affect amplitudes (fig. S3C). Finally, the durations of GSK (3 nM)–induced events were exponentially distributed (criterion 5), with a time constant of 37.0 ± 0.7 ms (Fig. 2C) (*12*). Thus, each quantal level appears to represent Ca^{2+} influx through a single TRPV4 channel in the plasma membrane of a vascular EC. By analogy to the L-type Ca^{2+} channel–mediated events first described in cardiac myocytes (*18*), we use the term TRPV4 sparklet to refer to the optically detected influx of extracellular Ca^{2+} through a single TRPV4 channel.

Each sparklet site exhibited up to four quantal levels interspersed with long quiescent periods. If these discrete amplitude steps represent independently functioning channels, their probabilities should follow a binomial distribution. The observed distribution deviated significantly from a binomial distribution ($P < 0.01$; χ^2 test), with an excess of double, triple, and quadruple events

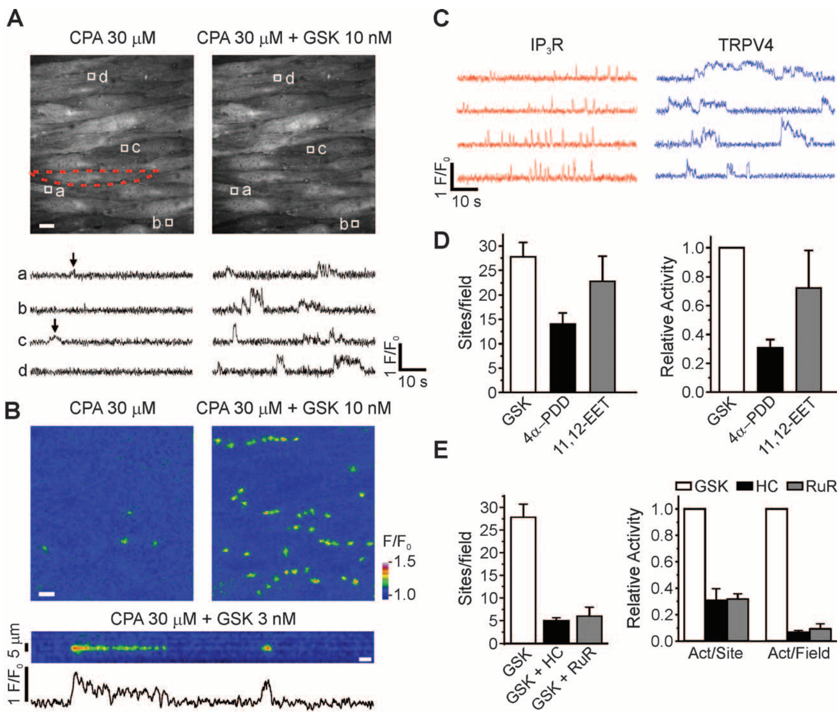

Fig. 1. GSK-induced Ca^{2+} signals represent Ca^{2+} influx through plasmalemmal TRPV4 channels. (**A**) Ca^{2+} imaging of an en face preparation of third-order mesenteric arteries from a GCaMP2-expressing mouse, showing changes in the activity of local, IP_3R-independent Ca^{2+} signals recorded over time (traces, below) from regions of interest (1.7 μm^2), denoted by boxes in images (above). An EC in the field is outlined by red dashes (above, left). Scale bar: 10 μm. Bottom left: Localized events (arrows) detected in the absence of IP_3R-mediated signaling; bottom right: localized events after addition of GSK (10 nM). (**B**) Top panels: Pseudocolor overlay images showing all IP_3R-independent Ca^{2+} signaling events detected in the absence or presence of GSK (10 nM) in a single field over a 94-s interval. Scale bar: 10 μm. Bottom panel and trace: Pseudo–line-scan image and associated trace recorded from a single site over the same interval. Scale bar: 2 s. Calibration bar at right indicates intensity of signals (F/F_0; fluorescence F divided by baseline fluorescence F_0). (**C**) Representative traces illustrating differences in the kinetic properties of IP_3R-mediated Ca^{2+} pulsars (left) and TRPV4-mediated Ca^{2+} events (right) from the same field of view in the presence of 10 nM GSK (without CPA). (**D**) Increased numbers of sites per 2 min per field and activity per field (right; $n = 4$ to 6 arteries) in the presence of GSK (10 nM), 4α-PDD (5 μM), or 11,12-EET (1 μM). (**E**) Inhibition of GSK-induced increases in activity per site and activity per field by HC (1 μM; $n = 5$) and RuR (5 μM; $n = 3$). Error bars (C and D), SEMs.

(Fig. 2D) (*12*), indicating that TRPV4 channels open cooperatively, likely reflecting potentiation of nearby TRPV4 channels by intracellular Ca^{2+} (*19*). The degree of spread and termination of sparklet activity may reflect inhibition by higher concentrations of intracellular Ca^{2+} (*17*). A fifth level, which should have been resolvable under the imaging conditions used, was not reliably detected, suggesting that TRPV4 channels form a four-channel metastructure.

Ca^{2+}-sensitive IK and SK channels are potentially important targets of Ca^{2+} influx through TRPV4 channels (*20*). Measurement of membrane currents in freshly isolated ECs using the perforated-patch configuration of the patch-clamp technique (*12*) showed that, at physiological salt concentrations and voltages (–50 mV), GSK (10 nM) induced an outward current that was substantially reduced by the IK blocker charybdotoxin (ChTx) and further reduced by subsequent addition of the SK blocker apamin (Fig. 3A). Using a voltage-ramp protocol (–100 to +40 mV, 200 ms), we found that activation of TRPV4 channels with GSK (10 nM) increased IK and SK channel current densities to 15.6 ± 2.5 and 3.6 ± 0.9 pA/pF (±SEM; n = 5 cells), respectively, at 0 mV, values similar to maximal IK and SK current densities obtained by dialyzing cells with 3 μM Ca^{2+} (Fig. 3B).

Our imaging data indicated that GSK (≤10 nM) activates a small number of channels per cell [average activity, 2.8 ± 0.4 (SEM) sparklets per cell with 10 nM GSK; n = 15 cells from five fields]. To estimate the number of TRPV4 channels per cell, we measured whole-cell K^+ currents through TRPV4 channels at +100 mV under conditions that minimize Ca^{2+} entry through TRPV4 (*12*). Under these conditions, TRPV4 current was 63 ± 27 pA with 10 nM GSK and 1228 ± 242 pA with 100 nM GSK (±SEM; n = 5 cells each; fig. S4), currents that correspond to the activation of 8 and 152 channels per cell, respectively.

Although TRPV4 activation by 3 to 10 nM GSK opened only a few TRPV4 channels in an EC (fig. S5 and movie S5), it hyperpolarized the smooth muscle membrane potential by about 10 mV (fig. S6) and led to a maximal, endothelium-dependent dilation of pressurized arteries (Fig. 3C) (*12*). GSK-induced dilations were blocked by RuR and HC and were absent in arteries from $TRPV4^{-/-}$ mice (Fig. 3C), conditions that did not affect dilations in response to the direct IK and SK channel agonist NS309 (Fig. 3C); they were also eliminated by removing the endothelium and unaffected by inhibition of smooth muscle Ca^{2+}-sensitive K^+ (BK) channels with paxilline (Fig. 3C). Notably, TRPV4-mediated dilations induced by 10 nM GSK were unaffected by inhibition of NOS and COX with nitro-L-arginine (L-NNA) and indomethacin, respectively (Fig. 3C). Block of IK channels with ChTx eliminated the dilation in response to 3 nM GSK and greatly reduced the dilation in response to 10 nM GSK (Fig. 3D). Treatment with apamin in the presence of ChTx completely prevented dilations in response to 10 and 30 nM GSK (Fig. 3D), indicating that the greater activation of TRPV4 channels at these higher GSK concentrations resulted in increased signaling through SK channels. Thus, local Ca^{2+} influx through TRPV4 channels acts through IK and SK channels and not through eNOS or COX, demonstrating a specific link between TRPV4 activation and the EDHF pathway of endothelial-mediated vascular dilation.

Muscarinic receptor activation by ACh or carbachol (CCh) induces vasodilation through both NO and EDHF mechanisms (*1*–*6*, *8*, *9*). The NO-dependent component of ACh-induced dilation is modestly reduced in larger mesenteric arteries from $TRPV4^{-/-}$ mice, whereas the EDHF-mediated dilation is more considerably reduced (*3*–*5*). Thus, NO-mediated dilation in response to muscarinic receptor activation may be driven primarily by IP_3R-mediated increases in global Ca^{2+} and Ca^{2+} pulsars, whereas the EDHF component may reflect the action of local increases in Ca^{2+} influx through a small number of TRPV4 channels. Global Ca^{2+} and Ca^{2+} pulsars were increased by muscarinic receptor stimulation and were eliminated by blocking PLC or SERCA (Fig. 4A) (*10*). ACh (5 μM) alone increased basal sparklet activity in the absence of IP_3R-mediated Ca^{2+} release and TRPV4 agonist [2.3 ± 0.3 (SEM)–fold, n = 4 arteries], indicating that the muscarinic signaling pathway can increase Ca^{2+} influx through TRPV4 channels. In the presence of a submaximal concentration of GSK

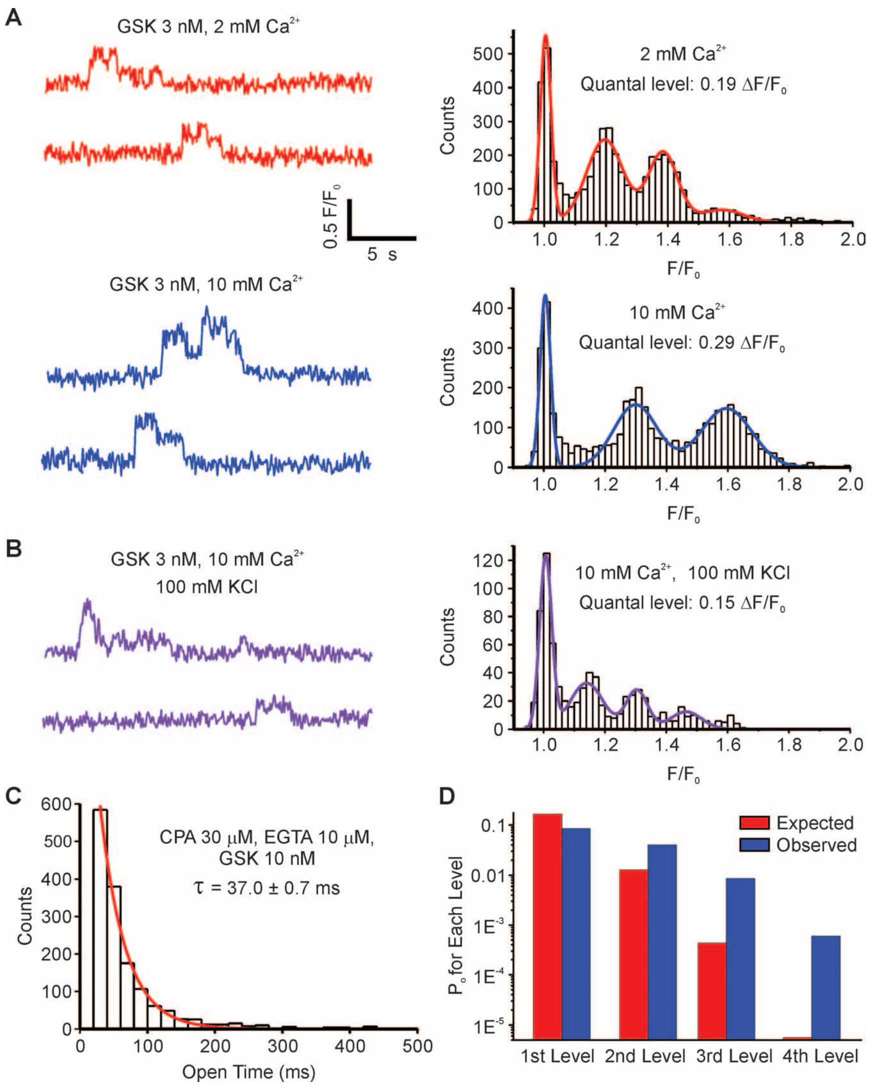

Fig. 2. TRPV4 Ca^{2+} sparklets as unitary events that exhibit cooperative activation. (**A**) A fit of multiple Gaussians to all-points histograms showing evenly spaced $\Delta F/F_0$ levels of 0.19 at 2 mM extracellular Ca^{2+} and 0.29 at 10 mM Ca^{2+}. (**B**) Effect of decreasing Ca^{2+} electrochemical gradient by membrane depolarization with 100 mM K^+ on Ca^{2+} signals. (**C**) Exponential distribution of the durations of GSK (10 nM)–induced sparklets with Fluo-4 and 10 μM EGTA-AM. Sampling rate, 50 to 60 images/s. τ, time constant. (**D**) Cooperative channel gating demonstrated by deviation of the frequencies of second, third, and fourth levels (measured as open probabilities, P_O) from a binomial distribution predictive of independent events. Same conditions as in (C).

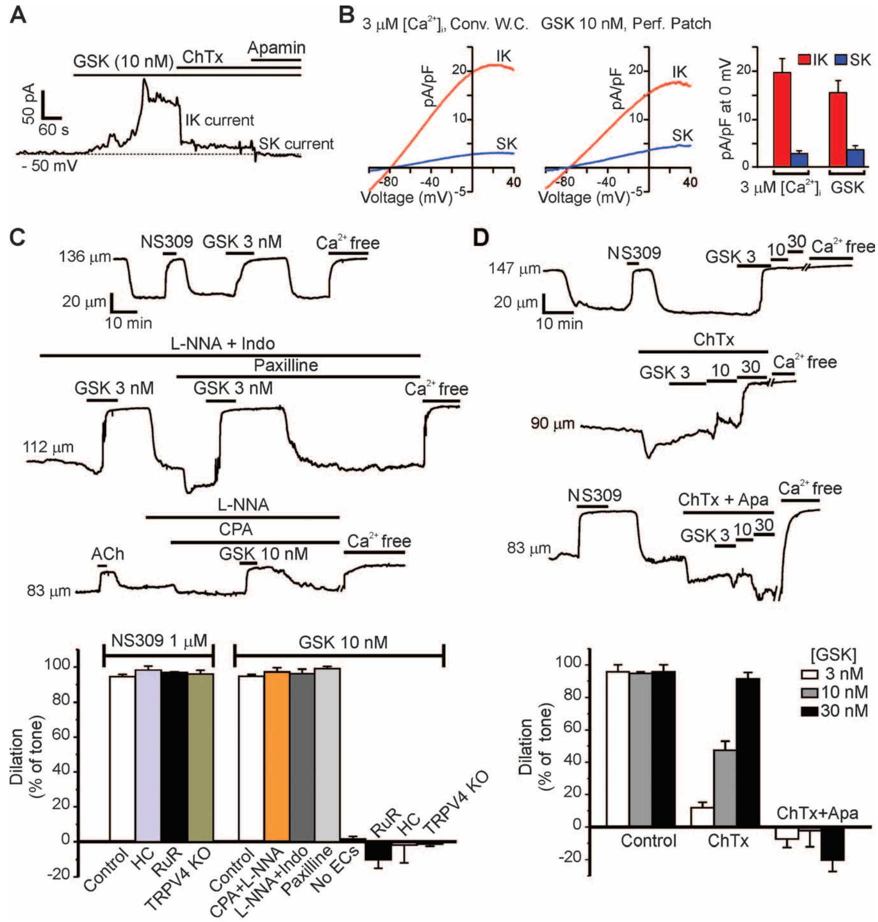

Fig. 3. Activation of IK and SK channels and induction of EDHF-dependent vasodilation by Ca^{2+} influx through TRPV4 channels. (**A**) Inhibition of GSK (10 nM)–induced outward current by 300 nM ChTx (n = 5 cells) or 300 nM apamin (n = 5 cells). (**B**) Densities of IK and SK channel currents in cells treated with GSK (10 nM) or in cells dialyzed with 3 μM Ca^{2+} (n = 8 cells). Conv. W.C., conventional whole-cell configuration; Perf. Patch, perforated-patch configuration. (**C**) Top trace: GSK (3 nM)–induced vasodilation of pressurized (80 mmHg) mesenteric arteries; middle trace: effects of 100 μM L-NNA + 10 μM indomethacin (Indo; n = 5), or 1 μM paxilline (n = 3) on GSK-induced dilations; bottom trace: effects of L-NNA and 30 μM CPA (n = 5) on GSK (10 nM)–induced dilations; bar graph (left): absence of effects of the TRPV4 antagonists HC (1 μM; n = 4) and RuR (5 μM; n = 4), and TRPV4 knockout (n = 3) on dilations induced by the IK and SK agonist NS309 (1 μM); bar graph (right): quantification of effects of CPA + L-NNA (n = 5), L-NNA + Indo (n = 5), paxilline (n = 3), endothelium removal (n = 5), RuR (n = 5), HC (n = 5), and TRPV4 knockout (n = 4) on GSK (10 nM)–induced dilations. (**D**) Vasodilation in response to GSK (3, 10, 30 nM) in the presence or absence of 200 nM ChTx (n = 7), or ChTx + 300 nM apamin (Apa). Effects on dilation [bar graphs in (C) and (D)] determined relative to initial tone [26 ± 1% (SEM), n = 10], defined as the percentage decrease in arterial diameter to pressure (80 mmHg) relative to the diameter in external Ca^{2+}-free solution. Error bars (B to D), SEMs.

(3 nM), ACh (5 μM) increased TRPV4 sparklet activity by 2.9 ± 0.4 (SEM)–fold (n = 5), an effect that was inhibited by the TRPV4 antagonist HC (Fig. 4B). Endothelial-dependent dilation by CCh of arteries constricted by intravascular pressure (80 mmHg) was dependent on NO (34%) and EDHF (66%) (Fig. 4C). Our demonstration that muscarinic receptor stimulation induces TRPV4 sparklets suggests that this pathway should cause vasodilation. Indeed, TRPV4 inhibition by HC reduced muscarinic receptor–induced EDHF dilations by 76% (Fig. 4C), indicating that the EDHF component of these dilations largely reflects TRPV4 sparklet–mediated activation of IK and/or SK channels.

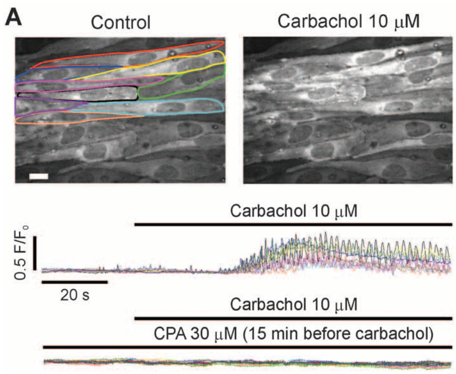

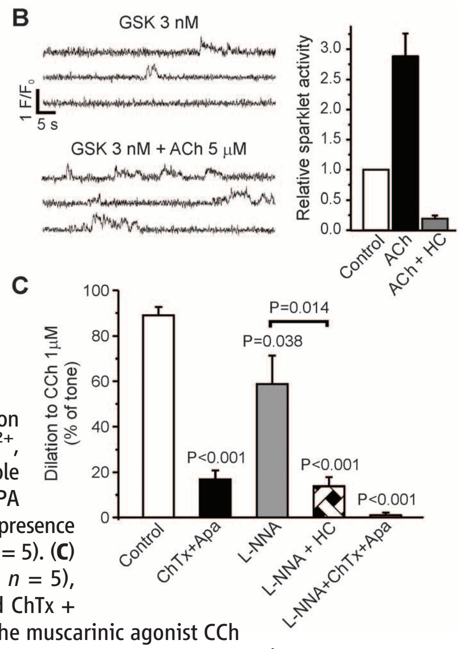

Fig. 4. Effects of muscarinic receptor activation on global Ca^{2+} and TRPV4 sparklets. (**A**) Global Ca^{2+}, shown as fractional fluorescence from outlined whole cells treated with CCh (10 μM) with and without CPA (30 μM). (**B**) GSK (3 nM)–induced sparklets in the presence or absence of 5 μM ACh (left) and 1 μM HC (right; n = 5). (**C**) Effects of 200 nM ChTx + 300 nM apamin (Apa; n = 5), 100 μM L-NNA (n = 6), L-NNA + HC (n = 5), and ChTx + Apa + L-NNA (n = 4) on dilations in response to the muscarinic agonist CCh (1 μM). Error bars (B and C), SEMs. Except where indicated by a bracket (Student's t test), P-values are for comparison to control (one-way analysis of variance).

Our results demonstrate that a small number of active TRPV4 channels (about three to eight per cell) mediate local Ca^{2+} signals that activate IK and SK channels (primarily IK) to cause maximal dilation of resistance arteries. We propose that cooperative activation of TRPV4 channels in a cluster leverages the large Ca^{2+} influx through a single TRPV4 channel to produce a more substantial Ca^{2+} signal (fig. S1), which is further boosted by the high Ca^{2+} sensitivity of IK and SK channels, conferred by calmodulin (*20*). The current caused by activation of IK and SK channels is likely spread to the surrounding smooth muscle through myoendothelial gap junctions, resulting in hyperpolarization of smooth muscle cells and vasodilation (*8*, *9*). IK channels are localized to endothelial projections where a portion (39%) of TRPV4 sparklets occur and myoendothelial gap junctions are concentrated (*10*, *21*, *22*), an arrangement that may facilitate activation of IK channels by a local Ca^{2+} signal.

Whereas low-level activation of TRPV4 channels with synthetic agonists (e.g., 3 to 10 nM GSK) or via muscarinic receptor stimulation caused significant vasodilation ($P < 0.0001$; paired two-sample t test), higher-level activation (100 nM GSK) led to rapid global Ca^{2+} overload in ECs and oscillations of blood-vessel diameter (fig. S7 and movie S6). Notable in this context, systemic activation of TRPV4 channels by GSK causes a reduction in blood pressure and generalized circulatory failure (*14*). Collectively, these observations indicate that small numbers of EC TRPV4 channels regulate vascular physiology and suggest that pathologies characterized by blood-pressure reduction and vascular permeability increases (e.g., septic shock) may involve excessive activation of EC TRPV4 channels.

References and Notes

1. V. Hartmannsgruber *et al.*, *PLoS ONE* **2**, e827 (2007).
2. S. A. Mendoza *et al.*, *Am. J. Physiol. Heart Circ. Physiol.* **298**, H466 (2010).
3. J. Saliez *et al.*, *Circulation* **117**, 1065 (2008).
4. D. X. Zhang *et al.*, *Hypertension* **53**, 532 (2009).
5. S. Earley *et al.*, *Am. J. Physiol. Heart Circ. Physiol.* **297**, H1096 (2009).
6. I. Fleming, R. Busse, *J. Mol. Cell. Cardiol.* **31**, 5 (1999).
7. N. V. Bogatcheva, M. G. Sergeeva, S. M. Dudek, A. D. Verin, *Microvasc. Res.* **69**, 107 (2005).
8. G. Edwards, M. Félétou, A. H. Weston, *Pflugers Arch.* **459**, 863 (2010).
9. H. A. Coleman, M. Tare, H. C. Parkington, *Clin. Exp. Pharmacol. Physiol.* **31**, 641 (2004).
10. J. Ledoux *et al.*, *Proc. Natl. Acad. Sci. U.S.A.* **105**, 9627 (2008).
11. Y. N. Tallini *et al.*, *Circ. Res.* **101**, 1300 (2007).
12. Materials and methods are available as supplementary materials on *Science* Online.
13. GlaxoSmithKline compound GSK1016790A: (*N*-((1*S*)-1-{[4-((2*S*)-2-{[(2,4-dichlorophenyl)sulfonyl]amino}-3-hydroxypropanoyl)-1-piperazinyl]carbonyl}-3-methylbutyl)-1-benzothiophene-2-carboxamide; HydraBiosciences compound HC067047: (2-methyl-1-[3-{4-morpholinyl}propyl]-5-phenyl-*N*-[3-{trifluoromethyl}phenyl]-1H-pyrrole-3-carboxamide.
14. R. N. Willette *et al.*, *J. Pharmacol. Exp. Ther.* **326**, 443 (2008).
15. W. Everaerts *et al.*, *Proc. Natl. Acad. Sci. U.S.A.* **107**, 19084 (2010).
16. I. Parker, I. F. Smith, *J. Gen. Physiol.* **136**, 119 (2010).
17. W. Everaerts, B. Nilius, G. Owsianik, *Prog. Biophys. Mol. Biol.* **103**, 2 (2010).
18. S. Q. Wang, L. S. Song, E. G. Lakatta, H. Cheng, *Nature* **410**, 592 (2001).
19. R. Strotmann, M. Semtner, F. Kepura, T. D. Plant, T. Schöneberg, *PLoS ONE* **5**, e10580 (2010).
20. J. Ledoux, M. E. Werner, J. E. Brayden, M. T. Nelson, *Physiology (Bethesda)* **21**, 69 (2006).
21. K. A. Dora *et al.*, *J. Vasc. Res.* **40**, 480 (2003).
22. S. L. Sandow, C. B. Neylon, M. X. Chen, C. J. Garland, *J. Anat.* **209**, 689 (2006).

Acknowledgments: We thank HydraBiosciences for HC-067047, Neurosearch A/S for NS309, and J. E. Brayden, K. Freeman, M. Koide, L. W. Nausch, and G. C. Wellman for comments on the manuscript. This work was supported by a grant from the COBRE Program of the National Center for Research Resources funded by the NIH (2-P20-RR-016435-06), an award from the American Heart Association Founders Affiliate and the Pulmonary Hypertension Association (10POST3690006) to S.K.S, and by grants NIH GM086736 to M.I.K.; FRSQ (Junior 1)/NIA (HSFC) to J.L.; and NIH HL044455, 1P01HL095488, R37DK053832, R01HL098243, and the Totman Medical Research Trust to M.T.N. The authors have no conflicts of interest.

Supplementary Materials

www.sciencemag.org/cgi/content/full/336/6081/597/DC1
Materials and Methods
Figs. S1 to S7
Movies S1 to S6
References (*23–29*)

7 November 2011; accepted 16 March 2012
10.1126/science.1216283

Multidimensional Optimality of Microbial Metabolism

Robert Schuetz,[1] Nicola Zamboni,[1] Mattia Zampieri,[1] Matthias Heinemann,[1,2] Uwe Sauer[1]*

Although the network topology of metabolism is well known, understanding the principles that govern the distribution of fluxes through metabolism lags behind. Experimentally, these fluxes can be measured by ^{13}C-flux analysis, and there has been a long-standing interest in understanding this functional network operation from an evolutionary perspective. On the basis of ^{13}C-determined fluxes from nine bacteria and multi-objective optimization theory, we show that metabolism operates close to the Pareto-optimal surface of a three-dimensional space defined by competing objectives. Consistent with flux data from evolved *Escherichia coli*, we propose that flux states evolve under the trade-off between two principles: optimality under one given condition and minimal adjustment between conditions. These principles form the forces by which evolution shapes metabolic fluxes in microorganisms' environmental context.

As a network of about a thousand enzymatic reactions, metabolism fuels growth by converting nutrients into building blocks and energy, but our understanding of the principles that govern the functional distribution of fluxes through this network is limited. Experimentally, intracellular fluxes can be determined by ^{13}C-based flux analysis (*1*, *2*). Based on empirically derived optimality principles (*3*, *4*), stoichiometric models of metabolism (*3*, *4*) can predict condition-dependent flux phenotypes (*5–9*) as the outcome of single environment evolution (*10*, *11*). However, a concept that integrates such incidental empirical observations into a consistent framework is lacking (*12*). Although cost-benefit theory indicates that evolution in a constant environment minimizes the expression of enzymes (*10*, *13*), in reality microbes must cope with continuous environmental changes. Thus, we investigated whether the incidental objectives of metabolic operation (*5–10*) can be integrated into a general optimality framework that explains an organism's evolution toward particular distributions of fluxes under fluctuating conditions.

The basis of our analysis is a stoichiometric reaction model of *Escherichia coli* central metabolism (table S1) that constrains metabolic fluxes at steady state in a convex space of feasible solutions (*3*, *4*). Assuming that optimality goals are tailored to conditions and that different, eventually competing, objectives cannot be optimized simultaneously, cells face a trade-off that is described by the Pareto surface (*14*) on which each point is Pareto optimal; that is, the value of one objective can be increased only at the cost of another. To identify the axes of such a multidimensional optimality space, we computationally predicted flux distributions with 54 single objective functions and quantified the deviation to 44 reported in vivo flux distributions (fig. S1a and table S2) obtained from ^{13}C-labeling experiments (*15–19*) (table S3). Five of the objective functions were found to be consistent with the in vivo fluxes under some conditions: maximum adenosine triphosphate (ATP), biomass, acetate, and carbon dioxide yields and minimum sum of absolute fluxes (fig. S1a). For all possible pairs and triplets of these, we computed the Pareto surface (fig. S1b). Although no dual combination could describe all measured fluxes adequately, the combination of the two efficiency objectives, maximum ATP yield and maximum biomass yield, with the optimal resource allocation objective minimum sum of absolute fluxes achieved the highest optimality, evidenced by all 44 in vivo flux distributions being very close to the Pareto surface (Fig. 1, A and E, and figs. S1b and S2).

On the Pareto surface, the in vivo flux distributions occupied distinct regions that cluster into biologically meaningful groups (Fig. 1A). Whereas aerobic cultures of various *E. coli* strains grown with nonlimiting glucose (blue) clustered in the upper right corner, cultures in which glucose was continuously supplied at a limiting amount (green) stretched according to their growth rate diagonally between the maximum ATP and biomass yield axes. The proximity of

[1]Institute of Molecular Systems Biology, Eidgenössische Technische Hochschule (ETH) Zurich, Zurich, Switzerland. [2]Molecular Systems Biology, Groningen Biomolecular Sciences and Biotechnology Institute, University of Groningen, Groningen, Netherlands.

*To whom correspondence should be addressed. E-mail: sauer@ethz.ch

in vivo flux distributions to the Pareto surface of this three-dimensional optimality space is statistically significant because it is much closer when compared to the average distance of random steady-state flux distributions ($P < 5 \times 10^{-16}$, *t* test) (Fig. 1, B to D). Furthermore, other bacterial species also locate close to the surface (Fig. 2, A and B), and their different locations on the surface indicate that each species features a distinct flux distribution under a given condition. Thus, metabolism of wild-type bacteria appears to generally operate close to the Pareto surface of the space that defines metabolic optimality as a combination of (i) network output in the form of biomass and energy yield and (ii) resource allocation. Akin to *E. coli* (Fig. 1B), mutations can eventually shift their flux distributions away from the surface, as shown for *Bacillus subtilis* mutants with strongly altered fluxes (*20*) that locate significantly ($P < 2 \times 10^{-33}$, *t* test) below the Pareto surface (Fig. 2C), supporting our hypothesis that Pareto optimality results from evolutionary adaptation.

Why are particular flux distributions manifested in *E. coli*? For this question, we tested how Pareto optimality constrains fluxes of individual reactions. We determined the values that each reaction flux can assume in the subspace immediately below the spot on the Pareto surface where the in vivo flux distributions of a certain condition clustered together (Fig. 1E). For each of the 18 degrees of freedom (table S4) that determine all fluxes, we calculated (by exhaustive sampling) the absolute range of fluxes that each reaction can assume within the subspaces of near metabolic optimality (figs. S3 and S4). For each reaction, we thereby obtained, as a function of the distance from the Pareto surface, a flux range; that is, a variability value that defines possible fluxes at a specific optimality value (Fig. 3, A to C). For most degrees of freedom, with increasing distance from the surface the flux variability initially increases drastically before converging to stable values (Fig. 3, D to H).

All experimentally determined flux distributions were found to locate at a distance from the Pareto surface (along the *x* axes) characterized by a significant variability; for example, in aerobic batch cultures the glucose-6-phosphate dehydrogenase (Zwf) flux locates at a distance where the flux can vary from 3 to 11 mmol/g per hour at the same optimality value (Fig. 3A). The specific location is typically where a further distance increase does not further increase flux variability (Fig. 3, D to H). The almost identical position of individual flux measurements along the *y* axis indicates that the 18 tested *E. coli* wild-type strains do not exploit the full optimality-preserving variability range but rather cluster at a particular flux value (Fig. 3, A to C, and fig. S3).

So far, we found that *E. coli* operates its metabolism slightly below the Pareto surface, where it can achieve a high degree of variability in most reactions while nearly preserving

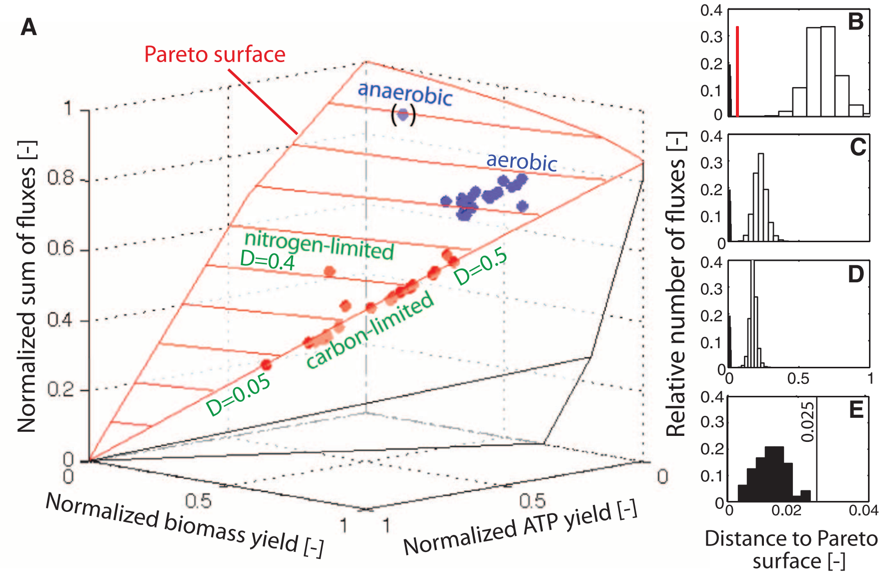

Fig. 1. (**A**) Projection of 44 ^{13}C-determined in vivo flux distributions of *E. coli* wild type into the solution space defined by three objectives. The Pareto surface is shown in red. Blue dots indicate cultures for which glucose was present in excess and green dots, continuous cultures at different dilution rates *D* (table S3) (*14–18*, *24*). Axes values are normalized such that the coordinates of the points on the Pareto surface range from 0 to 1, where 1 represents the theoretical minimum or maximum of an objective. Akin to the flux cone in flux balance analysis (*25*), the present space contains all mass-balanced fluxes, but the geometry is entirely different because the dimensions are objectives and not free fluxes. (**B** to **E**) Pareto surface distance of the 44 ^{13}C-determined (solid bars) and 10,000 random flux distributions (open bars) that are uniformly distributed within the full solution space (*26*). Random fluxes were chosen without imposing additional constraints (B), after elimination of futile cycles (C) and upon additionally constraining the biomass yield to at least 20% of the maximal theoretical value (D). The solid black line highlights the subspace of metabolic optimality that is relevant in vivo with a maximal distance of 0.025 units from the Pareto surface (E). Data were binned to reduce noise. The distance for the anaerobic condition is relative to its respective Pareto surface. The red bars in (B) represent the flux distribution of the *E. coli* triple mutant with deleted pyruvate formate lyase (*pfl*), lactate dehydrogenase (*ldhA*), and glucose phosphotransferase system enzyme II (*ptsG*) at CO_2 concentrations of 3, 10, and 50% (*27*).

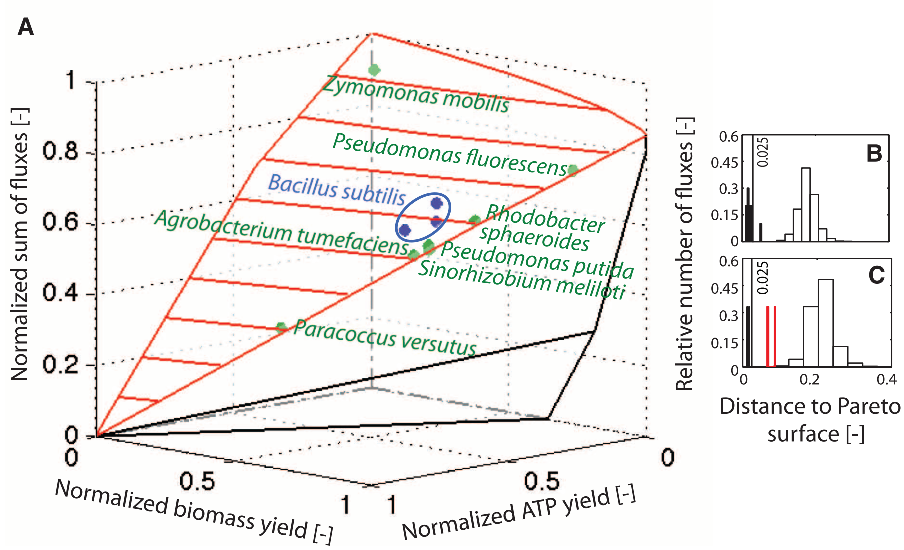

Fig. 2. (**A**) Projection of 10 ^{13}C-determined in vivo flux distributions of eight bacteria (*25*) into the metabolic optimality space of *E. coli*. The Pareto surface of *E. coli* is shown in red. The values on the axes are normalized as in Fig. 1. (**B**) Distance of the eight experimental (solid bars) and 10,000 random *E. coli* flux distributions (open bars) to each bacterium's own Pareto surface. (**C**) Distance to the Pareto surface of three *B. subtilis* wild types (solid bars); *ccpN*, *ccpN-gapB*, and *ccpN-src1 B. subtilis* mutants (*20*) (red solid bars); and 10,000 random *B. subtilis* flux distributions without futile cycles and biomass yield of at least 20% of the maximal theoretical value (open bars).

optimality. This led us to the hypothesis that additional selection criteria guide evolution toward particular flux distributions. A specific flux distribution at a certain condition might be chosen to minimize adjustment efforts to other conditions. To test this possibility, we systematically computed the average flux adjustments that would be required to switch between the five investigated environmental conditions (Fig. 4A). We calculated the range of average flux adjustments from the distances between 10,000 randomly chosen flux distributions from the optimality-preserving subspace underneath each condition (Fig. 3, A to C). We found that, although flux distributions at the Pareto surface are optimal for a given condition, they require relatively large flux adjustments to enable growth under alternative conditions (black dots in Fig. 4A). However, starting from the slightly less optimal values where the in vivo flux distributions locate, significantly smaller flux adjustments are necessary for growth under other conditions ($P < 1.4 \times 10^{-57}$, rank sum test). In the trade-off between optimality and adjustment, experimentally measured fluxes appear to minimize the adjustment efforts rather than the distance to the Pareto surface (fig. S5).

To obtain experimental evidence for minimization of flux adjustments between conditions as an evolutionary selection criterion for a flux distribution, we analyzed an *E. coli* population that was evolved for 1000 generations on alternating glucose and acetate batch cultures (*21*, *22*). The ancestor differentiated into two distinct ecotypes, that is, one exhibiting slow growth on glucose but fast to switch to acetate growth and the other with fast growth on glucose but slow to switch to acetate (*22*). Metabolically, one would expect that short switching times correspond to small flux adjustments and long switching times likewise

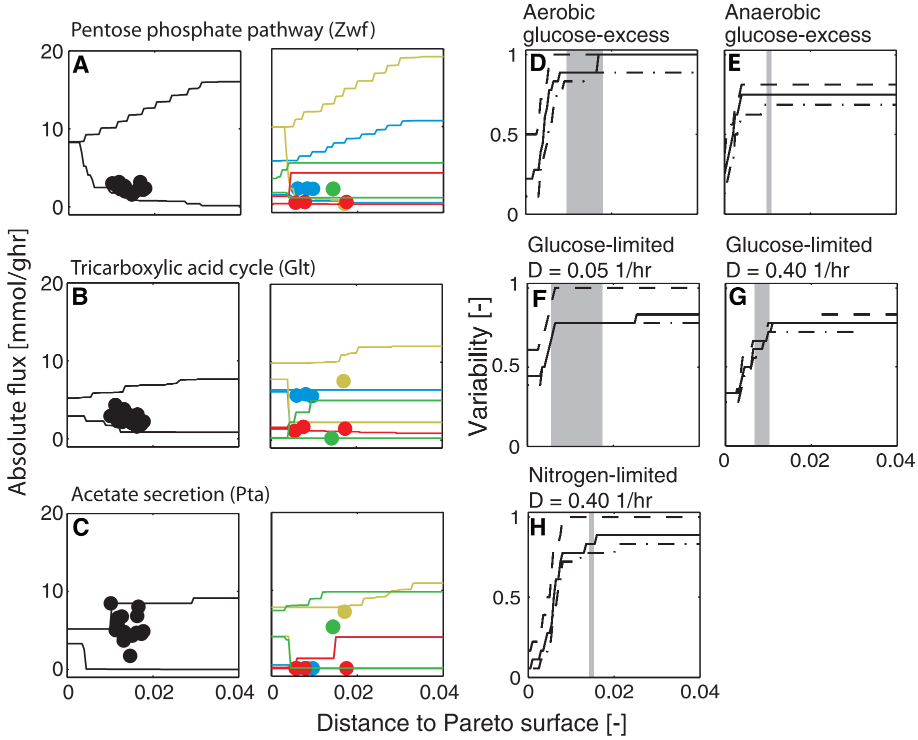

Fig. 3. Flux variability immediately below the Pareto surface for three key *E. coli* reactions. (**A** to **C**) Minimal and maximal optimal in silico fluxes (lines) and in vivo fluxes (dots) as a function of the distance to the Pareto surface in aerobic (black) and anaerobic (green) glucose batch cultures, glucose-limited continuous cultures with D = 0.09 1/hour (red) and 0.4 1/hour (light blue), and nitrogen-limited continuous cultures with D = 0.4 1/hour (dark yellow). Results for all 18 degrees of freedom are shown in figs. S3 and S4. (**D** to **H**) Variability of flux distributions as a function of their distance from the Pareto surface. Variability is defined as the fraction of degrees of freedom with a coefficient of variation (standard deviation/mean value) exceeding 10% (dashed lines), 50% (solid lines), or 80% (dashed-dotted lines) based on sampling of the metabolic optimality space. Gray areas indicate minimal and maximal distance of in vivo flux distributions.

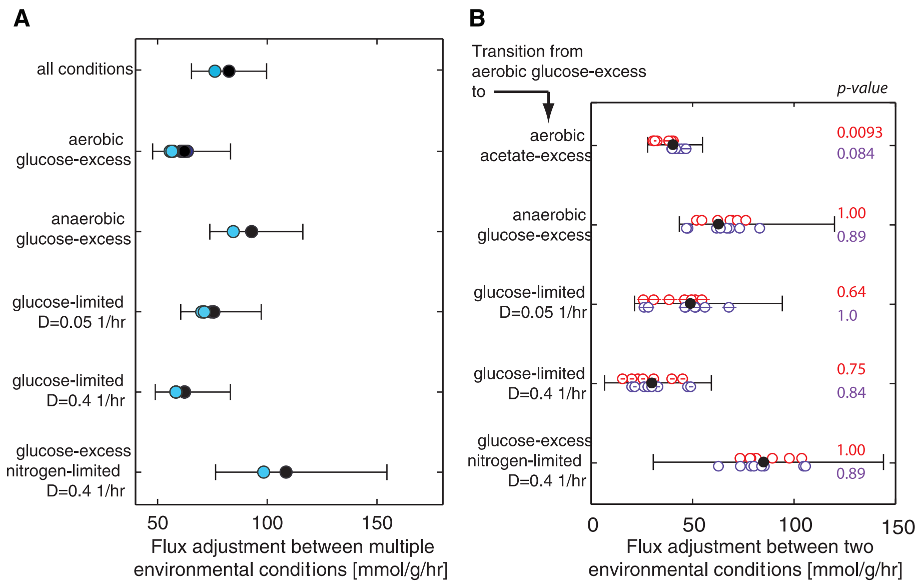

Fig. 4. Flux adjustment between multiple environmental conditions. Lines indicate the minimal and maximal average flux adjustment values based on randomly chosen flux distributions within the flexible subspace of metabolic optimality for each condition, that is, all flux distributions within a maximal distance of 0.025 units from the Pareto surface (Fig. 1E). (**A**) Average flux adjustment for switching of *E. coli* wild type from the indicated condition to any of the other four. Light blue and black dots indicate the average flux adjustment based on the in vivo realized and the hypothetical Pareto optimal flux distributions, respectively. (**B**) Flux adjustment for switching from aerobic growth on excess glucose to one of the indicated environmental conditions. Black dots indicate the unevolved strain, whereas red and green dots show evolved strains with fast or slow switching phenotypes, respectively, between aerobic growth on glucose and acetate. Average values are given where more than one experimental flux distribution was available (table S5).

correspond to large flux adjustments. Although we cannot make any predictions about the metabolism of the slow switchers, our hypothesis of minimization of flux adjustments predicts that the fast-switching strains have a flux distribution when grown on glucose that is closer to the flux distribution when grown on acetate and vice versa. Indeed, ^{13}C-labeling experiments with 15 randomly selected clones from this cyclic environment evolution (tables S5 and S6) revealed that the fast-switching ecotypes migrated toward Pareto optimality and an in-between flux distribution with, for example, higher tricarboxylic acid cycle fluxes on glucose (fig. S6) that lead to significantly ($P < 0.009$) reduced flux adjustments between growth on glucose and acetate (Fig. 4B and fig. S7). The slow switchers, in contrast, exhibited higher flux adjustment values than the ancestor. Consistent with our hypothesis, the flux adjustments from glucose batch growth to any other (not selected for) environmental condition scatter around the ancestor with no significant difference between the two ecotypes (Fig. 4B). Thus, within the optimality-preserving variability at one condition, evolution favors flux distributions that minimize adjustments to other environmental conditions.

The principles of variable, near-optimal metabolism and minimal flux adjustment suffice to explain all investigated flux distributions. The range of investigated bacteria and conditions suggests that these principles are prevalent. In contrast to the previously described adaptive prediction, in which regulation patterns evolved that anticipated sequential environmental changes (*23*), the adaptive property of minimal flux adjustment is not restricted to the temporal order of occurring environments. Instead, minimal flux adjustment represents more generally an optimal starting point for growth under multiple conditions, presumably reflecting an organism's natural habitat(s). An organism cannot be optimally adapted to all possible conditions, but the evolutionary benefit of an ideal starting point will be important for microbes that are not highly specialized to particular nutritional conditions. By this trade-off between (near) optimality under a given condition and minimal adjustment to alternative conditions, we provide a consistent theoretical framework to decipher optimality-based forces that shape metabolic fluxes in a microorganism's environmental context.

References and Notes

1. U. Sauer, *Mol. Syst. Biol.* **2**, 62 (2006).
2. N. Zamboni, S.-M. Fendt, M. Rühl, U. Sauer, *Nat. Protoc.* **4**, 878 (2009).
3. M. A. Oberhardt, B. O. Palsson, J. A. Papin, *Mol. Syst. Biol.* **5**, 320 (2009).
4. A. M. Feist, M. J. Herrgård, I. Thiele, J. L. Reed, B. O. Palsson, *Nat. Rev. Microbiol.* **7**, 129 (2009).
5. R. Schuetz, L. Kuepfer, U. Sauer, *Mol. Syst. Biol.* **3**, 119 (2007).
6. A. P. Burgard, C. D. Maranas, *Biotechnol. Bioeng.* **82**, 670 (2003).
7. H.-G. Holzhütter, *Eur. J. Biochem.* **271**, 2905 (2004).
8. D. Segrè, D. Vitkup, G. M. Church, *Proc. Natl. Acad. Sci. U.S.A.* **99**, 15112 (2002).
9. T. Shlomi, O. Berkman, E. Ruppin, *Proc. Natl. Acad. Sci. U.S.A.* **102**, 7695 (2005).
10. N. E. Lewis *et al.*, *Mol. Syst. Biol.* **6**, 390 (2010).
11. R. U. Ibarra, J. S. Edwards, B. O. Palsson, *Nature* **420**, 186 (2002).
12. A. M. Feist, B. O. Palsson, *Curr. Opin. Microbiol.* **13**, 344 (2010).
13. E. Dekel, U. Alon, *Nature* **436**, 588 (2005).
14. D. Nagrath *et al.*, *Ann. Biomed. Eng.* **35**, 863 (2007).
15. A. Perrenoud, U. Sauer, *J. Bacteriol.* **187**, 3171 (2005).
16. M. Emmerling *et al.*, *J. Bacteriol.* **184**, 152 (2002).
17. N. Ishii *et al.*, *Science* **316**, 593 (2007); 10.1126/science.1132067.
18. A. Nanchen, A. Schicker, U. Sauer, *Appl. Environ. Microbiol.* **72**, 1164 (2006).
19. E. Fischer, U. Sauer, *Eur. J. Biochem.* **270**, 880 (2003).
20. S. Tännler *et al.*, *J. Bacteriol.* **190**, 6178 (2008).
21. C. C. Spencer, J. Tyerman, M. Bertrand, M. Doebeli, *Proc. Natl. Acad. Sci. U.S.A.* **105**, 1585 (2008).
22. C. C. Spencer, M. Bertrand, M. Travisano, M. Doebeli, *PLoS Genet.* **3**, e15 (2007).
23. A. Mitchell *et al.*, *Nature* **460**, 220 (2009).
24. T. Fuhrer, E. Fischer, U. Sauer, *J. Bacteriol.* **187**, 1581 (2005).
25. N. D. Price, J. L. Reed, B. O. Palsson, *Nat. Rev. Microbiol.* **2**, 886 (2004).
26. D. Kaufman, R. Smith, *Oper. Res.* **46**, 84 (1998).
27. S. Lu, M. A. Eiteman, E. Altman, *J. Biotechnol.* **143**, 213 (2009).

Acknowledgments: R.S. is in the Life Science Zurich Ph.D. program on Systems Physiology and Metabolic Diseases, Zurich, Switzerland. We thank M. Doebeli for the mutants, E. Michlig for flux analysis, J. Banga for initial discussion on Pareto optimality, and V. Chubukov for proofreading. We acknowledge financial support via an ETH grant to U.S. Data and model described in this paper are presented in the supplementary materials.

Supplementary Materials
www.sciencemag.org/cgi/content/full/336/6081/601/DC1
Materials and Methods
Supplementary Text
Figs. S1 to S9
Tables S1 to S6
References (*28–38*)

21 November 2011; accepted 16 March 2012
10.1126/science.1216882

Radio-Wave Heating of Iron Oxide Nanoparticles Can Regulate Plasma Glucose in Mice

Sarah A. Stanley,[1] Jennifer E. Gagner,[2] Shadi Damanpour,[1] Mitsukuni Yoshida,[3] Jonathan S. Dordick,[4] Jeffrey M. Friedman[1,5]*

Medical applications of nanotechnology typically focus on drug delivery and biosensors. Here, we combine nanotechnology and bioengineering to demonstrate that nanoparticles can be used to remotely regulate protein production in vivo. We decorated a modified temperature-sensitive channel, TRPV1, with antibody-coated iron oxide nanoparticles that are heated in a low-frequency magnetic field. When local temperature rises, TRPV1 gates calcium to stimulate synthesis and release of bioengineered insulin driven by a Ca^{2+}-sensitive promoter. Studying tumor xenografts expressing the bioengineered insulin gene, we show that exposure to radio waves stimulates insulin release from the tumors and lowers blood glucose in mice. We further show that cells can be engineered to synthesize genetically encoded ferritin nanoparticles and inducibly release insulin. These approaches provide a platform for using nanotechnology to activate cells.

Remote activation of specific cells to trigger gene expression and peptide release in vivo could provide a useful research tool and, in time, potentially provide a means for regulated expression of proteins in clinical settings. Cell activation by direct stimulation with electrodes (*1*) is limited by nonspecific and variable activation, the need for permanent implants, and potential tissue damage (*2*, *3*). Ion channels, such as channelrhodopsin, regulate intracellular ions and cell activity (*4*) with anatomical specificity and temporal control, but, because light waves do not penetrate tissue, implanted devices are required. In contrast, low and medium radio frequencies (RFs) can penetrate deep tissues with minimal energy absorption (*5*, *6*). Unlike tissue, metal nanoparticles absorb energy and heat in response to RF (*7*, *8*). This heating, which depends on particle composition and size and RF field strength, (*9*) can be converted into a cellular signal by using a temperature-sensitive channel to allow ion entry. Targeting of nanoparticles can be achieved by coating with specific antibodies (*10*, *11*) to induce cell-specific, cell membrane

[1]Laboratory of Molecular Genetics, Rockefeller University, New York, NY 10065, USA. [2]Department of Materials Science and Engineering, Rensselaer Nanotechnology Center, Rensselaer Polytechnic Institute, Troy, NY 12180, USA. [3]Elizabeth and Vincent Meyer Laboratory of Systems Cancer Biology, Rockefeller University, New York, NY 10065, USA. [4]Department of Chemical and Biological Engineering, Department of Biology, Center for Biotechnology and Interdisciplinary Studies, Rensselaer Polytechnic Institute, Troy, NY 12180, USA. [5]Howard Hughes Medical Institute, New York, NY 10065, USA.

*To whom correspondence should be addressed. E-mail: friedj@mail.rockefeller.edu

temperature changes that are then transduced by a temperature sensitive channel into cellular responses.

We have applied these principles to develop a system that allows remote activation of protein production by engineered cells in vitro and in vivo. The method (Fig. 1A) uses iron oxide nanoparticles (FeNPs) that are coated with antibodies against His (anti-His) and that bind a modified TRPV1 channel with an extracellular His × 6 epitope tag ($TRPV1^{His}$). We reasoned that, with RF treatment, local heating of bound anti-His FeNPs would activate the temperature-sensitive TRPV1, resulting in a calcium current to activate a Ca^{2+}-sensitive promoter placed upstream of a modified human insulin reporter gene.

We used FeNPs for the following reasons: They heat at 465 kHz, a relatively low frequency that minimizes tissue heating; particles of 20 nM or less diffuse in the extracellular space (*11–13*); and these particles can be derivatized with antibodies. At 465 kHz (5 mT), substantial heating was observed for 20- and 25-nm FeNP suspensions (fig. S1). A 20-nm FeNP suspension had an initial heating rate of 0.15°C/s and a specific absorption rate (SAR) of 0.63 W/g, whereas the SAR of water at this field frequency and strength was less than 0.004 W/g. As shown by electron microscopy, a His-tag insertion into the first extracellular loop of TRPV1 provided a site for significant and specific FeNP binding (fig. S2) with direct heat transfer to the adjacent channel (fig. S3). Human embryonic kidney (HEK) 293T cells expressing $TRPV1^{His}$ and decorated with 20 nM FeNPs conjugated to anti-His showed a significant increase in intracellular Ca^{2+} after 10s of RF exposure (fig. S2D).

Calcium entry was next used to induce gene expression via a novel synthetic 5′ regulatory region composed of three Ca^{2+}response elements in cis: serum response element (SRE), cyclic adenosine monophosphate response element (CRE), and nuclear factor of activated T cell response element (NFAT RE) (*14*, *15*) with a minimal promoter. This was placed upstream of a modified human proinsulin gene with furin cleavage sites replacing beta-cell–specific convertase cleavage sites to allow insulin processing in non-beta cells (*16*) (fig. S4A).

HEK 293T cells expressing the Ca^{2+}-dependent human insulin construct and $TRPV1^{His}$ were incubated with functionalized FeNPs. RF treatment of the FeNP-decorated cells resulted in a significant increase in proinsulin release (RF-treated 671 ± 235% (SEM) basal versus 100 ± 13.9% for controls, $P < 0.02$) and insulin gene expression (RF-treated 2.20 ± 0.53 insulin gene expression relative to basal versus 1.0 ± 0.18 for controls, $P < 0.05$). These were blocked by the TRP channel inhibitor, ruthenium red (Fig. 1B). There was a trend toward an increase in proinsulin release after 15 min of RF treatment (likely through release of a small pool of preformed insulin-containing vesicles), with significant proinsulin release at 1 hour when insulin gene expression had also significantly increased (Fig. 1C). Control studies confirmed that proinsulin release required all system components (i.e., TRPV1, nanoparticles, and RF magnetic field) and that RF-dependent insulin secretion was confined to FeNP-decorated cells (fig. S4, B and C). RF treatment induced NFAT translocation into the nucleus, and RF-dependent proinsulin release was blocked by a calcineurin inhibitor, tacrolimus (fig. S4, D and E). RF treatment of cells incubated with FeNPs (1 to 8 mg/ml) did not induce apoptosis as assessed by immunohistochemistry for active caspase 3 (*17*) and terminal deoxynucleotidyl transferase–mediated deoxyuridine triphosphate nick end labeling (TUNEL) (*18*) (fig. S4, F and G). We also showed that RF could stimulate proinsulin release from mouse embryonic stem cells expressing $TRPV1^{His}$ and the Ca^{2+}-dependent human insulin construct (fig. S5).

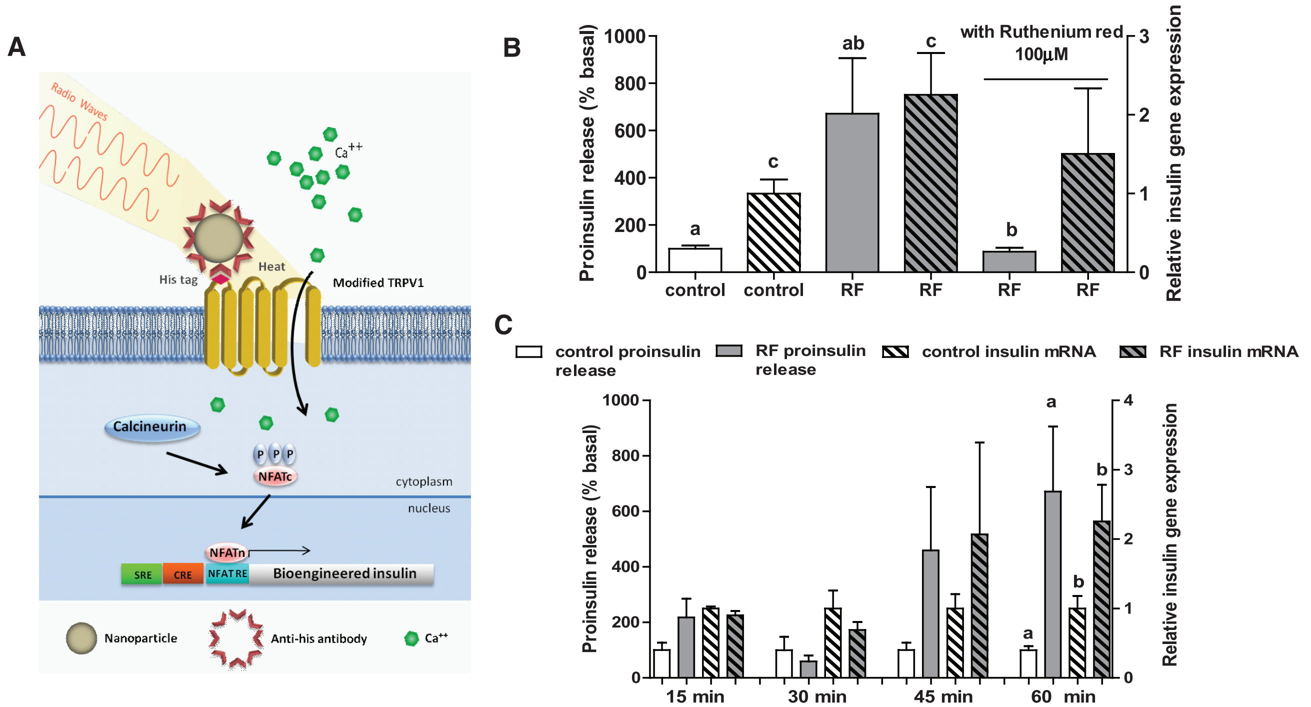

Fig. 1. Nanoparticles induced cell excitation to increase insulin expression and release in vitro. (**A**) Schema of nanoparticle-induced cell activation and gene expression. Antibody-coated ferrous oxide nanoparticles bind to a unique epitope, His × 6, in the first extracellular loop of the temperature-sensitive TRPV1 channel. Exposure to a RF field induces local nanoparticle heating, which opens temperature-sensitive TRPV1 channels. Calcium entry triggers downstream pathways, such as activation of calcineurin, leading to dephosphorylation of NFAT and translocation to the nucleus. Here, NFAT binds to upstream response elements to initiate gene expression of a bioengineered human insulin gene. Additional calcium-dependent signal transduction pathways also stimulate gene expression via binding to SRE and CRE. P indicates a phosphate group. (**B**) RF treatment increases proinsulin release and insulin gene expression in vitro. Nanoparticle-decorated HEK293T cells transfected with $TRPV1^{His}$ and calcium-dependent insulin show a significant increase in proinsulin release and insulin gene expression with RF treatment that is blocked by the TRP antagonist ruthenium red. (Columns marked with the same letter indicate significance, $P < 0.05$. Error bars indicate SEM) (**C**) Time courses of proinsulin release and insulin gene expression from nanoparticle-decorated HEK293T cells transfected with $TRPV1^{His}$ and calcium-dependent insulin with RF treatment.

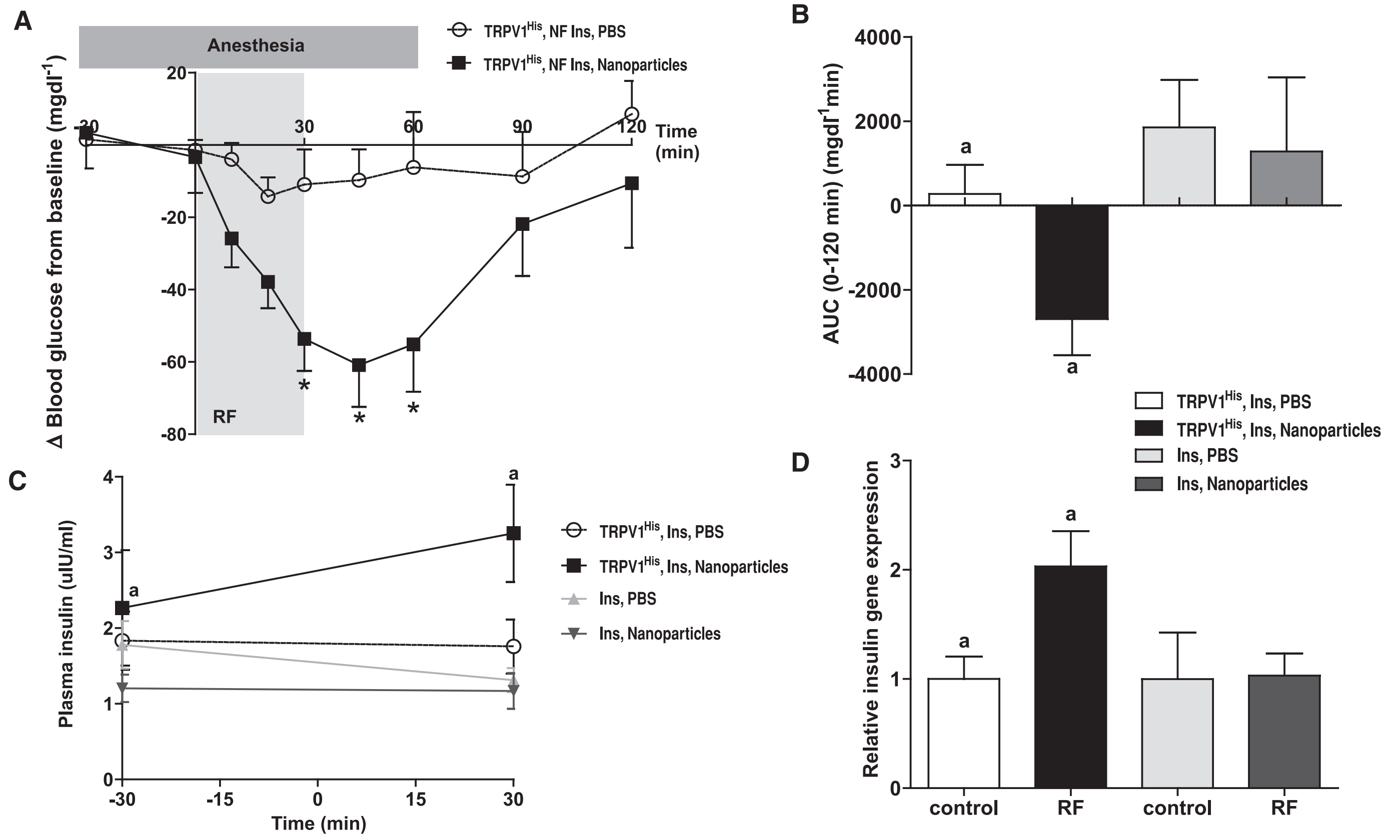

Fig. 2. Nanoparticle regulation of blood glucose in vivo. (**A**) Effects of RF treatment on blood glucose in PBS and nanoparticle-treated mice with tumors expressing TRPV1^{His} and calcium-dependent human insulin. RF treatment significantly reduces blood glucose in nanoparticle-treated mice compared with that of PBS-treated mice. (Asterisks indicate $P < 0.05$. Error bars indicate SEM.) (**B**) RF treatment of mice with tumors expressing TRPV1^{His} and calcium-dependent human insulin injected with nanoparticles significantly reduces blood glucose over the course of the study as assessed by the area under the curve. There is no effect in mice with tumors expressing calcium-dependent insulin alone without TRPV1^{His}. (Same letter indicates $P < 0.05$.) (**C**) Plasma insulin is significantly increased by RF treatment in nanoparticle-treated but not PBS-treated mice with tumors expressing TRPV1^{His} and calcium-dependent human insulin. There is no effect in mice with tumors expressing calcium-dependent insulin alone without TRPV1^{His}. (Same letter indicates $P < 0.05$). (**D**) Insulin gene expression is significantly increased in the tumors expressing TRPV1^{His} and calcium-dependent human insulin treated with nanoparticles and RF magnetic field but not in tumors expressing calcium-dependent human insulin alone without TRPV1^{His}.

Next, we compared our single-component system to a multicomponent system previously reported (*19*) and composed of (i) a membrane-tethered biotin acceptor protein, (ii) a bacterial biotin ligase to biotinylate this protein to enable binding of (iii) streptavidin-coated nanoparticles, and (iv) a wild-type TRPV1 as the effector. Although this system induced Ca^{2+} entry in vitro and activated endogenous temperature sensing of *Caenorhabditis elegans* neurons, the complete system was not tested in vivo because the exogenous TRPV1 channel was not used in this prior study. We found that our single-component system had denser nanoparticle binding, faster calcium entry, and a trend toward more robust proinsulin release (fig. S6, A to G). These attributes led us to test the single-component TRPV1^{His} system in vivo in mice by using xenografts of engineered neuroendocrine PC12 cells, which robustly secrete peptides via the regulated pathway for protein secretion.

Exposure of a PC-12 cell line stably expressing TRPV1^{His} and the calcium-dependent human insulin construct (PC12-TRPV1^{His}-Ins) to RF after FeNP application significantly increased proinsulin release and insulin gene expression in vitro (fig. S7, A to D). The PC12-TRPV1^{His}-Ins cells were injected subcutaneously into the flank of nude mice to form tumors (fig. S7F). There was no change in plasma glucose with tumor growth (fig. S7E). Phosphate-buffered saline (PBS) or FeNP (50-μl total volume, nanoparticle concentration of 8 mg/ml) were injected into the tumors of fasted mice, and blood glucose and plasma insulin were measured before, during, and after RF application (see fig. S8A for protocol). RF treatment resulted in a significant decrease in blood glucose in nanoparticle-treated PC12-TRPV1^{His}-Ins tumor mice (Fig. 2A) (The change in blood glucose at 30 min for FeNP-treated was -53.6 ± 8.90 mg/dl, versus PBS-treated, -11.0 ± 9.72 mg/dl; $P < 0.005$. At 45 min, the change in blood glucose for FeNP-treated mice was -60.9 ± 11.6 mg/dl versus PBS-treated -9.74 ± 8.52 mg/dl; $P < 0.005$. At 60 min, the change in blood glucose for FeNP-treated mice was -55.1 ± 13.2 mg/dl versus PBS-treated, -6.24 ± 15.3 mg/dl; $P < 0.0001$). There was also a highly significant difference in the cumulative change in blood glucose (area under the curve, AUC) between PBS-treated and FeNP-treated PC12-TRPV1^{His}-Ins tumor mice over the course of the study (Fig. 2B) [AUC (0 to 120 min) for PBS-treated was 272 ± 692 mg/dl min versus FeNP-treated, -2695 ± 858.3 mg/dl min; $P < 0.002$]. Plasma insulin was significantly increased after RF treatment in FeNP-treated but not PBS-injected mice (Fig. 2C) [plasma insulin for FeNP-treated (–30 min) was 2.26 ± 0.76 μI-U/ml (where 1 μI-U/ml = 0.006 pmol/l) versus FeNP-treated (30 min), 3.25 ± 0.64 μI-U/ml; $P < 0.05$. PBS-treated (–30 min) was 1.83 ± 0.38 μI-U/ml versus PBS-treated (30 min), 1.75 ± 0.36 μI-U/ml]. Lastly, insulin gene expression was significantly increased in RF-treated, FeNP-injected tumors (Fig. 2D) (relative insulin gene expression in FeNP-treated, no RF samples was 1.0 ± 0.2 versus FeNP-treated with RF, 2.0 ± 0.3, $P < 0.05$) without increasing c-fos expression (fig. S8B). Core temperature did not change significantly with RF exposure, and the intratumoral temperatures (23° to 31°C) remained well below the 42°C threshold of TRPV1, suggesting that cell

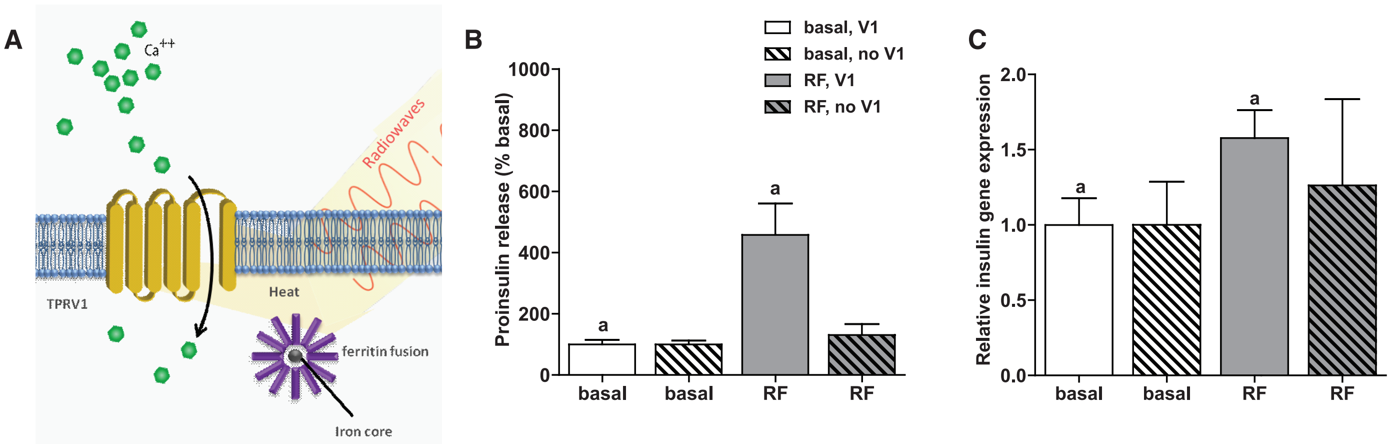

Fig. 3. Intracellular nanoparticle synthesis and cell activation. (**A**) Schema of intracellular nanoparticle synthesis and cell activation. A ferritin fusion protein is composed of a ferritin light chain fused to ferritin heavy chain with a flexible linker region. Heating of the iron core by a RF magnetic field opens the TRPV1 channel to trigger calcium entry, as previously described. (**B**) RF treatment increases proinsulin release in vitro. HEK293T cells transiently transfected with TRPV1, ferritin, and calcium-dependent human insulin show a significant increase in proinsulin release in response to RF treatment. (Same letter indicates significance, $P < 0.05$.) RF treatment does not increase proinsulin release from cells expressing ferritin in the absence of TRPV1. (**C**) RF treatment increases insulin gene expression in vitro. Insulin gene expression is significantly increased by RF treatment in cells transfected with TRPV1, ferritin, and calcium-dependent human insulin. (Same letter indicates significance, $P < 0.05$.) RF treatment does not increase insulin gene expression in cells expressing ferritin in the absence of TRPV1.

activation is due to localized, cell surface–specific gating of TRPV1. There was no difference in apoptosis between FeNP-injected tumors in the presence or absence of the RF magnetic field (fig. S8, C and D). A significant decrease in blood glucose was also seen with serial FeNP injection and RF treatment (fig. S8, E and F). To confirm that the effects on blood glucose were not due to nonspecific insulin release via thermal effects of nanoparticles on the tumor, we repeated the in vivo study, first in mice injected with PC12 cells expressing the Ca^{2+}-dependent human insulin construct but not TRPV1^{His} and then in mice with tumors expressing TRPV1^{His} and insulin but injected with nanoparticles without anti-His conjugation. There was no significant effect on blood glucose in either study after PBS or FeNP injection and RF treatment despite similar intratumoral temperatures (fig. S9, A to D).

The above approach requires direct application of nanoparticles to TRPV1 expressing cells by incubation (in vitro) or injection (in vivo). An alternative is to engineer cells to synthesize nanoparticles intracellularly. For this purpose, we chose the iron storage protein ferritin, which forms a naturally occurring paramagnetic iron nanoparticle (*20*, *21*) (Fig. 3A and fig. S10). Ferritin has been stably overexpressed in mice for over 2 years without evident pathology (*22*). A fusion peptide of ferritin light chain, flexible linker region, and ferritin heavy chain fixes the ratio of light to heavy chains and increases iron binding (*23*). Transfecting cells with ferritin fusion protein resulted in 12.6 ± 2.86 ferritin particles per 0.2 μm^2 with an average distance to the cell membrane of 60.3 ± 2.85 nm (fig. S10B). RF treatment of cells expressing the ferritin fusion protein, TRPV1, and Ca^{2+}-dependent human insulin significantly increased proinsulin release (RF treated, $457 \pm 103\%$ basal versus control, $100 \pm 14.9\%$ basal; $P < 0.005$) and insulin gene expression (relative insulin gene expression for RF treated, 1.58 ± 0.19 versus control, 1.0 ± 0.17; $P < 0.05$) (Fig. 3B). Intracellularly generated FeNPs were roughly two-thirds as effective in stimulating proinsulin release as exogenous FeNP. In the absence of TRPV1, insulin secretion and gene expression were unchanged in ferritin-expressing cells. Thus, ferritin expression may provide a genetically encoded source of nanoparticles for RF-mediated cell activation.

We have shown that both externally applied and endogenously synthesized nanoparticles can be heated by radio waves to remotely activate insulin gene expression and secretion. RF-mediated cell activation does not require a permanent implant, and the cells to be activated can in principle be localized (when using exogenous nanoparticles) or dispersed (by using genetically encoded nanoparticles). Genetically encoded ferritin nanoparticles may also provide a continuous source of nanoparticles for cell activation.

The use of an epitope-tagged TRPV1 with antibody-coated nanoparticles resulted in high nanoparticle density in proximity to the channel and could gate calcium in response to power levels of a 465-kHz RF field that are within Food and Drug Administration guidelines (*24*, *25*). The use of a single construct for particle binding and calcium entry also simplifies DNA delivery using viral vectors or other approaches (*26*). Lastly, an epitope-tagged channel offers the possibility of activating distinct cell populations in the same animal with different RFs to selectively and independently heat nanoparticles bound to cell specific tags. For endogenous particles, mutations of ferritin that alter the metal it encapsulates could potentially enable combinatorial cell activation (*27*).

In summary, we have developed a noninvasive, nonpharmacological means for cell stimulation and validated it in vitro and in vivo. This system provides a useful tool for basic research and represents an initial step toward noninvasive regulation of protein production for possible therapeutic purposes. If a practical means for delivery of the nanoparticles can be established, this approach could theoretically be used to treat protein deficiencies by providing regulated expression of proteins that are difficult to synthesize or to deliver [such as central nervous system (CNS) replacement of hexosaminidase A for Tay-Sachs] or to allow CNS delivery of recombinant antibodies to treat brain metastases. This approach could also potentially enable the activation of other Ca^{2+}-dependent processes, such as muscle contraction or firing of action potentials.

References and Notes

1. E. Gellhorn, R. Cortell, J. Feldman, *Science* **92**, 288 (1940).
2. G. Stock, V. Sturm, H. P. Schmitt, K. H. Schlör, *Acta Neurochir. (Wien)* **47**, 123 (1979).
3. C. C. McIntyre, W. M. Grill, *J. Neurophysiol.* **88**, 1592 (2002).
4. E. S. Boyden, F. Zhang, E. Bamberg, G. Nagel, K. Deisseroth, *Nat. Neurosci.* **8**, 1263 (2005).
5. J. H. Young, M. T. Wang, I. Brezovich, *Electron. Lett.* **16**, 358 (1980).
6. P. R. Strauffer, T. C. Cetas, R. C. Jones, *IEEE Trans. Biomed. Eng.* **31**, 235 (1984).
7. H. H. Richardson *et al.*, *Nano Lett.* **6**, 783 (2006).
8. K. Hamad-Schifferli, J. J. Schwartz, A. T. Santos, S. Zhang, J. M. Jacobson, *Nature* **415**, 152 (2002).
9. J. P. Fortin *et al.*, *J. Am. Chem. Soc.* **129**, 2628 (2007).
10. B. Samanta *et al.*, *J. Mater. Chem.* **18**, 1204 (2008).
11. A. Z. Wang *et al.*, *Expert Opin. Biol. Ther.* **8**, 1063 (2008).
12. J. DeFalco *et al.*, *Science* **291**, 2608 (2001).

13. R. G. Thorne, C. Nicholson, *Proc. Natl. Acad. Sci. U.S.A.* **103**, 5567 (2006).
14. G. E. Hardingham, H. Bading, *Microsc. Res. Tech.* **46**, 348 (1999).
15. A. Rao, *Nat. Immunol.* **10**, 3 (2009).
16. A. L. Shifrin, A. Auricchio, Q. C. Yu, J. Wilson, S. E. Raper, *Gene Ther.* **8**, 1480 (2001).
17. M. Tewari *et al.*, *Cell* **81**, 801 (1995).
18. Y. Gavrieli, Y. Sherman, S. A. Ben-Sasson, *J. Cell Biol.* **119**, 493 (1992).
19. H. Huang, S. Delikanli, H. Zeng, D. M. Ferkey, A. Pralle, *Nat. Nanotechnol.* **5**, 602 (2010).
20. J. L. Farrant, *Biochim. Biophys. Acta* **13**, 569 (1954).
21. B. Sana, E. Johnson, K. Sheah, C. L. Poh, S. Lim, *Biointerphases* **5**, FA48 (2010).
22. K. Ziv *et al.*, *NMR Biomed.* **23**, 523 (2010).
23. B. Iordanova, C. S. Robison, E. T. Ahrens, *J. Biol. Inorg. Chem.* **15**, 957 (2010).
24. D. Halperin *et al.*, in *Proceedings of the 2008 IEEE Symposium on Security and Privacy*, Oakland, CA, 18 to 21 May 2008, pp. 129–142.
25. S. A. Hanna, paper presented at the Third International Symposium on Medical Information and Communication Technology, Montreal, Canada, 24 to 27 February 2009.
26. A. C. Nathwani *et al.*, *N. Engl. J. Med.* **365**, 2357 (2011).
27. C. A. Butts *et al.*, *Biochemistry* **47**, 12729 (2008).

Acknowledgments: We thank Friedman laboratory members for helpful discussions, S. Korres for assistance with manuscript preparation, S. Tavazoie for helpful discussions, R. Toledo-Crow and S. Abeytunge for assistance with RF technology, and the staff of the Rockefeller University Electron Microscopy Resource center for their technical support in imaging. This project was supported by funding from the JPB Foundation and grant no. R01 GM095654 from the NIH. The authors have filed a patent related to this work.

Supplementary Materials
www.sciencemag.org/cgi/content/full/336/6081/604/DC1
Materials and Methods
Supplementary Text
Figs. S1 to 10
References (*28–35*)

17 November 2011; accepted 23 March 2012
10.1126/science.1216753

Substrate-Controlled Succession of Marine Bacterioplankton Populations Induced by a Phytoplankton Bloom

Hanno Teeling,[1]* Bernhard M. Fuchs,[1]* Dörte Becher,[2,5] Christine Klockow,[1,3] Antje Gardebrecht,[6] Christin M. Bennke,[1] Mariette Kassabgy,[1] Sixing Huang,[1] Alexander J. Mann,[1,3] Jost Waldmann,[1,2,3] Marc Weber,[1,3] Anna Klindworth,[1,3] Andreas Otto,[5] Jana Lange,[2] Jörg Bernhardt,[5,7] Christine Reinsch,[2] Michael Hecker,[2,5] Jörg Peplies,[8] Frank D. Bockelmann,[9] Ulrich Callies,[9] Gunnar Gerdts,[4] Antje Wichels,[4] Karen H. Wiltshire,[4] Frank Oliver Glöckner,[1,3] Thomas Schweder,[2,6]† Rudolf Amann[1]†

Phytoplankton blooms characterize temperate ocean margin zones in spring. We investigated the bacterioplankton response to a diatom bloom in the North Sea and observed a dynamic succession of populations at genus-level resolution. Taxonomically distinct expressions of carbohydrate-active enzymes (transporters; in particular, TonB-dependent transporters) and phosphate acquisition strategies were found, indicating that distinct populations of *Bacteroidetes*, *Gammaproteobacteria*, and *Alphaproteobacteria* are specialized for successive decomposition of algal-derived organic matter. Our results suggest that algal substrate availability provided a series of ecological niches in which specialized populations could bloom. This reveals how planktonic species, despite their seemingly homogeneous habitat, can evade extinction by direct competition.

Annually recurring spring phytoplankton blooms with high net primary production (NPP) characterize eutrophic upwelling zones and coastal oceans in higher latitudes. Coastal zones with water depths <200 m constitute ~7% of the global ocean surface (*1*), yet they are responsible for ~19% of the oceanic NPP (*2*) and globally account for 80% of organic matter burial and 90% of sedimentary mineralization (*1*). Heterotrophic members of the picoplankton—mostly *Bacteria*—reprocess about half of the oceanic NPP in the so-called "microbial loop" (*3*). The bulk of this bacterioplankton biomass is free-living, but up to 20% is attached to algae or particles (*4*).

The bacterial response to coastal phytoplankton blooms has been almost exclusively studied in microcosm/mesocosm experiments (*5–8*) or with limited resolution in time and biodiversity in situ (*9–11*). We observed bacterial populations during and after a phytoplankton bloom in spring 2009 at the island of Helgoland in the German Bight (54°11′03″N, 7°54′00″E; fig. S1A) with a high taxonomic and functional resolution. We sampled 500 liters of subsurface seawater twice a week during 2009. Samples were filtered into fractions dominated by free-living bacteria (3 to 0.2 μm in size) and algae/particle-associated bacteria (10 to 3 μm in size) (fig. S2). Algal composition was determined microscopically (fig. S3 and table S1), and microbial composition was identified via catalyzed reporter deposition fluorescence in situ hybridization (CARD-FISH, tables S2 and S3). At selected sampling times during and after the bloom, the data were complemented by comparative analysis of 16*S* ribosomal RNA (rRNA) gene amplicons (pyrotags, table S4) and by functional data from extensive metagenome and metaproteome analyses (table S5). In addition, physical and chemical parameters were measured daily, including temperature, turbidity, salinity, and concentrations of phosphate, nitrate, nitrite, ammonium, silicate, and chlorophyll a (table S6).

Pre-bloom bacteria (Fig. 1A) were dominated by *Alphaproteobacteria* (41 to 67%), composed roughly of two-thirds SAR11 clade and one-third *Roseobacter* clade (Fig. 1B and fig. S4B). SAR11 consisted almost exclusively of subgroup Ia (*Candidatus Pelagibacter ubique*) (table S4). This composition changed as the spring phytoplankton bloom commenced (*12*). In early April (3 to 9 April 2009), *Bacteroidetes* abundances increased fivefold within 1 week (from 1.5×10^5 to 7.7×10^5 cells/ml), whereas *Alphaproteobacteria* (from 2.1×10^5 to 5.0×10^5 cells/ml) and *Gammaproteobacteria* (from 0.8×10^5 to 1.8×10^5 cells/ml) abundances only approximately doubled. The *Bacteroidetes* consisted mostly of *Flavobacteria* (89 to 98%) (table S4), with a succession of *Ulvibacter* spp., followed by *Formosa*-related and *Polaribacter* species as the most prominent groups (Fig. 1C and fig. S4C). *Gammaproteobacteria* reacted later to algal decay, but with a more dense succession of peaking clades, with highest abundances in *Reinekea* spp. and SAR92 (Fig. 1D and fig. S4D). *Reinekea* spp. grew within 1 week from 1.6×10^3 cells/ml to above 1.6×10^5 cells/ml (estimated doubling time, 25 hours) and subsequently almost vanished within 2 weeks. *Roseobacter* clade members also showed a succession, with the NAC11-7 lineage dominating the early bacterioplankton bloom and the *Roseobacter* clade–affiliated (RCA) lineage dominating the late bloom (table S4).

Metagenomes were partitioned into taxonomically coherent bins (taxobins, fig. S5A) and then used for identification, annotation, and semiquantitative analyses of the metaproteome data (*12*). This allowed the investigation of shifts in gene content and expression within dominating bacterial populations (table S7).

[1]Max Planck Institute for Marine Microbiology, Celsiusstrasse 1, 28359 Bremen, Germany. [2]Institute of Marine Biotechnology, Walther-Rathenau-Strasse 49a, 17489 Greifswald, Germany. [3]Jacobs University Bremen, Campus Ring 1, 28759 Bremen, Germany. [4]Alfred Wegener Institute for Polar and Marine Research, Biologische Anstalt Helgoland, 27483 Helgoland, Germany. [5]Institute for Microbiology, Ernst-Moritz-Arndt University, Friedrich-Ludwig-Jahn-Strasse 15, 17487 Greifswald, Germany. [6]Pharmaceutical Biotechnology, Ernst-Moritz-Arndt University, Felix-Hausdorff-Strasse 3, 17487 Greifswald, Germany. [7]DECODON, Walther-Rathenau-Strasse 49a, 17489 Greifswald, Germany. [8]Ribocon, Fahrenheitstrasse 1, 28359 Bremen, Germany. [9]HZG Research Center, Max-Planck Strasse 1, 21502 Geesthacht, Germany.

*These authors contributed equally to this work.
†To whom correspondence should be addressed. E-mail: schweder@uni-greifswald.de (T.S.); ramann@mpi-bremen.de (R.A.)

A pronounced peak in the abundance of carbohydrate-active enzymes [CAZymes (*13*)] accompanied the bacterial succession (fig. S5B). CAZyme frequencies and expressions were taxonomically distinct (Figs. 2 and 3). For instance, *Flavobacteria* and *Gammaproteobacteria* dominated the abundant glycoside hydrolase family 16 (GH16). Most corresponding genes were annotated as laminarinases for decomposing the algal glucan laminarin. Likewise, expressed GH30-family proteins that include β-D-fucosidases mapped exclusively to *Flavobacteria*. *Flavobacteria* also dominated GH29/GH95-family genes containing α-L-fucosidases, as well as L-fucose permease genes. Fucose is a major constituent of diatom exopolysaccharides (*14, 15*). *Flavobacteria* were also dominating GH92-family glycoside hydrolases encoding mainly alpha-mannosidase, whereas *Gammaproteobacteria* dominated the glycoside hydrolase family 81. Likewise, *Gammaproteobacteria* (SAR92 clade) and *Flavobacteria* dominated expression within the GH3 family.

Many algal polysaccharides are sulfated (such as carragenans, agarans, ulvans, and fucans), and hence sulfatases are required for their complete degradation. Sulfatase gene frequencies peaked together with the CAZymes at 7 April and showed a mixed taxonomic composition, but the maximum in sulfatase expression occurred later in the bloom (Fig. 3) and was dominated by *Flavobacteria*. Expressed sulfatases were found in the *Polaribacter* taxobin, which corroborates recent reports of high numbers of sulfatases in *Polaribacter* (*16*). In contrast, glycoside hydrolases for decomposing nonsulfated laminarin (GH16, GH55, and GH117) had their expression maxima earlier during the initial algal die-off phase.

Glycolytic exoenzymes initiate bacterial utilization of complex algal polysaccharides. As a result, shorter sugar oligomers and monomers become increasingly available and allow fast-growing opportunistic bacteria with a broader substrate spectrum to grow. Differences in nutritional strategies were apparent even between taxonomic classes; for example, in the expression of transport systems for nutrient uptake (Fig. 4A).

TonB-dependent transporter (TBDT) components dominated expressed transport proteins in *Flavobacteria*, whereas adenosine triphosphate (ATP)–binding cassette (ABC), tripartite ATP-independent periplasmic (TRAP), and tripartite tricarboxylate transporters (TTT) for low-molecular-weight (LMW) substrates were expressed only at low levels (Fig. 4A). TBDTs, originally thought to be restricted to complexed iron(III) (*17*) and vitamin B12 uptake, allow uptake of compounds that exceed the typical 600- to 800-dalton substrate range of normal porins (*18, 19*). Within *Bacteroidetes*, TBDTs are often colocalized with carbohydrate degradation modules (fig. S6) (*16*, *20–22*), and thus the substrate spectrum of these transporters may be much wider than anticipated (*23*), including oligosaccharides. TBDTs constituted no less than 13% of the expressed proteins identified during the bacterioplankton bloom at 31 March but only 7% in a non bloom sample at 11 February (fig. S7). This observation highlights the importance of TBDTs and corroborates a report of high TBDT expression in a coastal upwelling zone (*24*). In high-NPP zones, the capacity to take up oligomers as soon as they become transportable may constitute a major advantage over competitors restricted to smaller substrates.

In the *Gammaproteobacteria*, SAR92 featured a similar transporter expression profile as the *Flavobacteria*, whereas *Reinekea* spp. exhibited high expression of ABC and, to a lesser extent, TRAP transporters, indicating a different nutritional strategy with emphasis on the uptake of monomers (Fig. 4A).

Likewise, *Alphaproteobacteria* showed high expression levels of ABC and TRAP transporters and low levels of TBDTs and TTTs. This reflects the ecological strategy of the dominating SAR11. The well-studied representative *Pelagibacter ubique* HTCC 1062 thrives under oligotrophic conditions by means of high-affinity ABC and TRAP transporters and a constitutively expressed energy-producing proteorhodopsin (*25–27*). Our data confirmed constitutive proteorhodopsin expression and transporter components as the most abundant expressed proteins in the SAR11 clade, which corroborates previous findings (*28*). Members of the metabolically diverse, opportunistic alphaproteobacterial *Roseobacter* clade (*29–31*) exhibited LMW transporter expression levels that exceeded those of SAR11 (Fig. 4A). Although *Roseobacter* clade cells were two to four times less abundant than SAR11, they are larger, which may explain greater *Roseobacter* transporter expression.

Multiple factors may contribute to bacterioplankton bloom termination, such as predation by flagellate protozoa, viral lysis, and nutrient depletion. Phosphate limitation can spur algal exudate production, which might serve to promote the growth of phycosphere bacteria that remineralize and acquire phosphate more effectively (*32*); however, under phosphate limitation, algae and bacteria will compete. Phosphate dropped below the detection limit early in the phytoplankton bloom (fig. S1C), and the expression of several phosphate and phosphonate ABC-type uptake

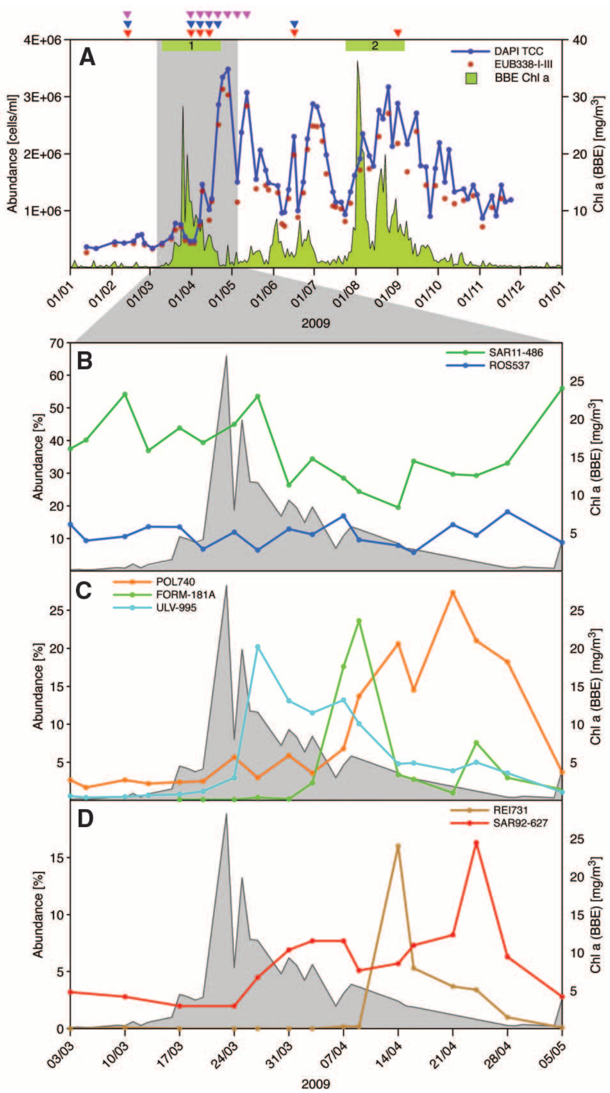

Fig. 1. Abundances of major bacterial populations during the bacterioplankton bloom as assessed by CARD-FISH. (**A**) Chlorophyll a (Chl a) concentration (measured with a BBE Moldaenke algal group analyzer), 4′,6-diamidino-2-phenylindole (DAPI)–based total cell counts (TCC), and bacterial counts (probe EUB338 I-III) during the year 2009; diatom-dominated spring blooms (1) and dinoflagellate-dominated summer blooms (2) are marked with green boxes; triangles on top mark accessory samples: metagenomics (red), metaproteomics (blue), and 16*S* rRNA gene tag sequencing (magenta). (**B**) Relative abundances of selected *Alphaproteobacteria*: SAR11 clade (probe SAR11-486) and *Roseobacter* clade (probe ROS537). (**C**) Relative abundances of selected *Flavobacteria*: *Ulvibacter* spp. (probe ULV-995), *Formosa* spp. (probe FORM-181A), and *Polaribacter* spp. (probe POL740). (**D**) Relative abundances of selected *Gammaproteobacteria*: *Reinekea* spp. (probe REI731) and SAR92 clade (probe SAR92-627). Further probes that are not shown for clarity are specified in the supplementary materials (tables S2 and S3).

Fig. 2. Abundances of CAZymes with relevance for external carbohydrate degradation. (**Left**) Copies of 20 CAZymes per megabase of metagenome sequence with class-level taxonomic classifications (*12*). Maximum abundances are highlighted in gray. (**Right**) Detailed taxonomic breakdown for four selected CAZymes showing differing taxonomic compositions; each histogram shows data for the five metagenome samples (from left to right: 11 February 2009, 31 March 2009, 7 April 2009, 14 April 2009, and 16 June 2009).

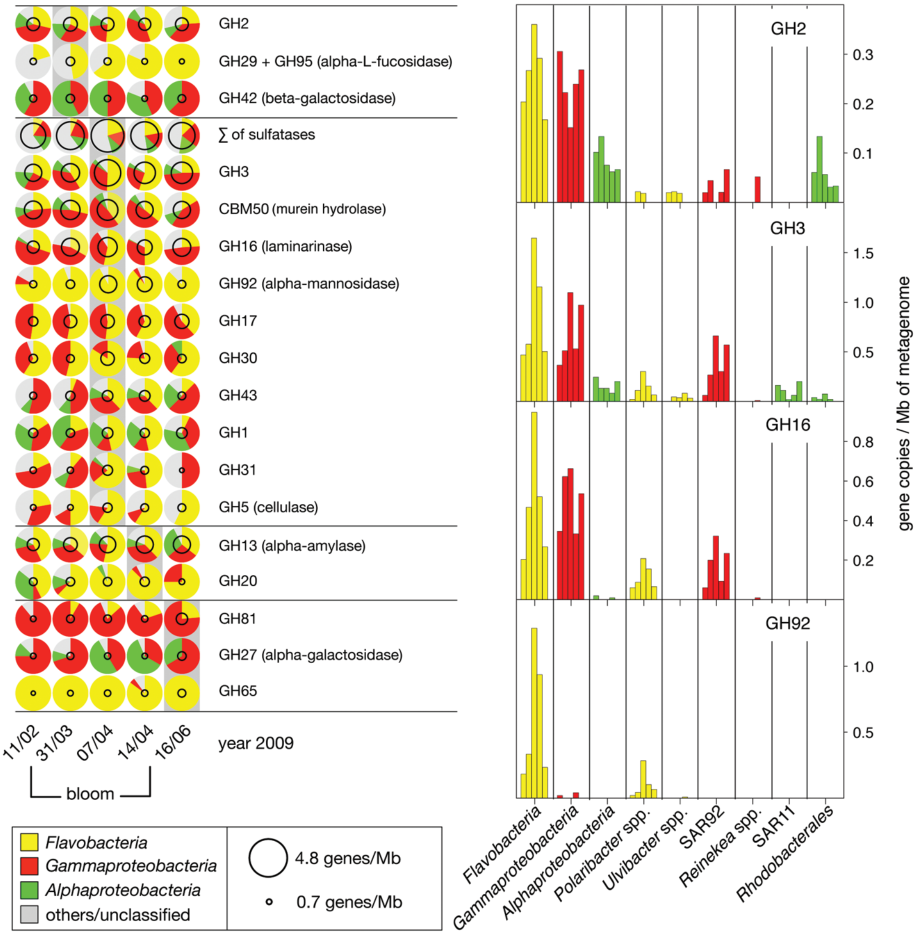

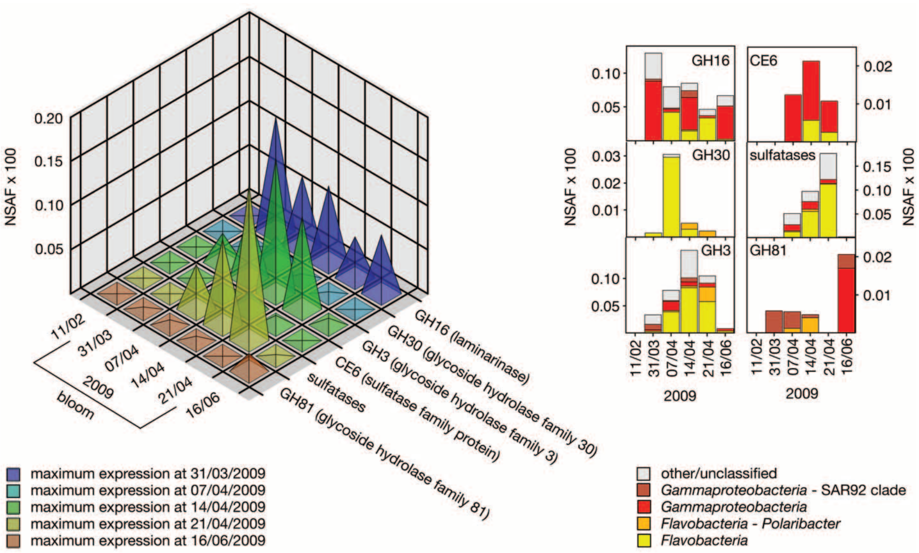

Fig. 3. Expression of CAZymes with relevance for external carbohydrate degradation; the proteome data were analyzed in a semiquantitative manner based on normalized spectral abundance factors (NSAFs) (*12*).

systems in various bacterial taxobins increased over the progression of the bloom (Fig. 4B). *Gammaproteobacteria* and SAR11 tended to use ABC-type phosphate transporters, as discovered in earlier studies (*28*), whereas flavobacterial *Polaribacter* spp. used phosphate:sodium symporters, and alphaproteobacterial *Rhodobacterales* spp. used phosphonate transporters.

In the first response to the phytoplankton bloom, flavobacterial *Ulvibacter* and *Formosa* spp. dominated (tables S2 and S4). Within these clades, TBDT components were among the proteins with the highest expression levels. This corroborates reports that specific *Flavobacteria* are tightly coupled to diatoms (*7*). *Bacteroidetes* have also been identified as major bacteria attached to marine snow (*33*, *34*), which agrees with their presumed role as fast-growing r strategists with specialization on the initial attack of highly complex organic matter (*16, 21, 35*). Hence, algal blooms lead to a multifold increase of colonization surfaces for *Bacteroidetes*, which respond with increased production of exoenzymes (*36*). After algal lysis, *Bacteroidetes* are the first to profit.

The second phase of the bacterioplankton succession coincided with a shift in algal composition (fig. S3) and was characterized by a pronounced peak of gammaproteobacterial *Reinekea* spp. that reached up to 16% of the bacteria (14 April 2009). *Reinekea* spp. featured a different expression profile, with high expression levels of transporters for peptides, phosphate, monosaccharides, and other monomers. These in situ data agree with the studies on cultured *Reinekea* species (*37–39*) that found broad generalist substrate spectra. The increase of alphaproteobacterial

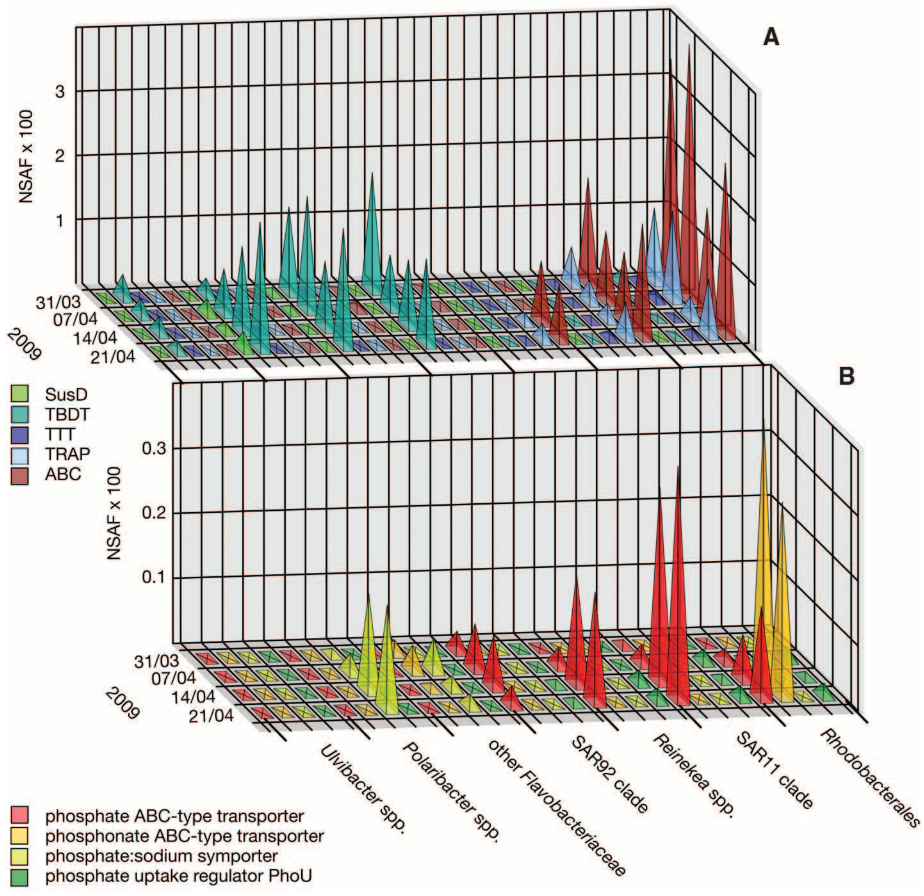

Fig. 4. Transporter components and phosphorus acquisition proteins of dominant taxa during the bacterioplankton bloom. (**A**) Expression of transporter components: starch utilization SusD-family proteins (SusD), TBDTs, TTTs, TRAPs, and ABCs. (**B**) Expression of proteins involved in phosphorus acquisition.

Roseobacter clade RCA during this phase might also be attributed to the *Roseobacter*'s opportunistic life-style (*29*) and is consistent with previous findings of free-living RCA phylotypes in the German Bight during diatom blooms (*40*).

The third phase of the spring 2009 bacterioplankton succession was dominated by flavobacterial *Polaribacter* and gammaproteobacterial SAR92 clade species, together with a secondary spike in *Formosa* spp. (Fig. 1, C and D). At this time, *Polaribacter* and *Formosa* dominated the particle/algae-attached fraction (table S8). Hence this phase with high sulfatase expression (Fig. 3) reflected another change of ecological niches (*12*).

Taken together, the bacterial response to coastal phytoplankton blooms was more dynamic than previously anticipated and consisted of a succession of distinct populations with distinct functional and transporter profiles. Thus, the diatom-induced growth of specific bacterioplankton clades most likely resulted from the successive availability of different algal primary products (bottom-up control), which provided the series of ecological niches in which specialized populations could bloom. As a result, we are now beginning to uncover the relevant predictors for defining the ecological niches of planktonic species (*41*) and thus can tackle the "paradox of the plankton" (*42*), which is how these species evade extinction by direct competition in a seemingly homogeneous habitat with limited resources.

References and Notes

1. J. P. Gattuso, M. Frankignoulle, R. Wollast, *Annu. Rev. Ecol. Syst.* **29**, 405 (1998).
2. C. B. Field, M. J. Behrenfeld, J. T. Randerson, P. Falkowski, *Science* **281**, 237 (1998).
3. F. Azam, *Science* **280**, 694 (1998).
4. F. Azam *et al.*, *Mar. Ecol. Prog. Ser.* **10**, 257 (1983).
5. J. Pinhassi *et al.*, *Aquat. Microb. Ecol.* **17**, 13 (1999).
6. L. Riemann, G. F. Steward, F. Azam, *Appl. Environ. Microbiol.* **66**, 578 (2000).
7. J. Pinhassi *et al.*, *Appl. Environ. Microbiol.* **70**, 6753 (2004).
8. J. M. Rinta-Kanto, S. Sun, S. Sharma, R. P. Kiene, M. A. Moran, *Environ. Microbiol.* **14**, 228 (2012).
9. L. B. Fandino, L. Riemann, G. F. Steward, R. A. Long, F. Azam, *Aquat. Microb. Ecol.* **23**, 119 (2001).
10. W. W. Lau, R. G. Keil, E. V. Armbrust, *Appl. Environ. Microbiol.* **73**, 2440 (2007).
11. Y. Tada *et al.*, *Appl. Environ. Microbiol.* **77**, 4055 (2011).
12. Further information is available as supplementary materials on *Science* Online.
13. B. L. Cantarel *et al.*, *Nucleic Acids Res.* **37** (Database issue), D233 (2009).
14. B. A. Wustman, M. R. Gretz, K. D. Hoagland, *Plant Physiol.* **113**, 1059 (1997).
15. V. B. Khodse, N. B. Bhosle, *Biofouling* **26**, 527 (2010).
16. P. R. Gómez-Pereira *et al.*, *Environ. Microbiol.* **14**, 52 (2012).
17. V. Braun, K. Hantke, *Curr. Opin. Chem. Biol.* **15**, 328 (2011).
18. T. K. Rostovtseva, E. M. Nestorovich, S. M. Bezrukov, *Biophys. J.* **82**, 160 (2002).
19. K. D. Krewulak, H. J. Vogel, *Biochem. Cell Biol.* **89**, 87 (2011).
20. M. Bauer *et al.*, *Environ. Microbiol.* **8**, 2201 (2006).
21. F. Thomas, J. H. Hehemann, E. Rebuffet, M. Czjzek, G. Michel, *Front. Microbiol.* **2**, 93 (2011).
22. B. M. Hopkinson, K. A. Barbeau, *Environ. Microbiol.* 10.1111/j.1462-2920.2011.02539.x (2011).
23. K. Schauer, D. A. Rodionov, H. de Reuse, *Trends Biochem. Sci.* **33**, 330 (2008).
24. R. M. Morris *et al.*, *ISME J.* **4**, 673 (2010).
25. S. J. Giovannoni *et al.*, *Science* **309**, 1242 (2005).
26. C. R. Reisch *et al.*, *Nature* **473**, 208 (2011).
27. J. Sun *et al.*, *PLoS ONE* **6**, e19870 (2011).
28. S. M. Sowell *et al.*, *ISME J.* **3**, 93 (2009).
29. M. A. Moran *et al.*, *Appl. Environ. Microbiol.* **73**, 4559 (2007).
30. T. Brinkhoff, H. A. Giebel, M. Simon, *Arch. Microbiol.* **189**, 531 (2008).
31. R. J. Newton *et al.*, *ISME J.* **4**, 784 (2010).
32. J. Tittel, O. Büttner, N. Kamjunke, *J. Plankton Res.* **34**, 102 (2012).
33. E. F. DeLong, D. G. Franks, A. L. Alldredge, *Limnol. Oceanogr.* **38**, 924 (1993).
34. D. Woebken, B. M. Fuchs, M. M. Kuypers, R. Amann, *Appl. Environ. Microbiol.* **73**, 4648 (2007).
35. J. L. Edwards *et al.*, *Genes* **1**, 371 (2010).
36. C. Arnosti, *Annu. Rev. Mar. Sci.* **3**, 401 (2011).
37. L. A. Romanenko, P. Schumann, M. Rohde, V. V. Mikhailov, E. Stackebrandt, *Int. J. Syst. Evol. Microbiol.* **54**, 669 (2004).
38. J. Pinhassi *et al.*, *Int. J. Syst. Evol. Microbiol.* **57**, 2370 (2007).
39. A. Choi, J. C. Cho, *Int. J. Syst. Evol. Microbiol.* **60**, 2813 (2010).
40. H. A. Giebel *et al.*, *ISME J.* **5**, 8 (2011).
41. S. J. Giovannoni, K. L. Vergin, *Science* **335**, 671 (2012).
42. G. E. Hutchinson, *Am. Nat.* **95**, 137 (1961).

Acknowledgments: We thank T. Hammer and T. Ferdelman for critical reading of the manuscript; M. Meiners, E. Karamehmedovic, B. Voigt, and V. Damare for sample processing; F. Ruhnau and L. Sayavedra for work on transporters; M. Zeder for automated counting; and R. Hahnke and J. Harder for help with probe testing. We are also grateful to our colleagues from the Bundesamt für Seeschifffahrt und Hydrographie for provision of operational model output. Analyses and visualizations used in fig. S1, D to F, were produced with the Giovanni online data system, developed and maintained by the NASA Goddard Earth Sciences Data and Information Service Center. We acknowledge the Moderate Resolution Imaging Spectroradiometer mission scientists and associated NASA personnel for these data. The sequence data reported in this study can be obtained from the European Bioinformatics Institute (study number ERP001227; www.ebi.ac.uk/ena/data/view/ERP001227). The German Federal Ministry of Education and Research (BMBF) supported this study by funding the Microbial Interactions in Marine Systems project (MIMAS, project 03F0480A, http://mimas-project.de).

Supplementary Materials

www.sciencemag.org/cgi/content/full/336/6081/608/DC1
Materials and Methods
Supplementary Text
Figs. S1 to S12
Tables S1 to S9
References (*43–102*)
Movie S1

22 December 2011; accepted 16 March 2012
10.1126/science.1218344

Don't Look Back in Anger! Responsiveness to Missed Chances in Successful and Nonsuccessful Aging

Stefanie Brassen,* Matthias Gamer, Jan Peters, Sebastian Gluth, Christian Büchel

Life-span theories explain successful aging with an adaptive management of emotional experiences like regret. As opportunities to undo regrettable situations decline with age, a reduced engagement into these situations represents a potentially protective strategy to maintain well-being in older age. Yet, little is known about the underlying neurobiological mechanisms supporting this claim. We used a multimodal psychophysiological approach in combination with a sequential risk-taking task that induces the feeling of regret and investigated young as well as emotionally successfully and unsuccessfully (i.e., late-life depressed) aged participants. Responsiveness to regret was specifically reduced in successful aging paralleled by autonomic and frontostriatal characteristics indicating adaptive shifts in emotion regulation. Our results suggest that disengagement from regret reflects a critical resilience factor for emotional health in older age.

There is an emerging literature showing that aging is accompanied by an increase in positive affect while negative emotions like anger decline (*1*–*3*). Motivational life-span theories propose that such emotional changes depend on adaptive shifts in emotional goals and strategies (*2*, *4*, *5*). One powerful predictor for these shifts is our subjective sense of remaining lifetime. When people perceive their time as "running out," they increasingly focus on regulating emotional states to optimize well-being (*2*). Lifelong experience with emotional situations probably facilitates the use of emotion-regulation strategies (*6*). Shifts toward emotional control strategies may also compensate for declining resources and opportunities in old age (*4*, *5*). The life-span theory of control (*4*, *5*) holds that these compensatory mechanisms lead to a reduced emotional engagement in regrets in aging. Because opportunities to undo consequences of regrettable behavior decline with age, responsiveness to regret becomes a critical factor for life satisfaction in older adults (*7*, *8*). At a young age, active attempts to overcome regretful situations may help to optimize future behavior. As people age, however, a more successful strategy may be disengagement (*5*, *7*–*9*). Regret fundamentally depends on the feeling of responsibility (*10*). Therefore, disengagement should be facilitated by an attenuated attribution of internal control. Indeed, compared to young adults, healthy elderly report lower levels of internal-control attributions, which is associated with a reduced intensity of long- and short-term regrets (*9*).

What are the psychophysiological modulators of an age-adapted management of regretful experiences in emotionally healthy aging? The experience of regret is elicited by counterfactual thoughts (*11*), that is, comparing "what is" with "what could have been." Thus, regret is typically induced by presenting people not only with the actual outcomes of their choices but also with missed opportunities (i.e., alternative outcomes that could have been obtained had the choice been different) (*12*–*15*). The influence of missed opportunities on future choices can be regarded as an indicator of regret responsiveness. A neural structure involved in regret processing is the ventral striatum, which codes the value not only of experienced rewards but also of missed opportunities (*12*, *15*–*17*) and has been suggested to modulate age-related changes in decision-making (*18*). It is densely connected to the anterior cingulate cortex (ACC) (*19*), a key player at the interface between emotion and cognition (*20*) that may regulate emotional experiences in successful aging (*21*).

We investigated the behavioral and neuronal responses to regretful events in emotionally successful aging using a sequential decision task that included feedback about alternative outcomes (Fig. 1A). On each trial, an array of eight boxes was presented, where seven boxes contained a gain ("gold") and one contained a loss ("devil"). Boxes could be opened from left to right. At any stage, volunteers could either open the next box or stop and collect the gains acquired so far in this round. Exposing the randomly distributed devil ended the trial, and all gains from this round were lost. If volunteers decided to stop and collect their gains, the position of the devil was revealed, indicating how far they could have safely continued ("missed chance").

In a functional magnetic resonance imaging (fMRI) study, 21 healthy young (mean age 25.4 years) and 20 older (65.8 years), as well as 20 late-life depressed (65.6 years) participants without cognitive deficits were scanned while playing 80 rounds of the task. Elderly participants diagnosed with late-life depression (first episode after the age of 55) were included to investigate whether the responsiveness to regret in older adults represents a resilience factor against emotionally unsuccessful aging.

We tested several predictions: (i) compared with the two other groups, emotionally healthy older adults will demonstrate a reduced behavioral response to missed opportunities; (ii) ventral striatal brain responses will differ between optimal and nonoptimal outcomes in young and depressed older subjects but not in the healthy elderly; and (iii) only emotionally healthy older adults will employ regret-limiting strategies involving cortical structures previously implicated in emotion regulation [i.e., ACC (*21*)].

Consistent with our previous findings in an independent young sample (*12*), the degree of missed chances predicted subsequent risk-taking behavior in healthy young and depressed old volunteers (Fig. 1B). Specifically, the greater the number of missed chances in the current trial, the more risk these subjects took in the next trial, despite the fact that consecutive rounds were explicitly independent. This behavioral response to missed chances was not observed in healthy

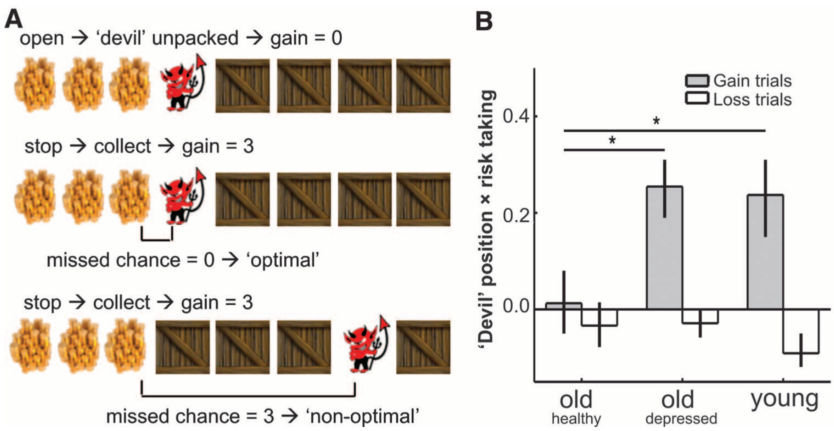

Fig. 1. (**A**) Outline of the possible choice outcomes. (**B**) Fisher *z* scores of the correlation between devil position and risk-taking in the next trial. Only in young and old depressed volunteers, the position of the devil in win trials (missed chance) predicted the risk taken in the next round ($P < 0.007$). No such effect was observed for the devil position in loss trials ($P > 0.83$), suggesting a selective influence of missed opportunities on future choice behavior. *$P < 0.05$ (two-tailed).

Department of Systems Neuroscience, University Medical Center Hamburg-Eppendorf, Hamburg, Germany.

*To whom correspondence should be addressed. E-mail: sbrassen@uke.de

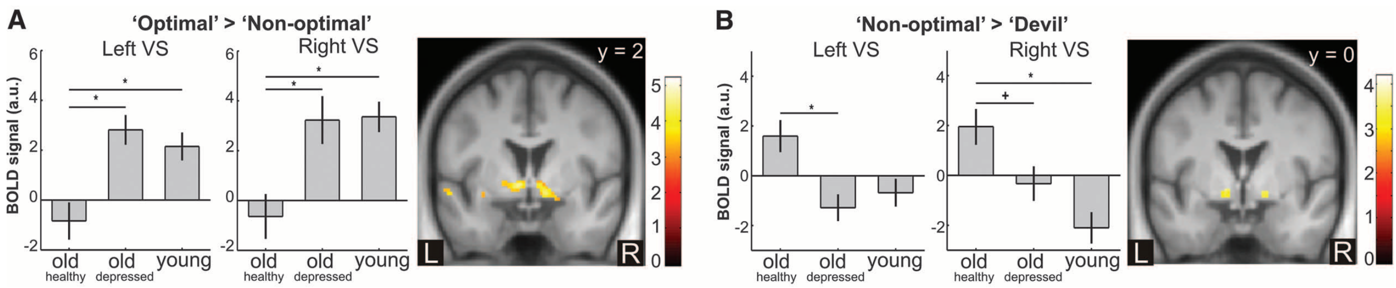

Fig. 2. Group differences in ventral striatal BOLD signal in response to missed opportunities. (**A**) As compared with healthy elderly, young and older depressed volunteers showed differential striatal responses to optimal and nonoptimal outcomes (i.e., a reduced BOLD signal during the presentation of a missed opportunity). Bar plots show contrast estimates of the peak voxel from the comparison $old_{depressed}$ + young > $old_{healthy}$ (peak coordinates *x*, *y*, *z*: –10, 0, –6, *Z* = 4.66 ; 12, 2, –10, *Z* = 4.34). (**B**) Unlike old depressed and young subjects, healthy older adults showed an enhanced striatal signal during nonoptimal win trials relative to actual loss trials (i.e., trials in which the devil was unpacked). Bar plots show the contrast estimates for the peak voxel from the comparison $old_{healthy}$ > $old_{depressed}$ + young (peak *x*, *y*, *z*: –10, 0, –6, *Z* = 3.59 ; 12, 4, –10, *Z* = 3.73). Activations are overlaid on the mean structural image of all participants (display threshold $P < 0.001$ uncorrected). $^*P < 0.05$; $^+P < 0.10$; small volume corrected for multiple comparisons.

elderly [young > $old_{healthy}$: $t(39) = 2.08$, $P < 0.05$; $old_{depressed}$ > $old_{healthy}$: $t(38) = 2.62$, $P < 0.02$]. To see whether these behavioral results were merely driven by the position of the devil, we compared the predictive value of devil position on subsequent choice behavior between gain and loss trials. Results show that our findings were limited to gain trials (Fig. 1B). Raw behavioral data are given in the supplementary materials (fig. S1A).

Enhanced responsiveness to missed chances in young and depressed old volunteers correlated with a decreased blood oxygen level–dependent (BOLD) signal in bilateral ventral striatum when a missed chance was presented (nonoptimal: missed chance > 0) compared with when there was no missed chance (optimal: missed chance = 0; tested contrast: optimal > nonoptimal, $P < 0.05_{corrected}$) (Fig. 2A). As reflected by the significant group interaction in this contrast ($P < 0.05_{corrected}$), healthy elderly showed a different pattern of ventral striatal response to missed opportunities. Similar signal increases were observed in all gain trials, regardless of whether there was a missed chance or not. Only during real loss trials (devil), the BOLD signal decreased significantly (tested contrast: nonoptimal > devil). This kind of neural differentiation between nonoptimal gains and actual losses was not observed in old depressed and young subjects ($P < 0.05_{corrected}$). Inspection of striatal signals in depressed and young subjects indicates that the signal decrease in response to nonoptimal wins was greater relative to actual loss trials (Fig. 2B and supplementary materials). Even though missed chances represent only fictive losses, they are coded similar to real losses in subcortical dopaminoceptive brain structures (*12*, *16*).

Analysis of BOLD signals in the ACC revealed further group differences in response to missed chances: As compared with young and depressed participants, healthy older adults showed an increased ACC engagement during nonoptimal relative to optimal trials ($P < 0.05_{corrected}$) (Fig. 3). This result most likely reflects the recruitment of cognitive control pro-

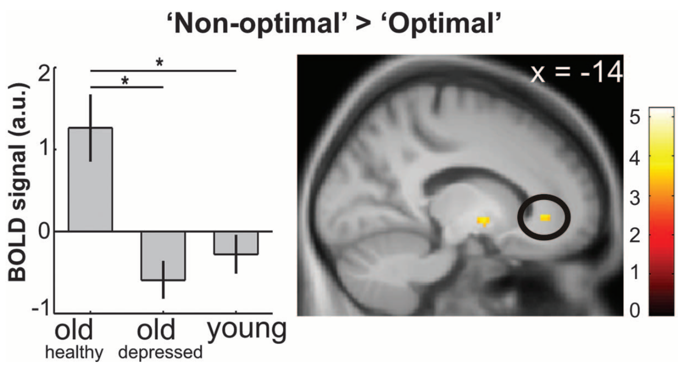

Fig. 3. Anterior cingulate activation during the presentation of missed opportunities relative to win trials without a missed chance was observed in healthy elderly but not in old depressed and young subjects. The left plot depicts the contrast estimates for the peak voxel from the comparison $old_{healthy}$ > $old_{depressed}$ + young (peak *x*, *y*, *z*: –20, 44, –4, *Z* = 4.32). Activations are overlaid on the mean structural image of all participants (display threshold $P < 0.001$ uncorrected). $^*P < 0.05$; small volume corrected for multiple comparisons.

cesses that support the regulation of regretful experiences.

After showing that only healthy older adults have a reduced regret responsiveness, in our second study we investigated how this effect is related to the emotional valuation of regret and autonomic responses. For this purpose, an independent group of 15 emotionally healthy older adults was compared with 15 newly recruited adults with late-onset depression. Volunteers performed the devil task while we recorded autonomic responses (i.e., skin conductance and heart rate). Because our paradigm likely evokes "hot" emotions of regret like anger (*22*), subjects rated how satisfied/angry they were with the current outcome and how much they regretted their last decision leading to that outcome. These ratings were given after each trial.

A positive relation between missed chances and subsequent risk-taking was observed in depressed subjects but was lacking in healthy older adults [$t(28) = 2.74$, $P < 0.01$], thus replicating the behavioral findings of the fMRI study (raw data are given in fig. S1B). Regret and anger ratings were positively correlated with the magnitude of missed chances in both groups (see supplementary materials for details). Like depressed subjects, healthy elderly were generally happier and less regretful when the missed opportunity was small. However, only in depressed subjects did the intensity of regret predict subsequent choice behavior [$t(28) = 2.42$, $P < 0.02$] (Fig. 4A). Healthy elderly were obviously able to apply counterfactual thinking during conscious ratings. However, their emotions did not affect future decisions.

Skin conductance responses (SCRs) were modulated by the presence of a missed opportunity only in older depressed participants [$t(14) = 2.43$, $P < 0.03$]. Subjects from both groups were less satisfied with nonoptimal relative to optimal outcomes, but only in depressed participants was this accompanied by a reduction in SCRs (Fig. 4B). The overall reduced SCR reactivity in these subjects replicates previous findings in depression (*23*) and thus clearly underlines the validity of our group classification. Most importantly, SCR results confirmed a further lack of differential physiological reactivity in healthy elderly to the nonoptimal outcome. Along similar lines, there was a significant group by trial type interaction regarding the discriminatory heart-rate response to missed opportunities [$F(1,28) = 4.37$, $P < 0.05$]. Inspection of the 5 poststimulus seconds indicates that this effect was mainly due to a stronger relative heart-rate decrease after nonoptimal outcomes in the depressed group

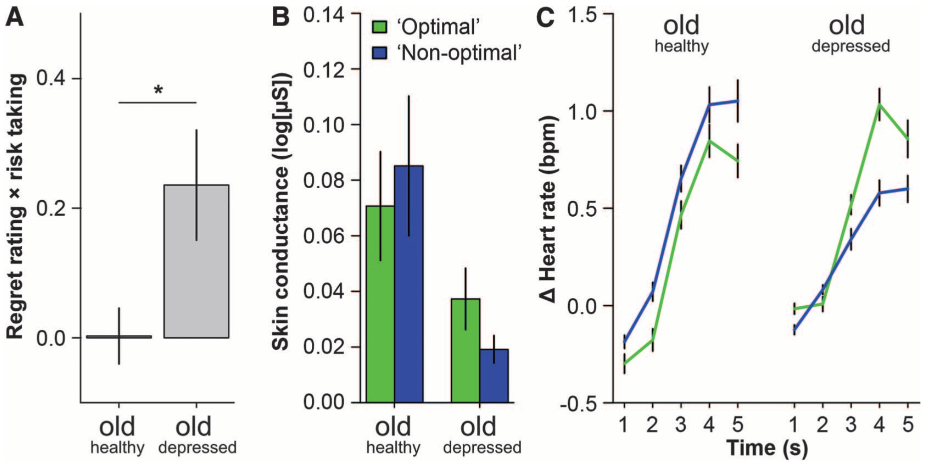

Fig. 4. (**A**) Only in depressed elderly, the regret intensity predicted subsequent choice behavior (Fisher *z* scores, **P* < 0.05, two-tailed). (**B**) A differential skin conductance response to missed opportunities was limited to depressed older adults. (**C**) There was a significant interaction of trial outcome and group on heart rate responses, mainly due to an attenuated acceleration in response to missed opportunities in depressed subjects.

(Fig. 4C). Thus, like BOLD responses, autonomic nervous system reactivity to missed opportunities discriminated successfully aged from nonsuccessfully aged subjects.

As in the fMRI study, all subjects were extensively screened for cognitive and affective functioning (see supplementary materials). Furthermore, in this second study, we characterized experiences with life regrets using a standardized interview (*8*). Here, as compared with depressed subjects, successfully aged participants reported lower emotional intensity, as well as lower intrusive thoughts associated with their life regrets (see supplementary materials).

Using a multimodal approach, our data show that emotionally healthy aging is associated with a reduced responsiveness to regretful events. Humans tend to avoid the negative feeling of regret (*11*, *24*) by changing future decision behavior. In the current study, these effects were restricted to healthy young and depressed older subjects. Importantly, the lack of such behavioral responses to fictive losses in healthy older adults had no negative effect on overall performance. Similar to other sequentially independent guessing tasks (*25*), the consideration of missed opportunities was irrelevant for performance in the independent rounds. Nonetheless, people process such fictive losses similar to real losses, reflected by a very similar neural response of dopaminoceptive brain structures like the ventral striatum (*12*, *16*). Decision-making is modulated by emotions, as indicated by changes in the autonomic nervous system (*26*). Feelings of regret and disappointment are related to changes in skin conductance (*13*) and heart rate declines in "frustrating" situations (*27*). In our study, both markers responded differentially to missed opportunities in depressed elderly who clearly demonstrated behavioral consequences of regret. All these responses were attenuated in healthy older adults, in accordance with their lack of a behavioral effect of regret on subsequent choices. When explicitly confronted with the alternative outcome, healthy elderly are able to think counterfactually. Therefore, the lack of behavioral and psychophysiological responses to regret in healthy aging is not due simply to a deficit in comparing actual with counterfactual outcomes. Recent epidemiological findings on large data sets have documented an increase in emotional well-being from middle age onward, whereas the experience of anger declines (*1*, *3*). Motivational life-span theories have assumed that focusing on positive and disengaging from negative experiences in late life depend on an active cognitive engagement (*2*, *4*, *5*). Our finding of ACC activation when healthy elderly are confronted with the negative experience of regret supports this notion and emphasizes that healthy older adults have changed compared with young and old depressed subjects. The ACC is known for its role in cognitive control of emotions and has been related to an attentional positivity bias in successful aging (*21*). We propose that healthy elderly use cognitive control strategies like external attribution (*9*) to successfully disengage from regretful experiences. For instance, it could be speculated that healthy older adults remind themselves that the devil is determined by factors they cannot influence (i.e., chance and the experimenters), whereas depressed elderly blame themselves for the outcome. Our results also indicate that a more youth-like processing of missed chances is evident in nonsuccessful aging such as late-life depression. Older depressives exhibit ACC dysfunction (*28*), and regret is related to reduced emotional well-being and depressive symptoms in aging (*7*, *8*). The lack of an age-adapted management of regret experiences may thus represent a risk factor for highly prevalent late-life depression. Disengagement from regret experiences at a point of life where the opportunities to undo regrettable behavior are limited may be a protective strategy to maintain emotional well-being and thus can be seen as a resilience factor. The ability to adapt to changes in life circumstances likely depends on several factors, including response styles (e.g., rumination versus distraction), cognitive flexibility, and lifelong emotional experience. Training these abilities using age-specific cognitive-behavioral programs might therefore be a promising approach to preserve affective health in old age.

References and Notes

1. D. G. Blanchflower, A. J. Oswald, *Soc. Sci. Med.* **66**, 1733 (2008).
2. L. L. Carstensen, *Science* **312**, 1913 (2006).
3. A. A. Stone, J. E. Schwartz, J. E. Broderick, A. Deaton, *Proc. Natl. Acad. Sci. U.S.A.* **107**, 9985 (2010).
4. P. B. Baltes, M. M. Baltes, in *Successful Aging: Perspectives from the Behavioral Sciences*, P. B. Baltes, M. M. Baltes, Eds. (Cambridge Univ. Press, New York, 1990), pp. 1–34.
5. J. Heckhausen, C. Wrosch, R. Schulz, *Psychol. Rev.* **117**, 32 (2010).
6. S. Scheibe, F. Blanchard-Fields, *Psychol. Aging* **24**, 217 (2009).
7. L. Lecci, M. A. Okun, P. Karoly, *J. Pers. Soc. Psychol.* **66**, 731 (1994).
8. C. Wrosch, I. Bauer, M. F. Scheier, *Psychol. Aging* **20**, 657 (2005).
9. C. Wrosch, J. Heckhausen, *Psychol. Aging* **17**, 340 (2002).
10. B. Mellers, A. Schwartz, I. Ritov, *J. Exp. Psychol. Gen.* **128**, 332 (1999).
11. D. Kahneman, A. Tversky, in *Judgment Under Uncertainty: Heuristics and Biases*, D. Kahneman, P. Slovic, A. Tversky, Eds. (Cambridge Univ. Press, New York, 1982), pp. 201–208.
12. C. Büchel, S. Brassen, J. Yacubian, R. Kalisch, T. Sommer, *Neuroimage* **57**, 1124 (2011).
13. N. Camille *et al.*, *Science* **304**, 1167 (2004).
14. G. Coricelli *et al.*, *Nat. Neurosci.* **8**, 1255 (2005).
15. A. Nicolle, S. M. Fleming, D. R. Bach, J. Driver, R. J. Dolan, *J. Neurosci.* **31**, 3320 (2011).
16. P. H. Chiu, T. M. Lohrenz, P. R. Montague, *Nat. Neurosci.* **11**, 514 (2008).
17. T. Lohrenz, K. McCabe, C. F. Camerer, P. R. Montague, *Proc. Natl. Acad. Sci. U.S.A.* **104**, 9493 (2007).
18. G. R. Samanez-Larkin *et al.*, *Nat. Neurosci.* **10**, 787 (2007).
19. S. N. Haber, B. Knutson, *Neuropsychopharmacology* **35**, 4 (2010).
20. K. N. Ochsner, J. J. Gross, *Trends Cogn. Sci.* **9**, 242 (2005).
21. S. Brassen, M. Gamer, C. Büchel, *Biol. Psychiatry* **70**, 131 (2011).
22. T. Gilovich, V. H. Medvec, D. Kahneman, *Psychol. Rev.* **105**, 602 (1998).
23. L. M. Bylsma, B. H. Morris, J. Rottenberg, *Clin. Psychol. Rev.* **28**, 676 (2008).
24. D. Bell, *Oper. Res.* **30**, 961 (1982).
25. J. Yacubian *et al.*, *J. Neurosci.* **26**, 9530 (2006).
26. A. R. Damasio, *Descartes' Error: Emotion, Reason, and the Human Brain* (Putnam, New York, 1994).
27. W. J. Kop *et al.*, *Biol. Psychol.* **86**, 230 (2011).
28. S. Brassen, R. Kalisch, W. Weber-Fahr, D. F. Braus, C. Büchel, *Biol. Psychiatry* **64**, 349 (2008).

Acknowledgments: S.B. is supported by the German Research Foundation (DFG, BR 2877/2-1). C.B. is supported by the Bundesministerium für Bildung und Forschung (Bernstein 01GQ0912). S.G. is supported by the DFG (GRK 1247, CINACS).

Supplementary Materials

www.sciencemag.org/cgi/content/full/science.1217516/DC1
Materials and Methods
Figs. S1 to S3
Tables S1 and S2
References (*29–36*)

6 December 2011; accepted 21 March 2012
Published online 19 April 2012;
10.1126/science.1217516

New Products: Software/Data Analysis

SEMIAUTOMATED DILUTER/DISPENSER SOFTWARE

Enhanced software for the Microlab 600 series diluter and dispensers provides important new functionality for users in many applications. A new package of compliance features for labs in regulated environments, password protection, and the ability to print documentation. These functions are tamper-evident for additional security and adhere to 21 CFR Part 11 and FDA GLP/GMP requirements. A new Configuration Wizard walks the user through the system setup, including security and method logging settings. The new Microlab 600 software, which is field-upgradable and included in all new instruments, is now available in 10 languages, adding convenience for customers worldwide. For labs that require report printing directly from the instrument, the software update integrates with a new printer accessory kit. It is also compatible with LyncStore, a PC-based log file management system that allows users to sort, filter, compare, save, and print files from any computer.

Hamilton Company

For info: 800-648-5950 | www.hamiltoncompany.com

PAPERLESS-LAB SOLUTION

Thermo Scientific CONNECTS for the Paperless Lab is a combined methodology, technology, and service offering that transforms laboratories into tightly integrated paperless environments. CONNECTS leverages existing investments in software systems, databases, and laboratory instrumentation from a wide variety of commercial vendors to bridge the islands of data generated in laboratories, transforming that data into information that can be used across the enterprise. CONNECTS is designed to enable real-time access to information and improve regulatory compliance and data integrity while helping save time and costs by automating processes and reducing manual data handling. CONNECTS for the Paperless Lab comprises three unique components—methodology, technology, and services—that, when combined, are designed to deliver seamless and continuous data flows from the lab into the enterprise to improve results analysis, enable faster decision-making, and improve productivity.

Thermo Fisher Scientific

For info: 800-395-5467 | www.thermoscientific.com/paperlesslab

GC SOFTWARE SOLUTION

The CompassCDS 3.0 software is designed for multi-instrument gas chromatograph (GC) laboratories. With its unique capacity for customization, CompassCDS provides operators with a powerful tool for a variety of analytical operations. Available as a standalone or fully networked client/server application, CompassCDS meets the broadest spectrum of customer's requirements. Designed to operate in 24/7 production environments with current Windows versions as well as with Virtualized and Citrix metaframe installations, CompassCDS controls all of the current Bruker GCs and custom analyzers manufactured for specific industrial analytical applications. CompassCDS provides operators with customizable, single-screen user interfaces that simplify day-to-day operation of GCs in routine analytical labs. Multichannel reporting, the ability to include complex custom calculations, and summary statistical reporting are all standard features. The CompassCDS product suite also includes a number of industry-focused plug-in modules for PIONA, Simulated Distillation, Detailed Hydrocarbon Analysis, Transformer Oil Gas Analysis, and Natural Gas Analysis.

Bruker Corporation

For info: 510-683-4300 | www.bruker.com/CompassCDS

GENE EXPRESSION ANALYSIS

The Ingenuity iReport for Real-Time PCR is optimized for TaqMan Gene Expression Assays. The new solution is an interactive report that extends analysis beyond C_t or fold-changes to an accurate and dynamic view of the biological information most relevant to a gene expression experiment. In contrast to time consuming manual searches for relevant publications and gene relationships, Ingenuity iReport for Real-Time PCR provides a more rapid and comprehensive understanding of pathways, processes, and diseases relevant to gene expression results. With its engaging and intuitive design, iReport for Real-Time PCR can be used by bench scientists to easily and accurately understand the biological meaning of their experiment within minutes. Peer-reviewed literature is cited throughout the report, allowing the underlying evidence to be easily accessed and referenced. iReport for Real-Time PCR has been optimized for several TaqMan Gene Expression assay formats, including TaqMan Array Card and OpenArray file types.

Ingenuity Systems/Life Technologies

For info: 650-381-5056 | www.lifetechnologies.com/ireport

LC/GC DATA MANAGEMENT

LabSolutions DB Software offers liquid and gas chromatography (LC/GC) laboratories fast and secure management for their LC/GC data. LabSolutions DB integrates a data management function with LabSolutions LC/GC control and analysis software. Optimally configured for PC-based laboratories, LabSolutions DB can be connected to up to four LC/GC instruments for simultaneous use. The integrated database is compliant with electronic records and electronic signature regulations. LabSolutions DB's project management function enables management suited to tasks and system operations. It improves the efficiency of data searches and management tasks by enabling equipment and user management, security policy, and data processing to be set on a project-by-project basis. The database allows multidata report creation using Microsoft Excel. This enables users to coordinate report creation with scheduled analyses, making it possible to quickly create reports when testing ends.

Shimadzu Scientific Instruments

For info: 800-477-1227 | www.ssi.shimadzu.com

Electronically submit your new product description or product literature information! Go to **www.sciencemag.org/products/newproducts.dtl** for more information.

Pico precision. Mega flexibility.

GeneArt® Precision TALs live up to the name.

Unlike other platforms, GeneArt® Precision TALs provide DNA-binding proteins for more precise targeting and genome editing. Target any locus in the genome. Choose your effectors and Gateway® technology–compatible vector. Your clone will typically be delivered within 3 weeks after submitting your order. For better results, start with better engineering.

See innovation at **lifetechnologies.com/TAL**

life technologies™


I seek the future.

New Products: Software/Data Analysis

SEMIAUTOMATED DILUTER/DISPENSER SOFTWARE

Enhanced software for the Microlab 600 series diluter and dispensers provides important new functionality for users in many applications. A new package of compliance features for labs in regulated environments, password protection, and the ability to print documentation. These functions are tamper-evident for additional security and adhere to 21 CFR Part 11 and FDA GLP/GMP requirements. A new Configuration Wizard walks the user through the system setup, including security and method logging settings. The new Microlab 600 software, which is field-upgradable and included in all new instruments, is now available in 10 languages, adding convenience for customers worldwide. For labs that require report printing directly from the instrument, the software update integrates with a new printer accessory kit. It is also compatible with LyncStore, a PC-based log file management system that allows users to sort, filter, compare, save, and print files from any computer.

Hamilton Company

For info: 800-648-5950 | www.hamiltoncompany.com

PAPERLESS-LAB SOLUTION

Thermo Scientific CONNECTS for the Paperless Lab is a combined methodology, technology, and service offering that transforms laboratories into tightly integrated paperless environments. CONNECTS leverages existing investments in software systems, databases, and laboratory instrumentation from a wide variety of commercial vendors to bridge the islands of data generated in laboratories, transforming that data into information that can be used across the enterprise. CONNECTS is designed to enable real-time access to information and improve regulatory compliance and data integrity while helping save time and costs by automating processes and reducing manual data handling. CONNECTS for the Paperless Lab comprises three unique components—methodology, technology, and services—that, when combined, are designed to deliver seamless and continuous data flows from the lab into the enterprise to improve results analysis, enable faster decision-making, and improve productivity.

Thermo Fisher Scientific

For info: 800-395-5467 | www.thermoscientific.com/paperlesslab

GC SOFTWARE SOLUTION

The CompassCDS 3.0 software is designed for multi-instrument gas chromatograph (GC) laboratories. With its unique capacity for customization, CompassCDS provides operators with a powerful tool for a variety of analytical operations. Available as a standalone or fully networked client/server application, CompassCDS meets the broadest spectrum of customer's requirements. Designed to operate in 24/7 production environments with current Windows versions as well as with Virtualized and Citrix metaframe installations, CompassCDS controls all of the current Bruker GCs and custom analyzers manufactured for specific industrial analytical applications. CompassCDS provides operators with customizable, single-screen user interfaces that simplify day-to-day operation of GCs in routine analytical labs. Multichannel reporting, the ability to include complex custom calculations, and summary statistical reporting are all standard features. The CompassCDS product suite also includes a number of industry-focused plug-in modules for PIONA, Simulated Distillation, Detailed Hydrocarbon Analysis, Transformer Oil Gas Analysis, and Natural Gas Analysis.

Bruker Corporation

For info: 510-683-4300 | www.bruker.com/CompassCDS

GENE EXPRESSION ANALYSIS

The Ingenuity iReport for Real-Time PCR is optimized for TaqMan Gene Expression Assays. The new solution is an interactive report that extends analysis beyond C_t or fold-changes to an accurate and dynamic view of the biological information most relevant to a gene expression experiment. In contrast to time consuming manual searches for relevant publications and gene relationships, Ingenuity iReport for Real-Time PCR provides a more rapid and comprehensive understanding of pathways, processes, and diseases relevant to gene expression results. With its engaging and intuitive design, iReport for Real-Time PCR can be used by bench scientists to easily and accurately understand the biological meaning of their experiment within minutes. Peer-reviewed literature is cited throughout the report, allowing the underlying evidence to be easily accessed and referenced. iReport for Real-Time PCR has been optimized for several TaqMan Gene Expression assay formats, including TaqMan Array Card and OpenArray file types.

Ingenuity Systems/Life Technologies

For info: 650-381-5056 | www.lifetechnologies.com/ireport

LC/GC DATA MANAGEMENT

LabSolutions DB Software offers liquid and gas chromatography (LC/GC) laboratories fast and secure management for their LC/GC data. LabSolutions DB integrates a data management function with LabSolutions LC/GC control and analysis software. Optimally configured for PC-based laboratories, LabSolutions DB can be connected to up to four LC/GC instruments for simultaneous use. The integrated database is compliant with electronic records and electronic signature regulations. LabSolutions DB's project management function enables management suited to tasks and system operations. It improves the efficiency of data searches and management tasks by enabling equipment and user management, security policy, and data processing to be set on a project-by-project basis. The database allows multidata report creation using Microsoft Excel. This enables users to coordinate report creation with scheduled analyses, making it possible to quickly create reports when testing ends.

Shimadzu Scientific Instruments

For info: 800-477-1227 | www.ssi.shimadzu.com

Electronically submit your new product description or product literature information! Go to www.sciencemag.org/products/newproducts.dtl for more information.

pXba DNA was digested with EcoRV-HF™ RE-Mix™ according to the recommended protocol. Lane L is the TriDye™ 2-Log DNA Ladder (NEB #N3270). The same results are obtained whether incubated for 5–15 minutes, 1 hour or overnight.

Blue-footed Booby (Sula nebouxii)
© Tui De Roy

Western U.S. Bioclusters:
The Pioneer Spirit

Scientists, entrepreneurs, and educators in the western U.S. bioclusters are trailblazers: energetic, enthusiastic, and optimistic. They live in hubs of creative research institutions and bold life sciences companies. As one biotech investor says, "the fear of failure here is zero." Bioclusters enliven their communities, raising scientific awareness and diversifying economic opportunities. Each western U.S. biocluster has its own history, unique personality, and distinct area of focus. Find your place in the pioneering West, whether your field is research, business, education, or global health. **By Chris Tachibana**

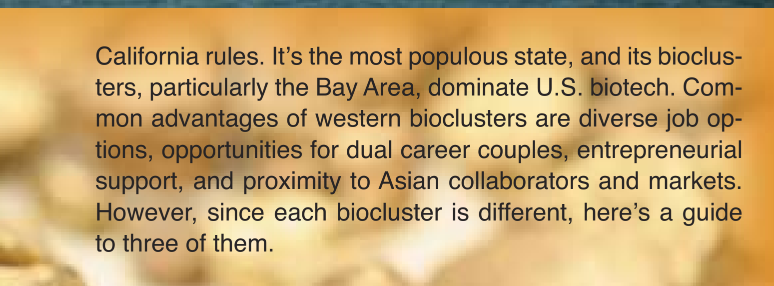

California rules. It's the most populous state, and its bioclusters, particularly the Bay Area, dominate U.S. biotech. Common advantages of western bioclusters are diverse job options, opportunities for dual career couples, entrepreneurial support, and proximity to Asian collaborators and markets. However, since each biocluster is different, here's a guide to three of them.

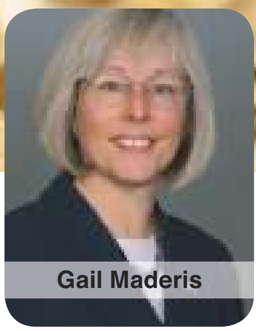

Gail Maderis

THE BAY AREA: GOLD RUSH GRANDDADDY

Los Angeles has the Rose Bowl, the granddaddy of college football contests. San Francisco has Genentech, the granddaddy of biotechnology. But the Bay Area was an entrepreneurial hub long before Genentech's founding in 1976, says **Gail Maderis,** president and CEO of BayBio, the region's life sciences industry organization. "The entrepreneurial spirit is in our culture, our history, and our DNA, starting from the risk-takers of the Gold Rush," she says. "They came to mine gold, we're now mining the genome."

Across the biotech and medtech spectrum, says Maderis, it's happening in the Bay Area: personalized medicine, stem cell therapy, molecular diagnostics, health information technology (IT), and industrial biotechnology, all supported by a strong academic environment and knowledgeable venture capitalists. And it's not just researchers and wine grapes thriving in the California climate. For every bench scientist, there are five other life science-related jobs such as patent agents, technical writers, and project managers.

If you're in the job market, Maderis has suggestions. The Bay Area has an acute shortage of certified clinical laboratory technicians. Consider going into green tech—bioremediation, biofuels, and bio-based chemicals—a field that saw 8 percent annual job growth over the last five years in California. In stem cell research, a 2004 state initiative is directing $3 billion over 10 years to regenerative medicine research. Intel, Apple, and Google all have venture funds for health IT, says Maderis, signaling potential expansion in that area, especially with the Affordable Care Act (President Obama's 2010 health care reform) promoting electronic health records and online government health services. Investors hope that health IT products will reach the market faster than drugs and devices that require a lengthy regulatory approval process.

Consumer digital health care is also growing, says **G. Steven Burrill,** founder and CEO of Burrill & Company, a San Francisco-based financial services firm for the life sciences industry. "We have seven billion people now, and six billion have a cellphone. We're going to live in a world where we spit on our BlackBerry and a microfluidics chip will do the same thing we do today in a diagnostic lab. This is how health care will be delivered." Burrill believes this revolution means big pharmaceutical companies will have a smaller impact in the future, paving the way for small, nimble biotechnology entrepreneurs.

Entrepreneurs have a home—or rather a garage—at QB3 in the Mission Bay area, a partnership of the University of California campuses of Berkeley, Santa Cruz, and San continued>

UPCOMING FEATURES

Biotech/Pharma: Navigating Mergers/Acquisitions—June 8

Diversity: Promoting New Perspectives—July 20

Annual Postdoc Survey—August 24

Bioclusters: Western U.S.

Francisco. Its incubator system, the QB3 Garage/Innovation Network, currently houses 45 startups, some in microlabs as small as 200 square feet. Director **Regis B. Kelly** says, "We're down in the weeds doing early lean startup with people who just have an idea and a credit card. Our best customers are not faculty members who already have jobs, but grad students and postdocs. We get them started at as little cost as possible." Resources are geared toward novices, such as QB3 Startup in a Box, a package of services for new entrepreneurs that includes mentoring, legal and business support, and assistance in getting small business grants. In its five years of existence, QB3 has had 10 companies graduate from the incubator, with an 80 percent success rate. QB3 also does funding through Mission Bay Capital, a seed-stage venture fund of which Kelly is a director. So far, QB3 companies have brought in $230 million in small business grants and venture funding and created about 250 jobs.

Graduate students and postdocs can take advantage of biocluster opportunities now, says Kelly, who was executive vice chancellor at the University of California, San Francisco before directing QB3. He says that 15 years ago, faculty members at Bay Area academic institutions noticed that more than half of their graduate students and postdocs were going to industry and changed their curriculum in response.

Dana Andersen benefitted from this change. He participated in Stanford University's NIH-funded graduate training program in biotechnology, including an internship at Genentech, where he is now senior director, pharmaceutical development. Seeing the contrast between academia and industry helped him refine his career goal of working on scientific problems with practical relevance, and brought him back to Genentech after postdoctoral research in Switzerland. The benefits of a biotechnology training program go beyond finding a potential job, he says. The program gave him experience in the multidisciplinary teams that are typical in life science industries. He says, "The training gave me regular meetings with people across the spectrum of biotech disciplines, and I worked with people in a lot of different fields. That's important because industry teams are highly cross-functional."

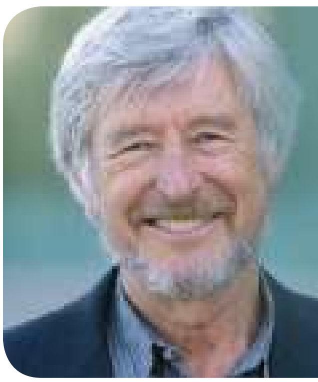

"Our best customers are not faculty members who already have jobs, but grad students and postdocs. We get them started at as little cost as possible."
—Regis B. Kelly

No matter what your role on a life sciences team, Andersen stresses the advantages of an education in science, technology, and engineering. "I run into people all the time with a science or engineering Ph.D. who are in marketing, planning, commercial analysis, project management, patent law—there are always opportunities for people with good scientific fundamentals and a technical background, at Genentech and similar companies."

Torrey Pine Trees in San Diego

SAN DIEGO: A GROWING FAMILY TREE

South of the Bay Area is the San Diego biocluster, whose history goes back not to the Gold Rush, but to a single company: Hybritech, which made monoclonal antibody-based diagnostics and therapies. Steven Burrill explains that when Hybritech was acquired by Eli Lilly in 1986, "former employees began starting other companies that emanated around Hybritech like a family tree."

One Hybritech alum with deep roots is **Abhay Kumar,** who started at Hybritech in 1992 as a research scientist. He is now associate director of corporate development at Life Technologies, a global biotechnology products, equipment and services company based in nearby Carlsbad, which he says maintains the culture of innovation that he remembers from Hybritech. San Diego still feels like a small town, he says. "When I attend a seminar, I spot dozens of familiar faces. It's sort of a reunion. The industry has grown but still has that family feel." Life Technologies is part of that family, sponsoring regional conferences and meetings and donating reagents to local school laboratories. The company hosts a global volunteer day, when the entire Life Technologies workforce worldwide does community volunteer work.

Family trees grow, and the San Diego biotech industry is now so large and diverse it's hard to keep track of, says **Duane Roth,** CEO of Connect, a regional life sciences networking organization. Connect held 300 educational and mentoring events last year and Biocom, the regional life science trade association, has nearly 500 member organizations. Despite these numbers, Roth says, the San Diego biotech community is unique for its compactness. "The Torrey Pines Basin has 81 research institutions in a three-mile radius," he says. These include the Sanford-Burnham Medical Research Institute, the Salk Institute for Biological Studies, the Scripps Research Institute, and the University of California, San Diego (UCSD). "You can almost walk across the street to meet with continued>

ALLEN INSTITUTE *for* BRAIN SCIENCE

Fueling Discovery

INVESTIGATOR POSITIONS
Apply by June 29, 2012

New initiatives. Big science. Unique opportunities.

The Allen Institute for Brain Science is embarking upon a large-scale experimental and computational effort to study coding in the visual cortex, and its associated satellite structures, in behaving mice. This effort is intended to uncover fundamental principles of brain function and yield publicly shared data, new tools and technologies that will further accelerate progress across the global research community.

To further these efforts, we are seeking a group of exceptional Investigators with experience equivalent to an assistant or associate professor at a first-class research university. The areas in which we seek to recruit include:

- neuroanatomy with light or electron microscopy
- cell type specific gene expression profiling
- recombinant viruses for gene delivery or anatomical tracing
- *in vivo* calcium imaging and optogenetics
- *in vitro* and *in vivo* electrophysiology
- rodent behavior
- biophysically accurate neuronal modeling
- large scale modeling of the visual system
- machine learning applied to neurobiological data
- Bayesian modeling

Requirements include a Ph.D. or M.D. in a relevant scientific, engineering, or medical field; a minimum of 2 years of post-doctoral work; a strong record of published research; and a commitment to collaborative team science.

To apply: Please submit a cover letter, CV and at least two letters of recommendation via our website at **http://alleninstitute.org/about_us/careers.html**. Applications must be received by **June 29, 2012** for consideration.

Suitable candidates will be invited to a recruiting symposium that will take place July 25-27, 2012 at the Allen Institute for Brain Science in Seattle, Washington. Participating candidates will give a brief talk on their work and interview with Allen Institute staff.

About the Allen Institute
The Allen Institute for Brain Science, located in Seattle, Washington, is dedicated to accelerating understanding of how the human brain works in health and disease. Using a team science approach, we generate useful public resources, drive technological and analytical advances, and discover fundamental brain properties through integration of experiments, modeling, and theory. For more information, visit **www.alleninstitute.org**. To explore our online public resources, visit the Allen Brain Atlas data portal at **www.brain-map.org**.

The Allen Institute for Brain Science is an Equal Opportunity Employer.

UNIVERSITY OF CALIFORNIA
UC RIVERSIDE

Health ▪ Sustainability ▪ Policy ▪ Technology

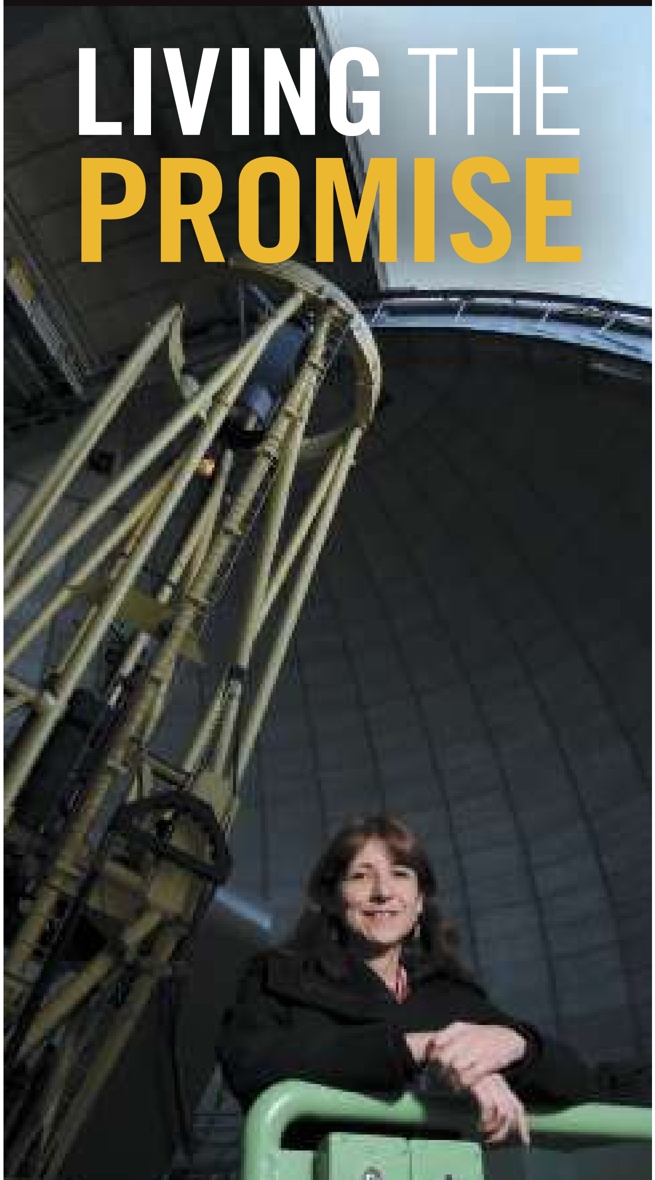

Breakthrough Research

Galaxy quest: UCR astronomers explore the universe and study the role of black holes in galaxy formation.

Explore more technology impacts
promise.ucr.edu

Bioclusters: Western U.S.

Mary Walshok

your external collaborators," says Roth. "We're all right on top of each other." Moving into the neighborhood in 2013 is a new building for the J. Craig Venter Institute for research on human and microbial genomics and synthetic biology.

Common roots, close proximity, and networking have resulted in stellar collaborations. An example is the Sanford Consortium for Regenerative Medicine, part of the state's stem cell research efforts, which required coordination between Salk, Scripps, Sanford-Burnham, UCSD, and the La Jolla Institute for Allergy and Immunology. "They got together to put up one building for scientists from five different organizations to work together," says Roth. "That's the kind of thing we're able to do here."

The San Diego life sciences industry is influenced by the local military base and wireless communications industry, says Roth, making wearable, wireless health sensors a growing field in San Diego. Like health IT, these fit national priorities to reduce health costs, allowing patient monitoring outside of hospitals, and creating opportunities for cost-saving preventive medicine.

Mary Walshok, UCSD associate vice chancellor of public programs, says interaction between local technology experts and business leaders to address national needs shows how San Diego is an innovation ecosystem. This includes academic institutions such as UCSD and San Diego State University, whose faculty enter research partnerships with industry and whose graduates provide businesses with educated employees. In turn, local biotech expands the job market, and gives universities insights into future technologies to guide the curriculum, especially for continuing education. Walshok is also UCSD dean of extension, which has 57,000 enrollees annually in practical programs such as clinical trials management and biotechnology production. She says these are "bridges to tech jobs—they respond directly to life science industry needs, helping mid-career adults retool their skills or new graduates gain the training they need for a job not only in biotech but in areas like marketing, management, and international trade."

Walshok, who has been involved in the San Diego technology culture for four decades, says the local innovation ecology includes the general public. "Industry and academia are connected to the larger community and our presence raises the public appreciation of science and understanding of the value of research."

SEATTLE: GOING GLOBAL

The core strengths of the Seattle biocluster also stem from its history, but the story is different from the California Gold Rush or the Hybritech family tree. Successful bone marrow transplantation was developed at Fred Hutchinson Cancer Research Center, so Seattle is strong in medical therapies,

Featured Participants

BAY AREA

Baybio
www.baybio.org

Burrill & Co
www.burrillandco.com

Genentech
www.gene.com

QB3
www.qb3.org

Stanford University
www.stanford.edu

University of California, San Francisco
www.ucsf.edu

SAN DIEGO

Connect
www.connect.org

Life Technologies Corporation
www.lifetechnologies.com

University of California San Diego
www.ucds.edu

SEATTLE, WASHINGTON

Novo Nordisk
www.novonordisk.com

Washington Biotechnology and Biomedical Association
www.washbio.org

Washington State University
www.wsu.edu

OTHER AREAS

Deloitte LLP
www.deloitte.com

Mt. Ranier near Seattle

devices, and health research. "Three of 21 drugs approved by the FDA in 2010 were discovered and developed in Seattle," says **Chris Rivera,** president of the Washington Biotechnology & Biomedical Association, the Washington State life science trade association. The University of Washington has a top medical school, nearby Bothell is a medical development and manufacturing hub, and Lee Hood's Institute for Systems Biology leads in personalized medicine.

Seattle has two new research centers funded by international pharmaceutical giant Novo Nordisk, known for insulin formulations and delivery systems. In 2009, the company opened an Inflammation Research Center investigating conditions such as chronic inflammatory bowel disease and rheumatoid arthritis. These are autoimmune diseases, so in summer 2012, Novo Nordisk is opening a complementary research center for type 1 diabetes, also an autoimmune condition. Eventually the two centers,

Chris Rivera

housed together in the South Lake Union neighborhood, will have over 100 employees. Novo Nordisk Chief Scientific Officer **Mads Krogsgaard Thomsen** says, "If we hit our milestones—our intention with type 1 diabetes is two projects in clinical trials in the first five years—we're willing to expand."

Novo Nordisk began autoimmunity research because of the company's expertise in therapeutic proteins and chronic conditions with injected therapies, says Thomsen. Seattle was chosen because the company had a connection to Zymogenetics in the 1980s, and the city has the Benaroya Research Institute studying autoimmune diseases and an autoimmune therapy success story in ENBREL from Immunex (acquired by Amgen in 2002). Thomsen says, "Type 1 diabetes research is part of our vision. Our scientists helped discover that it's an autoimmune disease and we're perceived as a diabetes leader, so we needed to do something about type 1."

Many bioclusters have outstanding research and development, though. A unique feature of the region, says Rivera, is that outside of Geneva, Switzerland, home of the World Health Organization, Seattle has the world's highest concentration of global health institutions. Besides the Novo Nordisk research centers, South Lake Union has Seattle Biomed, a nonprofit infectious disease research institute; PATH, an international global health organization; and the Bill & Melinda Gates Foundation, the global health and development philanthropy directed by the family of the Microsoft cofounder, Bill Gates, and the businessman Warren Buffett.

The global health focus extends 300 miles east of Seattle, to Washington State University. There, a $25 million Gates Foundation grant contributed to a new building for the Paul G. Allen School for Global Animal Health, named for the other Microsoft founder who contributed $26 million to the enterprise. Research focuses on livestock diseases that impede economic progress in developing countries, and the 70 percent of human infectious diseases that are transmittable from animals to humans, such as influenza.

Graduate programs at the Allen School for Global Animal Health include a traditional infectious disease and immunology degree, and an interdisciplinary option that reflects a broader goal, expressed by **Guy Palmer,** the school's director. "We see human health as including human equity and opportunity and having economic resources," he says. The interdisciplinary degree encourages students to explore science implementation and policy, and become social entrepreneurs, for example, developing both effective vaccines and sustainable programs to introduce them into low-income countries. The school, which is less than 10 years old, plans to grow to more than 100 graduate students by 2020. Half of the current 35 students are international. Many are scientists and veterinarians who will take their new expertise to their home country. On the dry, eastern side of the Cascade Mountains, Palmer says the School for Global Animal Health is connected to the drizzly Seattle biocluster in western Washington through partnerships with its infectious disease institutes and a complementary relationship to the biotech sector. With a focus on animal vaccines and health, says Palmer, "we fit into a different but related market sector."

AWAY FROM THE EPICENTERS

The biocluster epicenters of San Francisco, San Diego, and Seattle offer the excitement of a high concentration of people with common interests, professions, and goals. However, opportunities—and sometimes a lower cost of living— are found nearby, at Washington State University, or in California at UC Irvine, a hub for medical devices, or UC Davis, with expertise in agricultural biotechnology. **Matthew Hudes,** U.S. managing principal, biotechnology for Deloitte Consulting, says the Bay Area biocluster extends to San Jose and Santa Cruz, and Orange County has a significant medtech industry. "There are tremendous pockets of innovation across California," he says, "And a great deal going on at Oregon Health & Science University. These all have different characters and that diversity is important for the future of science." Another area to watch is the University of Utah. Its successful startup initiation program could seed a local biocluster.

You can tap into the western U.S. biocluster energy from anywhere. Gail Maderis advises scientists to get experience in managing outside contractors, especially in another city or country. Working with someone across the globe to design protocols and interpret data is a valuable skill with the growth in international collaborations and outsourcing. For now, however, a western biocluster is still the best place for a life sciences trailblazer to explore new territory. Even a true believer in cloud connections like Steven Burrill says, "I still have to go see people. Personal relationships are important and nothing is better than being in the Bay Area where you have everything around you."

Chris Tachibana is a science writer based in Seattle, USA, and Copenhagen, Denmark.

DOI: 10.1126/science.opms.r1200118

CREDIT: WASHINGTON STATE UNIVERSITY


CHINA RETURNEES
我想你 (I MISS YOU)
HEAD BACK TO CHINA NOW WITH LIFE TECHNOLOGIES.
A lot has happened since you've been away. Your mother turned 70. Your sister graduated from college. Your nephew took his first steps. Your China has transformed from a third world country to a world-class economy. And Life Technologies, the world's most innovative biotechnology company formed with the merger of Applied Biosystems and Invitrogen, is growing fast in China. So now there's no reason to keep missing out on the chance to be closer to your family and to be part of a team that makes science easier and life better everyday.
For more information, visit lifetechnologies.com/careers/cn
life technologies™
Invitrogen™
Applied Biosystems®
Gibco®
Molecular Probes®
Novex®
TaqMan®
Ambion®
Ion Torrent™

THE UNIVERSITY OF TEXAS
MD Anderson ~~Cancer~~ Center
Making Cancer History®

Department of Leukemia, Division of Cancer Medicine

Guillermo Garcia-Manero, M.D.
Department of Leukemia
The University of Texas
MD Anderson Cancer Center
1515 Holcombe Boulevard, Unit 428
Houston, Texas 77030

The Department of Leukemia provides expertise in the design, conduct and analysis of clinical and laboratory research projects; independently designs and executes the analyses of a broad range of biomedical research projects in leukemogenesis, biologic pathways and therapy; and prepares manuscripts for peer review, presents research results at national and international meetings, and prepares grant applications to support research.

The faculty member will plan, develop and prepare research projects to further develop and refine their area of expertise and to integrate this expertise with others in the laboratories of the Leukemia Department; will submit research proposals/grants for internal and external funding; and will perform other related scientific duties in the scope of the position as required. The successful candidate must be able to understand and respond to telephone conversations with physicians and members of the administrative staff, both within and outside the institution; and must be able to work within a context of very intense interpersonal relationships, including peers, physicians, patients and subordinates.

Requirements include a Ph.D. in a basic science or related field and two years in postgraduate training. The desired applicant should have experience in grant preparation and a prior record of successful funding for research.

Interested applicants should send a copy of their updated CV, bibliography, research synopsis and five professional references to: Guillermo Garcia-Manero, M.D., Department of Leukemia, 1515 Holcombe Boulevard, Unit 428, Houston, Texas 77030.

MD Anderson Cancer Center is an equal opportunity employer and does not discriminate on the basis of race, color, national origin, gender, sexual orientation, age, religion, disability or veteran status except where such distinction is required by law. All positions at The University of Texas MD Anderson Cancer Center are security sensitive and subject to examination of criminal history record information. Smoke-free and drug-free facility.

SCHOOL OF MEDICINE
INDIANA UNIVERSITY

FACULTY POSITION IN CHEMICAL BIOLOGY AND DRUG DISCOVERY

The Department of Biochemistry and Molecular Biology and IU Melvin and Bren Simon Cancer Center invite applications for a Tenure-Track Faculty Position at ALL RANKS. We are seeking innovative, energetic and collaborative individuals with strong expertise in chemical biology and drug discovery. Candidates with background in synthetic and medicinal chemistry are especially encouraged to apply. Successful applicants are expected to develop a strong, independent and extramurally funded research program addressing important problems in cancer biology and therapeutics. In addition, the selected candidate will be part of a dynamic and collaborative program at the interface of chemistry and biology to promote interdisciplinary and translational activities that directly impact therapeutic development. The state-of-the-art facilities at Indiana University School of Medicine house expertise in X-ray crystallography, proteomics, high-throughput small molecule screening, pharmacokinetics and in vivo therapeutic evaluation. Highly competitive salary, start-up funds and laboratory space will be provided. Applicants must have a Ph.D., M.D. or equivalent degree, post-doctoral experience, and clear evidence of research productivity. The search committee will begin consideration of applications immediately and continue until the position is filled.

Applicants should submit curriculum vitae, a brief summary of past accomplishments and future research plans, along with the names and email addresses of at least three references electronically to: **biomjobs@iupui.edu** please refer to **job number 12075** or by mail to:

Dr. Zhong-Yin Zhang, Professor and Chair
c/o Patty Dilworth
Department of Biochemistry and Molecular Biology
Indiana University School of Medicine
635 Barnhill Drive, MS 4053
Indianapolis, IN 46202-5122

Indiana University is an Equal Opportunity/Affirmative Action Employer, Educator and Contractor, M/F/D.

Georgia Health Sciences University
1828
College of Dental Medicine

Department Chair, Oral Biology
Reference #6143

The Georgia Health Sciences University College of Dental Medicine seeks candidates for a full-time Chair position appointed at the rank of Professor to its Department of Oral Biology. Applicants must possess a professional doctoral degree (PhD or equivalent degree, with post-doctoral experience and/or DDS, DMD or MD degrees). Applicants will have active extramural research funding and a strong track record of independent research that integrates well with craniofacial biology and medicine. Funding through NIH/NIDCR or similar federal agency is preferred. Preference will be given to applicants who have a research program in one or more of the following areas: regenerative medicine, cancer, oral/systemic health connections, immunology/microbiology, and/or public health.

The Chair will work closely with College of Dental Medicine faculty to enhance collaborations with other Georgia Health Sciences University Institutes/Centers/Special Units such as the Regenerative and Reparative Medicine and Cancer Institutes, and the Vascular Biology and Immunotherapy Centers.

A competitive salary package, commensurate with experience and academic qualifications is available. Applicants should send a letter of interest, a curriculum vitae and a list of three references to: **Dr. Christopher W. Cutler, Professor and Chairman, Department of Periodontics, 1120 15th Street, GC-1335, Georgia Health Sciences University College of Dental Medicine, Augusta, GA 30912; chcutler@georgiahealth.edu**.

AA/EEO/Equal Access/ADA Employer.

Group leader positions at the *Imagine* Institute of Genetic Diseases

imagine
INSTITUTE OF GENETIC DISEASES

The *Imagine* Institute of Genetic Diseases, based on the Necker Enfants malades Hospital campus in the heart of Paris, is inviting applications for group leader positions.

Imagine is an interdisciplinary research center with excellent core facilities for genomics, cell imaging, flow cytometry, bioinformatics, pathophysiology and animal housing for transgenic mice and zebra fish. The new tailor-made building (due to open in 2013) will offer cutting-edge research facilities.

Imagine is affiliated with Paris Descartes University, the INSERM national institute for medical research and the Paris Public Hospitals Group (Assistance Publique-Hôpitaux de Paris). It has recently been designated by the French government as a University Hospital Institute (Institut Hospitalo-Universitaire, IHU) supported by a Foundation. The Institute focuses on rare diseases, their genetic architecture and life-long outcomes. Imagine intends to address unmet basic and clinical research questions related to rare diseases, in order to increase knowledge in a major medical field that is currently insufficiently covered. This will result in the development of new biological concepts, diagnostic tools and innovative therapeutics. *Imagine* has a tradition of high-quality research and provides an outstanding, international research environment and a well-regarded graduate program. The Institute is currently composed of 250 staff members from 23 labs in the fields of immunology, infectious diseases, hematology, nephrology, developmental defects, metabolic diseases/encephalopathy, dermatology and gastroenterology. Applications can focus on any field related to the basis, pathophysiology and treatment of genetic diseases, with special emphasis on **development** (The Liliane Bettencourt Chair for developmental biology), **stem cells**, **computational biology** and **neuroscience**.
Appointments will be made at a junior or senior level, depending on experience.

Applications should be submitted to Professor Alain Fischer at the address below and must include:

- a full CV, including a list of publications
- past and current research interests (2 pages)
- future research proposals (5 pages)
- letters of recommendation by referees (3 pages in all) should be submitted with the application.

Further information can be found at **www.fondationimagine.org**

Address: **newgroups@fondationimagine.org -** Applications must be received by **September 14th, 2012**.

Imagine Institute, 156 rue de Vaugirard – 75015 Paris - France

---

EUMETSAT is the European satellite agency for monitoring weather and climate. Bringing together the resources of 26 Member States, we develop and operate a range of satellite systems surveying the atmosphere, land and ocean that deliver vital data 24 hours a day, 365 days a year. Our data contribute to weather forecasts that protect lives and property across Europe. EUMETSAT is now embarking on new and challenging satellite development programmes, shaping its long-term future.

Meteorological/Remote Sensing Scientist

Darmstadt, Germany (Four-year fixed term contract with the possibility of renewal)

Joining us with deep understanding of the physics of radiative transfer and applications to remote sensing, you will drive our development and deployment of optical imaging satellite instruments. Operating within a matrix structure, you will interact constantly with users of satellite data to enhance meteorological products extracted from observance of EUMETSAT Polar System/Metop satellites and to realise concepts for our Polar System – Second Generation, whilst building close relationships with partners in other agencies and industry. In particular, you will embed new scientific knowledge into prototype software, specify new operational product processors, undertake radiative transfer modelling and develop methods to calibrate visible and near-infrared satellite measurements.

Qualified to degree level in Meteorology, Atmospheric Physics or a related discipline, you will bring broad experience of physical remote sensing in the optical spectrum. This will have given you proven ability to initiate and lead scientific studies, support engineering colleagues and draft technical documents, and you should combine familiarity with meteorological satellite data with a good command of English and a working knowledge of French.

Attractive employment conditions are offered, in terms of salary, comprehensive benefits including health and social welfare provision, and extensive relocation assistance if applicable.

To learn more and apply online, please visit **www.eumetsat.int**

Closing date: 3 June 2012 (Ref: 12/06).

EUMETSAT is committed to providing an equal opportunities work environment for men and women and is seeking to recruit nationals from its Member States. Please see our website for further details.

Member States: Austria, Belgium, Croatia, Czech Republic, Denmark, Finland, France, Germany, Greece, Hungary, Ireland, Italy, Latvia, Luxembourg, The Netherlands, Norway, Poland, Portugal, Romania, Slovakia, Slovenia, Spain, Sweden, Switzerland, Turkey and the United Kingdom

EUMETSAT

LMU LUDWIG-MAXIMILIANS-UNIVERSITÄT MÜNCHEN

FACULTY OF CHEMISTRY AND PHARMACY

The **Faculty of Chemistry and Pharmacy** of the Ludwig-Maximilians-Universität München (LMU) invites applications for a

Full Professorship (W 3) of Molecular Biosystems

(6 years/tenure track)

commencing as soon as possible.

The successful candidate will represent the emerging field of molecular biosystems in research and teaching. He/she will be located on the campus Großhadern/Martinsried in the southwest of Munich, and will be affiliated with the LMU Gene Center, Department of Biochemistry, Faculty of Chemistry and Pharmacy, and the new Research Center for Molecular Biosystems.

The successful candidate will play a key role in the quantitative and mechanistic investigation of biological systems, and will complement and extend existing research activities in Munich. The newly appointed professor will have a strong, biomedically relevant and internationally visible research program in the broad area of genomic and cellular regulation and deregulation, preferably in higher eukaryotes. He/she will be active in the development of quantitative experimental and theoretical methods to describe biological systems. Active participation in local research networks such as national clusters of excellence in research, research network grants, and international graduate schools is desirable.

Prerequisites for this position are a university degree, a doctoral degree, teaching skills at university level, additional academic achievements and a productive and promising research program.

The initial appointment will be for six years. After a minimum of three years it may be converted to tenure pending a positive evaluation of the candidate's aptitude for teaching and research as well as the candidate's pedagogical and personal aptitude if all legal conditions are met. In exceptional cases involving candidates with outstanding qualifications who have already established an active research group, a tenured position may be offered from the outset.

Candidates for this position should be aged 51 or under at the time of appointment. Exceptions thereto may be considered in the case of outstanding candidates.

The LMU is an equal opportunity employer and aims to increase the number of female faculty members. Therefore, female candidates are explicitly encouraged to apply for this professorship. The LMU supports dual career couples. Information concerning equality of treatment may be obtained from the women's representative of the faculty (Martina.Rueffer@cup.uni-muenchen.de). Disabled candidates with essentially equal qualifications will be given preference.

Please submit your application comprising a letter of motivation, curriculum vitae, a short research summary and proposal, a summary of teaching experience, and a list of publications and invited lectures as a single pdf-file and in printed form to the **Dean of the Faculty of Chemistry and Pharmacy, Ludwig-Maximilians-Universität, Butenandtstr. 5-13, 81377 Munich, Germany, email: Dekanat@cup.uni-muenchen.de,** no later than **30 September 2012.** Informal enquiries may be sent to Prof. Patrick Cramer, email: cramer@genzentrum.lmu.de.

ETH

Eidgenössische Technische Hochschule Zürich
Swiss Federal Institute of Technology Zurich

Professor of Quantitative Imaging

The Department of Biology (D-BIOL) at ETH Zurich invites applications for a professorship in the area of Quantitative Imaging.

Candidates are expected to build a research programme focussing on the imaging of dynamic cellular and molecular processes. They may combine quantitative wet-lab experiments with mathematical simulation and modeling, or address the underlying biophysics, nanomechanics, biochemistry, and spatio-temporal control of cell function. Candidates with a strong focus in the development and usage of biosensors, image analysis and innovative imaging approaches are encouraged to apply. The professorship will ideally be installed in the Institute of Biochemistry, taking advantage of its strengths in light microscopy and its close vicinity to the light- and electron microscopy facilities (LMSC/LMC-RISC and EMEZ). She or he will be expected to teach undergraduate level courses (German or English) and graduate level courses (English).

Major strategic areas of the Department of Biology include cell- and molecular biology, systems biology, and molecular health sciences. Together with Life Science Zurich, the Department offers outstanding opportunities to participate in interdisciplinary research programmes and to establish close interactions with the local community through the Centre for Advanced Imaging (CIMST) and Systems Physiology of Metabolic Diseases (SPMD), Neuroscience Zurich, the National Centre for Competence in Research "Neural Plasticity and Repair", and the SystemsX.ch initiative.

Please apply online at **www.facultyaffairs.ethz.ch**. Your application should include your curriculum vitae, a list of publications, and a detailed research plan. The letter of application should be addressed **to the President of ETH Zurich, Prof. Dr. Ralph Eichler. The closing date for applications is 15 August 2012**. ETH Zurich is an equal opportunity and affirmative action employer. In order to increase the number of women in leading academic positions, we specifically encourage women to apply. ETH Zurich is further responsive to the needs of dual career couples and qualifies as a family friendly employer.

UCL Division of Biosciences

Research Department of Neuroscience, Physiology & Pharmacology and the Institute of Structural & Molecular Biology (ISMB)

Lecturer/Senior Lecturer in Structural Neuroscience

We are seeking a full-time Faculty member to fill a new Lectureship/Senior Lectureship to be held jointly between the Research Department of Neuroscience, Physiology and Pharmacology (NPP) and the Institute of Structural and Molecular Biology (ISMB) in the area of Structural Neuroscience of Receptors and Ion Channels.

We are interested in promising candidates working at the interface between neuroscience and structural biology, an area we wish to significantly expand. Teaching undergraduates and postgraduates in the fields of Pharmacology, Neuroscience and Structural Biology is an integral part of this post.

NPP and ISMB have been consistently rated in the top category of research (5*A or World leading) in all RAEs held to date. Our research is centred on the molecular neuroscience and structural biology of receptors and ion channels. We are strongly committed to an expansive research programme in this area and are able to offer newly refurbished space integrated on the Bloomsbury campus.

The salary range will be £39,818 - £46,972 per annum (Grade 8); £51,052 - £55,512 per annum (Grade 9), inclusive of London Allowance.

The successful candidate must hold a PhD in a relevant subject area and should show clear promise of excellence in structural neuroscience research and sufficient vision to sustain an active research programme. Of importance, they should be committed to interdisciplinary research in a multidisciplinary environment.

For further details about the vacancy and how to apply online please go to http://www.ucl.ac.uk/hr/jobs/ and search on Reference Number 1247299.

Please include a CV with three named referees and a one page research plan with your application.

Applicants can informally discuss this position with Professor Trevor Smart (t.smart@ucl.ac.uk ; Tel no. 020-7679-2013) and Professor Gabriel Waksman (g.waksman@ucl.ac.uk ; Tel no. 020-7631-6833). Further information about the Departments, UCL and associated specialist hospitals can be found at http://www.ucl.ac.uk/npp and http://www.ismb.lon.ac.uk/

If you have any queries regarding the application process, please contact Jeremy Guyer, email: jeremy.guyer@ucl.ac.uk .

We particularly welcome female applicants and those from an ethnic minority, as they are under-represented within University College London at this level.

Closing Date: 25th May 2012.

UCL Taking Action for Equality

POSITIONS OPEN

UIC Center for Cardiovascular Research
COLLEGE OF MEDICINE

TENURE-TRACK FACULTY POSITION
Center for Cardiovascular Research
University of Illinois at Chicago College of Medicine

The University of Illinois at Chicago (UIC) Center for Cardiovascular Research (CCVR) and Department of Medicine, Section of Cardiology seek outstanding tenure-track faculty candidates holding expertise in key areas of metabolism and cardiovascular science with research interests in translational or clinical research. Appointments will be made at the **ASSISTANT** or **ASSOCIATE PROFESSOR** level, commensurate with experience and qualifications.

Successful candidates will hold independent, extramural support for their own research and be able to lead comprehensive and innovative research addressing the metabolic basis of heart disease, with general emphasis in the areas of heart failure, hypertension, diabetes, obesity, or metabolic syndrome.The appointment also will include clinical activities within the Section of Cardiology.

The minimum degree requirement is an M.D. degree with three or more years of fellowship training; board certification in Cardiology preferred. Applicants will submit a letter of interest, stating a research plan, curriculum vitae, and the names of at least three references. For more information on the CCVR, visit **website: http://www.ccvr.uic.edu.**

Apply online only at **website: https://jobs.uic.edu/default.cfm?page=job&jobID=19131.**

UIC is an Affirmative Action/Equal Opportunity Employer.

POSTDOCTORAL POSITION in
Urologic Stem Cell Therapy

The Department of Urology at CWRU is seeking two junior scientists (MD or Ph.D.) with training and significant interest in studies of stem cells to take positions as postdoctoral fellows through an NIH Institutional Training Grant (T-32). The positions will focus on development of translational and clinical applications of mesenchymal stem cells in urology in collaboration with some of the most out renowned experts in the field. Competitive salary and benefits with the potential for recruitment after completion of fellowship will be offered. For additional information please contact **Laurel Jeffers** (**e-mail: laj17@case.edu** or **telephone: 216-844-1451**).

POSTDOCTORAL POSITION
Germline Stem Cells

Studies include culture, differentiation, and gene activity of male germline stem cells. See *Science* **316:**404, 2007 & *PNAS* **106:**21672, 2009. Send curriculum vitae, names of three references, and a letter describing research experience to: **R. L. Brinster, School of Veterinary Medicine, University of Pennsylvania. E-mail: cpope@vet.upenn.edu.**

POSITIONS OPEN

UNIVERSITY OF SOUTH CAROLINA
School of Medicine

FACULTY POSITION
Pharmacology, Physiology and Neuroscience
University of South Carolina
School of Medicine-Columbia

The Department of Pharmacology, Physiology and Neuroscience at the University of South Carolina School of Medicine in Columbia, South Carolina invites additional applications for a faculty position at the **ASSISTANT PROFESSOR** level. New faculty members will join a collegial and collaborative department at a university in the midst of an ambitious program to achieve national prominence in research and education. Candidates with research interests that complement the departmental research programs that focus on studying the molecular or cellular mechanisms underlying physiological processes, complex behaviors, or drug action are desirable, with priority given to our neuroscience-based research focus. Successful candidates will also be expected to participate in medical and graduate teaching. Applicants must have a doctoral degree and postdoctoral experience. Preference will be given to individuals with experience in medical education, funding success and potential, and research interests that enhance departmental programs targeting neurological and neuropsychiatric disorders. Substantial start-up funds and modern facilities will be provided. For junior investigators, the initial appointment could be a tenure stream position with transition into a tenure-track following establishment of a funded, independent research program and demonstration of teaching competency. Candidates with necessary credentials will be considered for immediate appointment on the tenure-track as an Assistant Professor.

Qualified applicants may apply by submitting a single electronic file (PDF or Word) that includes a cover letter summarizing qualifications, curriculum vitae and publication list, a statement of research plans and professional goals, and contact information for four references. The file should be attached to an e-mail message sent to **Dr. Lawrence Reagan** at **e-mail: ppn.search@uscmed.sc.edu** with "PPN Faculty Search" as the subject before June 15, 2012. For more information about the department including our research programs please visit **website: http://ppn.med.sc.edu/.**

The University of South Carolina is an Affirmative Action/Equal Opportunity Employer.

The Division of Basic Biomedical Sciences at the University of South Dakota's Sanford School of Medicine invites applications for a tenure-track faculty position at the **ASSISTANT PROFESSOR** level. Applicants should have a Ph.D. or M.D.-Ph.D. in Neuroscience, Molecular Biology, or a related discipline and at least two years of postdoctoral experience. We seek energetic, interactive individuals whose research interests include cellular mechanisms of learning and memory, stress, brain injury, addiction or nociception (see **websites: http://www.usd.edu/medical-school/biomedical-sciences/neurogroup/faculty.cfm** for a list of Neuroscience faculty and **http://www.usd.edu/medical-school/biomedical-sciences/faculty-and-staff.cfm** for a complete list of faculty within the Division of Basic Biomedical Sciences). Successful candidates will be expected to develop an independent, externally funded research program and to participate in teaching graduate or medical students. Excellent startup funds, state-funded salary commensurate with experience, and state-of-the-art research facilities in the new Lee Medical Science Building (Vermillion, South Dakota) will be provided. Application should include curriculum vitae, a summary of past research and teaching experience, a statement of research interests and future plans, as well as the names of three references. All materials should be sent to The University of South Dakota online employment **website: https://yourfuture.sdbor.edu.** Review of applications will begin on June 5, 2012 and continue until position is filled. *Women and minorities are encouraged to apply. Affirmative Action/Equal Opportunity Employer.*